



**CHANGES IN STRUCTURAL HEALTH MONITORING SYSTEM  
CAPABILITY DUE TO AIRCRAFT ENVIRONMENTAL FACTORS**

DISSERTATION

Jeffrey D. Kuhn, Major, USAF

AFIT/DS/ENV/09-S01

**DEPARTMENT OF THE AIR FORCE  
AIR UNIVERSITY**

**AIR FORCE INSTITUTE OF TECHNOLOGY**

**Wright-Patterson Air Force Base, Ohio**

APPROVED FOR PUBLIC RELEASE; DISTRIBUTION UNLIMITED.

The views expressed in this dissertation are those of the author and do not reflect the official policy or position of the United States Air Force, Department of Defense, or the United States Government.

CHANGES IN STRUCTURAL HEALTH MONITORING SYSTEM  
CAPABILITY DUE TO AIRCRAFT ENVIRONMENTAL FACTORS

DISSERTATION

Presented to the Faculty

Department of Systems and Engineering Management

Graduate School of Engineering and Management

Air Force Institute of Technology

Air University

Air Education and Training Command

In Partial Fulfillment of the Requirements for the

Degree of Doctor of Philosophy

Jeffrey D. Kuhn, BS, MS

Major, USAF


September 2009

APPROVED FOR PUBLIC RELEASE; DISTRIBUTION UNLIMITED.


CHANGES IN STRUCTURAL HEALTH MONITORING SYSTEM  
CAPABILITY DUE TO AIRCRAFT ENVIRONMENTAL FACTORS

Jeffrey D. Kuhn, BS, MS  
Major, USAF

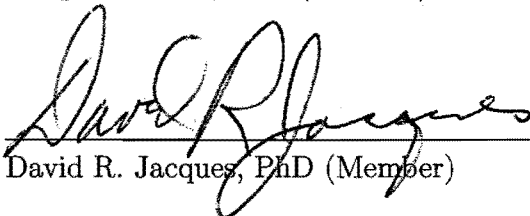
Approved:

  
\_\_\_\_\_  
Som R. Soni, PhD (Chairman)

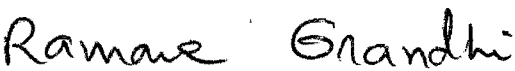
7 AUG 09  
Date

  
\_\_\_\_\_  
Joseph W. Carl, PhD (Member)

2009 August 7  
Date


  
\_\_\_\_\_  
David R. Jacques, PhD (Member)

12 AUG 09  
Date

  
\_\_\_\_\_  
Ramana V. Grandhi, PhD (Member)

8/7/09  
Date

Accepted:

  
\_\_\_\_\_  
M. U. Thomas, PhD  
Dean, Graduate School of  
Engineering and Management

9/1/09  
Date



*For my father; a man who spent years of his life doing the things he had to do so his children could grow up and do the things they want to do. For his sacrifices, I am eternally grateful.*

*Abstract*

Structural Health Monitoring (SHM) promises to decrease the maintenance cost and increase the availability of aging aircraft fleets by fundamentally changing the way structural inspections are performed. But this promise can only be realized through the consistent and predictable performance of a SHM system throughout the entire remaining life of an aircraft. In a sensor-based SHM system, sensor signal changes are analyzed and interpreted to identify structural flaws. But aircraft environmental factors such as temperature fluctuations, cyclic strain and exposure to various aircraft fluids also have the potential to change SHM sensor signals, raising questions about long term SHM system capability.

This research begins by analyzing the current USAF inspection paradigm, known aircraft environmental factors, representative structural inspection locations for the F-15 and C-130, and current SHM technologies. A design of experiments approach is used to build and execute an experiment to determine the effect of one aircraft environmental factor (cyclic strain) on a common SHM technology (PZT-based sensors). Analysis of the experimental results shows the sensors to be significantly affected by cyclic strain, and that the effects can be estimated using a power equation model.

A “probability of detection (POD) degradation model” is then developed by extending existing nondestructive evaluation (NDE) POD analysis techniques. This model demonstrates how changes in sensor performance due to an aircraft environmental factor can be used to estimate the change in overall performance of the SHM system. This POD degradation model provides a common framework to predict changes in SHM system performance over the remaining life of an aircraft. An example combining the experimental results with an existing SHM POD analysis shows how the POD degradation model can be applied to current SHM research.

## *Acknowledgements*

Thanks to my advisor Dr. Som Soni and to Dr. Joe Carl for the sound guidance and always interesting conversation. Thanks to my other committee members, Dr. David Jacques and Dr. Ramana Grandhi, for bringing this work full circle and providing much appreciated input during the many iterations of this effort. Many thanks also to Lt. Col Eric Swenson at AFIT, Dr. Jim Blackshire at AFRL and Dr. Eric Lindgren at AFRL for technical guidance and advice concerning PZT testing and POD(*a*) analysis. Thanks to the F-15 and C-130 System Program Offices at Robins AFB, GA for access to their technical documentation and to the Dayton Area Graduate Studies Institute for support and funding. And thanks to Bev Grunden at the Wright State University Statistical Consulting Center for excellent advice concerning the statistical analysis of my experimental results.

Recognition must also be given to the mentors and friends who have impacted my development as an officer, making this entire effort possible. To Col (ret.) Greg Postulka for starting me on this path, to Lt. Col Kelly Jost for being an excellent role model and friend during my transition from “engineer” to “Maintenance Officer”. To Chief (ret.) Dale Hulleman and Chief (ret.) Greg Hilliard for teaching me to recognize which battles should be fought and which should not. And to the men and women of Predator maintenance, serving in the arena every day with distinction.

Finally, to my family. Thanks to my mother and father for giving me two things I cherish most in my life: a healthy dose of common sense and a love of books. Most of all, I would like to thank my wife. Without her, I am nothing.

Jeffrey D. Kuhn

# Table of Contents

	Page
Abstract . . . . .	vi
Acknowledgements . . . . .	vii
List of Figures . . . . .	xii
List of Tables . . . . .	xvii
List of Abbreviations . . . . .	xx
List of Symbols . . . . .	xxii
I. Introduction . . . . .	1
1.1 Overview . . . . .	1
1.2 Uniqueness and Substantiality of Research . . . . .	1
1.3 Statement of Research Question . . . . .	2
1.4 Hypotheses and Research Objectives . . . . .	3
1.5 Assumptions/Limitations . . . . .	3
1.6 Dissertation Overview . . . . .	4
II. Background, Literature Review and Analysis . . . . .	6
2.1 Structural Health Monitoring as an Inspection Paradigm . . . . .	6
2.1.1 A Systems Engineering Approach to Structural Health Monitoring . . . . .	6
2.1.2 Designing a SHM System . . . . .	8
2.1.3 General Structural Health Monitoring Requirements . . . . .	12
2.1.4 Structural Health Monitoring Inspection Technologies . . . . .	14
2.2 The Current USAF Structural Inspection Paradigm . . . . .	18
2.2.1 MIL-STD-1530: The Aircraft Structural Integrity Program . . . . .	18
2.2.2 The USAF Nondestructive Inspection Program . . . . .	22
2.2.3 A Survey of Legacy Aircraft Inspection Locations . . . . .	27
2.3 Issues for Implementation of SHM on a Legacy Fleet . . . . .	33
2.3.1 Questions Concerning Long Term SHM Capability . . . . .	33
2.3.2 Critical Crack Length vs. Repairable Crack Length . . . . .	37
2.3.3 Organizational Roadblocks . . . . .	39

	Page
III. Experimentally Determining Changes in SHM Performance . . .	40
3.1 Introduction . . . . .	40
3.2 Selecting A SHM Technology for the Experiment . . . . .	41
3.3 A Brief Introduction to Lamb Waves and Their Use in SHM . . . . .	41
3.3.1 Lamb Waves Described . . . . .	41
3.3.2 Lamb Waves in Structural Health Monitoring . . . . .	45
3.3.3 Previous PZT Durability Testing . . . . .	47
3.4 Test Objectives for the Sensor Degradation Experiment . . . . .	53
3.5 General Test Elements . . . . .	53
3.5.1 Excitation Signal . . . . .	53
3.5.2 Response Variable . . . . .	54
3.5.3 The PZT Pitch-Catch Pair “Sensor” . . . . .	56
3.5.4 Test Specimens . . . . .	56
3.5.5 Test and Data Collection Equipment . . . . .	58
3.6 Experimental Design . . . . .	58
3.6.1 Defining Experimental Factors . . . . .	58
3.6.2 Mitigation of Nuisance Factors . . . . .	60
3.7 Establishing Experimental Phases . . . . .	63
3.8 Defining Phase 0: Test Definition and Preparation . . . . .	64
3.8.1 Objectives . . . . .	64
3.8.2 PZT Layout . . . . .	64
3.8.3 Validation of Specimen Fabrication Procedures . . . . .	67
3.8.4 Data Analysis MATLAB Code . . . . .	68
3.9 Defining Phase I: Static Strain Testing . . . . .	68
3.9.1 Objectives . . . . .	68
3.9.2 Setting the Maximum Strain Level . . . . .	69
3.9.3 Hypotheses for t-tests . . . . .	69
3.9.4 Required Sample Size and Factor Levels . . . . .	69
3.10 Defining Phase II: Cyclic Strain Testing . . . . .	72
3.10.1 Objective . . . . .	72
3.10.2 Hypotheses for t-tests . . . . .	72
3.10.3 Setting the Maximum Number of Cycles . . . . .	72
3.10.4 Required Sample Size and Factor Levels . . . . .	73
3.11 Summary of Test Specimens and Test Conditions . . . . .	75
3.12 Analysis Techniques for Experimental Results . . . . .	75
3.12.1 General Analysis Techniques . . . . .	75
3.12.2 Population Characterization . . . . .	75
3.12.3 Statistical t-tests . . . . .	77
3.12.4 Analysis of Variance . . . . .	81
3.12.5 Modeling the Results . . . . .	82

	Page
IV. PZT Cyclic Strain Experimental Results and Analysis . . . . .	83
4.1 Introduction and Overview . . . . .	83
4.2 Analysis of Baseline Results . . . . .	85
4.2.1 Pooling Baseline Results from the Seven Specimens . . . . .	85
4.2.2 Baseline Population Characterization . . . . .	85
4.2.3 Actual Response $\sigma$ vs. Assumed $\sigma$ and Required Analysis Adjustments . . . . .	88
4.2.4 t-test Results . . . . .	89
4.3 Static Test Results . . . . .	90
4.3.1 Feature Analysis . . . . .	90
4.3.2 t-test Results . . . . .	90
4.4 Cyclic Test Results: 800 $\mu\epsilon$ . . . . .	93
4.4.1 Feature Analysis . . . . .	93
4.4.2 t-test Results . . . . .	95
4.5 Cyclic Test Results: 1700 $\mu\epsilon$ . . . . .	97
4.5.1 Run 1 Results . . . . .	97
4.5.2 Run 2 Results . . . . .	100
4.5.3 Run 3 Results . . . . .	103
4.5.4 Combined Results . . . . .	106
4.5.5 Feature Analysis . . . . .	106
4.5.6 t-test Results . . . . .	106
4.6 Cyclic Test Results: 2600 $\mu\epsilon$ . . . . .	109
4.6.1 Run 1 Results . . . . .	109
4.6.2 Run 2 Results . . . . .	112
4.6.3 Combined Results . . . . .	115
4.6.4 Feature Analysis . . . . .	115
4.6.5 t-test Results . . . . .	116
4.7 Summary of t-test Results and General Observations . . . . .	118
4.8 Modeling the Results . . . . .	123
4.8.1 Power Equation Models . . . . .	123
4.8.2 Other Modeling Attempts . . . . .	128
V. Linking Experimental Results to Changes in Probability of Detection . . . . .	129
5.1 Introduction . . . . .	129
5.2 Building a POD( $a$ ) curve using MIL-HDBK-1823 . . . . .	129
5.3 Building a Notional ROC Curve . . . . .	133
5.4 Incorporating Sensor Degradation Information into POD( $a$ ) . . . . .	137
5.4.1 SHM Systems where $\hat{a}$ Increases with Increasing Crack Size . . . . .	138

	Page
5.4.2 Changes to the MIL-HDBK-1823 Technique when $\hat{a}$ Decreases with Increasing Crack Size . . . . .	143
5.5 A POD( $a$ ) “Degradation” Model . . . . .	146
5.5.1 Modifying the Regression Intercept, $\beta_0$ , Using Degradation Coefficient $\alpha_d$ . . . . .	147
5.5.2 Modifying the Regression Slope, $\beta_1$ , Using Degradation Coefficient $\gamma_d$ . . . . .	149
5.5.3 Modifying the Threshold Detection Value, $\hat{a}_{th}$ , Using Degradation Coefficient $\rho_d$ . . . . .	152
5.5.4 Modifying the Regression Residual Standard Deviation, $\delta$ , Using Degradation Coefficient $\psi_d$ . . . . .	153
5.6 Applying the POD( $a$ ) Degradation Model Using Experimental Data . . . . .	155
5.6.1 Degradation of a Single Parameter . . . . .	155
5.6.2 Simultaneous Degradation of Multiple Parameters . . . . .	159
5.6.3 A POD( $a, n$ ) Surface . . . . .	162
5.7 An Illustrative Example Using an Ultrasonic SHM Sensor POD( $a$ ) . . . . .	163
5.7.1 System Introduction . . . . .	163
5.7.2 Cobb’s POD( $a$ ) Curve . . . . .	164
5.7.3 Building a ROC Curve With Cobb’s Data . . . . .	166
5.7.4 The Effects of Sensor Degradation . . . . .	168
5.7.5 Degradation Coefficients for Cobb’s Data . . . . .	170
5.8 Summary . . . . .	172
VI. Conclusions . . . . .	174
6.1 Addressing the Research Objectives . . . . .	174
6.2 Conclusions Based on Experimental Results and Analysis . . . . .	175
6.3 General Conclusions . . . . .	176
6.4 Recommendations for Application . . . . .	177
6.5 Recommended Questions for Future Research . . . . .	178
Appendix A. PZT Installation Instructions . . . . .	180
Appendix B. Representative Test Plan . . . . .	191
Bibliography . . . . .	209

## *List of Figures*

Figure		Page
2.1.	Notional SHM System Overview . . . . .	7
2.2.	Members of the USAF SHM community . . . . .	8
2.3.	SHM System Design Using AFRL's Hot Spot Monitoring Program	9
2.4.	SHM System Requirements Development Activity Model [3] . .	10
2.5.	Representative SHM Physical Configuration . . . . .	11
2.6.	Representative SHM Architecture . . . . .	12
2.7.	Comparative Vacuum Monitoring Sensor Design and Application	15
2.8.	Comparative Vacuum Monitoring Example POD( <i>a</i> ) Curve . . .	16
2.9.	PZT Pitch Catch Sensor Concept . . . . .	16
2.10.	Experimental POD( <i>a</i> ) Data for Pitch Catch PZTs on an Aluminum Lap Joint . . . . .	17
2.11.	Representative Crack Size vs. Operating Hour Curves . . . . .	20
2.12.	Field Level F-15C/D IAT Inspection Locations . . . . .	22
2.13.	Example Probability of Detection Curves . . . . .	26
2.14.	Eddy Current POD( <i>a</i> ) Curve . . . . .	27
2.15.	Florescent Penetrant POD( <i>a</i> ) Curve . . . . .	28
2.16.	Ultrasonic Inspection POD( <i>a</i> ) Curve . . . . .	28
2.17.	X-ray Inspection POD( <i>a</i> ) Curve . . . . .	29
2.18.	C-130 Major Components . . . . .	30
2.19.	Representative C-130 Inspection Location . . . . .	31
2.20.	Crack Growth Curve for the C-130 Inspection Location . . . .	32
2.21.	F-15 Major Components . . . . .	32
2.22.	Representative F-15 Inspection Location . . . . .	34
2.23.	DTA Parameters for a Representative F-15 Inspection Location	35
2.24.	Cause and Effect Diagram for SHM Response Changes . . . . .	36



Figure		Page
2.25.	Cause and Effect Diagram for SHM Response Changes due to Environmental Factors . . . . .	37
3.1.	Representative SHM Sensor Distribution . . . . .	40
3.2.	Lamb Wave Mode Forms . . . . .	43
3.3.	Lamb Wave Group Velocity . . . . .	45
3.4.	$S_0$ and $A_0$ Excitation Based on Frequency . . . . .	46
3.5.	Lamb Wave Excitation Signal . . . . .	47
3.6.	Experimental Response Variable . . . . .	54
3.7.	Dogbone Specimen Prior to Sensor Installation . . . . .	57
3.8.	Flat Plate Specimen . . . . .	57
3.9.	Completed Dogbone Test Specimen . . . . .	58
3.10.	Data Acquisition System . . . . .	59
3.11.	Instrumentation Variability Test Results . . . . .	62
3.12.	Initial PZT Pitch-Catch Configuration . . . . .	65
3.13.	Simulated PZT Layouts . . . . .	66
3.14.	Test Specimen Fabrication . . . . .	67
3.15.	Final Test Equipment Configuration . . . . .	68
3.16.	Experimental Load Levels Plotted on the 6061-T6 Stress-Strain Curve . . . . .	74
3.17.	Initial Experimental Data Sample Description . . . . .	76
3.18.	Method to Apply Multiple t-tests . . . . .	81
4.1.	Final Experimental Data Sample Description . . . . .	84
4.2.	Baseline MBond Responses by Specimen . . . . .	86
4.3.	Baseline Epoxy Responses by Specimen . . . . .	86
4.4.	Baseline Responses by Glue Type . . . . .	88
4.5.	MBond Static Test Results . . . . .	91
4.6.	Epoxy Static Test Results . . . . .	91
4.7.	Average Static Test Results . . . . .	92

Figure		Page
4.8.	MBond 800 $\mu\epsilon$ Cyclic Test Results . . . . .	94
4.9.	Epoxy 800 $\mu\epsilon$ Cyclic Test Results . . . . .	94
4.10.	Average 800 $\mu\epsilon$ Cyclic Test Results . . . . .	95
4.11.	MBond 1700 $\mu\epsilon$ Cyclic Test Results from Run 1 . . . . .	97
4.12.	Epoxy 1700 $\mu\epsilon$ Cyclic Test Results from Run 1 . . . . .	98
4.13.	Average 1700 $\mu\epsilon$ Cyclic Test Results from Run 1 . . . . .	98
4.14.	MBond 1700 $\mu\epsilon$ Cyclic Test Results from Run 2 . . . . .	100
4.15.	Epoxy 1700 $\mu\epsilon$ Cyclic Test Results from Run 2 . . . . .	101
4.16.	Average 1700 $\mu\epsilon$ Cyclic Test Results from Run 2 . . . . .	101
4.17.	MBond 1700 $\mu\epsilon$ Cyclic Test Results from Run 3 . . . . .	103
4.18.	Epoxy 1700 $\mu\epsilon$ Cyclic Test Results from Run 3 . . . . .	104
4.19.	Average 1700 $\mu\epsilon$ Cyclic Test Results from Run 3 . . . . .	104
4.20.	Average 1700 $\mu\epsilon$ Cyclic Test Results . . . . .	106
4.21.	MBond 2600 $\mu\epsilon$ Cyclic Test Results from Run 1 . . . . .	109
4.22.	Epoxy 2600 $\mu\epsilon$ Cyclic Test Results from Run 1 . . . . .	110
4.23.	Average 2600 $\mu\epsilon$ Cyclic Test Results from Run 1 . . . . .	110
4.24.	MBond 2600 $\mu\epsilon$ Cyclic Test Results from Run 2 . . . . .	112
4.25.	Epoxy 2600 $\mu\epsilon$ Cyclic Test Results from Run 2 . . . . .	113
4.26.	Average 2600 $\mu\epsilon$ Cyclic Test Results from Run 2 . . . . .	113
4.27.	Average 2600 $\mu\epsilon$ Cyclic Test Results . . . . .	115
4.28.	Combined MBond Pitch-Catch Pair Test Results . . . . .	123
4.29.	Combined Epoxy Pitch-Catch Pair Test Results . . . . .	124
4.30.	Power Function, $x^n$ . . . . .	124
4.31.	Best-fit Power Equation Exponents Plotted Against Cyclic Strain Level . . . . .	126
4.32.	Power Model Fit to MBond Pitch-Catch Responses . . . . .	127
4.33.	Power Model Fit to Epoxy Pitch-Catch Responses . . . . .	127
5.1.	POD( $a$ ) Derivation . . . . .	130

Figure		Page
5.2.	Relationship Between Threshold Detection Level and $POD(a)$ .	132
5.3.	$\ln(a)$ vs. $\ln(\hat{a})$ Regression Line Generated from MIL-HDBK-1823 Data . . . . .	133
5.4.	$POD(a)$ Curve Generated from MIL-HDBK-1823 Data . . . . .	134
5.5.	Crack Detection Confusion Matrix . . . . .	135
5.6.	Values Used to Build ROC Curves . . . . .	135
5.7.	Notional ROC Curve Based on MIL-HDBK-1823 Data . . . . .	137
5.8.	Response Distribution Locations for SHM Systems with $\hat{a}$ Increasing with Increasing $a$ . . . . .	139
5.9.	20% “Degraded” MIL-HDBK-1823 Data . . . . .	140
5.10.	Sensor Response Distribution Change Due to Degradation . . . . .	140
5.11.	20% “Degraded” $POD(a)$ Curve from MIL-HDBK-1823 Data . . . . .	141
5.12.	20% “Degraded” ROC Curve from MIL-HDBK-1823 Data . . . . .	141
5.13.	Sensor Response Distribution Shift Due to Degradation . . . . .	143
5.14.	Response Distribution Locations for SHM Systems with $\hat{a}$ Decreasing with Increasing $a$ . . . . .	144
5.15.	Notional Linear Regression When $\hat{a}$ Decreases With Increasing Crack Size . . . . .	145
5.16.	Changes in Distance Between Undamaged and Damaged Mean $\hat{a}$ due to Sensor Degradation . . . . .	145
5.17.	$POD(a)$ Changes due to Changing $\alpha_d$ . . . . .	148
5.18.	ROC Curve Changes due to Changing $\alpha_d$ . . . . .	148
5.19.	Regression Line Changes due to Changing $\alpha_d$ . . . . .	149
5.20.	$POD(a)$ Changes due to Changing $\gamma_d$ . . . . .	150
5.21.	ROC Changes due to Changing $\gamma_d$ . . . . .	150
5.22.	Regression Line Changes due to Changing $\gamma_d$ . . . . .	151
5.23.	$POD(a)$ Changes due to Changing $\rho_d$ . . . . .	152
5.24.	$POD(a)$ Changes due to Changing $\psi_d$ . . . . .	153
5.25.	ROC Changes due to Changing $\psi_d$ . . . . .	154

Figure		Page
5.26.	Signal Degradation Due to Cycling at $1700 \mu\epsilon$ . . . . .	156
5.27.	POD( $a$ ) Changes Based on Experimental Results . . . . .	157
5.28.	ROC Curve Changes Based on Experimental Results . . . . .	157
5.29.	POD( $a$ ) Changes Based on Experimental Results Cycling at $2600 \mu\epsilon$ . . . . .	160
5.30.	ROC Curve Changes Based on Experimental Results Cycling at $2600 \mu\epsilon$ . . . . .	161
5.31.	A POD( $a, n$ ) Surface . . . . .	162
5.32.	Ultrasonic SHM Technique Used by Cobb [79] . . . . .	164
5.33.	Regression Line Recreated from Cobb's Data . . . . .	166
5.34.	POD( $a$ ) Curve Recreated from Cobb's Data . . . . .	167
5.35.	ROC Curve Derived from Cobb's Data . . . . .	168
5.36.	Degrading Cobb's Regression . . . . .	169
5.37.	Degrading Cobb's POD( $a$ ) Curve . . . . .	170
5.38.	Degrading Cobb's ROC Curve . . . . .	170
5.39.	Degradation of Cobb's POD( $a$ ) Curve . . . . .	171
5.40.	Degradation of Cobb's ROC Curve . . . . .	172
5.41.	POD( $a, n$ ) Surface for Cobb's Data Based on Numbers of Cycles	173

## *List of Tables*

Table		Page
2.1.	SHM System-Level Requirements . . . . .	13
2.2.	SHM Inspection-level Requirements . . . . .	14
2.3.	Minimum Critical Crack Lengths for C-130 Major Components	30
2.4.	Minimum Critical Crack Lengths for C-130 Major Components	33
2.5.	Repairable Crack Size Based on Oversized Fastener Diameters .	38
3.1.	AFRL PZT Durability Testing Parameters . . . . .	48
3.2.	AFRL PZT Durability Testing Results . . . . .	48
3.3.	Metis Corp PZT Durability Testing Parameters [22] . . . . .	50
3.4.	Metis Corp SHM Durability Tests and Summary Results [22] .	51
3.5.	Accellent Technologies PZT Sensor Load Testing Parameters [66]	52
3.6.	Accellent Technologies Sensor Load Tests [62] . . . . .	52
3.7.	Potential Experimental Design Factors . . . . .	59
3.8.	Potential Experimental Nuisance Factors . . . . .	60
3.9.	Specimen Properties . . . . .	69
3.10.	General Static Test Hypotheses . . . . .	70
3.11.	Probability of Type II Error for Multiple Sample Sizes . . . . .	72
3.12.	Determining Required Number of Pith-Catch Pairs . . . . .	72
3.13.	Static Strain Test Schedule . . . . .	72
3.14.	General Cyclic Strain Test Hypotheses . . . . .	73
3.15.	Cyclic Strain Load Schedule . . . . .	75
3.16.	Guidelines for Interpreting t-test Effect Sizes, from [28] . . . . .	77
4.1.	Test Runs and Specimen Names . . . . .	84
4.2.	MBond Baseline Response ANOVA Results . . . . .	87
4.3.	MBond Baseline Response ANOVA Results . . . . .	87
4.4.	Static Strain Test Results . . . . .	92

Table		Page
4.5.	800 $\mu\epsilon$ Cyclic Test Results . . . . .	96
4.6.	1700 $\mu\epsilon$ Run 1 Cyclic Test Results . . . . .	99
4.7.	1700 $\mu\epsilon$ Run 2 Cyclic Test Results . . . . .	102
4.8.	1700 $\mu\epsilon$ Run 3 Cyclic Test Results . . . . .	105
4.9.	1700 $\mu\epsilon$ Combined Cyclic Test Results . . . . .	107
4.10.	2600 $\mu\epsilon$ Run 1 Cyclic Test Results . . . . .	111
4.11.	2600 $\mu\epsilon$ Run 2 Cyclic Test Results . . . . .	114
4.12.	2600 $\mu\epsilon$ Combined Cyclic Test Results . . . . .	116
4.13.	Summary of Static Strain t-test Results . . . . .	118
4.14.	Summary of 800 $\mu\epsilon$ Cyclic Strain t-test Results . . . . .	119
4.15.	Summary of MBond Pair 1700 $\mu\epsilon$ Cyclic Strain t-test Results .	119
4.16.	Summary of Epoxy Pair 1700 $\mu\epsilon$ Cyclic Strain t-test Results . .	120
4.17.	Summary of MBond Pair 2600 $\mu\epsilon$ Cyclic Strain t-test Results .	121
4.18.	Summary of Epoxy Pair 2600 $\mu\epsilon$ Cyclic Strain t-test Results . .	122
4.19.	MBond Response Power Fit Coefficients . . . . .	125
4.20.	Epoxy Response Power Fit Coefficients . . . . .	125
4.21.	JMP Analysis Initial Conditions . . . . .	126
5.1.	Degradation Impacts on Detection Capabilities . . . . .	139
5.2.	Original and Degraded $\ln(a)$ vs. $\ln(\hat{a})$ Data . . . . .	142
5.3.	Baseline POD( $a$ ) Coefficients . . . . .	147
5.4.	$\alpha_d$ Impact On $a_{90}$ and FAR . . . . .	149
5.5.	$\gamma_d$ Impact On $a_{90}$ and FAR . . . . .	151
5.6.	$\rho_d$ Impact On $a_{90}$ . . . . .	152
5.7.	$\psi_d$ Impact On $a_{90}$ and FAR . . . . .	154
5.8.	$\alpha_d$ Calculations Based on Experimental Results . . . . .	156
5.9.	False Alarm Rate and $a_{90}$ Increases Due to Experimentally Ad- justed $\alpha_d$ Cycling at 1700 $\mu\epsilon$ . . . . .	158
5.10.	False Alarm Rate and $a_{90}$ Increases Due to Experimentally Ad- justed $\alpha_d$ Cycling at 2600 $\mu\epsilon$ . . . . .	160

Table		Page
5.11.	Cobb's [27] Ultrasonic SHM Data . . . . .	164
5.12.	Degradation Coefficients Used to Show Changes in Cobb's POD( $a$ )	172

## *List of Abbreviations*

AF	Aft Fuselage
AFRL	Air Force Research Laboratory
ANOVA	Analysis of Variance
ASIP	Aircraft Structural Integrity Program
CF	Center Fuselage
CVM	Comparative Vacuum Monitoring
CW	Center Wing
DTA	Damage Tolerance Analysis
ER	Energy Raio
FAR	False Alarm Rate
FF	Forward Fuselage
FSMP	Force Structural Maintenance Plan
$H_0$	Null hypothesis for statistical t-tests
HS	Horizontal Stabilizer or Horizontal Stabilator (when referring to the F-15)
IAT	Individual Aircraft Tracking
IW	Inner Wing
JCIDS	Joint Capabilities Integration and Development System
kip	1000 pound force
MTS	Material Test System
NDE	Nondestructive Evaluation
NDI	Nondestructive Inspection
NDS	Normalized Degraded Signal
OC	Operating Characteristic
OW	Outer Wing
Pk	Peak
POD	Probability of Detection
POD( $a$ )	Probability of Detection of flaw size $a$
POI	Probability of Inspection
Pr	Probability
PZT	Piezoelectric Transducer



ROC	Receiver Operating Characteristic
RSS	Root Sum Square
SHM	Structural Health Monitoring
SPO	System Program Office
TBD	To be determined
TOF	Time of Flight
VS	Vertical Stabilizer
USAF	United States Air Force

## *List of Symbols*

$\alpha$	Probability of committing a Type I error
$\alpha_d$	Degradation coefficient to model $\beta_0$ changes in the POD( $a$ ) calculation
$\beta$	Probability of committing a Type II error
$\beta_0$	Intercept of the regression line derived from $a$ vs. $\hat{a}$ data
$\beta_1$	Slope of the regression line derived from $a$ vs. $\hat{a}$ data
$\gamma_d$	Degradation coefficient to model $\beta_1$ changes in the POD( $a$ ) calculation
$\delta$	Standard deviation of the residuals of a linear regression fit to $a$ vs. $\hat{a}$ data
$\varepsilon$	Residuals of a linear regression fit to $a$ vs. $\hat{a}$ data
$\epsilon$	Strain measured in inches per inch (in/in)
$\epsilon_{ty}$	Yield strain
$\eta/\eta_0$	Ratio of current and original sensor signal amplitude used by Kusaka [62] to measure changes in SHM sensor performance
$\mu$	Natural log of the crack length detected 50% of the time when modeling POD( $a$ ) using the log-logistic function
$\mu_{Specimen}$	Average response of all pitch-catch PZT pairs of one glue type on the given specimen prior to testing
$\mu\epsilon$	Microstrain (Strain * $10^6$ )
$\nu_1$	Numerator degrees of freedom when calculating $\Phi$ for use in operating characteristic curves
$\nu_2$	Denominator degrees of freedom when calculating $\Phi$ for use in operating characteristic curves
$\xi_0, \xi_1, \text{etc.}$	Coefficients to model changes in SHM sensor response
$\rho_d$	Degradation coefficient to model $\hat{a}_{th}$ changes in the POD( $a$ ) calculation
$\sigma$	Scale parameter when modeling POD( $a$ ) using the log-logistic function
$\sigma$	Response variable standard deviation when calculating $\Phi$ for use in operating characteristic curves
$\sigma$	Response standard deviation of a group of PZT pitch-catch pairs at a given test condition

$\Phi$	Parameter plotted against the probability of committing a Type II error in an Operating Characteristic curve
$\Phi(z)$	Standardized normal probability when calculating probability of detection
$\phi$	Potential function in the plane strain wave equations for longitudinal and shear waves in a free plate
$\psi$	Potential function in the plane strain wave equations for longitudinal and shear waves in a free plate
$\psi_d$	Degradation coefficient to model $\delta$ changes in the POD( $a$ ) calculation
$\omega$	Angular or circular frequency
$A_k$	Antisymmetric Lamb wave mode with wave number “k” ( $A_0$ , $A_1$ , etc)
$a$	Structural crack size or flaw size
$a$	Number of “Factor A” levels when calculating $\Phi$ for use in operating characteristic curves.
$\hat{a}$	Measured response of a NDE system to a flaw of size $a$ . Units depend on the inspection system, but may be in millivolts, scale divisions, counts, etc.
$a_{50}$	Crack size at 50% probability of detection
$a_{90}$	Crack size at 90% probability of detection
$a_{min}$	Minimum detectable crack size for a given NDI technique
$a_{test}$	Cross sectional area of the dogbone specimen test area
$\hat{a}_{th}$	Signal threshold for a NDE system. The value of $\hat{a}$ below which the signal is indistinguishable from noise.
$b$	Number of “Factor B” levels when calculating $\Phi$ for use in operating characteristic curves.
$c_g$	Lamb wave group velocity
$c_L$	Longitudinal wave speed
$c_p$	Phase velocity of a given Lamb wave mode
$c_T$	Transverse wave speed
$D$	Desired change in response variable to be considered significant when calculating $\Phi$ for use in operating characteristic curves.
$d$	Statistic to calculate the “effect size” of a t-test (see [28, 65])
$E$	Dogbone specimen elastic modulus
$f$	Frequency

$fd$	Lamb wave frequency * plate thickness
$F_{ty}$	Yield strength
$g(\hat{a} a)$	Probability density function of $\hat{a}$ values given crack size $a$
$i$	$\sqrt{-1}$
$k$	Lamb wave number
lbf	Pound force
$n$	Number of sensors when calculating $\Phi$ for use in operating characteristic curves.
$n$	Power equation exponent when modeling changes in PZT pitch-catch pair response
$S_k$	Symmetric Lamb wave mode with wave number “k” ( $S_0$ , $S_1$ , etc)
T	Aircraft operating hours
t	Time

# CHANGES IN STRUCTURAL HEALTH MONITORING SYSTEM CAPABILITY DUE TO AIRCRAFT ENVIRONMENTAL FACTORS

## I. Introduction

### *1.1 Overview*

The United States Air Force (USAF) currently has a robust aircraft Structural Health Monitoring (SHM) system for legacy aircraft: airmen physically inspecting airplanes. But is there a better way? After more than a decade of intensive world-wide research into sensing, prognostics, modeling and integration technologies, the outline of a structural inspection paradigm that relies more on a technology intensive sensing-predicting philosophy than the current manpower intensive inspecting-reacting philosophy is beginning to emerge. But two interrelated issues still hamper the transition to this new paradigm: questions surrounding long-term SHM system cost and capability. A practical technology-based SHM system must prove to be more cost effective and provide an equivalent (if not higher) level of flight safety than the current inspection paradigm. While an obvious and simple statement, the analysis and testing required to prove a given SHM system contains these attributes is neither obvious, nor simple.

This dissertation looks at current structural inspection analysis techniques to define SHM durability experiments and analyses to assist in the transition away from the current labor-intensive structural inspection paradigm.

### *1.2 Uniqueness and Substantiality of Research*

Knowledge of the long term behavior of SHM systems is critical for their implementation. A SHM system that deteriorates unpredictably or excessively will itself require maintenance, reducing the labor savings that justified the system's installation. This research develops and demonstrates a method to model changes in SHM

system capability due to extended exposure to the aircraft environment. The method reaches past basic SHM sensor performance criteria and begins to address questions such as: “How does this sensor perform after being attached to a center wing spar in a C-130 fuel tank for 10 years?” It also reaches past the traditional definition of failure rates to address the fact that SHM sensor responses may change due to environmental factors without the sensor “failing” in the traditional sense.

This research investigates SHM sensor response changes using a design of experiments approach. Frequently, SHM durability studies subject a small number of sensors to a set of conditions and report the resulting changes in signal [15, 62]. By using design of experiments, a statistically significant sample size can be found to make inferences concerning the effects of an aircraft environmental factor on SHM sensor performance. But changes in raw sensor performance do not necessarily relate directly to changes in SHM system performance. With the goal of SHM sensors being to detect structural flaws, a 10% change in sensor performance may not produce a 10% drop in detectable flaw size. This research modifies Probability of Detection (POD) techniques currently used in the non-destructive evaluation field to define the capability of a given SHM system. Response models built from experimental data then demonstrate how changes in raw SHM sensor response can change SHM system capability in terms readily understandable by engineers responsible for ensuring aircraft structural safety.

By rooting measures of SHM performance in methods currently in use by structural engineers in the non-destructive evaluation field and in aircraft System Program Offices (SPO), this research provides a path to move the USAF from a 100% manual inspection paradigm toward a future where technology-based inspections are commonplace.

### ***1.3 Statement of Research Question***

How can changes to the capability of a Structural Health Monitoring system due to aircraft environmental factors be determined and modeled?

## ***1.4 Hypotheses and Research Objectives***

It is hypothesized that aircraft environmental factors will detrimentally impact the performance of a SHM system. It is also hypothesized that these effects can be identified and modeled, and changes in SHM performance can be estimated by modifying techniques used to characterize the performance of current non-destructive evaluation systems. To confirm these hypotheses, the following research questions are investigated:

1. What environmental conditions must a feasible SHM system withstand?
2. How can changes in SHM performance due to environmental factors be determined in a statistically significant manner?
3. How can changes in SHM performance due to aircraft environmental factors be modeled?
4. Demonstrate how models that define changes in SHM performance due to environmental factors can be incorporated into existing SHM system performance calculations.

## ***1.5 Assumptions/Limitations***

Depending on the audience, the phrase “structural health monitoring” cover activities ranging from the mining of existing maintenance data, through the design of detailed finite element models of large aircraft structural components, to the development of sensors to detect structural flaws at the micron scale. This research limits the breadth and scope of the SHM field to the most basic element of an on-aircraft SHM system: sensor-airframe interaction. By focusing on one aspect of this interaction (sensor changes due to strain), methods and models have been developed that can measure changes in SHM capability that can then be applied to a wide range of changing conditions.

## ***1.6 Dissertation Overview***

This research presentation begins with a description of how the USAF currently maintains the structural health of its aircraft, and ends by presenting a method to determine how aircraft environmental factors affect the performance of an SHM system after installation. Often, SHM is presented as a “revolutionary” change to the way aircraft structural health is maintained. This research treats SHM as an “evolutionary” change that can be readily incorporated into the existing Air Force structure and methods that have been developed over the last 50 years.

Chapter II establishes the baseline by (1) describing the current methods for ensuring aircraft structural health; (2) conducting a survey of current structural inspection locations for a USAF legacy fighter (F-15) and cargo (C-130) aircraft; (3) reviewing current proposals for aircraft SHM systems; (4) describing current SHM technologies under development and (5) identifying potential roadblocks the USAF faces in the implementation of SHM on its legacy aircraft fleets.

Chapter III begins to address one of the SHM implementation roadblocks by building an experiment to evaluate the changes in SHM sensor performance due to an aircraft environmental factor. The chapter (1) provides a technical overview of the SHM technology under test, (2) describes the general test set-up to be used, (3) uses design of experiments techniques to identify experimental factors and required sample sizes and (4) presents hypotheses for testing and modeling techniques to be used for data analysis.

Chapter IV presents the results and initial analysis of the test designed and described in Chapter III. Results from hypothesis tests are presented, and several model forms are fit to the experimental data.

Chapter V expands a current method of determining NDE capability to SHM techniques. Specifically, this chapter presents modifications to probability of detection calculations to account for changes in SHM sensor performance due to aircraft environmental factors. The modified probability of detection model is then used to combine



the experimental results from Chapter IV with existing probability of detection of crack size  $a$  ( $\text{POD}(a)$ ) calculations from a similar SHM technology to demonstrate how degradation of sensor performance can affect SHM system capability.

Chapter VI summarizes research conclusions and provides recommendations for applications and topics for further research. Several appendices include test sample fabrication instruction, detailed test plans, raw test data, MATLAB data analysis code, and supporting information from other research efforts.

## II. Background, Literature Review and Analysis

### 2.1 *Structural Health Monitoring as an Inspection Paradigm*

No agreed definition of “structural health monitoring” exists. To some in the aerospace community, the term describes the goal of a specific sensor research project currently under way. To others, “structural health monitoring” exists only as a small subset of an overall integrated vehicle health management system. Given SHM’s broad reach, this section sets the perspective and defines the scope of this research by introducing a high level notional SHM system and then decomposing it to the level of interest. The section also describes the roles and positions of several USAF SHM stakeholders who provided guidance concerning the SHM perspective described below.

#### 2.1.1 *A Systems Engineering Approach to Structural Health Monitoring.*

2.1.1.1 *The Need for Systems Engineering.* Figure 2.1 provides an overview of a representative notional SHM system for a legacy aircraft. The figure depicts a SHM system using various sensors to monitor structural locations and aircraft parameters on an aircraft fleet, and providing information to various users including not only individual aircraft health and required maintenance actions, but also information on overall fleet health for decision makers at higher levels.

The large number of engineering disciplines required for the successful development and implementation of a SHM system can be inferred from the figure. As described by Beard, et al. [6], “Structural health monitoring technology is perceived as a revolutionary method of determining the integrity of structures involving the use of multidisciplinary fields including sensors, materials, signal processing, system integration and signal interpretation”. Because of SHM’s expansive nature, systems engineering approaches are particularly suited to SHM problems. The International Council on systems engineering defines Systems Engineering as an “interdisciplinary approach and means to enable the realization of successful systems. It focuses on defining customer needs and required functionality early in the development cycle,

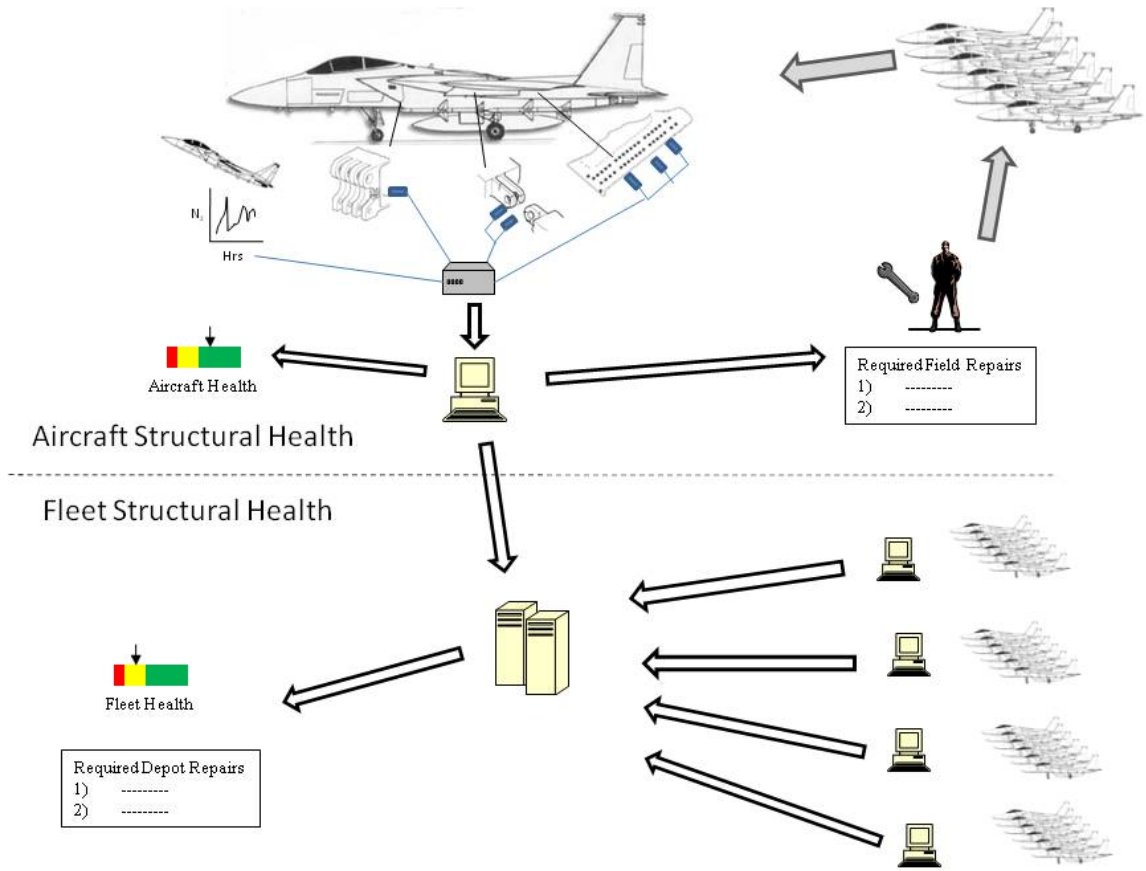


Figure 2.1: SHM could monitor both individual aircraft and fleet structural health documenting requirements, then proceeding with design synthesis and system validation while considering the complete problem of Operations, Cost and Schedule, Performance, Training and Support, Test, Disposal and Manufacturing” [55]. Previous systems engineering analyses used *structured analysis* activity models [3] and Joint Capabilities Integration and Development System (JCIDS) analysis [19] to define “top-level” SHM requirements and analyze the activities required to implement a SHM system on an aging aircraft (see section 2.1.2.1).

*2.1.1.2 The USAF SHM Community.* To ensure the relevance of this research, USAF SHM stakeholders were consulted concerning the requirements and direction of USAF SHM development efforts. Figure 2.2 shows the stakeholders and

their focus areas. Unlike the centralized development of a weapon system with a controlling SPO, the USAF SHM community consists of a set of independent groups, each pursuing a particular aspect of SHM development or focused on a particular SHM project. No centralized organization to coordinate efforts or to disseminate lessons-learned exists within the USAF. Figure 2.1 reflects the SHM perspectives concerning legacy aircraft SHM systems.

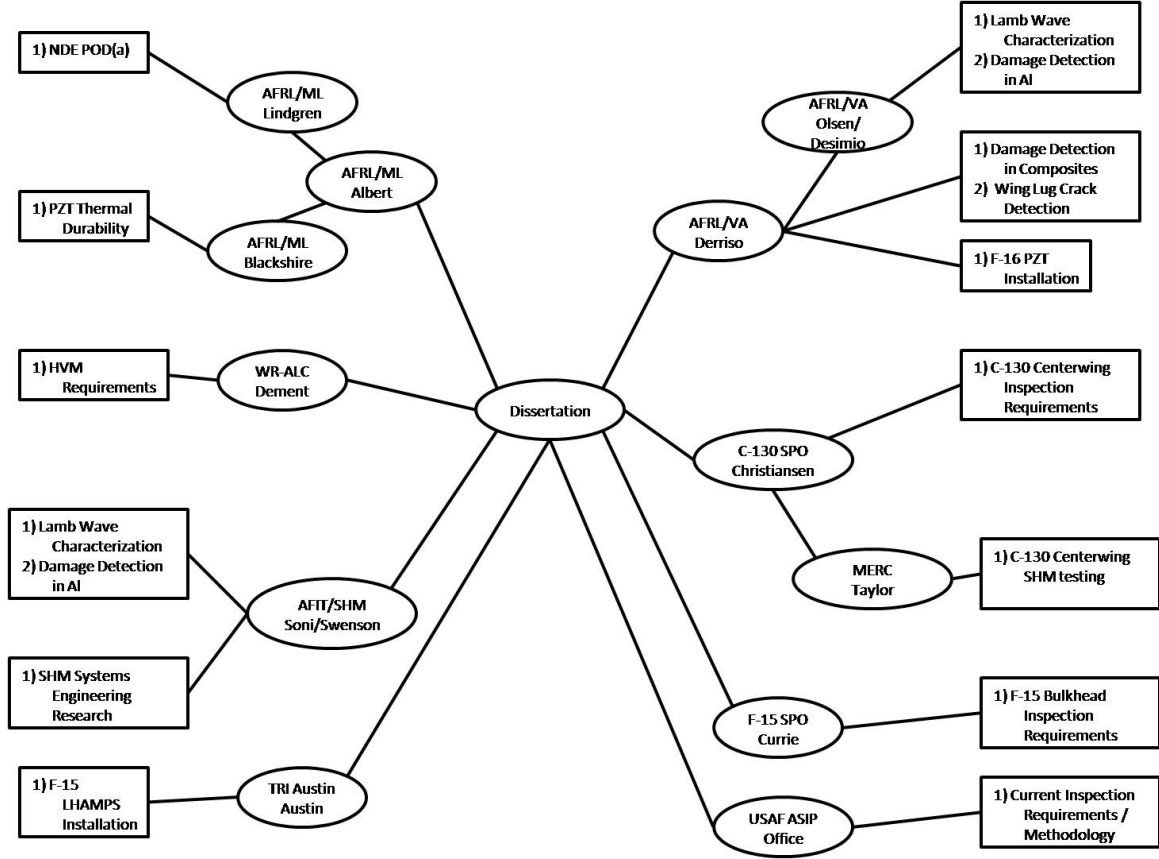


Figure 2.2: Members of the USAF SHM community consulted during research

### 2.1.2 Designing a SHM System.

#### 2.1.2.1 Methods to Define SHM Systems.

The SHM literature contains limited discussion about how to develop a SHM system. The literature's primary foci are specific technologies, generic architectures and general requirements. But two works do propose methodologies to develop SHM systems.

Malkin, et al. [72], discuss the development of SHM systems in the context of the Air Force Research Lab’s (AFRL) “Hot Spot Monitoring Program”. This program focuses on developing SHM technologies and systems to automatically determine the amount of structural damage that exists at predefined locations [44, 45]. Figure 2.3 shows the developmental steps proposed by AFRL.

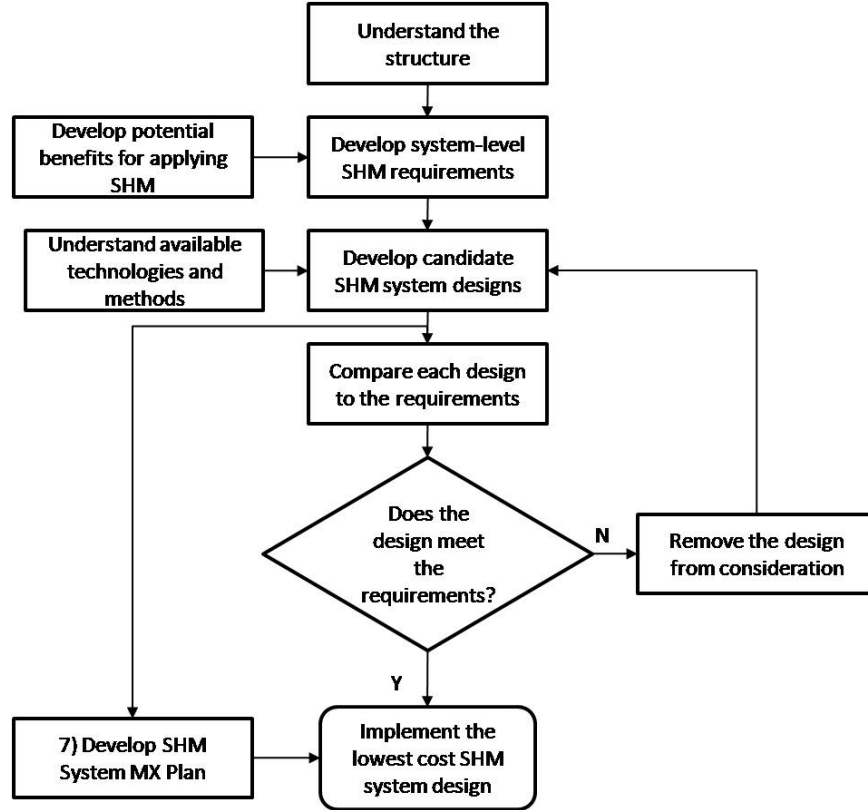


Figure 2.3: SHM system design steps for AFRL’s Hot Spot Monitoring Program [72]

Alan, et al. [3], focused on the SHM requirements generation process and identified four major functions to define a SHM system. Figure 2.4 uses IDEF0 modeling as described by Buede [21] to show the proposed functions with corresponding inputs, controls, outputs and mechanisms.

*2.1.2.2 Proposed SHM Architectures.* SHM architectures have been proposed for three primary reasons: 1) to implement a specific technology or sensor

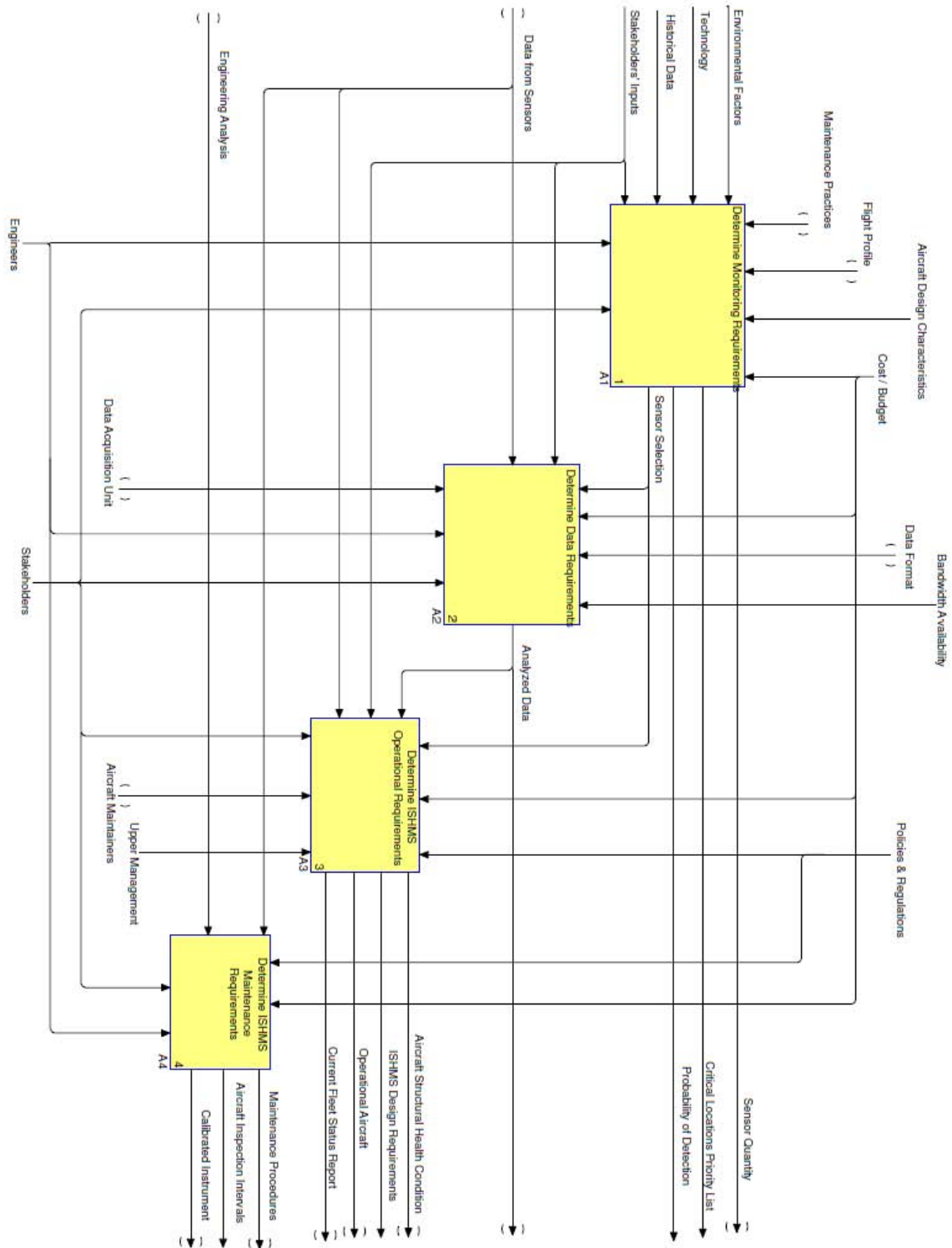


Figure 2.4: Activity model for SHM system requirements development proposed by Albert, et al. [3]

development program [6]; 2) to summarize the experiences of an ongoing program [60,61,112]; or 3) to show the general approach taken by an aerospace company [17,54].

Common themes for physical architectures include modular systems for scalability and for ease of component replacement. This modularity usually takes the form of sensors working through intermediate processors located in a particular “zone”. These intermediate processors then connect to a central master controller [54,61,112]. Figure 2.5 provides a notional representative SHM physical configuration.

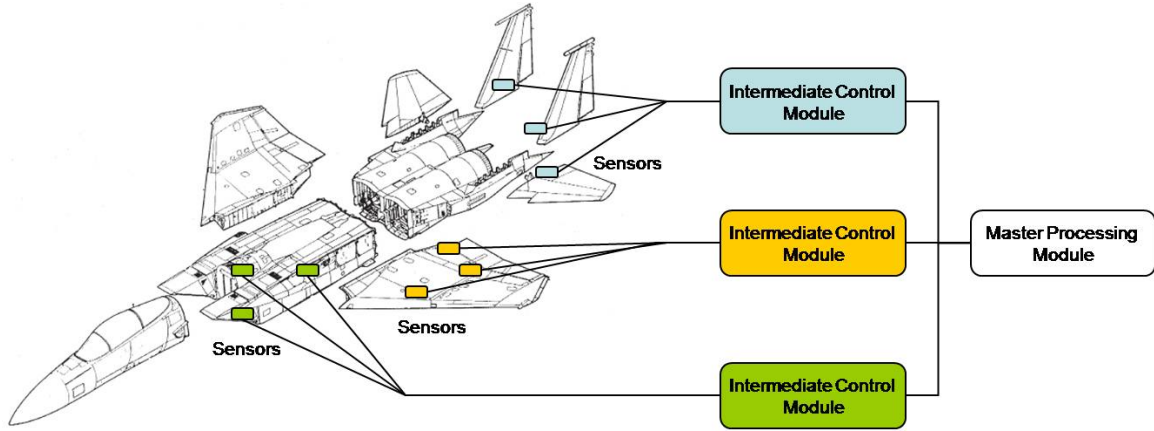


Figure 2.5: Representative SHM physical configuration [54,61,112]

From a functional standpoint, two main distinctions exist. The first distinction exists between “global” versus “local” health monitoring. Buderath assigned *classes* to the two different requirements. For Class 1, fatigue criticality or location of crack initiation is well known. For Class 2, the critical location of the component is not exactly known. He discusses this distinction in terms of sensor placement decisions: “For Class 1, the the decision might be easy so long the geometry [*sic*] allows sensor placement close to the critical location. For Class 2, sensor placement has to be supported by finite element or other structural optimization methods . . . this area requires still a lot of research [20]”.

The second functional distinction relates to “damage detection” and “life usage” determinations. While damage detection consists generally of processing specific sensor data to determine the extent of damage in a particular location, life usage

determinations include aircraft load history, repair history, finite element or other models to predict when the component has reached the end of it's useful life. Figure 2.6 shows a representative SHM architecture featuring both damage detection and life management components.

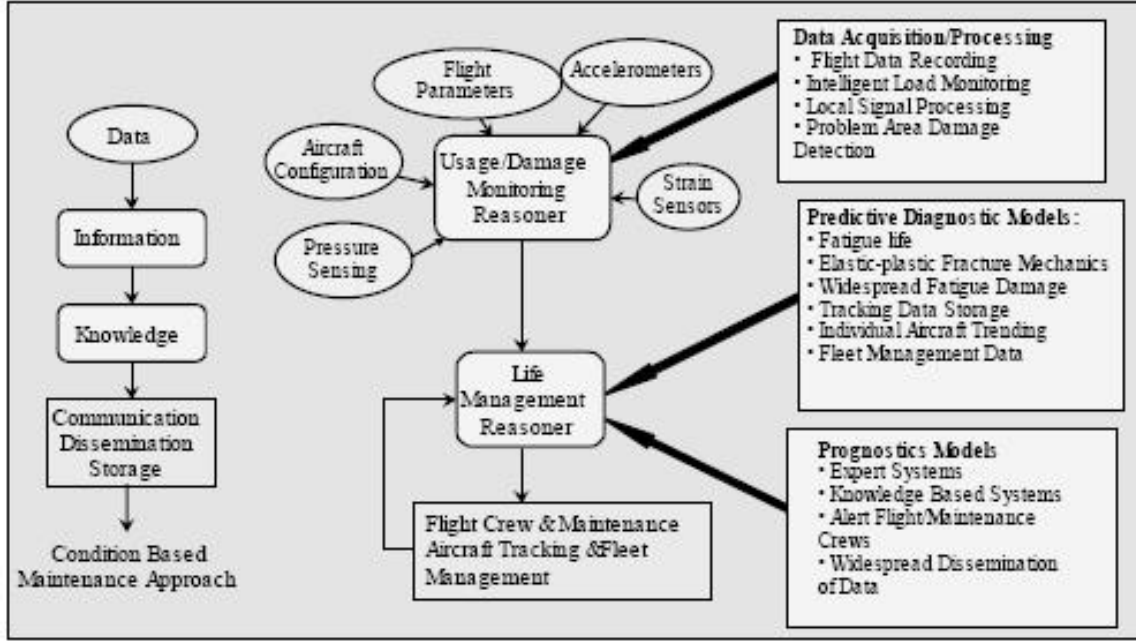


Figure 2.6: Representative SHM architecture [54]

*2.1.3 General Structural Health Monitoring Requirements.* Brown and Hansen [19] identified four capability gaps relating to the current inspection paradigm when performing a JCIDS analysis on a proposed F-15 SHM system. The capability gaps included:

1. Reduce Sustainment: The current SHM method is manual inspections, which are not cost-effective and do not truly embody the right support, right place, right time, in the right quantities concept, but are preventative measures.
2. Facilitate Informative Decision-Making: Current method does not meet the Focused Logistics [goal] as being a real-time, net-centric system providing asset visibility. Assets are only visible while grounded, during inspection periods.



3. Maintain Situational Awareness: Current methods do not have a robust network of sensors and thus are not capable of monitoring and tracking assets, at least not in the structural sense. This information could be used by others to increase overall situational awareness.
4. Assess Performance and Implementation Improvements: Data capture and analysis is critical to successful redesigns and future designs. Currently, data is only captured during inspections and not while in-flight. Without in-flight data capture, flight loading analysis can only be accomplished during operational testing.

SHM literature also identifies several general requirements to implement a SHM system similar to the notional system shown in Figure 2.1. These requirements have been summarized into two general categories:

1. System-level Requirements: SHM system requirements independent of specific aircraft structural characteristics. See Table 2.1.

Table 2.1: System-level requirements for a SHM system

Requirements	Reference(s)
Data easily downloadable from aircraft	[54]
Data compatible with existing infrastructure	[54]
Quickly sort large amounts of data for critical information	[24]
Software handles, stores and interprets large amounts of data	[54]
Easy to replace sensors	[16]
Signal processing can compensate for slight sensor misalignments	[16]
Software handles high and low sample rate data	[112]
Address both real time and long term structural issues	[60], [87]
Ease of maintenance and installation	[60]
Redundancy and fail safe operation	[60]

2. Inspection-level Requirements: SHM system requirements directly relating to the quantity and type of parameters to be collected. See Table 2.2.

Given the general requirements for SHM systems, application-specific requirements such as “detect a 0.1 inch crack from this fastener hole in a 6061-T6 aluminum wing

Table 2.2: Inspection-level requirements for a SHM system

Requirements	Reference(s)
Record strain data	[54], [61], [87]
Record aircraft flight parameter data	[54], [112], [87]
Record inspection location environment (loads, accelerations, moisture, etc.)	[54], [61], [112], [87]
Record temperature data	[54], [112]
Sense structural crack growth	[54]
Sense composite delamination	[112]

spar” can (and must) be derived from engineering experience, design documentation and existing information for a particular airframe.

*2.1.4 Structural Health Monitoring Inspection Technologies.* Boller [17] describes technology based SHM as the effort to attach sensors to aircraft structure to monitor signals relating to a physical parameter (e.g. strain, vibration modes, acoustic waves, temperature, electrical resistance, etc.). The existence and/or extent of structural damage is then determined through signal analysis. Active research on a vast range of sensor technologies is ongoing to meet the general requirements outlined in section 2.1.3. Sandia National Laboratories recently analyzed the current state of the art for SHM sensor technologies [98]. The most promising current technologies identified during the program include comparative vacuum monitoring (CVM), piezoelectric transducers and fiber optic sensors. Each technology is briefly described below.

*Comparative Vacuum Monitoring.* This technology places self-adhering sensors in areas of known crack growth. The sensors contain “channels” with alternating low vacuum and atmospheric pressure situated perpendicular to the expected direction of crack growth. As a crack grows, the low vacuum channels are penetrated, and a vacuum cannot be maintained. In laboratory fatigue measurements, a crack was deemed detected when vacuum could not be maintained even when the fatigue loading was reduced to zero. Figure 2.7 shows general schematics of a CVM sensor, and a sensor installed on a riveted lap joint.

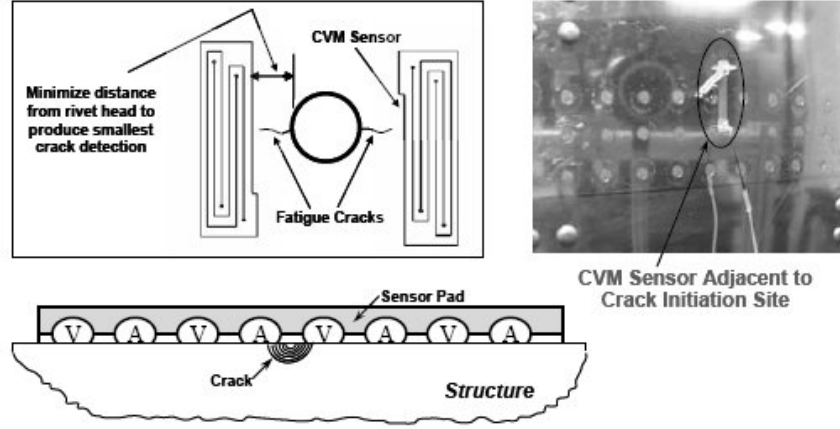


Figure 2.7: CVM sensor design and application [98]

Unpublished results from a joint FAA/industry laboratory and field evaluation of CVM technology [101] provided a measure of the CVM technology capability in terms of a  $\text{POD}(a)$  curve.  $\text{POD}(a)$  curves plot crack size  $a$  against a probability of detection for a range of crack sizes (additional description of  $\text{POD}(a)$  curves is given in section 2.2.2.3). Figure 2.8 presents the  $\text{POD}(a)$  curve for CVM sensors detecting cracks in a 0.040 inch thick 2024-T3 aluminum panel. No supporting data was provided to reproduce the curve. The system used to evaluate the technology was developed by Structural Health Monitoring Systems Ltd, located in Osborne Park Australia. This specific system is currently undergoing long term flight trials with 22 sensors installed on 4 Delta and Northwest airlines aircraft.

*Piezoelectric Transducers.* This technology adheres piezoelectric wafers to aircraft structure to transmit and detect elastic waves within the structure. Using either “pitch-catch” methods where one piezoelectric transducer (PZT) acts as a transmitter and another as a receiver, or “pulse-echo” methods where one PZT performs both functions, structural damage is detected by identifying changes in the elastic wave transmission velocity, phase, amplitude and/or wave reflections from a damage site. Figure 2.9 demonstrates the basic PZT pitch-catch concept. This technology was used in the experimental portion of this research, and a technology overview is given in section 3.3.

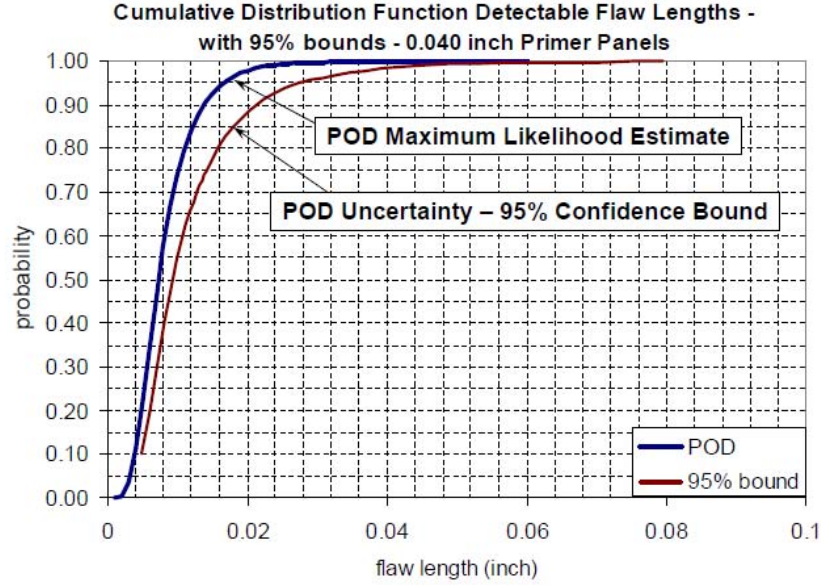


Figure 2.8: CVM Example  $POD(a)$  curve [101]

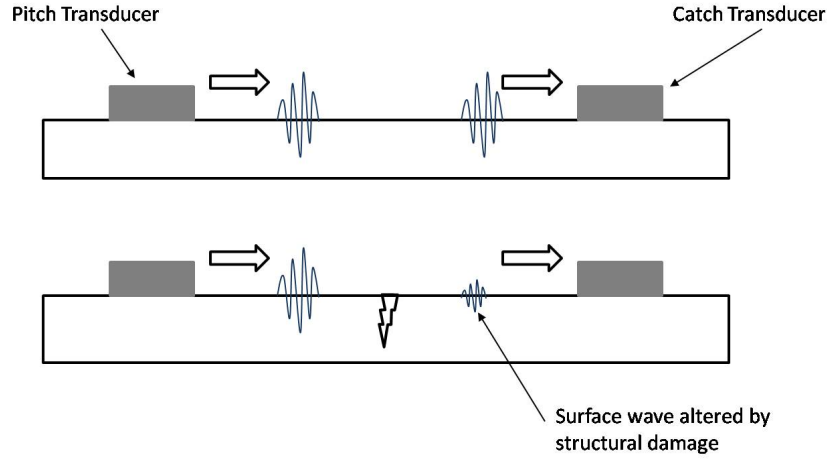


Figure 2.9: Structural damage changes surface waves generated by PZTs

Extensive research is ongoing concerning the use of PZTs in SHM (see [49,50] for an overview of the ongoing research). But despite this basic research, limited numbers of  $POD(a)$  studies have been accomplished using this technology. Ihn and Chang [53] performed a  $POD(a)$  experiment for the detection of cracks around fastener holes in an aluminum lap joint specimen using an array of 12mm diameter piezo-ceramic disks in a pitch-catch configuration. Eddy current inspections were also conducted during

the testing for comparison. Figure 2.10 presents Ihn and Channg's  $POD(a)$  results. No curve fits or additional data were provided to reproduce the curve.

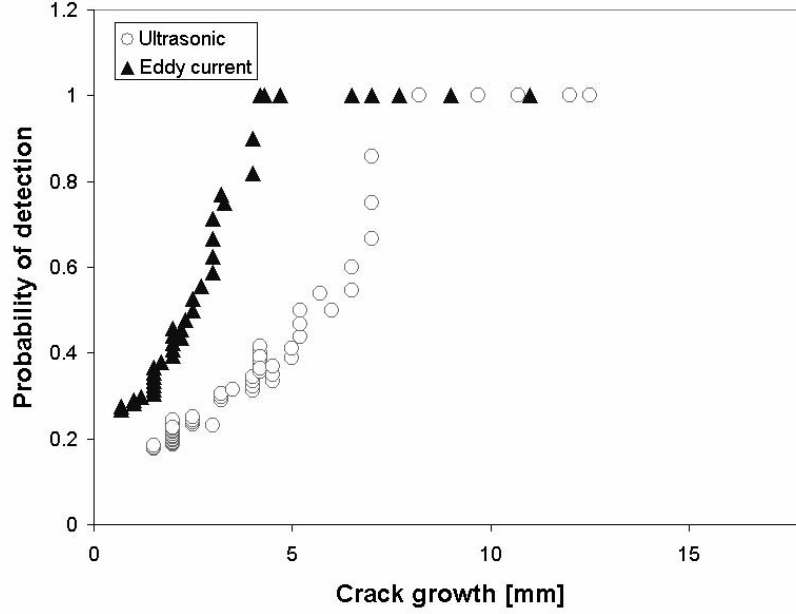


Figure 2.10: Ihn and Chang [53] compared PZT pitch-catch crack detection to conventional eddy current scans

Cobb Michaels and Michaels [27] have also completed a  $POD(a)$  study using a similar ultrasonic technology. Their work was used in conjunction with the experimental portion of this research in Chapter V, and an extensive discussion of their work is given in section 5.7.

*Fiber optic sensors.* This technology uses changes in light intensity, magnitude and/or phase of light within a fiber optic filament to detect changes in the surrounding environment. Different sensor configurations can detect vibration, strain, temperature, pressure, corrosion, moisture and humidity. Surface strains can be detected by adhering fiber optic filaments with known index of refraction to the structure (Fiber-Optic Bragg Grating approach). As the structure strains, the filament expands or contracts, changing the characteristics of the light transmitted through the filament. Corrosion detection can be accomplished through the use of sacrificial corrosion sen-

sors mounted at the end of a fiber optic line. Changes in the reflected light intensity can be correlated to corrosion of the sensor and surrounding structure.

Fiber optics can indirectly detect the presence of structural damage. Fiber optic sensors glued to the surface of the structure (or embedded in composite materials) detect increased strain due to structural damage in adjoining locations (see [51, 71, 84, 97]). Traditional  $POD(a)$  curves for crack detection have not been included in current research.

## ***2.2 The Current USAF Structural Inspection Paradigm***

Starting with a crew chief’s preflight visual inspections, through a phase inspection’s moderate disassembly for non-destructive inspection (NDI), to a depot’s near total aircraft disassembly for comprehensive inspection, USAF aircraft undergo near continuous health monitoring from the day they leave the factory until the day they are retired. The nature and timing of these inspections play a significant role in the costs of maintaining a legacy aircraft fleet, and it has been shown that the need for inspections (as well as repairs) accelerates as an aircraft reaches its design service life [94]. Since SHM has the potential to fundamentally alter the nature and timing of these inspections, a general background of how the Air Force currently performs structural inspections will form the baseline concerning the implementation of SHM.

*2.2.1 MIL-STD-1530: The Aircraft Structural Integrity Program.* For nearly 50 years, the United States Air Force has used the Aircraft Structural Integrity Program (ASIP) to “ensure the desired level of structural safety, performance, durability, and supportability with the least possible economic burden throughout the aircraft’s design service life” [33, 85]. Generally, the ASIP (as specified in MIL-STD-1530C) requires tests and analyses to identify critical structural components, determine if these components may fail before reaching the aircraft’s design service life, and establish inspection intervals for these components to ensure flight safety. The overriding

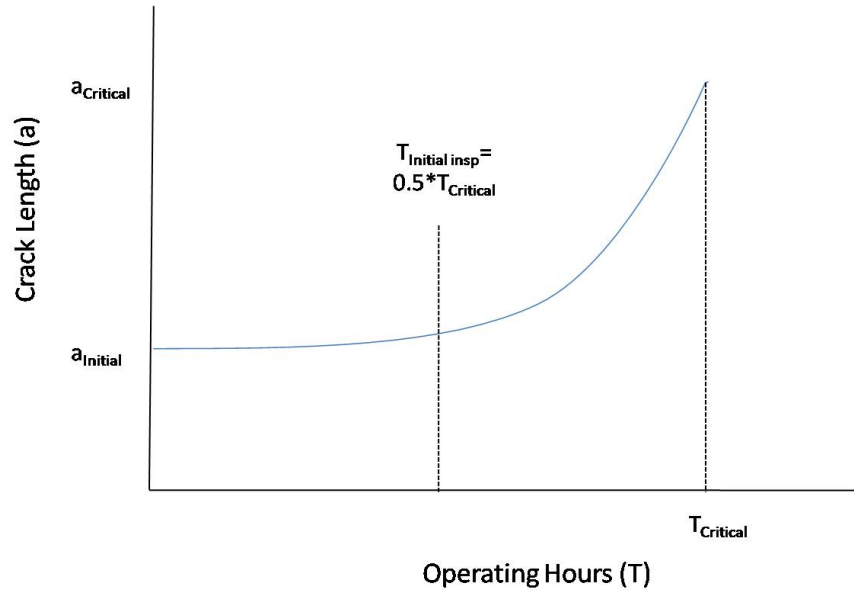
ASIP philosophy of “damage tolerance” guides the determination of the structural inspection intervals. This philosophy assumes a certain level of undetected damage exists at critical structural locations, and requires the structure to be able to survive the existence and growth of this damage for a period of time until it can be detected and repaired [33, 59, 67]. The ASIP allows two damage tolerant design concepts:

1. Fail-safe structure, where the structure retains the required residual strength for a period of unrepaired usage after the failure or partial failure of safety-of-flight structure.
2. Slow damage growth structure, where periodic inspections ensure flaws, defects or other damage are not allowed to attain the size required for unstable, rapid propagation failure. This concept cannot be used for single-load-path and non-fail-safe multiple load path structures.

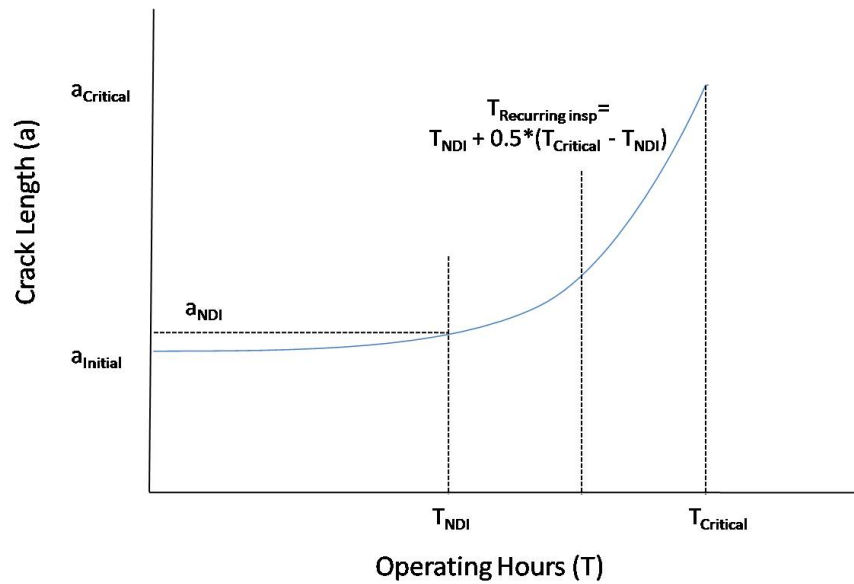
Based on these concepts, *damage tolerance analysis* (DTA) techniques have been developed using fracture mechanics analysis, NDI capabilities, and component initial flaw sizes [29]. One critical product from a DTA is the crack growth vs. operating hours (a vs. T) curve. Values from this curve form the baseline for initial and recurring structural inspection intervals based on the following MIL-STD-1530C requirements [33]:

1. The initial inspection for slow damage growth concepts shall occur at or before one-half the life from the assumed maximum probable initial flaw size to the critical flaw size.
2. The repeat inspection intervals for [both fail-safe and slow damage growth structure] shall occur at or before one-half the life from the assumed maximum detectible flaw size (based on probability of detection) to the critical flaw size.

Figure 2.11 shows how initial inspection times and recurring inspection intervals can be determined from an “a vs. T” curve.



(a) Determining Initial Inspection Time



(b) Determining Recurring Inspection Interval

Figure 2.11: Determining inspection times from a generic “ $a$  vs.  $T$ ” curve (adapted from [78])

But even with calculated crack growth curves for critical locations, actual damage accumulation can vary widely from aircraft to aircraft due to various in-service mission differences, unique structural repairs and different operating locations across a fleet of aircraft. For example, critical locations in the centerwing of an AC-130U



gunship can have a usage severity over 6 times that of a standard C-130E [78]. And Wallace, et al., found that F-16 usage is approximately eight times more severe than the usage for which it was designed [114]. To address the uncertainties in the amount of damage relating to individual aircraft variations, the ASIP requires Individual Aircraft Tracking (IAT) programs that “shall be used to adjust the inspection, modification, overhaul, and replacement times based on actual, measured usage of the individual aircraft.” and “determine the equivalent flight hours (or other appropriate measures of damage such as landings, pressure cycles, etc.) and adjust the required maintenance schedule for all critical locations on each individual aircraft” [33].

In addition to the DTAs described above, the ASIP requires several other documents for each aircraft type. Building of the ASIP Master Plan starts at the beginning of system development, and outlines how all of the MIL-STD-1530C requirements will be met. Updates to this plan throughout the life of the aircraft system provide historical documentation concerning structural test results, and describe design changes implemented due to test and in-service experience. The Force Structural Maintenance Plan (FSMP) provides detailed information concerning the execution of the inspection program. It defines the “when, where and how” of the inspections, and along with being a technical reference, the FSMP is a primary document for the budgetary, force structure and maintenance planning for the aircraft type. Updates to the FSMP occur with any significant changes in the operational use of the aircraft type, or when discovered damage warrants changes to the inspection program [33].

The US Air Force executes aircraft structural inspection programs using a three tiered maintenance structure with different levels of inspection occurring at the Organizational (flightline), Intermediate (backshop) and Depot levels [43]. Individual bases perform Organizational and Intermediate maintenance on their assigned aircraft, while one or more centralized locations perform Depot inspections for an entire fleet. Organizational level inspections consist primarily of visual inspections of readily accessible areas performed during pre- and post-flight inspections. The majority of the structural inspections performed by an individual air force base occur at the Inter-

mediate level, where the aircraft is removed from service and partially disassembled for structural and component inspection / replacement. Required field level IAT inspections occur at this level. For the F-15C/D aircraft, the field level IAT inspections consist of NDI of wing skins, attachment lugs, wing spars and fuselage bulkheads [38]. Figure 2.12 gives the general aircraft locations of the F-15C/D field-level IAT inspection locations. Depot level IAT inspections generally use the same NDI techniques, but pre-inspection aircraft preparation can be extensive. For example, 6 of the 11 depot level IAT inspections for the wings of the F-15 require the original production jigs to remove the upper wing skins to gain access to the inspection locations [38,39].

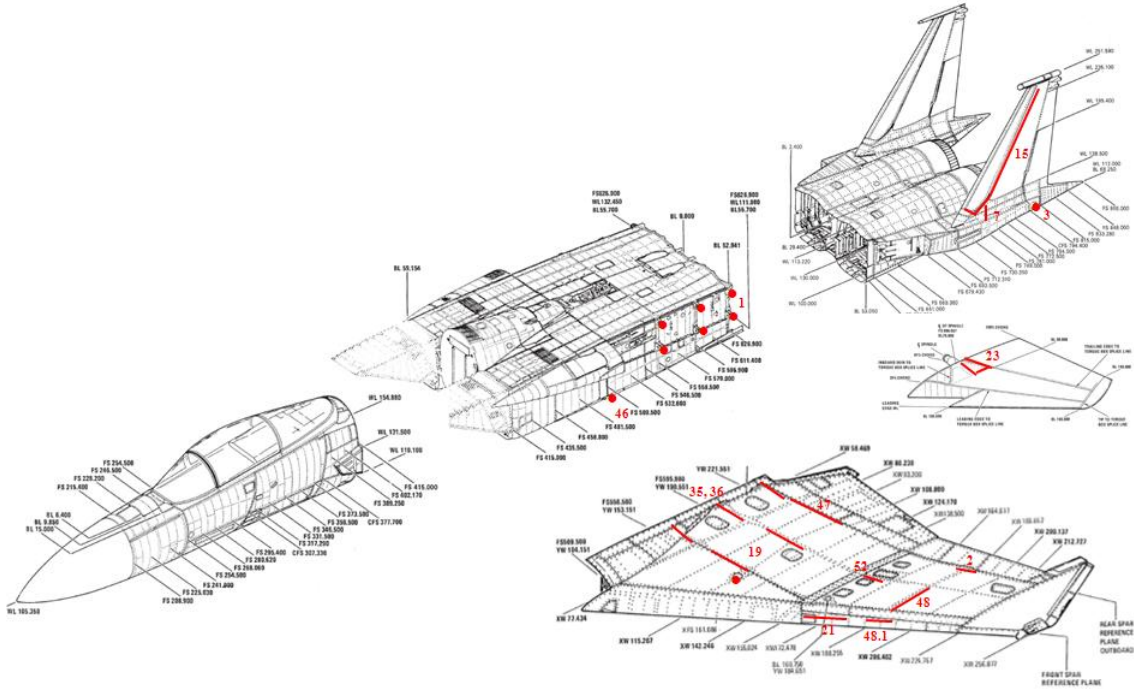


Figure 2.12: Field level F-15C/D IAT inspection locations (left side only)

*2.2.2 The USAF Nondestructive Inspection Program.* The successful execution of the ASIP depends on the capabilities of the nondestructive evaluation (NDE) techniques used to perform the structural inspections. MIL-HDBK-6870, Inspection Program Requirements Nondestructive for Aircraft and Missile Materials and Parts [sic] [34] provides general guidelines to establish an NDE program for aircraft and

missiles including the acceptable NDE processes, procedures and personnel training requirement.

*2.2.2.1 Technologies.* The USAF currently uses several NDE technologies to execute the structural inspection program. The technology used for a given inspection depends on a variety of factors including part composition, accessibility and expected damage location [35]. Commonly used technologies include [40]:

1. Liquid Penetrant: This method utilizes a dye containing fluid which penetrates surface discontinuities through capillary action. The trapped penetrant increases the visibility of the discontinuity by providing a visual contrast between the discontinuity and the surrounding surface.
2. Magnetic Particle: This method is limited to ferrous components. The inspected component is magnetized and small ferrous particles are suspended in a bath of oil or water on the component. Cracks and similar types of discontinuities cause disruptions in the magnetic field of magnetized parts, in turn attracting these ferrous particles to the leakage site. This allows the inspector to visualize the locations of the discontinuities.
3. Eddy Current: This method detects discontinuities in parts that can conduct electricity. An eddy current “probe” induces an alternating magnetic field in the inspected component that is disrupted in a detectable manner when encountering a structural discontinuity.
4. Ultrasonic: This technique uses sound waves at a frequency greater than 20kHz to detect internal discontinuities ranging from cracks to disbands on almost any material.
5. Radiographic: This technique uses X-rays to detect surface and internal discontinuities in ferrous and nonferrous metals, ceramics, plastics and other materials.

Technical order 33B-1-1, Nondestructive Inspection Methods, Basic Theory [40] provides extensive information including concepts, principles, advantages, disadvan-

tages, rules of thumb, equipment familiarity and typical results for each inspection type. Rummel and Matzkanin also discuss the relative merits and drawbacks of each inspection type in [100].

*2.2.2.2 Probability of Detection Testing.* As described in section 2.2.1, the detection capability of the selected NDI technique provides the starting point to determine a critical structural component’s recurring inspection interval. One metric commonly used to describe the capability of a given NDI technique is the probability of detection of a given crack size  $a$ . When the POD is plotted against a range of crack sizes, a  $\text{POD}(a)$  curve is formed. These curves are traditionally built using one of two methods. The first method, outlined by MIL-HDBK-1823 [35], builds the  $\text{POD}(a)$  curve from experimental data obtained from testing components with known flaw sizes. Since this technique will be modified for use in Chapter V, the specific MIL-HDBK-1823 methodology is described in detail in section 5.2.

*2.2.2.3 Probability of Detection Modeling.* The second method to describe the  $\text{POD}(a)$  curve involves combining a large number of NDI test results and fitting a corresponding mathematical model [35, 100]. To determine a baseline model, Berens and Hovey [9] evaluated seven potential models for  $\text{POD}(a)$  functions, using approximately 22,000 inspections of several NDI types performed in a USAF study. The log-logistic function provides the best fit to the data, and has been used in several follow-on analyses [7, 8, 10, 82, 100]. The  $\text{POD}(a)$  log-logistic function takes the form [10]:

$$POD(a) = \begin{cases} (1 + \exp(-[\frac{\pi}{\sqrt{3}} \frac{\ln(a-a_{min})-\mu}{\sigma}]))^{-1} & \text{if } a > a_{min} \\ 0 & \text{if } a \leq a_{min} \end{cases}$$

where:

(2.1)

$a$  = size of the crack being inspected

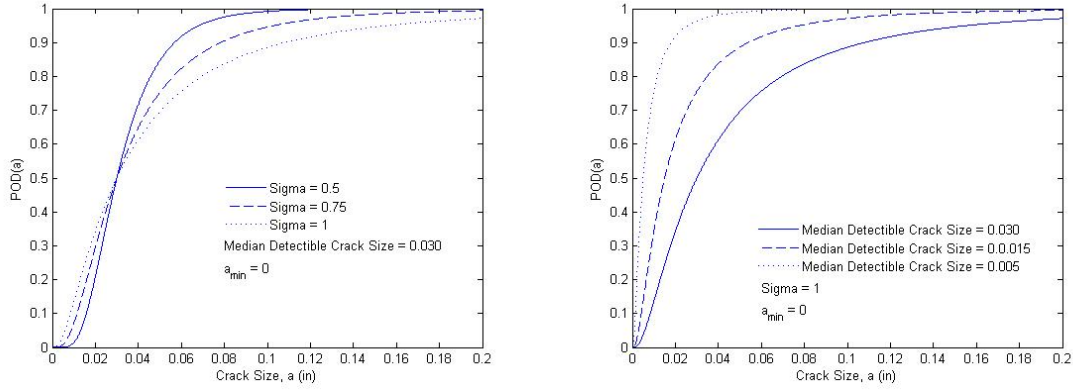
$a_{min}$  = minimum detectible crack size

$\mu$  = natural log of the crack length detected 50% of the time

$\sigma$  = scale parameter

It has been shown that the cumulative lognormal statistical distribution, with the same parameters  $\mu$  and  $\sigma$ , is essentially identical to the  $POD(a)$  function given above. Parameter variations adjust the model to specific NDI inspection types and physical inspection scenarios. Figure 2.13 shows the cumulative lognormal  $POD(a)$  function for several values of  $\mu$  and  $\sigma$ . The scale parameter  $\sigma$  models the “quality” of the inspection. Increasing  $\sigma$  flattens out the  $POD(a)$  curve, giving less probability of detection at large crack sizes (Figure 2.13a). In terms of the current inspection paradigm,  $\sigma$  values for fully automated off aircraft eddy current inspections can have values in the range of 0.2 to 0.7, while manual or semi-automated depot-level eddy current inspections can have  $\sigma$  values greater than 1 [82]. Reducing the median detectible crack size,  $\mu$ , causes the curve to become more upright for a given crack size, improving the probability of detection (Figure 2.13b). Adding a minimum detectible crack size,  $a_{min}$ , translates the curve to the right, and can account for an installed fastener preventing the detection of a crack until it clears the fastener head [82]. This model can also estimate an NDE technique’s probability of miss based on crack sizes, where Probability of Miss = 1-  $POD(a)$  [10].

But depending on the experiment and/or data used to generate the  $POD(a)$  curve, the model may not adequately represent the probability of technicians finding cracks in damage structure during field inspections. Environmental and human factors



(a)  $POD(a)$  with a varying scale parameter      (b)  $POD(a)$  with a varying median detectible crack size

Figure 2.13:  $POD(a)$  parameters describe NDI technique capabilities

(e.g. cramped inspection locations inside a wing fuel tank, boredom involved in performing large numbers of “no defect” inspections, etc.) can have a large effect on the probability of finding damage [104]. The general impact of these effects has been described as the Probability of Inspection (POI) [18]. Generalized estimates for POI values have not been published, but one ASIP Manager reported the POI for a specific high interest inspection was as low as 50% [25].

*2.2.2.4 Current USAF Structural Inspection Capabilities.* Rummel and Matzkanin [100] discuss the relative merits and drawbacks of each NDE inspection type. Their study collects experimental results and 411  $POD(a)$  curves from various NDE studies into a single source. Selected  $POD(a)$  curves from their study provide a general idea of the crack size detection capability of each inspection type described above, and also allows general comparisons to be made. Figures 2.14 through 2.17 present one representative  $POD(a)$  curve from eddy current, florescent penetrant, ultrasonic and X-ray hit-miss testing on aluminum panel samples. For each inspection type, samples with known crack lengths were inspected. If a sample crack was detected, a “hit” was recorded for the given crack size. If a sample crack was not detected, a “miss” was recorded. Hits and misses were then plotted at 100% POD or 0% POD for each crack size (denoted by an “x” on the figures), and a log-logistic

function (see equation 2.1) was fit to define the  $POD(a)$  curves. MIL-HDBK-1823 [35] provides guidance on the type and number of test specimens required to build a representative  $POD(a)$  curve. As shown by the figures, inspection type can greatly affect the detectability of various crack sizes.

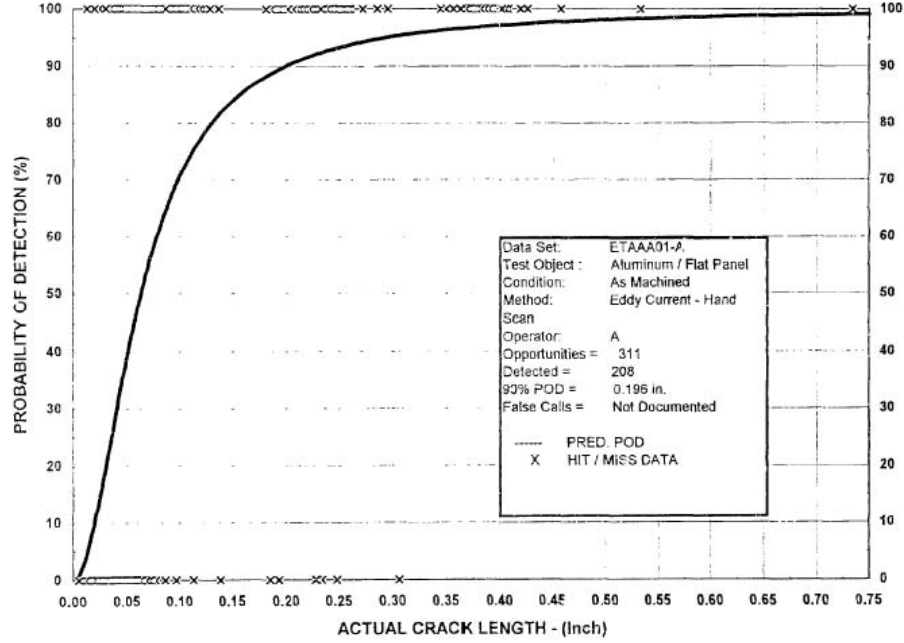


Figure 2.14: Representative eddy current inspection  $POD(a)$  curve for cracks in an aluminum panel [100]

*2.2.3 A Survey of Legacy Aircraft Inspection Locations.* As noted in the introduction, the USAF currently has a robust SHM system for all of its current airframes: airmen physically inspecting aircraft structure. Since the final design of any technology-based SHM system depends on the structural locations to be monitored, it is beneficial to study current inspection locations in greater detail. Sections 2.2.3.1 and 2.2.3.2 summarize the critical inspection locations, critical crack lengths and structural materials for two legacy USAF aircraft, the C-130 transport and the F-15 fighter. Information contained in the sections has been condensed from ASIP documentation provided by the C-130 and F-15 System Program Offices at Robbins Air Force Base, Georgia.

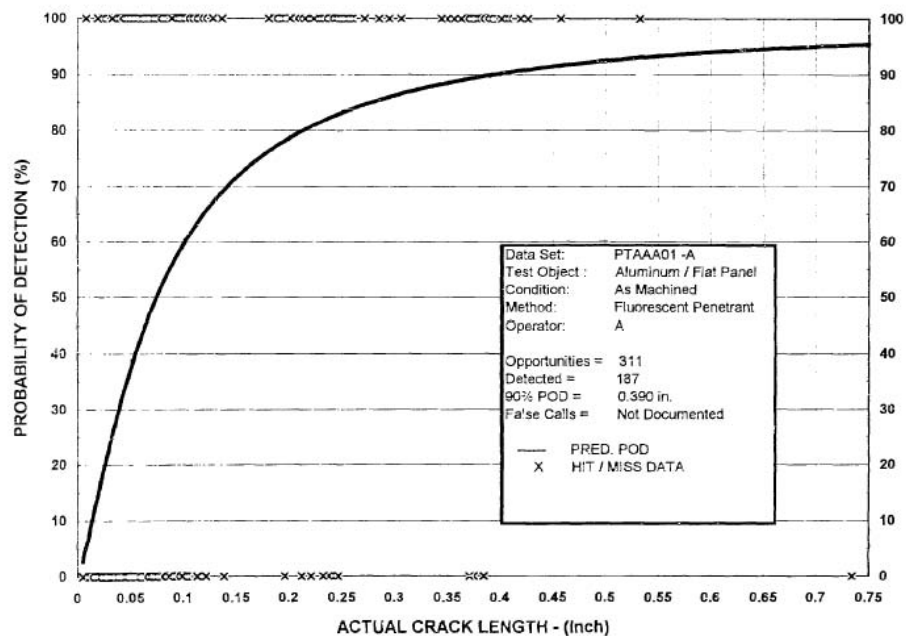


Figure 2.15: Representative florescent penetrant inspection  $POD(a)$  curve for cracks in an aluminum panel [100]

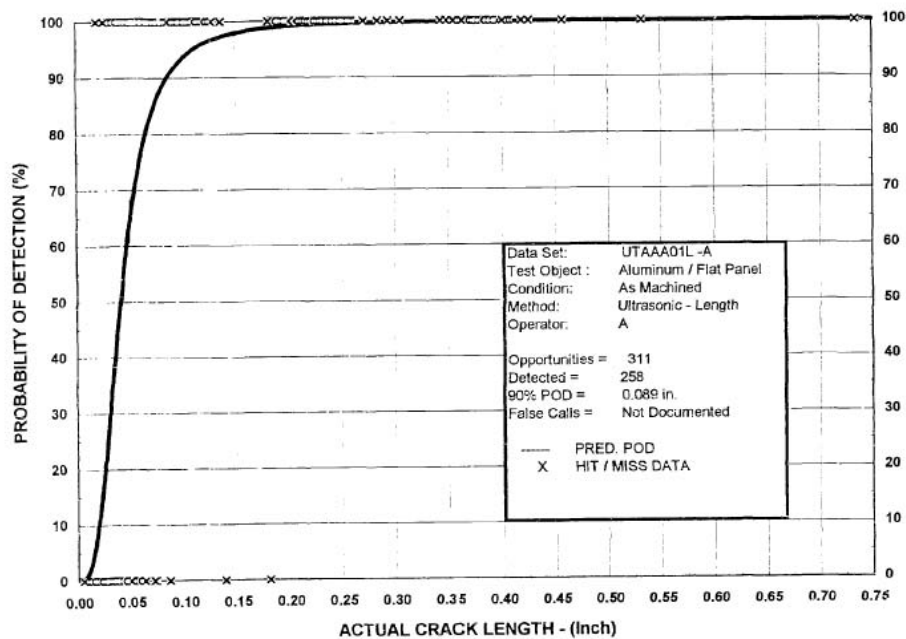


Figure 2.16: Representative ultrasonic inspection  $POD(a)$  curve for cracks in an aluminum panel [100]



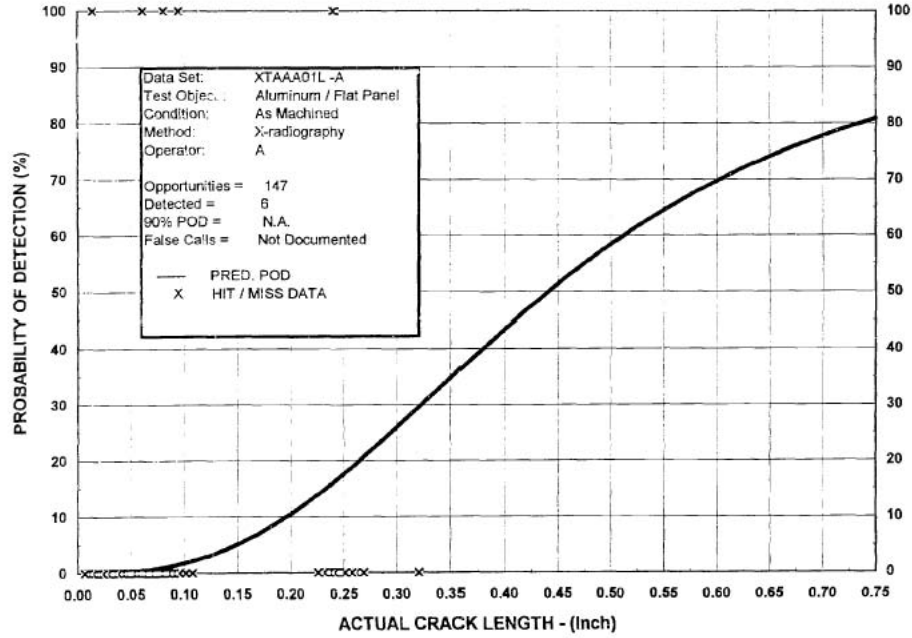


Figure 2.17: Representative X-ray inspection  $POD(a)$  curve for cracks in an aluminum panel [100]

*2.2.3.1 A Cargo Aircraft: The C-130.* For identification and classification of inspection locations, the C-130 structure is divided into seven major components: center wing (CW), outer wing (OW), forward fuselage (FF), center fuselage (CF), aft fuselage (AF), horizontal stabilizer (HS), and vertical stabilizer (VS) [78]. Figure 2.18 shows the major C-130 components. The original aircraft manufacturer and the C-130 SPO have identified 86 critical inspection locations within the seven major components using damage tolerance analyses and in-service damage findings. According to an inspection interval re-baseline contained in [78], 76 of these critical locations require recurring inspections at less than 10,000 airframe hours for the C-130H, with the typical C-130 usage being 500 airframe hours per year.

Table 2.3 presents the number of critical inspection locations per major component. The table also includes the shortest critical crack length for a structural part in each major component and corresponding part material. Crack lengths and damage type were obtained from [78], part material information was obtained from [41] and [37].

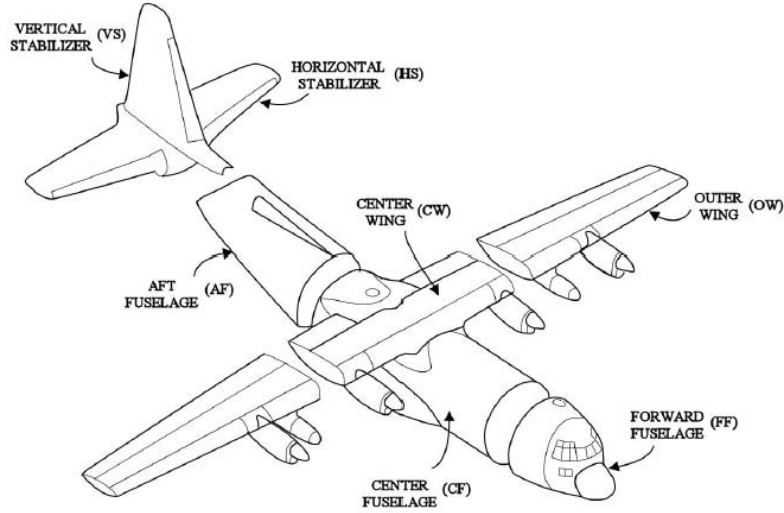


Figure 2.18: The C-130 is divided into seven major components for structural inspection identification and tracking

Table 2.3: Critical inspection locations and minimum critical crack sizes for the seven major C-130 components

Major Component	Number of Critical C-130H Inspection Locations	Minimum Critical Crack Length (in)	Damage Type	Part Material
CW	37	1.072	Fastener hole crack	7075-T73 Al
OW	21	0.616	Fastener hole crack	7075-T73 Al
FF	6	0.559	Fastener hole crack	7075-T6 Al
CF	7	1.35	Fastener hole crack	7075-T6 Al
AF	2	0.558	Fastener hole crack	7075-T6 Al
HS	1	1.714	Fastener hole crack	7075-T6 Al
VS	2	Not Provided	Bracket Failure	7075-T6 Al

The service life of the major structural components is based on specific inspection locations [78]. Since the centerwing contains the majority of the inspection locations, the service life limiting inspection for the centerwing was investigated in greater detail. The C-130 damage tolerance analysis lists the limiting inspection location as the lower wing skin panel, rear beam cap and attach angle at butt line 61, fuselage station 597, shown in Figure 2.19. The inspection is a bolt hole eddy current scan of four fastener holes, looking for cracks in the 7075-T651 [37] lower wing panel where the centerwing attaches to the fuselage. The crack growth curve

shown in Figure 2.20 [78] shows a critical crack length of 6.2 inches, with a recurring inspection interval of 16,560 equivalent baseline hours (NOTE: “Equivalent Baseline Hours” represent operating hours multiplied by a severity factor at a given location to account for various C-130 mission types. For instance, an AC-130 gunship has a higher mission severity factor than a C-130H due to the higher airframe stress imposed by flying the gunship mission. Using equivalent baseline hours allows direct comparisons across all C-130 mission types.)

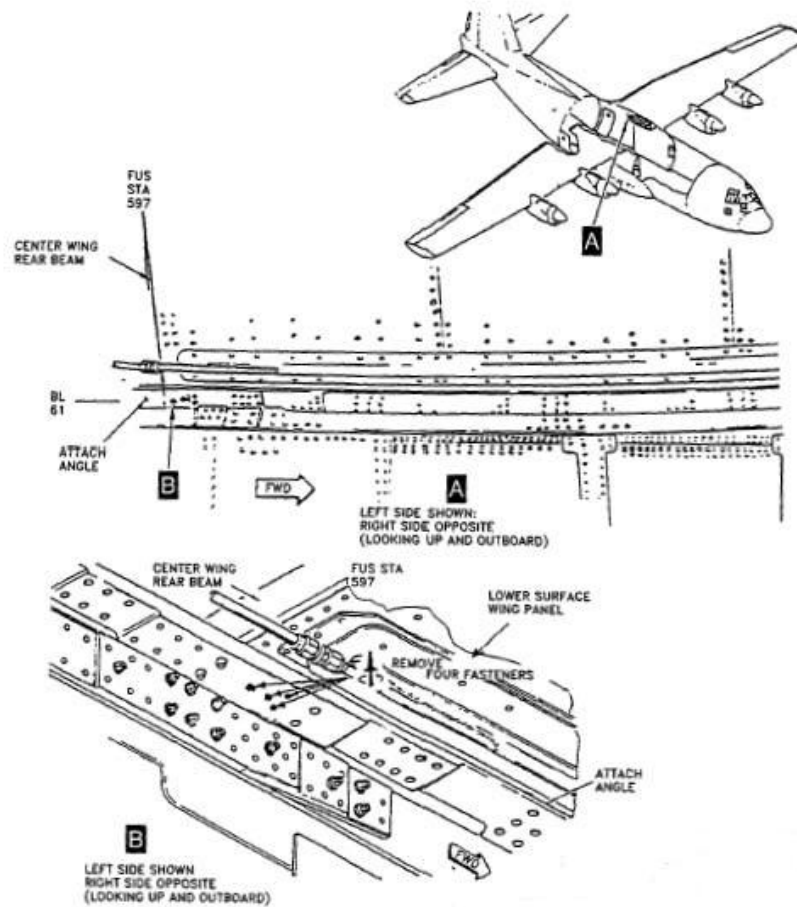


Figure 2.19: C-130 centerwing service life is determined by this inspection location [78]

*2.2.3.2 A Fighter Aircraft: The F-15.* For identification of inspection locations, the F-15 is divided into seven major components: forward fuselage (FF), center fuselage (CF), inner wing (IW), outer wing (OW), aft fuselage (AF), horizontal

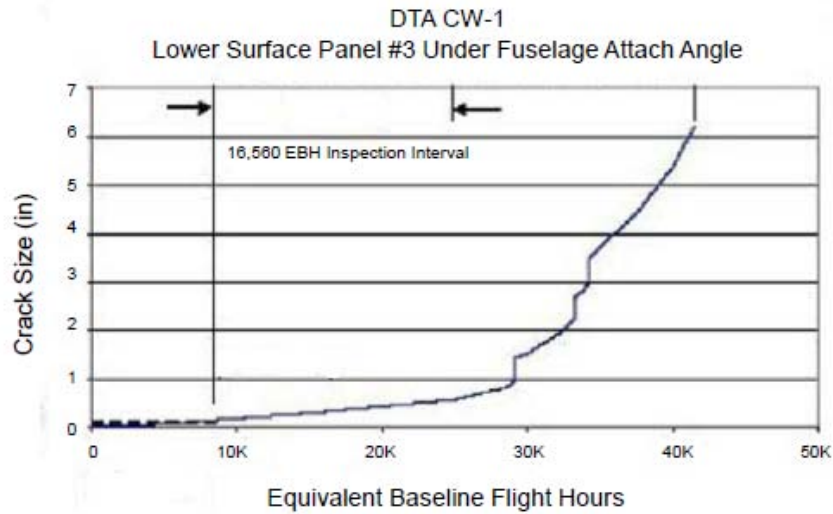


Figure 2.20: Crack growth curve for the representative C-130 inspection location [78]

stabilator [sic] (HS) and vertical stabilizer (VS). Figure 2.21 shows the major F-15 components.

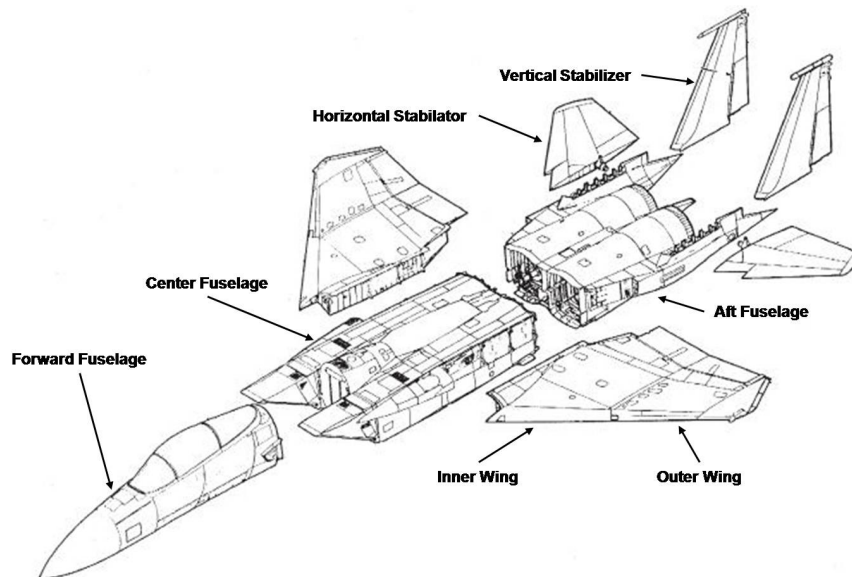


Figure 2.21: The F-15 is divided into seven major components for structural inspection identification and tracking

Damage tolerance assessment [76] has identified 66 fatigue critical locations to be tracked in the F-15 fatigue damage tracking system. Table 2.4 lists 25 inspection locations divided among the major components. Only 25 are listed because several

left/right components are tracked separately, but are treated as a single location in the damage tolerance analysis. These inspections also do not list *all* structural inspections, only those tracked in the F-15 fatigue damage tracking system.

Table 2.4: Critical inspection locations and minimum critical crack sizes for the seven major F-15 components

Major Component	Number of Critical F-15C/D Inspection Locations	Minimum Critical Crack Length (in)	Damage Type	Part Material
FF	1	0.27	Fastener hole crack	7075-T76 Al
CF	0	N/A	N/A	N/A
IW	13	0.14	Fastener hole crack	Ti-6Al-4V
OW	4	0.165	Fastener hole crack	7075-T7352 Al
AF	4	0.1515	Surface crack	Cres Ph13-8Mo
HS	1	0.56	Fastener hole crack	Ti-6Al-4V
VS	2	0.29	Fastener hole crack	Ti-6Al-4V

A representative inspection location in the F-15 inner wing is DTA item 181: Inner Wing Shoulder Rib Machining at Intermediate Spar, part number 68A112118. Manual inspection of this location requires upper wing skin removal during periodic depot maintenance [39], and was the 5th most required depot-level IAT inspection in FY07 [42]. Because of the difficulty to access and the frequency of the inspection, this location was examined in more detail. Figure 2.22 shows the inspection area, and expected structural crack orientation. The inspection consists of bolt hole eddy current inspections of eight fastener holes to find cracks in the 7075-T7352 wing rib [39]. Figure 2.23 from [76] gives the critical crack length of approximately 0.23 inches, with a safety limit of 13,700 flight hours.

### 2.3 Issues for Implementation of SHM on a Legacy Fleet

*2.3.1 Questions Concerning Long Term SHM Capability.* While SHM technologies continue to advance, SHM systems have yet to gain a foothold on the flightline of an aging aircraft fleet. The good safety record of the current inspection paradigm,

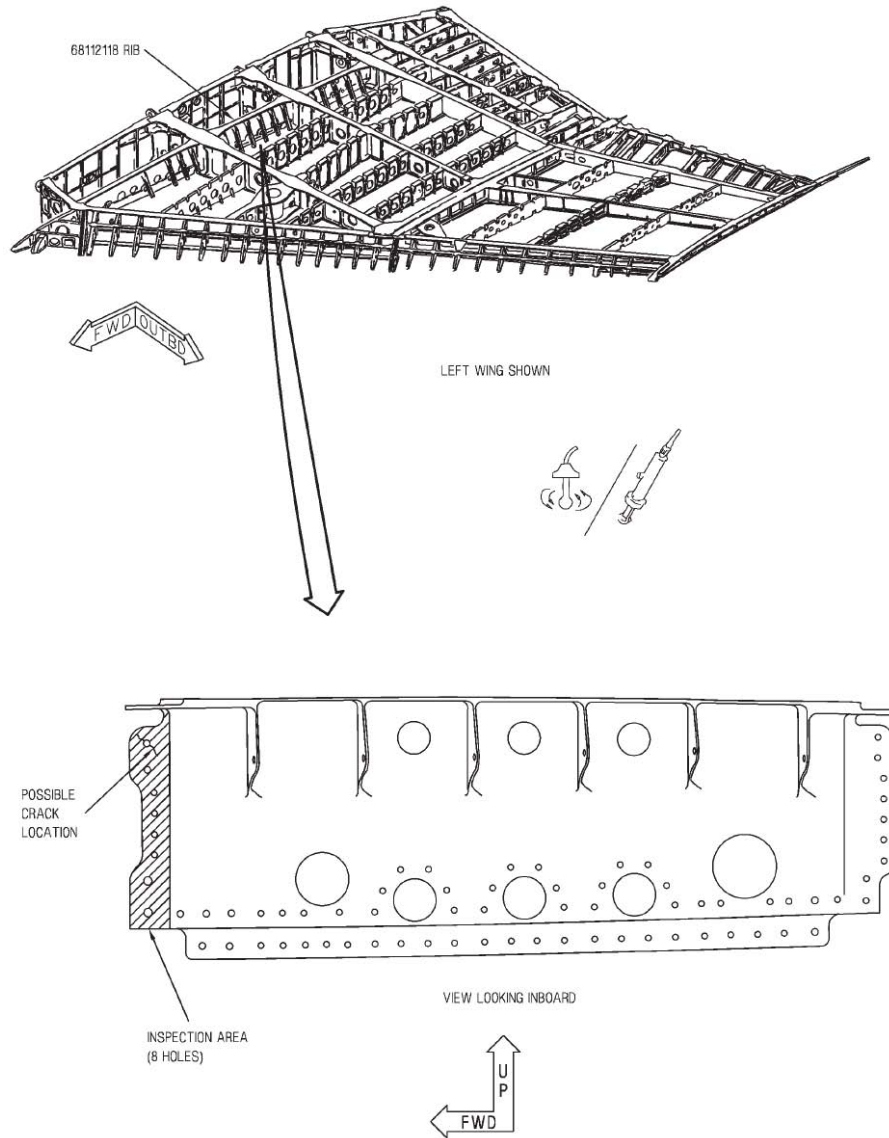


Figure 2.22: Representative F-15 inspection location [39]

combined with uncertainties in SHM affordability, capability and maintainability contribute to the lack of widespread SHM implementation [1, 45].

In order for SHM systems to gain acceptance, a greater understanding is needed of how a given SHM system will be affected by extended exposure to the aircraft environment. A common method for SHM technology development has been to pursue a promising technology or system, then install representative sensors and/or processors on test aircraft for an in flight evaluation [5, 56, 93, 98]. While this technique may be

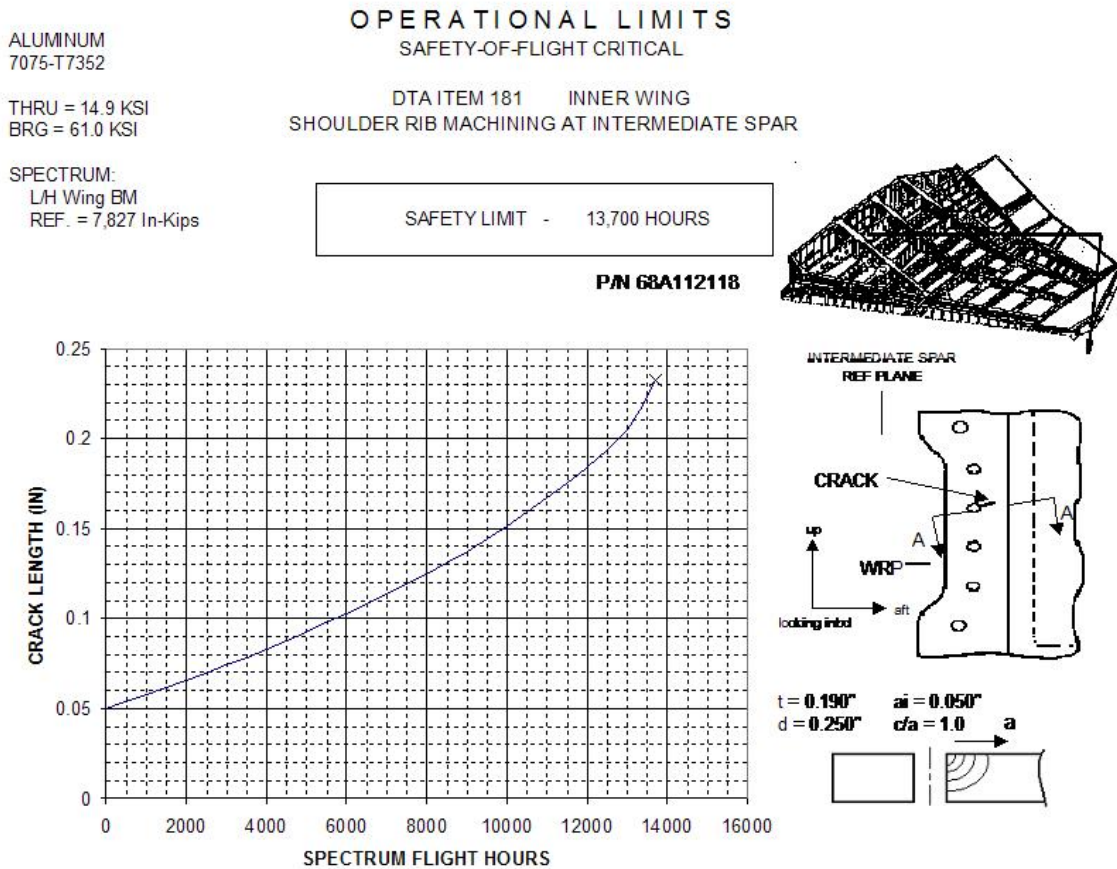


Figure 2.23: DTA parameters for IAT location 59.0 [76]

practical for short duration SHM technology demonstrations, the impact of long term exposure to the aircraft environment on SHM technologies has not been adequately addressed. Additional research is required to determine the effects of thermal/mechanical cycling, electromagnetic interference, various aircraft fluids, and other factors on SHM technologies (see [23, 57]). Research is also needed on how identified effects can be mitigated, or at the very least, taken into account.

Using Figure 2.5 (see page 11) as a rough guide, a cause and effect diagram has been developed to identify the potential causes for changes in SHM system response from both intended (e.g. structural damage) and unintended (e.g. SHM component failure) factors. Figure 2.24 shows the diagram, with the primary categories of SHM

response changes being the aircraft structure, the SHM system and the analysis of the SHM data.

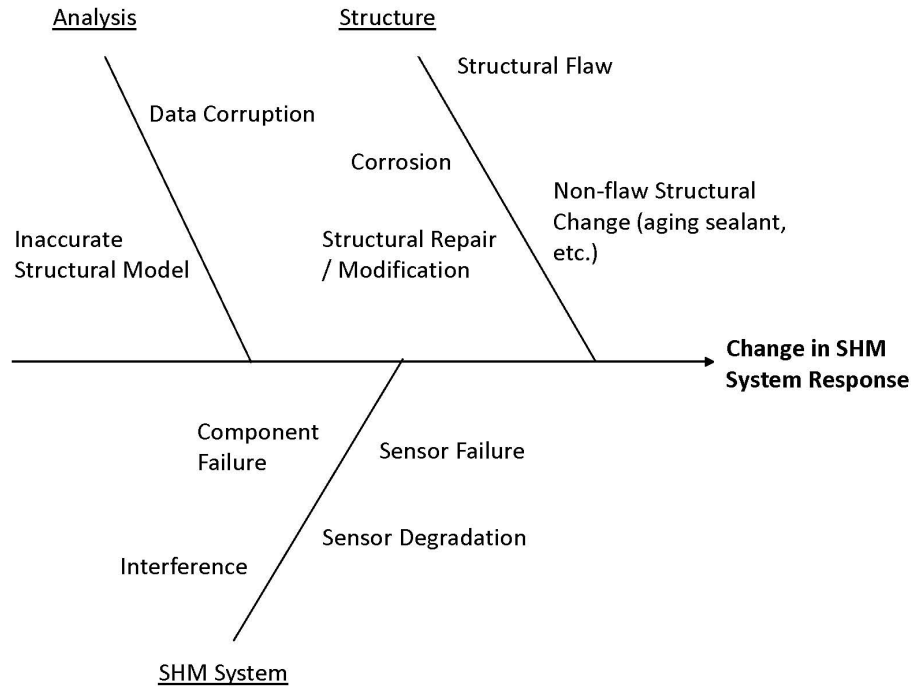


Figure 2.24: Changes in SHM response can result from a wide range of factors

Performing a similar analysis on sensor degradation and sensor failure provides insight into the potential causes of SHM response changes due to changes in the SHM system rather than changes in the aircraft structure. Environmental factors that may cause SHM response changes can be found in existing aircraft component reliability specifications such as MIL-HDBK-781, Handbook for Reliability Test Methods, Plans and Environments for Engineering, Development Qualification and Production [31]; MIL-STD-810, Test Method Standard for Environmental Engineering Considerations and Laboratory Tests [32]; and RTCA/DO-160, Environmental Conditions and Test Procedures for Airborne Equipment [95]. The latter document is recommended by the FAA for aircraft environmental standards. Figure 2.25 presents the cause and effect



diagram for changes in SHM response due to environmental factors. The factors listed in the specifications given above are classified into six primary causes: thermal effects, mechanical effects, electrical effects, mission specific effects, foreign object effects and fluid effects.

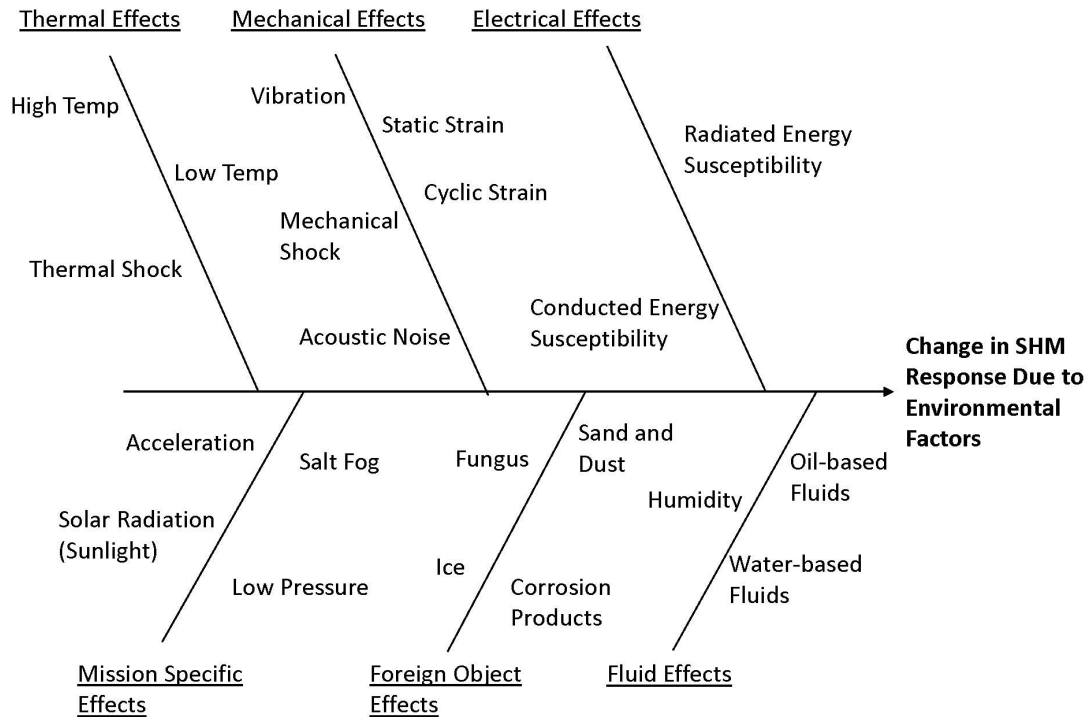


Figure 2.25: Aircraft environmental factors potentially affecting SHM responses

*2.3.2 Critical Crack Length vs. Repairable Crack Length.* Study of the damage tolerance analyses for the C-130 and F-15, in the context of SHM applications revealed two distinct levels of crack detection requirements depending on the overall goal of the SHM system installation. As Tables 2.3 and 2.4 show, cracks emanating from fastener holes represent the largest portion of the listed critical inspection locations. This is generally the case for the other inspection locations discussed in the damage tolerance analyses. If the goal of the SHM system is to prevent structural

failure, the system must be able to reliably detect cracks before they reach critical size with the smallest critical crack size being 0.14 inches for the F-15 and 0.558 inches for the C-130.

But the general repair instructions included in the damage tolerance analyses recommend oversizing the damaged hole up to the next fastener size to clear the crack, and if oversizing is unsuccessful, install a doubler after receiving engineering repair disposition [76]. This general disposition matches the author’s experience as a structural engineer on the C-130. If the goal of the SHM system is to reduce the cost of repair, the system must be able to reliably detect cracks before reaching a length that cannot be cleared by increasing the fastener hole size to install the next oversize fastener. The standard rivet hole sizes contained in [2] can be used to calculate the maximum size of a repairable crack by using an oversized fastener. The maximum allowable crack size is the difference between the radius of the original fastener hole and the radius of the oversize fastener hole. Table 2.5 shows that to allow the use of an oversize fastener repair, a SHM system must be able to reliably detect cracks of 0.0155 or 0.0315 inches, depending on the use of a first oversize or next nominal size fastener. These “repairable” crack lengths represent nearly an order of magnitude reduction verses the minimum critical crack lengths in the F-15 or C-130.

Table 2.5: Crack sizes less than 0.0155 or 0.0315 inches should be reliably detected to reduce repair cost. \* indicates oversize replacements

Rivet Diameter (in)	Max Allowable Hole Radius per [2] (in)	Difference Between Nominal and First Oversize Radii (in)	Difference Between First and Second Nominal Radii (in)
3/16	0.101	0.0155	0.0315
7/32*	0.1165		
1/4	0.1325	0.0155	0.0315
9/32*	0.148		
5/16	0.1635	0.0155	0.0315
11/32*	0.179		
3/8	0.195	0.0155	
13/32*	0.2105		

*2.3.3 Organizational Roadblocks.* As shown in Figure 2.2 (on page 8), the USAF SHM community consists of a set of independent groups, each pursuing a particular aspect of SHM development or focused on a particular SHM project, without a central body to focus efforts and disseminate lessons learned across the entire community. At the aircraft sustainment level, individual System Program Offices have become individual islands of SHM that are forced to address all aspects of SHM, including sensor development, testing and data analysis using existing aircraft sustainment budgets.

### III. Experimentally Determining Changes in SHM Performance

#### 3.1 Introduction

SHM promises to decrease the maintenance cost and increase the availability of aging aircraft fleets by fundamentally changing the way aircraft inspections are performed. But this promise can only be realized through the consistent and predictable performance of a SHM system throughout the entire remaining life of a given aircraft. Questions remain concerning the performance, durability and reliability of SHM systems after long-term exposure to the hostile aircraft environment. These questions have been a serious impediment to the large-scale implementation of SHM on legacy aircraft fleets. This chapter describes the design of an experiment to determine changes in SHM performance due to factors in the aircraft environment. Chapter IV provides the results and analysis of the experiment.

To limit the scope of this experimental design, the overall focus is placed on SHM sensors. Sensors will have the widest distribution across the airframe, as shown in Figure 3.1 (discussed in Chapter II and reproduced below), and will therefore be exposed to the greatest range of aircraft environmental factors.

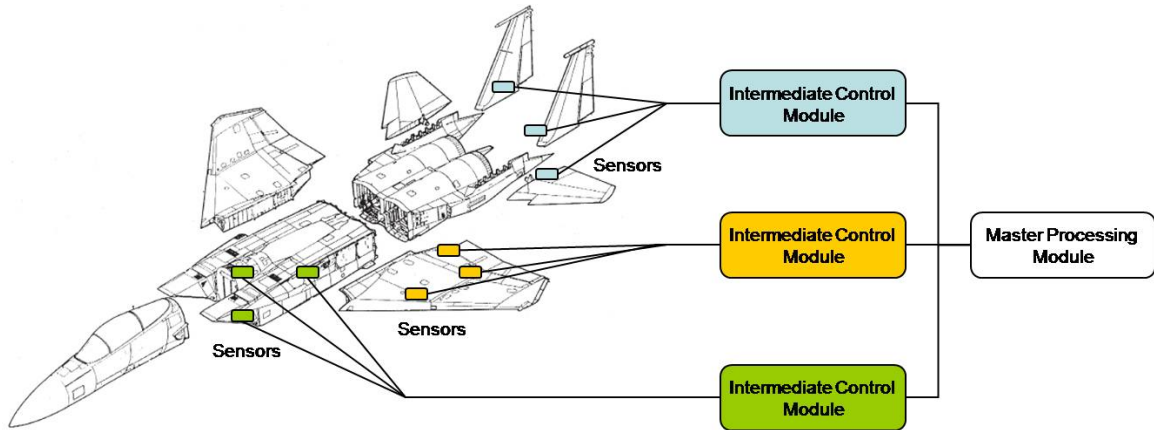


Figure 3.1: Sensors of a SHM system have the greatest potential to be subjected to a harsh aircraft environment due to their distribution over the airframe

This chapter has the following structure: Sections 3.2 and 3.3 define the SHM technology to be tested, provide a brief technical overview of the physical mechanism

used to detect aircraft structural damage, and provide background information concerning durability research performed by other researchers on the technology. Section 3.4 gives specific test objectives, and section 3.5 describes the physical test set-up. Sections 3.6 through 3.11 use design of experiments techniques to establish experimental factors and required sample sizes for subsequent statistical analysis. Finally section 3.12 describes the statistical analysis and modeling to be conducted on the experimental results.

### ***3.2 Selecting A SHM Technology for the Experiment***

Section 2.1 introduced several SHM technologies currently under development. One SHM technology in particular has a wide research base due to promising capabilities and low implementation cost: the use of PZTs to transmit and receive surface waves (specifically Lamb waves) within a thin aluminum aircraft structure [49, 88]. This technique analyzes wave changes between two PZT disks in a “pitch-catch” configuration or with a single PZT disk in a “pulse-echo” configuration. Changes in the waves are used to determine the presence of structural damage. Previous work by Swenson, Crider and Underwood [30, 109, 111] used PZT disks in experiments to detect simulated and actual fatigue cracks in simulated aircraft structure. Their work provided the initial baseline for the experiment described in the following sections.

### ***3.3 A Brief Introduction to Lamb Waves and Their Use in SHM***

This general discussion of the basic physics of Lamb waves and their use in SHM is meant to provide a common framework to describe the sensor degradation experiment. More extensive descriptions of Lamb waves and their uses are available in many other publications, including [30, 49, 89, 99, 109].

*3.3.1 Lamb Waves Described.* Lamb waves fall under the more general category of guided waves, with Lamb waves defined as waves of plane strain occurring in a free plate, with surface traction forces (forces caused by interaction with surrounding

materials, e.g. friction, fluid pressure, contact forces [96]) equal to zero at the upper and lower surfaces [99].

Rose [99] uses the plane strain wave equations for longitudinal and shear waves (equations 3.1 and 3.2) to describe the displacements and velocities of Lamb waves in a thin plate.

$$\frac{\partial^2 \phi}{\partial x^2} + \frac{\partial^2 \phi}{\partial y^2} = \frac{1}{c_L^2} \frac{\partial^2 \phi}{\partial t^2} \quad (3.1)$$

$$\frac{\partial^2 \psi}{\partial x^2} + \frac{\partial^2 \psi}{\partial y^2} = \frac{1}{c_T^2} \frac{\partial^2 \psi}{\partial t^2} \quad (3.2)$$

with:

$\phi, \psi$  = Potential functions

$x, y$  = Displacements

$c_L, c_T$  = Longitudinal and transverse wave speeds, respectively

and having general solutions:

$$\phi = A_1 \sin(py) + A_2 \cos(py) \exp[i(kx - \omega t)] \quad (3.3)$$

$$\psi = B_1 \sin(qy) + B_2 \cos(qy) \exp[i(kx - \omega t)] \quad (3.4)$$

with:

$A_1, A_2, B_1, B_2$  = Constants to be determined

$$p = \sqrt{\frac{\omega^2}{c_L^2} - k^2}$$

$$q = \sqrt{\frac{\omega^2}{c_T^2} - k^2}$$

$t$  = time

$\omega$  = Angular frequency

$k$  = Lamb wave number

$$i = \sqrt{-1}$$

The general solutions can then be split into two modes: symmetric and antisymmetric [49]. For symmetric wave modes, each plate surface has a peak or trough at the same

in-plane location. For antisymmetric wave modes, a peak at one surface corresponds to a trough at the other surface, as shown in Figure 3.2 [30, 49, 89].

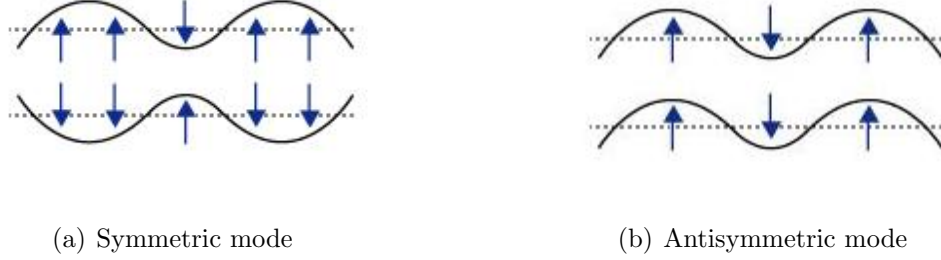


Figure 3.2: Wave peaks occur simultaneously at each plate surface for symmetric wave modes, and peaks at one surface correspond with troughs at the other for antisymmetric wave modes

Lamb wave velocity (or velocities) at a given frequency can be determined by applying the zero surface traction boundary conditions to the general wave equation solutions given above, and then deriving the Rayleigh-Lamb frequency relations for the symmetric and antisymmetric Lamb wave modes. Rose also notes that even though the Rayleigh-Lamb relations look relatively straightforward, they can only be solved through numerical methods (see [99]). Equations 3.5 and 3.6 give the Rayleigh-Lamb frequency relations for symmetric and antisymmetric modes respectively.

$$\frac{\tan(qd)}{\tan(pd)} = -\frac{4k^2pq}{(q^2 - k^2)^2} \quad (3.5)$$

$$\frac{\tan(qh)}{\tan(ph)} = -\frac{(q^2 - k^2)^2}{4k^2pq} \quad (3.6)$$

with:

$p, q, k$  = As defined on page 42

$h$  = One half plate thickness

Wave velocities can be determined using the wave number,  $k$ , and wave frequency through the relation given in equation 3.7.

$$c_p = \frac{\omega}{k} \quad (3.7)$$

with:

$c_p$  = Phase velocity of the Lamb wave mode

$\omega$  = Angular frequency =  $2\pi f$

$f$  = Linear frequency (in cycles per second)

For a given frequency, an infinite number of “k’s” satisfy equations 3.5 and 3.6, resulting in an infinite number of waves (both symmetric and antisymmetric) that can exist within a plate at a given time. Specific notation ( $S_0, S_1, S_2$ , etc. and  $A_0, A_1, A_2$ ) is used to identify Lamb wave modes and wave numbers that occur under a given set of conditions.

It must also be noted that in any application of structural excitation, the actual excitation signal occurs over a range of frequencies, resulting in multiple symmetric and antisymmetric waveforms, each with its own corresponding velocity within the structure [49, 89].

As the multiple Lamb waveforms travel across a plate, they tend to coalesce into wave packets. At certain excitation frequencies and plate thicknesses, these packets are dominated by a given Lamb wave mode ( $A_0, S_0$ , etc.) and travel at a group velocity derived from the phase velocity  $c_p$ , given by equation 3.8 [99].

$$c_g = \frac{d\omega}{dk} = c_p^2 [c_p - (fd) \frac{dc_p}{d(fd)}]^{-1} \quad (3.8)$$

The dependence of group velocity on frequency and plate thickness can be shown by plotting the frequency thickness ( $fd$ ) product against group velocity for a given wave number. Figure 3.3 shows Lamb wave group velocities for the  $S_0$  and  $A_0$  waveforms as a function of  $fd$  for aluminum as calculated by Crider [30]. Of note in Figure 3.3 are the steep changes in group velocities for the  $S_0$  wave packet between  $fd \approx 1.5$  - 2.5, and for the  $A_0$  wave packet between  $fd \approx 0$  - 0.5. These sharp changes in group



velocity based on frequency (given a constant plate thickness) tend to disperse the wave packets. This dispersal must be taken into account when selecting a  $fd$  product for a SHM application.

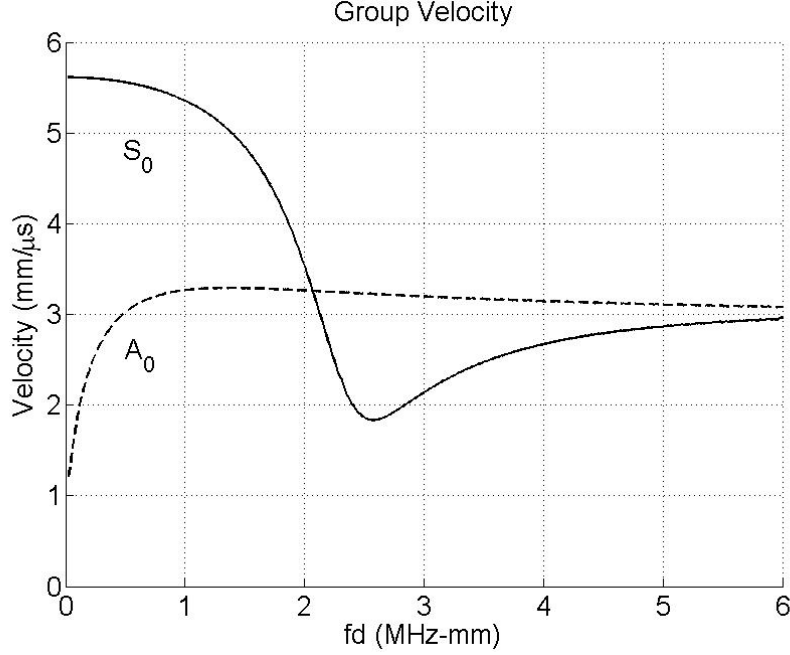


Figure 3.3: Lamb wave group velocity depends on wave frequency and plate thickness

*3.3.2 Lamb Waves in Structural Health Monitoring.* General benefits of using Lamb waves in structural health monitoring include large propagation distance and through-thickness wave components. These wave characteristics potentially allow for the monitoring of large areas with relatively few sensors, and the capability to detect both surface and internal structural defects [89]. The introduction of relatively inexpensive PZT disks allows Lamb waves to be excited and detected within a thin plate simply by gluing the transducers directly to the surface and driving the PZT with a known waveform.

Giurgiutiu [49] found that specific Lamb wave modes could be excited (“tuned” in his terminology) in plates using specific driving excitation frequencies, greatly assisting in the task of identifying the form of the original signal and changes in Lamb

wave structure due to physical damage. Giurgiutiu derived displacement equations describing the effect, and experimentally determined that below 200 kHz the  $A_0$  mode was predominately excited, while at around 300 kHz the  $S_0$  mode dominated. The  $A_0$  mode then returned to dominate at around 500 kHz. Figure 3.4 shows the theoretical changes in  $S_0$  and  $A_0$  wave amplitude verses driving frequency using a 0.635mm diameter PZT to generate Lamb waves in a 3mm thick aluminum plate. Calculation is based on Giurgiutiu [49] and presented in Underwood [109].

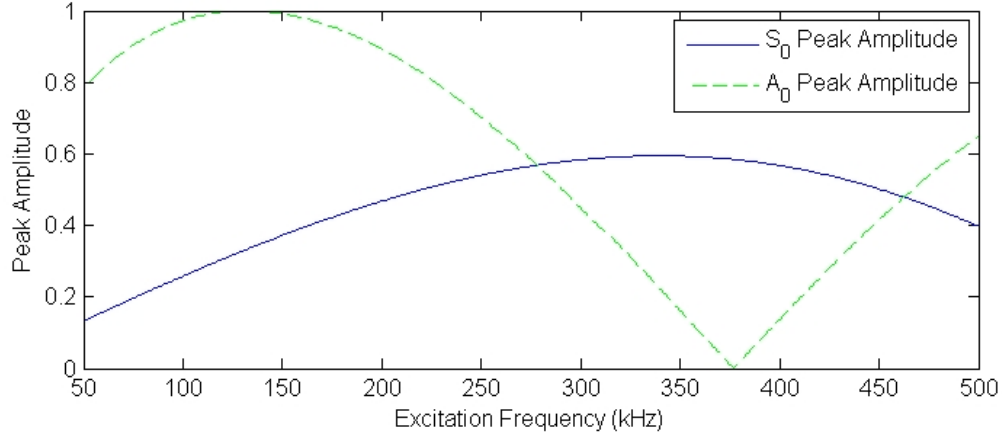


Figure 3.4: Specific lamb wave modes can be targeted using specific excitation signal frequencies

As noted above, at certain ranges of the  $fd$  product, large changes in Lamb wave group velocity can occur over relatively small changes in excitation frequency, causing increased dispersal of the Lamb wave packets. To limit the impact of the range of frequencies contained in an excitation signal, tone burst signals can be filtered through a Hanning window to reduce the excitation of multiple frequencies associated with sharp transitions at the start and end of a traditional tone burst [48]. A Hanning window, rather than the more common Hamming window, is used in this instance due to the Hanning window’s faster side lobe decay [63, 70]. Figure 3.5 shows a representative Hanning windowed sine wave “packet” used for PZT excitation at a desired frequency.

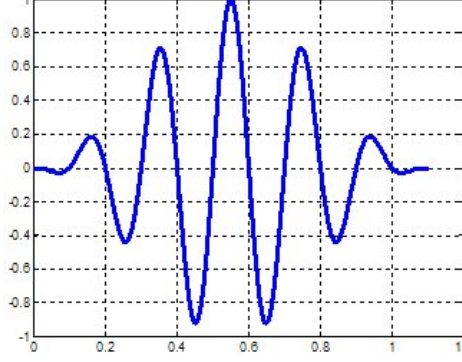


Figure 3.5:  $5\frac{1}{2}$  cycle windowed sine wave excitation signal “packets” are used to excite Lamb waves at a desired frequency

*3.3.3 Previous PZT Durability Testing.* Three groups have published experimental results relating to the “durability” of PZT-type sensors in relation to the aircraft environment. The first group, located at AFRL has performed basic research concerning the change in PZT vibration amplitude and signal strength due to thermal cycling, corrosive environment exposure, vibration exposure and controlled disbond. The other two groups conducted tests in an effort to “certify” specific SHM sensor and system designs for use on aircraft. The following sections detail each effort.

*3.3.3.1 Air Force Research Lab PZT Durability Testing.* The NDE Branch of AFRL has been investigating the behavior of PZTs adhesively bonded to aluminum under a series of environmental factors. Table 3.1 lists the type of sensors and parameters used in AFRL’s tests. Peak displacement of the PZT was the primary measure and for the tests. This displacement was measured through the use of a laser interferometer that allows surface displacements to be determined down to the nanometer level. PZT disbonding and cracking were also determined using this device by noting changes from a concentric-circle surface wave pattern to a non-uniform pattern on the surface of the PZT.

AFRL’s published results to date include high temperature and low temperature thermal cycling, extended outdoor exposure, vibration testing and exposure to one type of corrosive environment. In all testing except the corrosive environment, the

Table 3.1: AFRL PZT durability testing parameters

Parameter	Description	Ref
Sensor Type	1 cm dia, 200 $\mu$ m thk piezoelectric disk	[11–15, 73]
Adhesive Type	M-Bond 200 strain gauge adhesive	[11–13, 15]
Substrate	Aluminum, temper not specified	[14, 73]
Input Signal	1-cycle, 100 kHz 10Vpp toneburst	[11–13]
	Various driving frequencies	[14, 15, 73]
Measurand	Peak PZT displacement in nanometers	[11–15, 73]
	Signal strength	[14, 15]

capability of the sensor (as measured through peak displacement) was generally reduced from 40 to 60%. Table 3.2 gives general descriptions of the tests, and summary of the results.

Table 3.2: AFRL PZT durability testing results

Test	Description	Summary Results	Ref
Thermal Cycling (Low)	40 12 hr cycles between 5F (-15C) and 75F (24C), measurements taken after samples returned to 75F	<ul style="list-style-type: none"> <li>- Reduction in PZT displacement</li> <li>- Quadratic trend</li> <li>- Ave displacement -1.8%/cycle</li> <li>- Reduction slowed after 35 cycles</li> <li>- No evidence of cracks / disbonds</li> <li>- 44% reduction over 40 cycles</li> </ul>	[11–13]
Thermal Cycling (High)	40 1 hr cycles between 175F (80C) and 75F (24C), measurements taken after samples returned to 75F	<ul style="list-style-type: none"> <li>- Reduction in PZT displacement</li> <li>- Quadratic trend</li> <li>- Ave displacement -4.7%/cycle</li> <li>- 17% reduction after 1 cycle</li> <li>- Reduction slowed after 10 cycles</li> <li>- No evidence of disbonds</li> <li>- 1 small stable crack after 1 cycle</li> <li>- 56% reduction over 40 cycles</li> </ul>	[11–13]
Outdoor Exposure	63 weeks of outdoor exposure	<ul style="list-style-type: none"> <li>- Indications of cracking, edge disbonding</li> </ul>	[12]
Corrosion Cell	15 cycles in a 3.5% NaCl electrolyte solution with platinum electrode, exposure time not specified	<ul style="list-style-type: none"> <li>- Minimal impact on PZT displacement</li> </ul>	[11, 13]
Vibration	70 Hz nominal frequency 2093 $\mu$ in/in maximum strain level, exposure time not specified	<ul style="list-style-type: none"> <li>- Disbonding, cracking and fracture</li> </ul>	[11, 13]

Blackshire [14, 73] has also performed initial investigations to determine how changes in the glue type used to attach the PZTs to the test specimen affect PZT performance. One goal of the investigations is to determine the glue type that minimizes the effect of very low frequency strain (due to thermal or mechanical cycling) while maintaining the strong mechanical coupling required at high PZT excitation frequencies. Investigated glue types range from strain gage adhesive (providing a very stiff bond) to vacuum grease (providing a very compliant bond). Durability tests comparing PZT performance with multiple glue types have not been published.

### *3.3.3.2 Metis Design Corp SHM Sensor Durability Research and Testing.*

The Metis Design Corporation has conducted several studies into the requirements for SHM system certification, specifically focusing on a piezoelectric sensor developed by the company. Initial studies [23,57] researched existing military and civilian specifications attempting to identify current certification requirements for aircraft equipment that are applicable to SHM, and to identify gaps in the current specifications. The initial analysis focused on three existing specifications: 1) RTCA/DO-160E: Environmental Conditions and Test Procedures for Airborne Equipment, recommended by the FAA for environmental standards; 2) MIL-STD-810F: Environmental Engineering Considerations and Laboratory Tests; and 3) MIL-STD-461E: Requirements for the Control of Electromagnetic Interference Characteristics of Subsystems and Equipment [22, 23]. Ten general certification areas were identified from the specifications, and testing in those areas was conducted on an integrated PZT disk / circuitry sensor developed by the Metis Design Cooperation. Table 3.3 gives the general test parameters, and Table 3.4 gives the 10 areas of focus, specific test scenarios and results for three sensors undergoing each test.

From analysis of the first wave packet to arrive at the sensor, the author concluded the change in wave time of flight (TOF) metric did not represent a good measure of SHM performance because all changes occurred below the measurement threshold. But the change in peak voltage metric did represent a good measure. A

general summary of the results concluded that the high temperature, humidity and the water based fluid susceptibility tests had the greatest influence on the sensors [22]. It should be noted that the sensor degradations observed in the testing result from multiple failure modes (integrated circuitry issues, USB port connectivity issues and potential for bond degradation) and the reports did not identify the effects caused by specific failure modes.

Table 3.3: Metis corp PZT durability testing parameters [22]

Parameter	Description
Sensor Type	Metis Corp METI-Disk 3, integrated PZT and circuitry “node”
Adhesive Type	AE-10 epoxy
Substrate	2024-T3 aluminum
Input Signal	Five-sine wave in a Hanning window, 60 kHz 5.8 Vpp Pulse - echo measurement
Measurand	$\Delta$ peak voltage between pre- and post-test signals $\Delta$ wave packet time of flight between pre- and post-test signals

*3.3.3.3 Acellent Technologies Inc. SHM Sensor Static Load and Fatigue Testing.* Acellent Technologies Inc. investigated the changes in performance of their SMART Layer<sup>TM</sup> integrated PZT sensor due to fatigue loading of the underlying structure [62] (see [66] for information on the SMART Layer<sup>TM</sup> sensor). Table 3.5 gives the general test parameters, and Table 3.6 gives details of the specific tests conducted and summary results. The measureand was the relative change in signal amplitude after a given load history,  $\eta/\eta_0$ . Kusaka’s conclusions [62] state the performance of the PZT-based SMART Layer<sup>TM</sup> remains unchanged when the applied strain does not exceed the static failure strain of the device for both static and fatigue loading. For fatigue loading, Kusaka also states the degradation of the PZT-based SMART Layer<sup>TM</sup> is considerably stable after several cycles of loading if the applied strain exceeds the static failure strain of the layer.

Table 3.4: Metis corp SHM durability tests and summary results [22]

Environment	Test Description	First Wave Packet Results
High Temperature	2°C/min ramp from 25C to 85C, hold 2 hrs, return to 25C	-30.6%±29% $\Delta$ Pk voltage 22%±63.1% $\Delta$ TOF No node or adhesive changes noted
Low Temperature	-2°C/min ramp from 25C to -55C, hold 2 hrs, return to 25C	-8.1%±17% $\Delta$ Pk voltage -15%±13.2% $\Delta$ TOF Intermittent loss of PC-node connectivity
Thermal Shock	-10°C/min ramp from 25C to -55C, hold 30 min, 10°C/min ramp to 85C, hold 30 min, 10°C/min ramp to -55C, hold 1 hr, 10°C/min ramp to 25C, hold 30 min. Repeat sequence twice	-8.1%±17% $\Delta$ Pk voltage -15%±13.2% $\Delta$ TOF No node damage noted
Humidity	65C, 95% relative humidity for 2 hr ramp to 38C, 85% RH over 16 hrs	-36.7%±39% $\Delta$ Pk voltage -15%±13.2% $\Delta$ TOF Potential connectivity disruption with one node
Oil-based Fluids susceptibility	24 hr immersion	9.3%±16% $\Delta$ Pk voltage 19.4%±17.3% $\Delta$ TOF No node changes noted
Water-based Fluids susceptibility	24 hr immersion	-44%±5% $\Delta$ Pk voltage -11.4%±10.3% $\Delta$ TOF Potential fluid penetration into node
Altitude	Altitude of 21,336m (4.4 kPa) for 2 hrs	-5.9%±2.7% $\Delta$ Pk voltage -5.6%±9.6% $\Delta$ TOF No node damage noted
Decompression	Decompression to 21,336m in < 15 sec, hold for 10 min	-10.3%±8.4% $\Delta$ Pk voltage -20.7%±23% $\Delta$ TOF
Overpressure	Pressure to -4,572m (170 kPa), hold for 30 min	3.4%±5% $\Delta$ Pk voltage 0%±0% $\Delta$ TOF
Static-strain	In [22]: Strain coupon near yield, 2.2 kN steps to 275 MPa, 4.4 kN steps back to 0 NOTE: Not a DO-160E requirement	-16.4% $\Delta$ Pk voltage -20% $\Delta$ TOF No node damage noted
	In [23]: Strain levels stepped to near test coupon yield	-46% $\Delta$ Pk voltage 0.5% $\Delta$ TOF

Table 3.5: Acellent Technologies PZT sensor load testing parameters [66]

Parameter	Description
Sensor Type	Acellent Technologies SMART Layer <sup>TM</sup> actuator/sensor with 2 PZT discs, 6.35mm dia, 0.254 thk
Adhesive Type	Epoxy “adhesive film”
Substrate	A6063 aluminum extrusion, 3.2mm thk
Input Signal	Five-cycle sinusoidal tone burst, 60 kHz frequency, 50V amplitude Pitch - catch measurement
Measurand	Change in amplitude at a given load history, $\eta/\eta_0$

Table 3.6: Acellent Technologies sensor load tests [62]

Test	Description	Summary Results
Continuous static loading	Increasing stress from 0 to 250 MPa (strain from 0 to 2%)	$\eta/\eta_0 = 1$ up to $\varepsilon \cong 0.3\%$ , $\sim$ lognormal $\eta/\eta_0$ decrease for $\varepsilon \geq 0.3\%$ , $\eta/\eta_0 \cong 0.055$ at $\varepsilon=1.5\%$
Discontinuous static loading	Specimen repeatedly loaded to 250 MPa and unloaded	$\eta/\eta_0 = 1$ up to $\varepsilon \cong 0.3\%$ , $\sim$ lognormal $\eta/\eta_0$ decrease for $\varepsilon \geq 0.3\%$ , $\eta/\eta_0 \cong 0.055$ at $\varepsilon=1.5\%$
Fatigue loading	$N = 10^6$ cycles at 10Hz, 0.1min/max strain ratio Tests at 0.1% to 1.5% max $\varepsilon$	$\eta/\eta_0 \cong 1$ for $\varepsilon \leq 0.2\%$ up to $N= 10^6$ , $\eta/\eta_0$ decreased for $\varepsilon \geq 0.2\%$ , most degradation occurring for $N < 10^2$

*3.3.3.4 Underwood Fatigue Crack Detection Experiment.* Although not a PZT durability test *per se*, Underwood’s fatigue crack detection experiment [109] illustrates how environmental factors can affect the response of PZT transducers. Underwood attempted to detect a fatigue crack grown across a test specimen using Lamb waves generated by PZTs. PZTs were placed in a pitch-catch configuration and readings were taken at several points before and after the fatigue crack grew across the pitch-catch path. Underwood did detect signal loss after the fatigue crack passed the pitch-catch path, but Underwood also detected an approximate 10-25% signal loss before the crack passed the pitch-catch path. Underwood attributed this change to



the initial fatigue cycling of the test specimen, but did not attempt to quantify the impact.

### ***3.4 Test Objectives for the Sensor Degradation Experiment***

Based on the results discussed above, it is clear that aircraft environmental factors can affect the responses of PZT transducers glued to the aircraft structure. What is not clear, however, is how the form of the changes can be identified and taken into account in relation to a functional SHM system. Also, the effects of changing glue type to improve performance of PZTs subjected to aspects of the aircraft environment have only begun to be investigated (see Blackshire [11, 12]).

The following sections define a sensor degradation experiment to subject PZT transducers to one aspect of the aircraft environment (strain of the underlying structure) in order to meet the following objectives:

1. Quantify PZT signal changes due to applied static and cyclic strain.
2. Determine if changing PZT adhesive type from a stiff adhesive (MBond 200) to a compliant adhesive (two part epoxy) has a statistically significant impact on item 1
3. Provide data to characterize the degradation of a PZT-based SHM system due to mechanical strain

### ***3.5 General Test Elements***

*3.5.1 Excitation Signal.* In accordance with common practice, [4, 47, 89, 109] this experiment uses a Hanning windowed sine wave as the excitation signal in all experiments. Figure 3.5 shows a representative excitation signal. The excitation signal sent from the “pitch” PZT is a  $5\frac{1}{2}$  cycle Hanning windowed sine wave, with excitation occurring from 50 to 500 kHz, in increments of 10 kHz.

In addition to the reduction in wave packet dispersion described in section 3.3.2, the maximum amplitude of the Hanning windowed excitation signal serves as a refer-

ence point to calculate wave packet times of flight and times of arrival [89] from the exciting sensor to the receiving sensor.

*3.5.2 Response Variable.* The measured response variable at the “catch” PZT is the root sum squares (RSS) of the received signal amplitude over a given response window, as used by Underwood [109]. This RSS amplitude is shown as the shaded area in Figure 3.6 and given by equation 3.9.

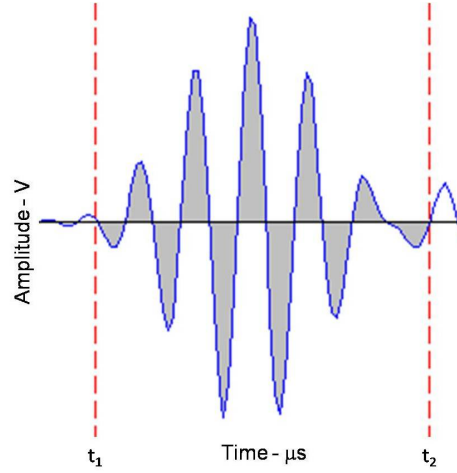


Figure 3.6: Graphical representation of the root sum squares of the signal amplitude

$$y = \sqrt{\sum_{t_1}^{t_2} x_i^2} \quad (3.9)$$

with:

$y$  = Calculated response variable

$x$  = Signal amplitude at the “catch” PZT

$t_1, t_2$  = Beginning and ending times of the response window

The RSS amplitude response variable depends on the choice of the response window,  $t_1$  to  $t_2$ . The size of the window is determined by adding the width of the excitation signal in the time domain (5.5 cycle Hanning windowed sine wave

as described above) to the expected dispersion of the Lamb waveform that occurs between the sensor’s “pitch” and “catch” PZTs.

Underwood, Swenson and Soni [109,111] describe the determination of the time limits for the response window based on speeds of the  $A_0$  and  $S_0$  wave packets, the distance between pitch and catch PZTs, and the distance of the first free edge that causes wave reflection. At a given excitation frequency, wave packet speeds are used to determine five discrete points in time in relation to the “catch” PZT: the arrival and the end of the  $A_0$  wave packet, the arrival and the end of the  $S_0$  wave packet, and the arrival of the first reflected  $S_0$  wave packet. Below 180 kHz excitation, the response window is set by the arrival and end times of the  $A_0$  wave packet, since the  $A_0$  mode dominates the response as shown in figure 3.4. Above 180 kHz, the response window begins at the arrival of the  $S_0$  wave packet, and ends at either the end of the  $S_0$  wave packet or at the arrival of the first reflected  $S_0$  wave packet whichever occurs first.

It should be noted that analysis of the waveform itself, as used in other Lamb wave studies [58,64,88,90,91], was originally attempted to determine changes due to experimental conditions. But to perform waveform studies, it is desirable to have a pure wave packet that is free of reflections. The restricted geometry of the dogbone test area (see section 3.5.4) prevents the capture of a pure waveform packet without also capturing a portion of the free edge reflection. Using 150 kHz excitation as a baseline, the 5.5 cycle excitation signal takes  $36.7 \mu s$  to pass a given point, and the 3.125 mm thick dogbone gives a  $fd$  product of 0.469 MHz-mm. Figure 3.4 shows that the  $A_0$  Lamb wave mode dominates at 150 kHz, and Figure 3.3 shows an  $A_0$  wave packet velocity of approximately  $3 \text{ mm}/\mu s$  at  $fd = 0.469 \text{ MHz-mm}$ . If no edge reflection is desired in the “catch” signal, the entire  $A_0$  wave packet must pass before the first edge reflection arrives. Assuming the pitch and catch PZTs can be placed 1 mm apart on the centerline of the 80 mm wide dogbone test section (not practical from an installation standpoint, but assumed here for illustrative purposes) the beginning of the reflected wave packet arrives at the catch PZT in  $\frac{2*(39mm)}{3 \frac{mm}{\mu s}} = 26 \mu s$ , which is

less than the  $36.7 \mu\text{s}$  it takes for the entire  $A_0$  wave packet to pass the catch PZT. Waveform simulation in MATLAB confirmed that pitch catch PZT pairs could not be placed in the test section without signal interference from the first reflection. Due to this interference, changes in waveform analysis were not pursued, and the change in RSS amplitude was selected as the response variable to determine changes in PZT performance.

*3.5.3 The PZT Pitch-Catch Pair “Sensor”.* The “sensor” used in all phases of the experiment consisted of two PZT transducers configured in a pitch-catch layout. Since the object of the experiment was to determine statistically significant sensor degradation, a clear, repeatable signal at the catch PZT was essential. Single PZT pulse-echo configurations resulted in different amounts of reflected energy returning to the PZT due to the different PZT locations on the test specimen. Pitch-catch pairs installed a consistent distance apart within the test section avoided signal changes between sensors due to differences in reflections. See section 3.8.2 for discussion on the calculations used to determine the final test specimen PZT layout.

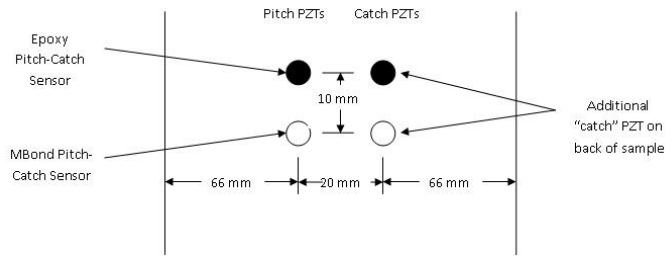
*3.5.4 Test Specimens.* Testing was conducted on two types of test specimens, both fabricated from 0.125 inch thick 6061-T6 aluminum. Initial testing, validation and data analysis were performed on a 6 inch x 12 inch x 0.125 inch flat plate as shown in Figure 3.8. Static strain and cyclic strain testing was performed on dogbone specimens with a test area of 3.15 inches x 4.72 inches x 0.125 inches (80mm x 10mm x 3.175mm). Figure 3.7 shows a dogbone specimen before sensor installation.

*3.5.4.1 Process and System Validation Specimens.* The specimen shown in Figure 3.8 contained one pitch-catch sensor pair glued to the center of the specimen using MBond 200 and one glued using the two part epoxy. In addition, one PZT of each glue type was glued to the other side of the specimen directly opposite the catch PZTs to confirm the Lamb wave mode arriving at the primary catch PZT.

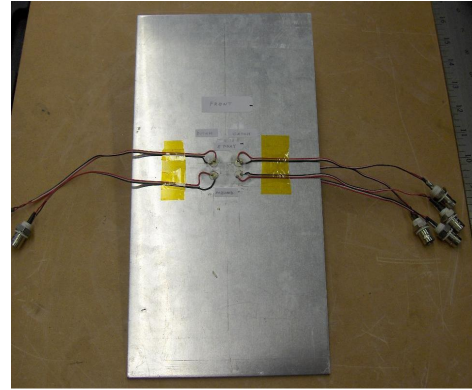


Figure 3.7: Dogbone specimen prior to sensor installation

This specimen was also used to form and validate the PZT installation procedures described in section 3.8.3



(a) Phase 0 Specimen Schematic



(b) Fabricated Specimen

Figure 3.8: Flat plate specimen for process validation

One dogbone specimen was also used for Material Test System (MTS) process and load validation. One Micro Measurements Inc strain gage type CEA-06-125UN-120 was installed on the center of the dogbone with MBond 200 in accordance with [77] and validation tests were run to compare the strain gage measurements against the strain values computed by the MTS.

*3.5.4.2 Static and Cyclic Strain Test Specimens.* Seven specimens were fabricated for static and cyclic strain testing. Ten pitch-catch PZT pairs of each glue type were installed on each test specimen. Figure 3.9 shows the layout and an

example of a completed dogbone test specimen. Subsequent sections detail the PZT layout and pitch-catch pair sample size.

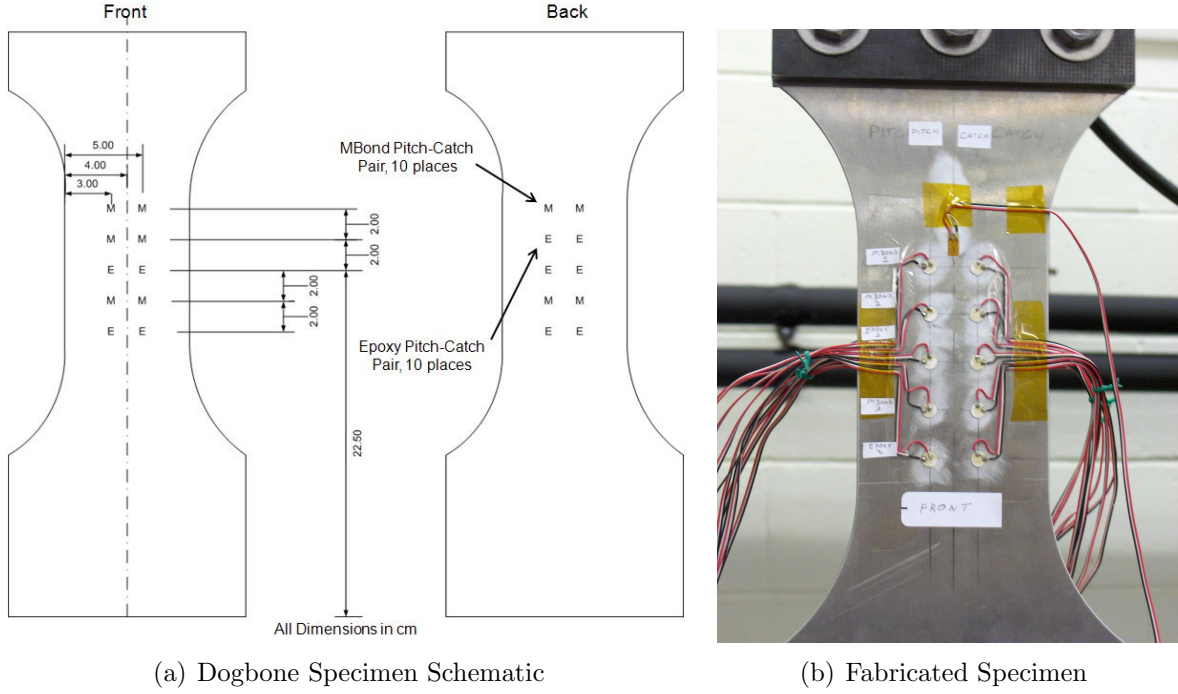


Figure 3.9: Example specimen used for static and cyclic strain testing

**3.5.5 Test and Data Collection Equipment.** The signal generation and data collection equipment used in the experiment is similar to the equipment used by Underwood [109]. The system consists of an Agilent 33120A arbitrary waveform generator, a Hewlett Packard 54621A oscilloscope, and a National Instruments PCI-6133 data acquisition card controlled in a LabVIEW environment. The DAQ card samples up to eight channels at 2.5 MHz. Static and cyclic strain is applied with a 110,000 pound force (110 kip) MTS 810 hydraulic test machine. Figure 3.10 shows the data acquisition system used for the experiment.

### 3.6 Experimental Design

**3.6.1 Defining Experimental Factors.** To build the experiment to test the effects of both strain level and number of cycles on PZT pitch-catch sensor pair

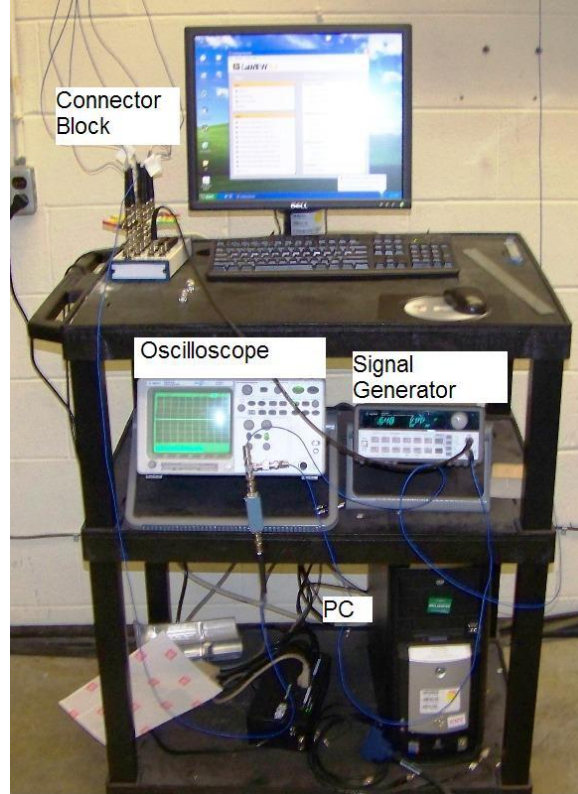


Figure 3.10: Data acquisition system used for all data collection

performance, two types of experimental factors were considered: potential design factors and potential nuisance factors.

*3.6.1.1 Potential Design Factors.* Table 3.7 identifies potential factors in the experiment. Range and levels for factors 2 through 4 are derived in paragraphs 3.9.2 through 3.10.

Table 3.7: Potential experimental design factors

	Potential Factor	Levels
1	Glue Type	MBond and 2 part epoxy
2	Static Strain Level	Strain range and specific levels to be determined (TBD)
3	Cyclic Strain Level	Strain range and specific levels TBD
4	Number of Cycles	Total number of cycles and increments TBD
5	Excitation Frequency	Fixed at 150 kHz

*3.6.1.2 Potential Nuisance Factors.* Nuisance factors are those which may have large effects on the experimental data, and must be taken into account in the experimental design. Table 3.8 lists the potential nuisance factors identified for the experiment, and paragraph 3.6.2 describes the mitigation plans and results to control the nuisance factors.

Table 3.8: Potential experimental nuisance factors

	<b>Factor Category</b>	<b>Potential Factor</b>
1	Specimen Variability	Sensor installation variability
		Specimen material variability
2	Testing Variability	Data collection system variability
		MTS variability
		Temperature changes during testing

### *3.6.2 Mitigation of Nuisance Factors.*

*3.6.2.1 Controlling Specimen Variability.* Specimen variability consists of material variability and PZT installation variability. Material variability was addressed by fabricating all dogbone specimens from the same sheet of 6061-T6 aluminum with the length of the dogbone in the LT grain direction.

PZT installation variability was addressed by several methods. First, installation of individual PZTs followed standardized strain gauge installation instructions published by the education division of Measurements Group Inc. (see [77]). But since these instructions only addressed installation of PZTs with MBond 200, minor changes to the instructions had to be made for PZTs installed with 2 part epoxy (the primary change was substituting isopropyl alcohol for MBond Conditioner A in the installation preparation steps). Appendix A contains the PZT installation instructions and modifications required for the specimen fabrication. Six PZTs were installed on the initial Phase I flat plate sample to validate the standardized installation procedures prior to any PZT installations on the dogbone specimens.



Second, sensor pair location on the dogbone specimen and installation order were addressed. Sensor pair location was determined using the random digit table contained in Vardeman [113], with two caveats. Since sensors were placed on both sides of the dogbone specimen, MBond pairs were glued opposite MBond pairs and Epoxy pairs were glued opposite epoxy pairs to allow Lamb wave data to be collected on both sides of the specimen simultaneously for Lamb wave mode analysis. Also, once specified with the random digit table, the pitch-catch PZT pair location did not change from specimen to specimen (i.e. the top PZT pair on the “front” of the dogbone was always a MBond pair). This identical placement between specimens was implemented in case the five pitch-catch pair responses were not consistent on individual specimens due to different reflected Lamb wave arrival time. At the worst case, there would be at least one consistent result for each pitch-catch pair across all specimens. This precaution was unneeded because consistent signals were received for all pitch-catch pairs within and among the specimens as described in section 4.2.

PZT pair installation order was also determined using the random digit table in Vardeman, and installation PZT pair installation order was changed for each dogbone specimen.

*3.6.2.2 Controlling Data Collection System Variability.* Data collection system variability was addressed in three parts: first, by determining the level of response variable standard deviation due to instrumentation; second, by defining test procedures to reduce the possibility of data collection errors; and third, by limiting and accounting for data system configuration changes over the time testing was performed (approximately 7 months).

Response variable standard deviation due to the data collection system was determined using the flat plate test specimen described in paragraph 3.5.4. Figure 3.11 presents scatterplots of the RSS amplitude response variable for ten pitch-catch readings from the MBond and Epoxy PZT pair installed on the test specimen. Pair 1

shows the results from the MBond pair, and Pair 2 shows the results from the Epoxy pair.

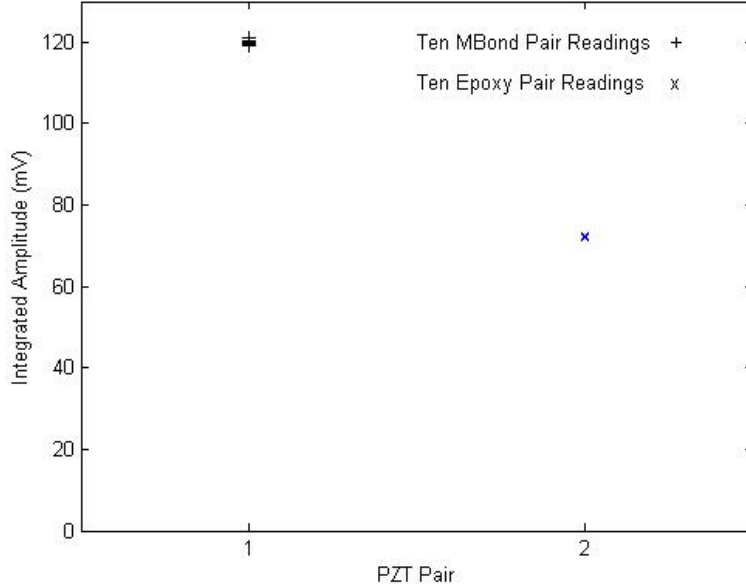


Figure 3.11: Ten repeated measurements to determine instrumentation variability

As Figure 3.11 demonstrates, the variability due to the data collection system is small in relation to the average of the ten signals. For the MBond pair, the average of the ten signals is 120.3 mV with a standard deviation of 0.76 mV, or 0.63%. For the Epoxy pair, the average of the ten signals is 72.8 mV with a standard deviation of 0.076 mV, or 0.11%. Subsequent calculations have shown these values to be less than 0.% of the total response standard deviation.

Specific test procedures were developed to limit the possibility of data collection errors. Due to the limited number of input-output channels (6) on the data collection system and the number of PZT pitch-catch pairs installed on each dogbone specimen (10), multiple connector changes and data filename changes were required each time data was collected. A similar test configuration was used by Underwood [109], and the large number of filename changes caused several instances of data loss due to overwriting of data files [110]. Appendix B provides a representative test plan (for 50% cyclic strain testing) developed to standardize MTS and data collection equipment set-

up, data file name changes, and PZT excitation / response cable changes to prevent similar data file loss for this experiment.

*3.6.2.3 Controlling MTS Variability.* During MTS validation testing, it was found that the strain readings given by the MTS did not match the strain readings given from the strain gauge installed on the MTS validation test specimen. Originally, the cycling rate was set to 6 Hz, which prevented full load application at each cycle. Cycling rate was slowed to 5 Hz, and the load levels increased to align the strain gauge readings with the strain readings internal to the MTS.

### ***3.7 Establishing Experimental Phases***

The experiment consisted of four phases to meet the test objectives listed in section 3.4. The phases allowed incremental development test parameters and verification of test procedures. The test phases were as follows:

#### *Phase 0: Test Definition and Preparation*

This phase established the general test requirements, parameters and design. The test specimen design and fabrication steps were also defined. Initial testing was conducted to validate the test techniques and the operation of the data collection equipment and analysis software.

#### *Phase I: Static Strain Testing*

This phase subjected pitch-catch PZT sensor pairs to increasing levels of single cycle strain up to the maximum level allowed by the test specimen. Results were used to determine changes in PZT-pair performance due to large strains and to provide data concerning strain levels for cyclic strain testing.

#### *Phase II: Initial Cyclic Strain Testing*

This phase subjected specimens with multiple pitch-catch PZT pairs to 510,000 strain cycles at one of three strain levels. This testing provided data concerning the general form of signal changes due to strain levels and number of cycles. Data from

this phase was used to determine additional testing performed in Phase III, and to perform initial statistical significance tests for changes in the mean response signal between baseline and post-cycling readings.

#### *Phase III: Follow-on Cyclic Strain Testing*

Additional testing was performed to verify Phase II results and to increase PZT pitch-catch pair sample size for analysis.

### **3.8 Defining Phase 0: Test Definition and Preparation**

#### *3.8.1 Objectives.*

1. Design PZT layout for static and cyclic strain specimens;
2. Validate specimen fabrication procedures;
3. Validate data collection procedures for PZT pitch-catch sensor pairs;
4. Build / modify data analysis MATLAB code;

For continuity, portions of the results from Phase 0 have been incorporated into the general test elements section described earlier. Additional information on the completion of the test objectives is presented below.

*3.8.2 PZT Layout.* To build an adequate PZT pitch-catch pair sample size for testing, a clear, consistent and repeatable signal at the catch PZT was essential. Installing several PZT pairs on each test specimen is also desirable due to the time required to perform each test run. Analysis to determine an adequate PZT pitch-catch pair layout focused on two primary areas:

1. Analysis of wave and reflection arrivals at the catch PZTs to ensure consistency across pairs
2. Sufficient physical distance between PZTs to allow consistent installation

As described in section 3.3.1, at certain excitation frequencies and plate thicknesses, Lamb waves in thin plates coalesce into wave packets dominated by a primary

wave mode. The arrival of the beginning of the wave packet, the end of the wave packet, the arrival of the first reflection and the end of the first reflection all contribute to the energy received at the catch PZT over the time window used to calculate the response variable (discussions are limited to the first reflection due to the placement of the response window as described in section 3.5.2). Section 3.5.2 also discussed the fact that due to the restricted geometry of the test section, the first edge reflection will arrive at the catch PZT prior to the end of the primary  $A_0$  wave packet. Starting with the vertical pitch-catch configuration used by Underwood [109], shown in Figure 3.12, MATLAB simulations of the signal received at the catch PZT were performed for several other sensor configurations in an attempt to allow a larger portion of the  $A_0$  packet to be captured before the arrival of the first reflection. Figure 3.13 shows the primary configurations simulated.

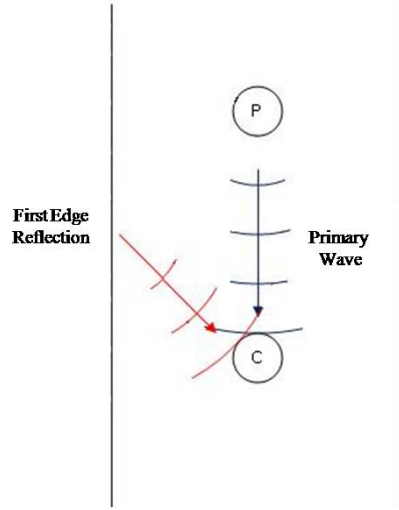


Figure 3.12: Underwood's vertical pitch-catch configuration [109]

MATLAB simulations showed that while increasing the distance between the pitch and catch PZTs using configurations (a) through (c) in Figure 3.13 did result in a larger portion of the  $A_0$  signal arriving at the catch PZT separate from the first reflection, all configurations except (d) showed the first reflections arriving at different times depending on the location of the catch PZT. This change in reflection arrival time affected the calculation of the RSS amplitude response based on a calculated time

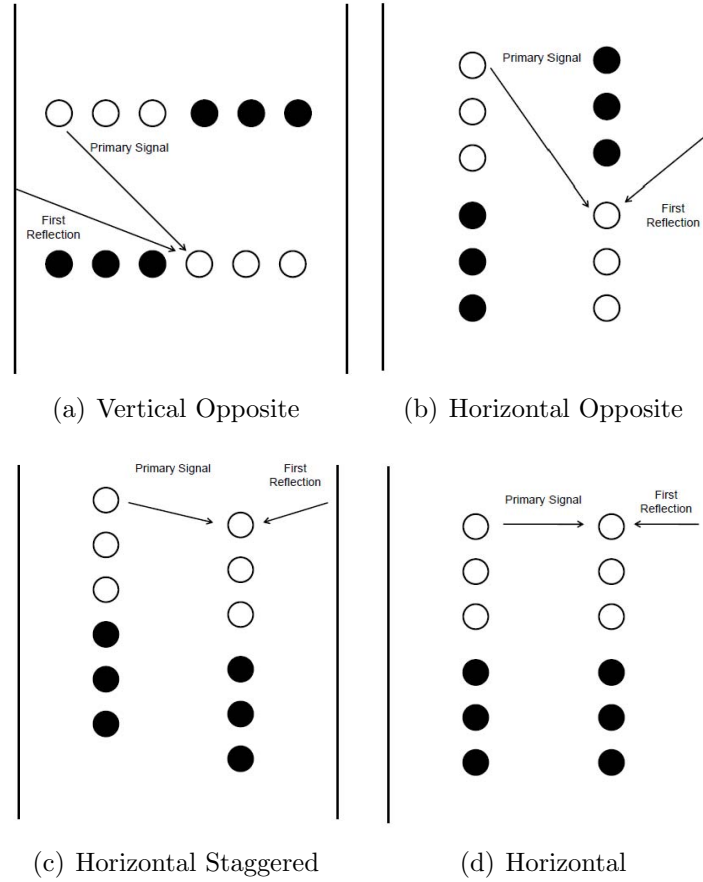


Figure 3.13: MATLAB simulations were used to determine the response at the “catch” PZT from several PZT layouts (dark and light circles indicate different glue types)

window, and produced different response values for “identical” PZT pairs. Horizontal placement of the PZT pairs provides equal reflection distances for each pair and produces equal responses for each horizontal pitch-catch pair on the specimen.

The final distance of 20 mm between pitch and catch PZTs results from installation trials on the flat plate specimen described in paragraph 3.5.4. A critical installation step includes wet sanding the aluminum surface using MBond Conditioner A or isopropyl alcohol and 400 grit sandpaper at the installation location. Based on installation experience gained with the flat plate specimen, 20mm was chosen as an adequate distance between PZTs to perform the wet sanding while preventing the slurry from contacting previously glued PZTs.

3.8.3 *Validation of Specimen Fabrication Procedures.* As discussed in section 3.6.2, PZT pitch-catch pairs were installed in random order using modified strain gage installation procedures originally found in [77]. Appendix A contains the modified installation instructions based on installation glue type. After PZT installation, leads were soldered from the PZTs to coaxial connectors installed on a break-out panel. Coaxial cables could then be used to pass signals to and from the data acquisition system shown in Figure 3.10. Figure 3.14 shows various aspects of the specimen fabrication.

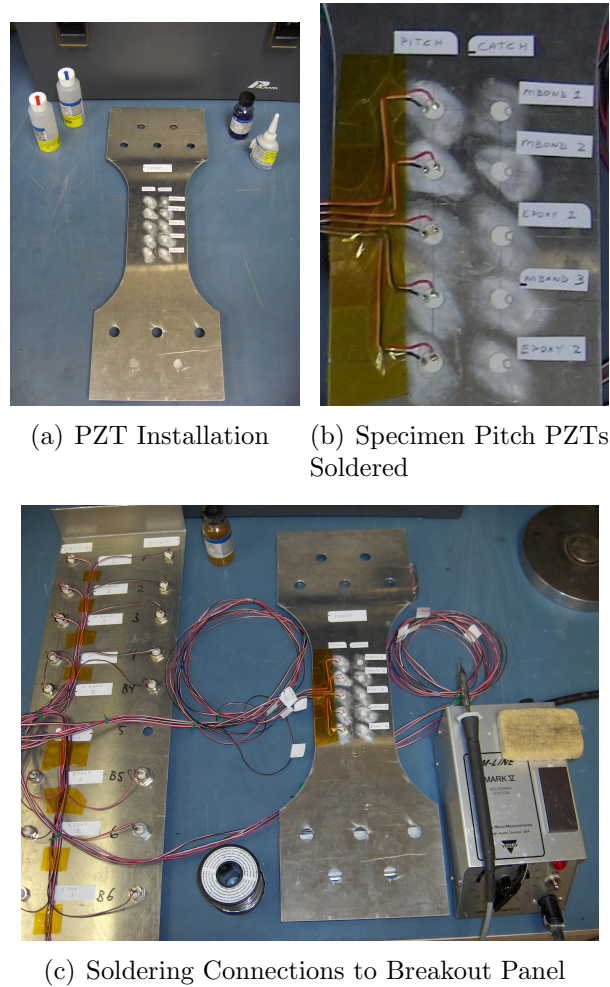


Figure 3.14: PZTs were installed and wired using modified strain gage installation procedures

Figure 3.15 shows the complete testing configuration, including the data acquisition system, a dogbone test specimen with PZT pitch-catch pairs installed, and the MTS system used to apply static and cyclic strains.



Figure 3.15: Final test equipment configuration

*3.8.4 Data Analysis MATLAB Code.* MATLAB code modified from Underwood [109] condensed the LabVIEW data files from each specimen and calculated the RSS amplitude response variable for each test condition as described in section 3.5.2. MATLAB code was also written to perform initial statistical analysis and plotting of results before exporting data to Excel and JMP for further analysis.

### ***3.9 Defining Phase I: Static Strain Testing***

#### *3.9.1 Objectives.*

1. Validate the sensor standard deviation assumptions



2. Find and model static load effects on pitch-catch PZT signal amplitude for two adhesive types
3. Find the static load that had a statistically significant impact on pitch-catch PZT signal amplitude (with  $\alpha$  levels defined in section 3.12.3.1)

*3.9.2 Setting the Maximum Strain Level.* To obtain the widest strain range possible for testing, the maximum allowable strain was calculated based on the properties of 6061-T6 aluminum and the cross sectional area of the dogbone specimen test section. Table 3.9 lists the test section dimensions described in paragraph 3.5.4 and relevant 6061-T6 properties as listed in Chapter 3 of MIL-HDBK-5J [36].

Table 3.9: Specimen properties (from [36]) used to calculate strain levels

Specimen Property	Symbol	Value
Yield strength	$F_{ty}$	35ksi
Elastic modulus	$E$	$9.9 \times 10^3$ ksi
Test area cross section	$a_{test}$	0.39375 in <sup>2</sup>

Yield strain,  $\epsilon_{ty}$ , calculated from the properties listed above:

$$\epsilon_{ty} = \frac{F_{ty}}{E} = \frac{35 \text{ ksi}}{9900 \text{ ksi}} = 0.0035 \text{ in/in} = 3500 \mu\epsilon \quad (3.10)$$

As a precaution to prevent specimen yield, the maximum strain applied was  $3000\mu\epsilon$

*3.9.3 Hypotheses for t-tests.* The Static Strain testing was designed as a two-factor factorial experiment to address the hypotheses listed in Table 3.10

*3.9.4 Required Sample Size and Factor Levels.* The sensor sample size and number of static strain levels were calculated using the method given by Montgomery [83], where a desired significant change in the value of a response variable is selected, and the sample size and number of levels of the experimental factors are iterated such

Table 3.10: General static test hypotheses

Hypothesis Set	General Null Hypothesis
S1	Average MBond sensor response equals average Epoxy sensor response at baseline
S2	Average MBond sensor response at baseline equals MBond sensor response after an applied static strain (strain level TBD)
S3	Average Epoxy sensor response at baseline equals Epoxy sensor response after an applied static strain (strain level TBD)

that if the difference between any two treatment means exceeds a specified value, the null hypothesis should be rejected.

The method uses operating characteristic (OC) curves (curves available in Montgomery and in Pearson [92]) to plot the probability of committing a Type II error,  $\beta$ , against a parameter  $\Phi$ , where:

$$\Phi^2 = \frac{naD^2}{2b\sigma^2} \quad (3.11)$$

with:

n = Number of trials (sensors for this experiment)

a = Number of levels of Factor A

b = Number of levels of Factor B

D = Desired change in response variable to be considered significant

$\sigma$  = Estimate of the response variable standard deviation

To use the OC charts, a D value is selected; a  $\sigma$  value is assumed; and  $\Phi$  is calculated for several values of sample size, n. For each value of  $\Phi$ , the OC chart gives a corresponding  $\beta$  value, allowing a sample size to be selected based on a desired  $\beta$ .

Estimates for D and  $\sigma$  derive from the experiments performed by Underwood [109]. Underwood found a 15 mV decrease in Lamb wave response amplitude between pitch-catch” PZTs when the signal passed over a fatigue crack (see figures 4.12 and 4.16 of [109]). Underwood’s plots also show a response amplitude variation of approx-

imately 5 mV when signals are repeatedly passed between pitch-catch PZTs with no fatigue crack present (see figures 4.15 through 4.17 of [109]). Based on these findings, a change of response amplitude greater than 10 mV is considered significant ( $D = 10$ ), with a signal standard deviation of 5 mV ( $\sigma = 5$ ).

Setting parameters based on static load testing:

n = Number sensors for this experiment (TBD)

a = Factor A: Number of adhesive types (2)

b = Factor B: Number of static load levels (initially 11,  
changed to 9 as described below)

D = 10 mV

$\sigma = 5$  mV

The number of degrees of freedom for the numerator and denominator of equation 3.11 must be identified to use the OC curves in Montgomery and Pearson. Montgomery [83] gives the degree of freedom calculations as:

$$\nu_1 = b - 1$$

$$\nu_2 = ab(n - 1)$$

Setting  $a = 2$  and  $b = 11$ ,  $\nu_1$  will equal 10 and  $\nu_2$  will change based on the selected value of  $n$ . Montgomery and Pearson give OC curves for  $\nu_1 = 8$  and 12. Table 3.11 gives  $\beta$  values obtained from interpolating between the  $\nu_1 = 8$  and 12 curves for increasing numbers of sensors in each experiment. Five sensors per glue type per sample is considered the limit due to the configuration of the data collection system. Table 3.11 shows that for 5 or fewer sensors per sample, the chance of a Type II error is near an unacceptable 20%.

To reduce  $\beta$ , the number of static load levels was reduced from 11 to 9, changing  $\nu_1$  from 10 to 8. Table 3.12 shows that 5 sensors per sample gives a 9% probability of committing a Type II error. This value is considered acceptable for the experiment.

Table 3.13 gives the strain levels and MTS load schedule for the static strain testing based on the calculations above.

Table 3.11: Probability of Type II error ( $\beta$ ) given the number of pitch-catch sensors  $n$  (with 11 load levels and  $\alpha = 0.05$ )

$n$	$\Phi$	$\nu_1$	$\nu_2$	$\beta$
2	0.8528	10	22	0.65
3	1.044	10	44	0.525
4	1.206	10	66	0.295
5	1.348	10	88	0.195

Table 3.12: 5 Sensors are Required to Reduce Probability of Type II Error ( $\beta$ ) Below 10% with 9 load levels and  $\alpha = 0.05$

$n$	$\Phi$	$\nu_1$	$\nu_2$	$\beta$
2	0.9428	8	18	0.62
3	1.154	8	36	0.475
4	1.333	8	54	0.24
5	1.496	8	72	0.09

Table 3.13: Static strain test schedule

Level	$\mu\epsilon$	% $\epsilon$	MTS Load (lbf)
1	25	0.0025	96.7
2	375	0.0375	1450.2
3	750	0.075	2900.4
4	1125	0.1125	4350.6
5	1500	0.15	5800.8
6	1875	0.1875	7251.0
7	2250	0.2250	48701.2
8	2625	0.2625	10151.4
9	3000	0.3	11601.6

### 3.10 Defining Phase II: Cyclic Strain Testing

*3.10.1 Objective.* Characterize the degradation of PZT performance due to a controlled number of component strain cycles

*3.10.2 Hypotheses for t-tests.* The cyclic strain testing was designed as a two-factor factorial experiment to address the hypotheses listed in Table 3.14

*3.10.3 Setting the Maximum Number of Cycles.* The total number of cycles used in cyclic strain testing was based on the loadings experienced by F-15 DTA item

Table 3.14: General cyclic strain test hypotheses

Hypothesis Set	General Null Hypothesis
C1	Average MBond sensor response at baseline equals MBond sensor response after cycling at a predetermined strain level (strain level and number of cycles TBD)
C2	Average Epoxy sensor response at baseline equals Epoxy sensor response after cycling at a predetermined strain level (strain level and number of cycles TBD)

181, IAT location 59.0 identified in paragraph 2.2.3.2. The F-15 SPO provided the DTA for this location, including general part geometry, crack growth information and load exceedance curves [76]. The load exceedance curve showed that the total number of loads experienced at IAT 59.0 is approximately 65,000. Using the reported average of 250 flying hours per year [75] the total number of loadings at IAT 59.0 is assumed to be  $(10 \text{ yrs}) \cdot (250 \text{ hrs/yr}) \cdot (65,000 \text{ loads}/1000 \text{ hrs}) = 162,500$  loads over 10 years. Including a safety factor of 1.5, the total number of expected loads is assumed to be approximately 240,000. The calculation of sample size and cycling levels are both based on this assumed value.

At the time of test execution, it was decided to repeat the given cycle test on each sample thereby increasing the total number of cycles to 510,000 (unless specimen failure occurred during a specific test). The decision to repeat the test was made primarily due to the time involved in specimen fabrication/test preparation, and to provide additional cyclic “run-out” data for analysis.

*3.10.4 Required Sample Size and Factor Levels.* As with the static strain testing, the maximum allowable strain level for the dogbone specimen determined the strain levels for the cyclic testing. Using 250,000 cycles as a baseline, the best fit stress-cycle (S-N) curve for 6061-T6 aluminum gave a maximum allowable testing stress of approximately 35 ksi (assuming min/max stress ration  $R=0$ ) [36] to prevent dogbone specimen failure at test completion.

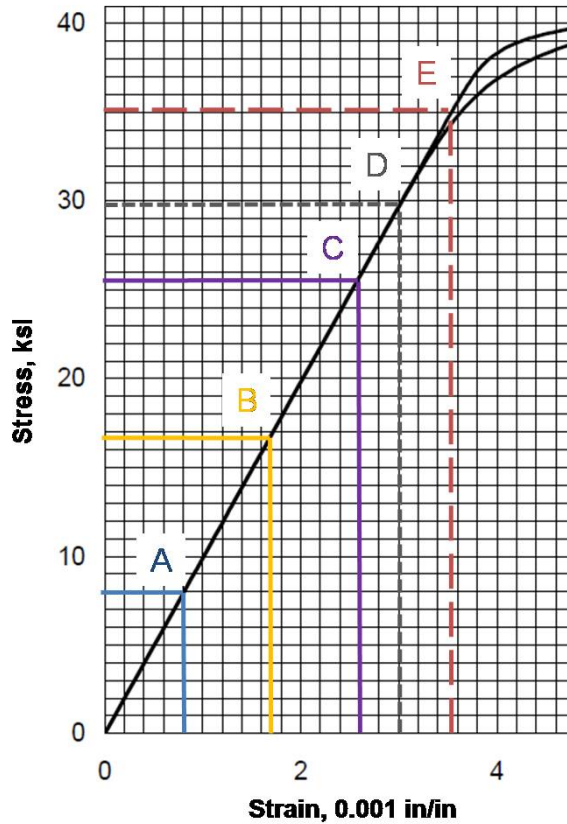


Figure 3.16: Experimental Load Levels Plotted on the 6061-T6 Stress-Strain Curve

As with equation 3.10, the maximum allowable stress equates to approximately  $3500 \mu\epsilon$ . Since dogbone specimens are tested at a single strain level only, the number of strain levels determines the number of dogbone specimens to be fabricated and the time required to complete the testing. To cover the largest strain range with a small number of dogbone specimens, “low”, “medium” and “high” strain levels were selected based on approximately 25%, 50% and 75% of the maximum allowable strain for 250,000 cycles. Figure 3.16 shows the experimental strain levels plotted on the 6061-T6 aluminum stress strain curve [36]. Points A, B and C plot the stress and strain locations for the three cyclic load levels. Point D plots the maximum static stress-strain point of  $3000 \mu\epsilon$ , and point E plots the material yield point of 35 ksi.

Table 3.15 gives the strain levels and MTS load schedule for the cyclic strain testing.

Table 3.15: Cyclic Strain Load Schedule

Level	$\mu\epsilon$	% $\epsilon$	MTS Load (lbf)
1	800	0.08	3118.5
2	1700	0.17	6627.0
3	2600	0.26	10135.0

To define the sample size, the total number of cycles was divided into “Cycle sets” and the same calculation performed in paragraph 3.9.4 was performed with “Cycle sets” replacing “load levels”, resulting in 8 cycle sets of 30,000 cycles each (9 data collection points) to reach approximately 240,000 cycles. The 30,000 cycle increment was maintained throughout the test repetition described in paragraph 3.10.3.

### 3.11 Summary of Test Specimens and Test Conditions

Figure 3.17 shows the arrangement of test specimens and pitch-catch pairs specified in sections 3.9 and 3.10. Twenty pitch-catch pairs of each glue type were installed on 4 dogbone specimens for initial baseline readings. One dogbone containing 5 pitch-catch pairs of each glue type was then subjected to one of four tests: static strain,  $800\mu\epsilon$ ,  $1700\mu\epsilon$  or  $2600\mu\epsilon$  cyclic strain.

### 3.12 Analysis Techniques for Experimental Results

*3.12.1 General Analysis Techniques.* Data analysis occurred in three steps: (1) plotting of the sensor responses by glue type for general response characterization; (2) statistical analysis to determine significant differences in results based on glue type, number of cycles, strain level, etc., and to identify significant effects; and (3) fitting models to the results based on the form of the responses.

Sections 3.12.2 and 4.3.2 provide detail on the statistical analyses to be presented.

*3.12.2 Population Characterization.* Baseline responses from each specimen were used to characterize the overall population. Baseline RSS amplitude response

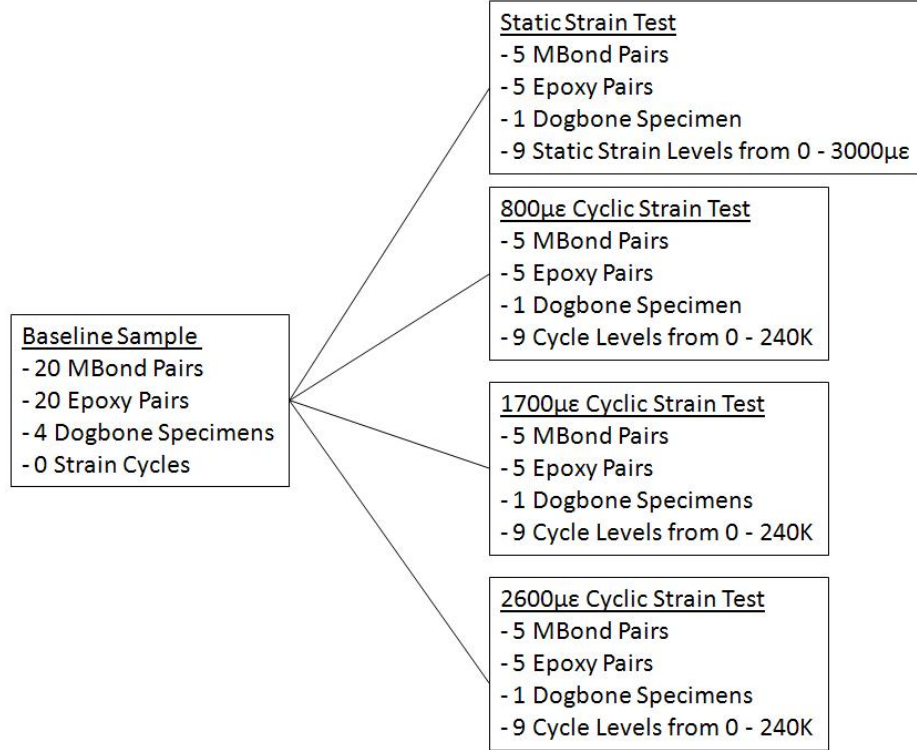


Figure 3.17: 40 baseline pitch-catch pairs divide into 4 test specimens

readings were taken before any static or cyclic strain loading occurs, thus providing a larger sample size to estimate initial average responses and response standard deviation for each glue type. The response standard deviation from this baseline sample was compared to the assumed value of 5 mV, and changes in the statistical significance calculations in section 3.9.4 were adjusted as necessary.

Normality of the baseline data will be tested by applying the Shapiro-Wilk normality test [103] using the JMP statistical software package [65]. Mickey [81] states the Shapiro-Wilk test can be used as a data “screening” device: if the Shapiro-Wilk null hypothesis ( $H_0$  = The given sample data set is normally distributed) is not rejected, assume normality, and if the null hypothesis is rejected, more information is required. Lehman [65] also states “In general, you should reject the null hypothesis of normality only when the  $p$  value is less than 0.05.” This convention will be followed in the subsequent analyses.



3.12.3 *Statistical t-tests.* If the populations pass the normality tests described in section 3.12.2, standard and paired two sided t-tests will be performed to test the statistical significance of the hypotheses identified in Tables 3.10 and 3.14 using 2 factors (e.g.  $H_0$  = Average MBond pair response equals average Epoxy pair response at baseline). The non-parametric Wilcoxon rank sum test [102] will also be performed to test the equality of the group means. If the hypotheses of normality are rejected in section 3.12.2, only the the non-parametric Wilcoxon rank sum test will be performed.

Lehman [65] provides a post-hoc test to determine the *effect size* for standard t-tests that show a statistically significant effect ( $p \leq 0.05$ ). The formula for effect size  $d$ :

$$d = \frac{|\overline{X_1} - \overline{X_2}|}{S_p} \quad (3.12)$$

with:

$\overline{X_1}$  = the observed mean of sample 1

$\overline{X_2}$  = the observed mean of sample 2

$S_p$  = the pooled estimate of the population standard deviation

Cohen [28] then gives guidelines to determine if  $d$  represents a small, medium or large difference. Where appropriate in the following analysis, the effect size will be stated. Table 3.16 contains the threshold levels cited by Lehman:

Table 3.16: Guidelines for interpreting t-test effect sizes, from [28]

Effect Size	Computed $d$ Statistic
Small	0.20
Medium	0.50
Large	0.80

When performing t-tests on the means of two sample responses, the general assumption is that the two means are independent of one another [81, 108]. Certain combinations of sensor responses in the static/cyclic strain experiment cannot be

considered independent. Specifically, sensor readings on a specimen taken at 0 cycles are not independent from sensor readings taken from the same sensors on the same specimen at 30K, 60K, 90K, etc. cycles. This lack of independence violates a basic assumption behind analysis of variance (ANOVA) and regression analysis techniques [65, 81], preventing their direct application for the experimental results.

To account for the dependence of pitch-catch pairs within a sample, paired t-tests will be used to compare responses at a given number of cycles to the baseline responses. Twisk [108] states paired t-tests can be used in this situation to test the hypothesis that the mean difference between the two responses equals zero. Because differences from each **individual** are used in the paired test, the fact that these observations are dependent on each other is taken into account (emphasis in Twisk). Due to the small pitch-catch pair sample size for a given specimen (generally 5 pairs), the non-parametric equivalent to the paired t-test, again the Wilcoxon rank sum test, will also be performed.

*3.12.3.1 Required  $\alpha$  Adjustments for Multiple t-tests.* One application of the paired t-tests described above will be to determine if pitch-catch pair responses are significantly different between two levels of cycles at a given level of strain (did a significant change in sensor response occur between 0 and 60K cycles at  $1700\mu\epsilon$ , for example). If the  $p$ -value for the example is significant, a second test could be performed to determine if there is a significant change between 0 and 30K cycles, giving a better indication of when the effect begins. But multiple t-tests performed on a given data set can increase the probability of committing a Type I error (reject the null hypothesis when it is true) [52]. Individually, the t-tests may have an  $\alpha = 0.05$ , but if taken together, the *combined* confidence level is not 0.05. Vardeman [113] states that under this type of multiple test scenario, confidence levels are not easy to determine, but he gives two recommendations:

1. Use individual confidence levels, and interpret them as such

2. State the lower bound for the combined confidence level using Bonferroni's inequality, and decrease the individual p-values if needed to obtain the desired combined lower bound confidence level

Neter [86] describes the use of Bonferroni's inequality in terms of events. For 2 t-tests, let:

Event A = Test 1 commits a Type I error

Event B = Test 2 commits a Type I error

By definition , for  $\alpha = 0.05$ ,  $P(A) = P(B) = 0.05$ . Bonferroni's inequality states:

$$P(\bar{A} \cap \bar{B}) \geq 1 - P(A) - P(B) \quad (3.13)$$

Therefore, if two t-tests are conducted over the same set of circumstances, both with  $\alpha = 0.05$ , the probability of no Type I error is  $\geq 1 - 2*(0.05) = 0.90$ , giving a combined  $\alpha$  of 0.1. Individual  $\alpha$  values for each t-test must be adjusted in this case if a combined  $\alpha$  value less than 0.1 is desired. The following section explains how t-tests will be applied in the subsequent analysis.

*3.12.3.2 Method for Applying Multiple t-tests.* Two basic test scenarios exist for analysis: (1) static strain testing where response may change over nine static strain levels, and (2) cyclic strain testing where response may change over 18 cycle levels. A maximum of five paired t-tests will be used with a given set of test results to determine or provide information on the following (in priority order):

1. Does a significant change in average response occur?
2. If a significant change occurs, when does the significant change begin?
3. If a significant change occurs, does the signal continue to change in a significant way over the span of the test?
4. If significant changes do not continue, when do they cease?

A maximum of five t-tests provides a combined  $\alpha \leq 0.05$ , with individual  $\alpha$  values at 0.01.

Figure 3.18 shows the basic outline to be used for applying multiple t-tests described in the following steps to determine if a significant change occurs, and if so, when. Using the general null hypothesis  $H_0 = \text{No change in average response}$ :

1. Conduct a paired t-test between the first and last test conditions (baseline and  $3000\mu\epsilon$  static strain or baseline and 510K cycles at a given strain level). If  $H_0$  fails to reject, evidence does not exist that a significant change occurred.
2. If the paired t-test rejects  $H_0$ , adjust  $\alpha$  and conduct a paired t-test between the first and second test condition. If this test rejects  $H_0$ , evidence exists that a significant change occurred between the first and second test conditions.
3. If the second paired t-test does not reject  $H_0$ , adjust  $\alpha$  and conduct a paired t-test between the first and third test condition. If this test rejects  $H_0$ , evidence exists that a significant change occurred between the first and third test conditions. If this test does not reject  $H_0$ , adjust  $\alpha$  and perform another paired t-test with the first and fourth test condition. Continue until  $H_0$  is rejected or until five t-tests are performed.

If a significant change in response is found, and a conclusion is reached about when the change occurs before five paired t-tests are accomplished, the following steps will be used to provide information on whether the changes continue to occur over the span of the test, and if not, when they cease.

1. Conduct a paired t-test between the last and next to last test conditions ( $2625\mu\epsilon$  and  $3000\mu\epsilon$  static strain or 480K and 510K cycles at a given strain level). If this test rejects  $H_0$ , evidence exists that significant changes in signal occur over the entire span of the test.
2. If the paired t-test does not reject  $H_0$ , adjust  $\alpha$  and conduct a paired t-test between the last and next previous test condition. If this test rejects  $H_0$ , evidence

exists that significant changes may not continue after this test condition. If this test does not reject  $H_0$ , adjust  $\alpha$  and continue to test until  $H_0$  is rejected or five paired t-tests have been completed.

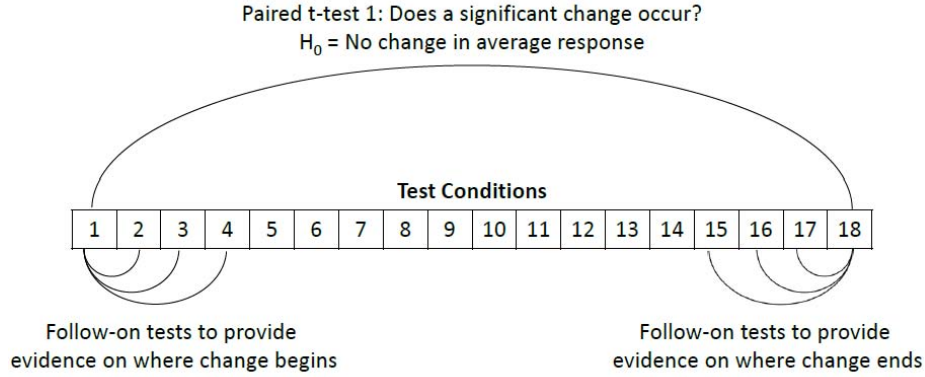


Figure 3.18: If the initial paired t-test identifies a significant change over the entire range of test conditions, follow-on tests will collect additional information on where the change begins and ends

*3.12.4 Analysis of Variance.* As stated in section 4.3.2, lack of independence between responses of a given pitch-catch pair at different numbers of cycles (or static strain levels) prevents ANOVA from being performed to analyze changes in response over the entire test. But before testing begins, the seven test specimens each containing 5 pitch-catch pairs of each glue type, represent independent samples. ANOVA will be used to determine if baseline pitch-catch pair response readings for a given glue type are significantly different across the seven samples. If the average baseline responses are not statistically significant, the results will be pooled for further analysis, see section 4.2.1. For each ANOVA, a summary table will be provided containing the null hypothesis, the sources of variance, the degrees of freedom, the sum of squares values, the mean square values, the F ratio, and the probability of obtaining, by chance, an F statistic as large or larger if the null hypothesis were true ( $\Pr \geq F$ ) [65]. The null hypothesis will be rejected if  $\Pr \geq F$  is less than 0.05.

*3.12.5 Modeling the Results.* As stated in section 4.3.2, the pitch-catch pair responses at different levels of “cycles” are not independent from one another, violating an assumption behind the use of regression analysis and modeling techniques. Equation fits will instead be used to define models for the results. Depending on the form of the responses over cycles and strain level, five equation fits will be applied to the data: linear, polynomial, log(cycles), and power. Log(cycles) is included because it is the common transformation used to model material failures due to cyclic strain [29]. Linear and power equation fits will be applied strictly depending on the form of the results.

Two level best fit models will be established for each glue type using the appropriate model forms listed previously. First, best fit equations for the average responses over the range of cycles will be established at each strain level for each glue type (6 equations of the same form, each with their own coefficient values). As an example, the linear model will have the following form:

$$\text{Response}_{\text{Glue Type}} = \xi_0 + \xi_1 * \left( \frac{\text{Number of Cycles}}{1000} \right) \quad (3.14)$$

with values of  $\xi_0$  and  $\xi_1$  dependent on the cyclic strain level. The number of cycles has been divided by 1000 to increase the coefficient values.

Once the three sets of coefficient values have been determined for a given glue type, they will be plotted against strain level to determine if a relation exists to generalize the coefficients. See section 4.8.1 for the application of this technique.

## IV. PZT Cyclic Strain Experimental Results and Analysis

### 4.1 *Introduction and Overview*

This chapter presents the results and analysis of the PZT cyclic strain experiment described in Chapter III. Seven dogbone fatigue specimens (one for Phase I, three for Phase II, and three for Phase III) were fabricated and tested, with an overall total of 70 pitch-catch pairs. Total test time consisted of 870 hours on test, 110 hours of data collection at 120 different test conditions. The first four sections of this chapter present basic plots of the test results for each test run, and describe any data variations from particular pitch-catch pairs that preclude their use in data analysis. The remaining sections analyze the response data to verify/update initial assumptions (such as response standard deviation), to test various hypotheses concerning the data, and to generate prediction models based on the test results.

Figure 4.1 is an update of Figure 3.17 on page 76, reflecting changes to the arrangement of test specimens between test planning and test execution. Test replication was performed to confirm results from the initial test runs and to increase pitch-catch pair sample size for statistical analysis. The  $1700\mu\epsilon$  test was performed two additional times, increasing sample size to 13, and the  $2600\mu\epsilon$  test was performed one additional time, increasing sample size to 9. The static strain and  $800\mu\epsilon$  tests were not replicated due to the limited number of PZTs available and the lack of statistically significant results from the initial testing (see sections 4.3 and 4.4). Table 4.1 lists the names of the dogbone specimens that will be used in the following analysis. The general testing technique for the static and cyclic strain testing on a given specimen was as follows:

1. Collect baseline sensor data at a nominal strain value on a given specimen prior to any strain cycling
2. Perform a predetermined number of strain cycles at a predetermined strain setting
3. Return specimen to the nominal strain value and collect sensor data

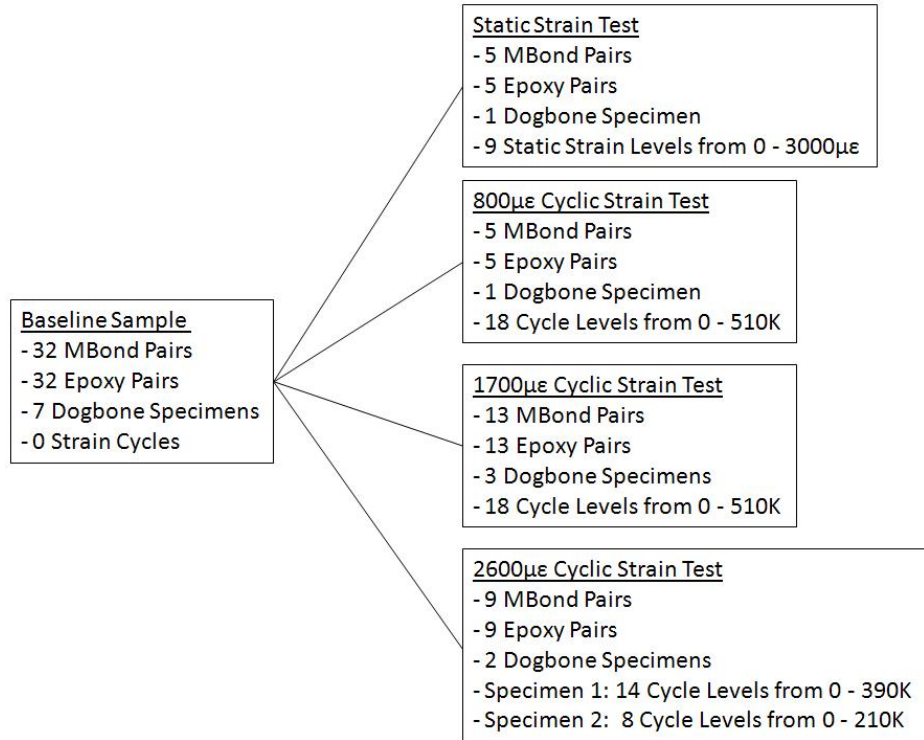


Figure 4.1: 64 baseline pitch-catch pairs divide into 7 specimens for 4 tests

4. Repeat step 2 until test completion or specimen failure

Table 4.1: Test runs and specimen names

Test Run	Specimen Name
Static Strain	Static
Cyclic Strain at 800µε	800
Cyclic Strain at 1700µε Run 1	1700-1
Cyclic Strain at 1700µε Run 2	1700-2
Cyclic Strain at 1700µε Run 3	1700-3
Cyclic Strain at 2600µε Run 1	2600-1
Cyclic Strain at 2600µε Run 2	2600-2



## 4.2 Analysis of Baseline Results

Before applying static or cyclic strain loads to a specimen, a baseline data reading was taken at a nominal  $25\ \mu\epsilon$  to be compared with data readings taken at various test conditions. Since all specimens were subject to this baseline data collection before loading, the baseline readings represent a 32 pair sample size for each glue type that can be used for population characterization and comparison with the assumed population standard deviation of 5mV. (Note: Cable failure from three pitch-catch pairs reduce the sample size from 35 to 32 (see sections 4.5.2, 4.5.3 and 4.6.2).

*4.2.1 Pooling Baseline Results from the Seven Specimens.* Before combining the baseline results for analysis, initial analysis of the “per-specimen” results must be completed to determine if significant between-specimen differences exist that could influence the combined results. Figures 4.2 and 4.3 show the baseline responses plotted by specimen. Neither figure indicates that a significant difference in the average baseline pitch-catch pair response exists due to the test specimen.

To determine if the differences in average response between specimens was statistically significant, ANOVA was completed for each glue type as described in Section 3.12.4. Tables 4.2 and 4.3 contain the ANOVA results for the MBond and Epoxy baseline readings, respectively. Both sets of ANOVA results give no evidence to reject the null hypotheses of equal baseline average responses between test specimens at the  $p = 0.05$  confidence level.

*4.2.2 Baseline Population Characterization.* Figure 4.4 shows the pooled baseline pitch-catch pair responses for each glue type. Average baseline response from the Epoxy pitch-catch pairs is slightly below the response from the MBond pairs at 103.5 vs. 106.7 mV. The Epoxy pair standard deviation is also higher than the MBond standard deviation at 6.67 vs. 4.52 mV.

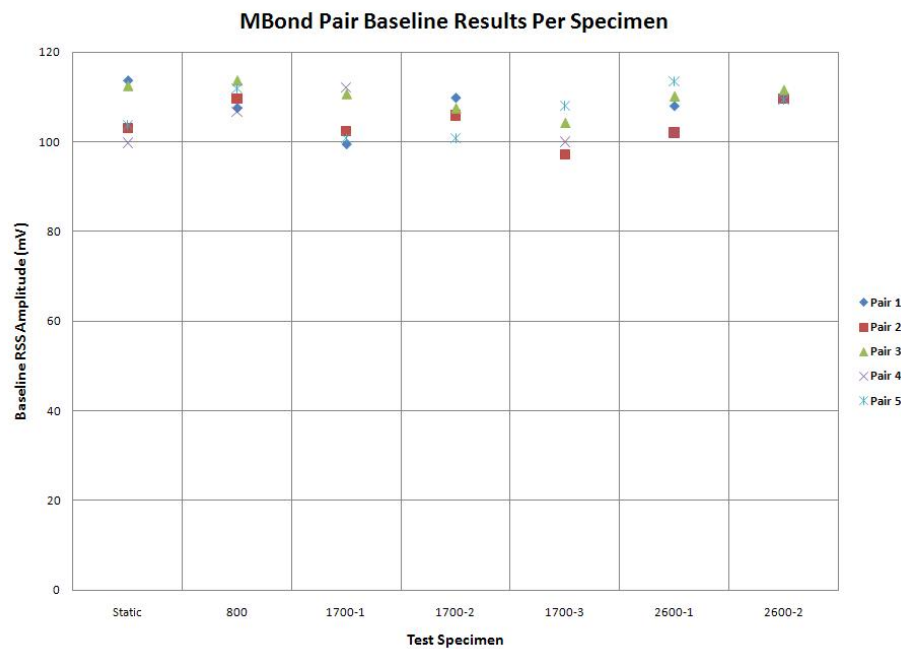


Figure 4.2: MBond baseline responses plotted by specimen show no significant outliers

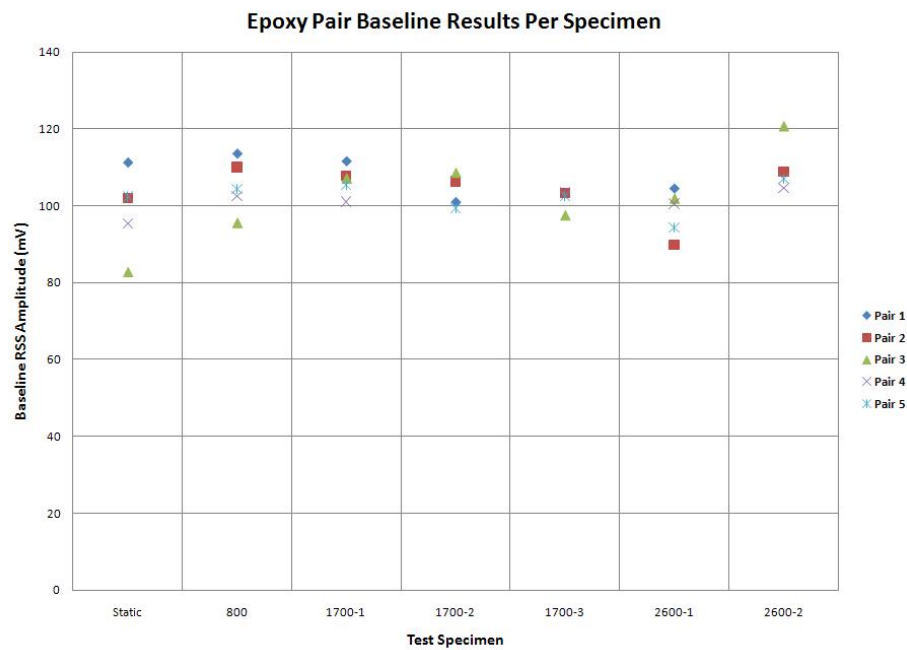


Figure 4.3: Epoxy baseline responses plotted by specimen show no significant outliers

Table 4.2: ANOVA results show no significant difference in MBond baseline response between specimens

$H_0 = \text{No difference in average baseline MBond pitch-catch pair response between the 7 test specimens}$ $\mu_{BaselineStatic} = \mu_{Baseline800} = \mu_{Baseline1700-1} = \mu_{Baseline1700-2}$ $= \mu_{Baseline1700-3} = \mu_{Baseline2600-1} = \mu_{Baseline2600-2}$					
Source of Variance	Degrees of Freedom	Sum of Squares	Mean Square	F Ratio	Pr $\geq$ F
Test Specimen	6	188.9	31.5	1.452	0.2348
Error	25	541.9	21.7		
Total	31	730.8			

Table 4.3: ANOVA results show no significant difference in Epoxy baseline response between specimens

$H_0 = \text{No difference in average baseline Epoxy pitch-catch pair response between the 7 test specimens}$ $\mu_{BaselineStatic} = \mu_{Baseline800} = \mu_{Baseline1700-1} = \mu_{Baseline1700-2}$ $= \mu_{Baseline1700-3} = \mu_{Baseline2600-1} = \mu_{Baseline2600-2}$					
Source of Variance	Degrees of Freedom	Sum of Squares	Mean Square	F Ratio	Pr $\geq$ F
Test Specimen	6	509.8	85.0	1.984	0.1061
Error	25	1070.4	42.8		
Total	31	1580.2			

As discussed in section 3.12.2, statistical t-tests assume normality of the tested data samples. Mickey [81] states the Shapiro-Wilk test [103] can be used to determine if a set of data can be assumed to come from a normal distribution. The null hypothesis for this test is that the observations form a random sample from a normally distributed population ( $H_0 = \text{The given sample data set is normally distributed}$ ). The null hypothesis is rejected for p-values below the specified level. Specifically, if the Shapiro-Wilk null hypothesis is not rejected, assume normality, and if the null hypothesis is rejected, more information is required. And Lehman [65] also states “In general, you should reject the null hypothesis of normality only when the  $p$  value is less than 0.05.” The Shapiro-Wilk normality tests give  $p$  values of 0.0782 and 0.3915 for MBond and Epoxy baseline responses respectively. Given that the Shapiro-Wilk null hypothesis has not been rejected in either case (calculated p-values are not less

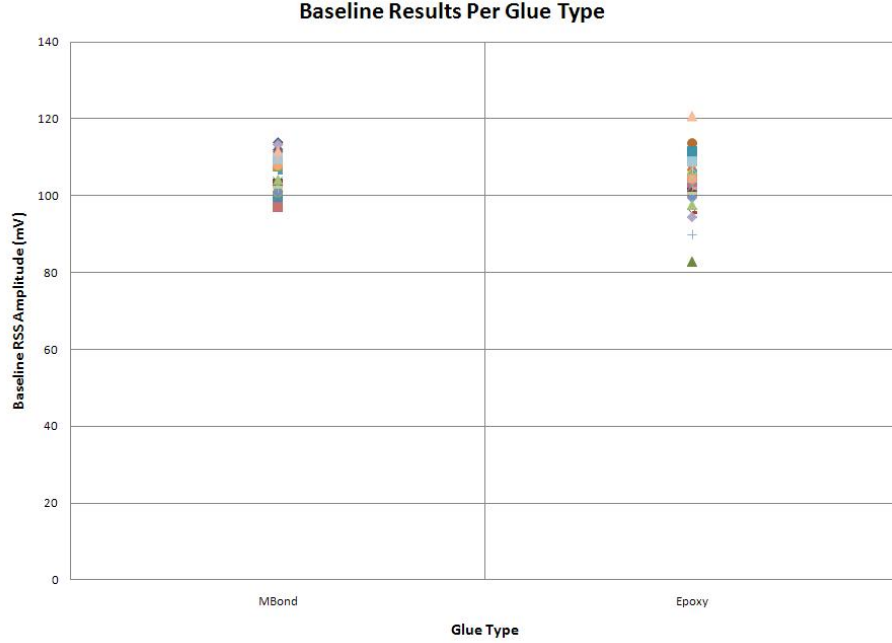


Figure 4.4: MBond PZT pairs have a slightly higher response and lower standard deviation

than 0.05), normal distribution is assumed. Based on the MBond  $p$  value that is close to significance, 0.0782 vs 0.05, the non-parametric equivalent of the t-test (the Wilcoxon rank sum test) will also be performed when comparing baseline values.

#### 4.2.3 Actual Response $\sigma$ vs. Assumed $\sigma$ and Required Analysis Adjustments.

As detailed in sections 3.9 and 3.10, the experimental sample size was determined using OC curves contained in Montgomery [83]. Sample size was iterated based on the desired change in response needed to be considered statistically significant, the desired level of  $\alpha$ , and the desired level of  $\beta$ .

The governing calculation uses equation 3.11 with the following parameters: 2 Factor A levels (glue types), 9 Factor B levels (number of specimens, number of static loads, or number of cycle sets), 10 mV signal change to be considered significant,  $\alpha = 0.05$ , and an assumed a value of 5 mV for the response standard deviation,  $\sigma$ . This combination gives  $\beta = 0.09$ , as shown in Table 3.12.

Since OC curves are highly sensitive to the assumed value of  $\sigma$ , the actual values of  $\sigma$  obtained through the pooled baseline responses provide an opportunity to validate the initial assumption, and adjust analysis techniques if necessary.

The standard deviation of the baseline MBond responses is lower than the assumed value with  $\sigma_{MBond} = 4.52$  mV. This increases the value of parameter  $\Phi$  calculated in equation 3.11 from 1.491 to 1.649, reducing  $\beta$  from 0.09 to 0.06. No adjustments to the MBond analysis techniques will be made.

The standard deviation of the baseline Epoxy responses is higher than the assumed value with  $\sigma_{Epoxy} = 6.67$  mV. This decreases the value of  $\Phi$  from 1.491 to 1.117, increasing  $\beta$  from 0.09 to over 0.5. Since the sample size has been set, other parameter values in equation 3.11 must change to return  $\beta$  to an acceptable value. Comparisons between two glue types (Factor A) are still desired, but a reduction of Factor B levels can be made to return  $\Phi$  to the original value of 1.491. Fixing  $\Phi$  at 1.491 and solving for the reduced number of Factor B levels using equation 3.11:

$$\text{Number of Factor B Levels} = \frac{n\alpha D^2}{2\Phi^2\sigma^2} = \frac{(5) * (2) * (10)^2}{(2) * (1.491)^2 * (6.67)^2} = 5.05 \quad (4.1)$$

Based on the increased  $\sigma$  for the Epoxy pitch catch pairs, and the subsequent re-calculation of Factor B levels, one of two choices must be made for an analysis comparing both glue types over a range of Factor B levels (number of specimens, number of static loads, or number of cycle sets): (1) any analysis cannot contain more than 5 Factor B levels to maintain a  $\beta$  of 0.09, or (2) accept the reduced Power ( $1-\beta$ ) for tests with more than 5 Factor B levels. In general, method (1) will be used to maintain the desired  $\beta$  level.

*4.2.4 t-test Results.* The pooled baseline data addresses the first hypothesis listed in Table 3.10,

$H_0 = \text{Average MBond sensor response equals average Epoxy sensor response at baseline: } \mu_{\text{BaselineMBond}} = \mu_{\text{BaselineEpoxy}}$

Using the JMP statistical program to perform a standard two sided t-test as described in section 4.3.2 gives a  $p$ -value = 0.0292 assuming equal variances between the samples, and  $p = 0.0297$  assuming unequal variances. Both  $p$  values indicate  $H_0$  should be rejected. The two sided non-parametric Wilcoxon Rank Sum test also indicates  $H_0$  should be rejected, giving a  $p$ -value of 0.0356. Determining the effect size  $d$  using equation 3.12 gives  $d=0.56$ , indicating a “medium” sized effect due to glue type per Lehman and Cohen [28,65].

### 4.3 Static Test Results

As described in Section 3.9, one dogbone specimen with five pitch-catch pairs of each glue type was subjected to static loading ranging from 25  $\mu\epsilon$  to 3000  $\mu\epsilon$ . Figures 4.5, 4.6 and 4.7 present the results of the static load testing. Figures 4.5 and 4.6 present the individual MBond and Epoxy pair results plotted against the strain level. Summary Figure 4.7 presents the five pair averages for each glue type with corresponding error bars placed at one standard deviation for each glue type.

**4.3.1 Feature Analysis.** General feature analysis of the curves shows consistent standard deviation for each glue type and a slight downward trend in average response starting at approximately the 1875  $\mu\epsilon$  level. Table 4.4 provides average responses and standard deviations for each strain level.

**4.3.2 t-test Results.** The static test data can be used to address the second and third null hypotheses in Table 3.10.

$H_0 = \text{Average MBond (or Epoxy) baseline sensor response equals the average MBond (or Epoxy) sensor response after applied static strain from 0 to 3000 } \mu\epsilon.$

Figure 4.7 shows no large downward trend that may indicate a statistically significant change in response for either MBond or Epoxy pitch-catch pairs between

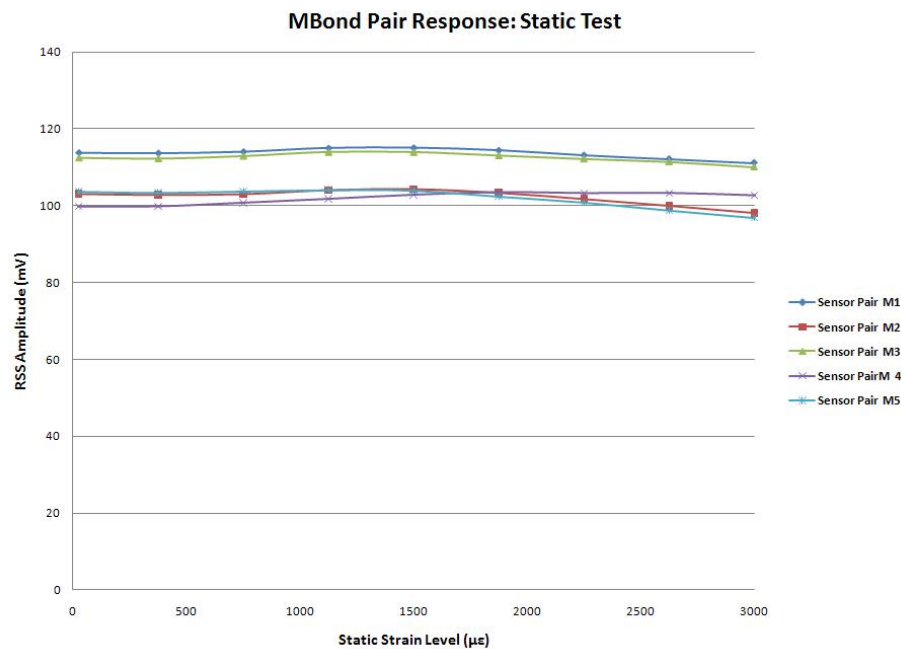


Figure 4.5: MBond sensor pairs showed steady response during the static strain testing

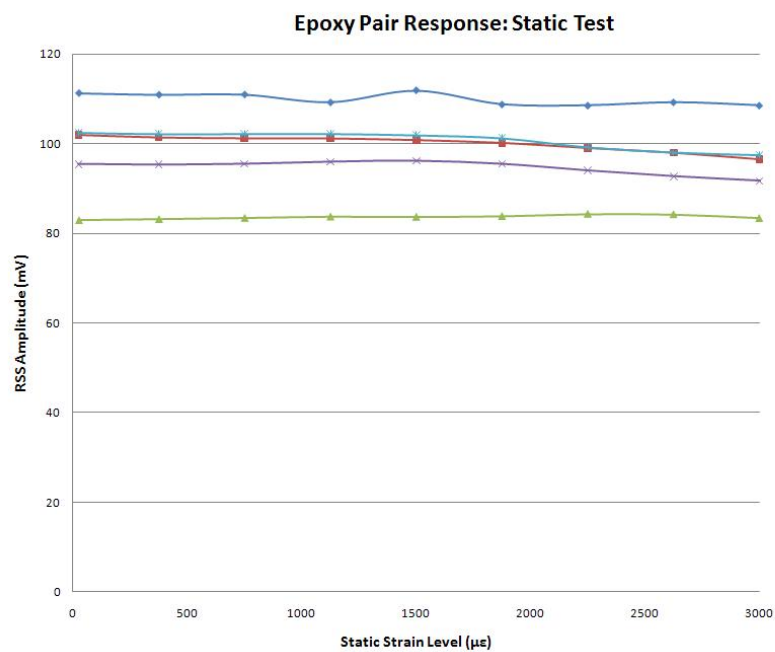


Figure 4.6: Epoxy sensor pairs showed steady response during the static strain testing

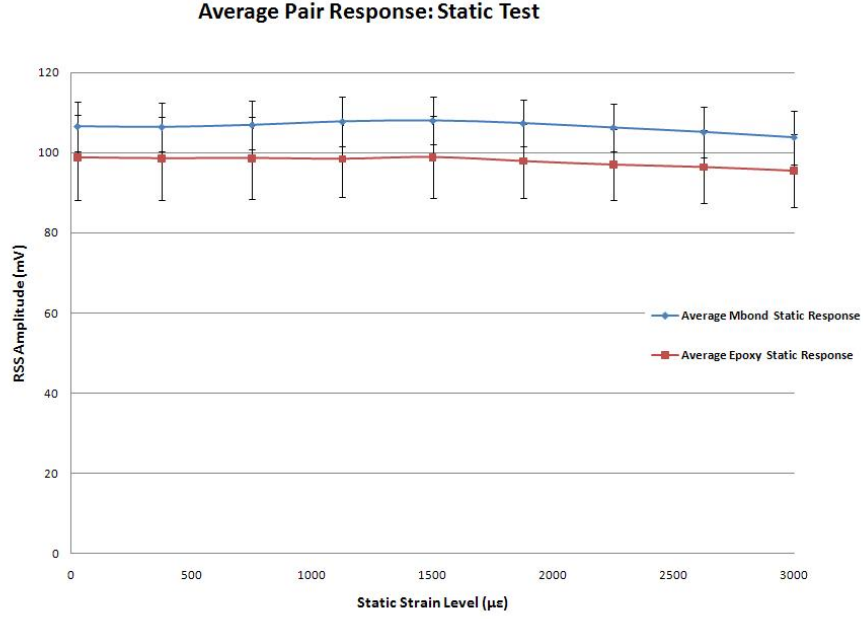


Figure 4.7: Response and standard deviation were steady during the static strain testing

Table 4.4: Static strain test average responses and standard deviations

Static Strain Level ( $\mu\epsilon$ )	Average MBond Response (mV)	MBond $\sigma$ (mV)	Average Epoxy Response (mV)	Epoxy $\sigma$ (mV)
25	106.6	6.194	98.79	10.53
375	106.4	6.175	98.58	10.29
750	106.9	6.122	98.64	10.17
1125	107.8	6.205	98.44	9.051
1500	108.0	5.953	98.87	10.26
1875	107.3	5.859	97.88	9.212
2250	106.2	5.933	97.00	8.848
2625	105.1	6.304	96.42	9.125
3000	103.8	6.613	95.50	9.173

the 25  $\mu\epsilon$  and 3000 $\mu\epsilon$  static strain applications. Following the basic process outlined in section 4.3.2, a single paired t-test between 25  $\mu\epsilon$  and 3000  $\mu\epsilon$  responses was made to determine if  $H_0$  should be rejected for each glue type.



For the MBond pitch-catch pairs, the  $p$ -value was 0.1639, indicating  $H_0$  should not be rejected. The non-parametric Wilcoxon test also indicated  $H_0$  should not be rejected, with a  $p$ -value of 0.3125.

Tests from the Epoxy responses produced conflicting results, requiring further analysis. The paired t-test gave a  $p$ -value of 0.0356, indicating  $H_0$  should be rejected but the Wilcoxon test gave a  $p$ -value of 0.1250 indicating that  $H_0$  should not be rejected.

A second paired t-test between the baseline responses and the responses after the 2625  $\mu\epsilon$  strain application provides additional information on the impact of static strain on the Epoxy pairs. The paired t-test between baseline and post-2625  $\mu\epsilon$  strain responses is 0.0794, indicating  $H_0$  should not be rejected under either the original  $\alpha = 0.05$  or the adjusted  $\alpha = 0.025$ . The Wilcoxon test gave a  $p$ -value of 0.1250, again indicating that  $H_0$  should not be rejected.

Figure 4.7 does show a slight downward trend in Epoxy pair signal response starting at 1875  $\mu\epsilon$ , but as stated above, this change is not significant at 2625  $\mu\epsilon$ . The 1 mV change in average Epoxy response between the 2625  $\mu\epsilon$  and 3000  $\mu\epsilon$  strain applications may be enough to cause a statistically significant change from baseline, but the insignificant Wilcoxon  $p$ -value indicates the parametric paired t-test  $p$ -value after the 3000  $\mu\epsilon$  strain application may be a Type II error, incorrectly rejecting the null hypothesis when it is true.

#### **4.4 Cyclic Test Results: 800 $\mu\epsilon$**

Figures 4.8, 4.9 and 4.10 present the results of the 800  $\mu\epsilon$  cyclic strain test. A dogbone specimen with five pitch-catch PZT pairs adhered with each glue type was subjected to 510K cycles at 800  $\mu\epsilon$ . Data was collected every 30K cycles at a nominal 25  $\mu\epsilon$ .

*4.4.1 Feature Analysis.* General feature analysis shows no notable change to either the average MBond or Epoxy pairs, and like the static load testing, the

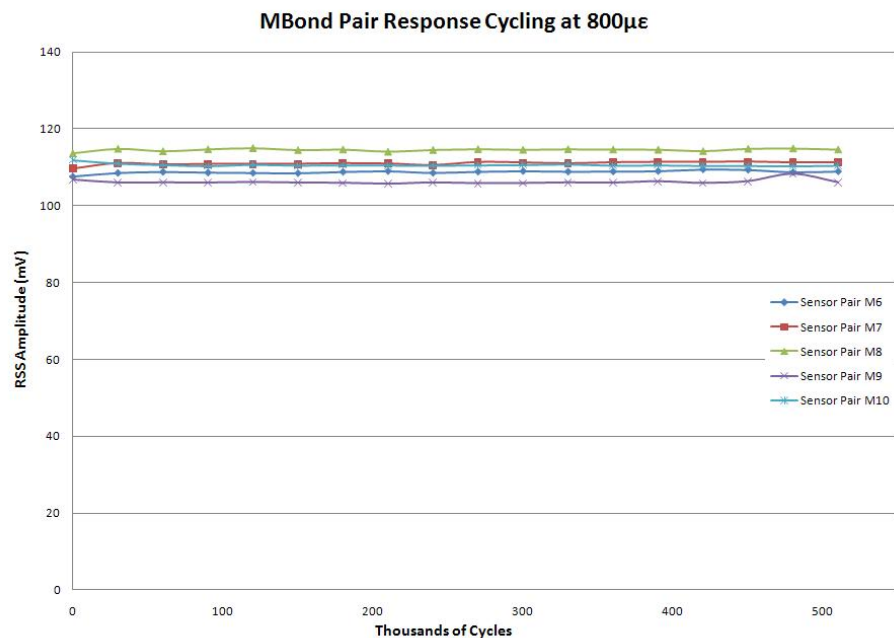


Figure 4.8: MBond sensor pairs showed steady response during the 800  $\mu\epsilon$  cyclic strain testing

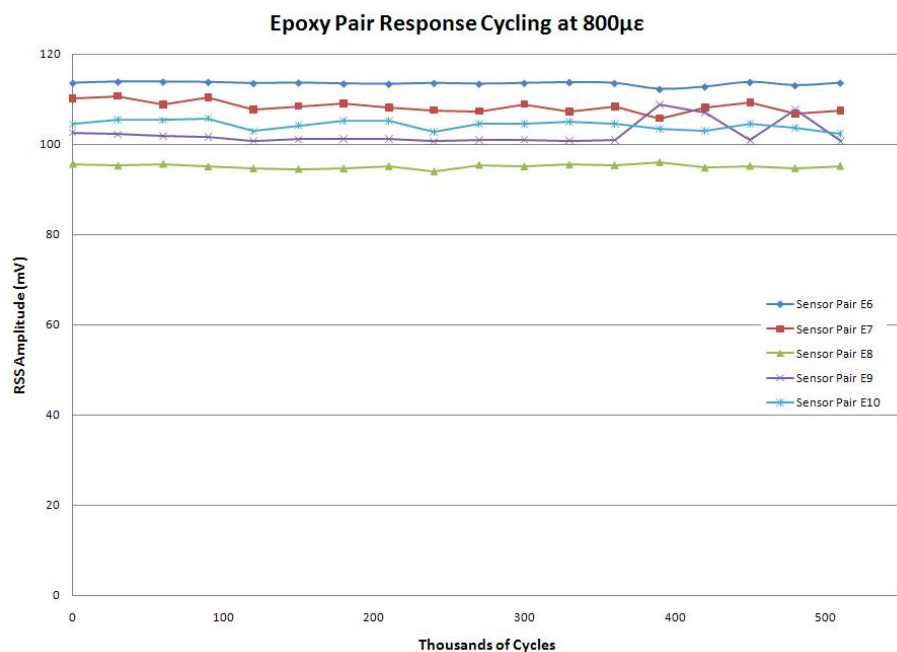


Figure 4.9: Epoxy sensor pairs showed steady response during the 800  $\mu\epsilon$  cyclic strain testing

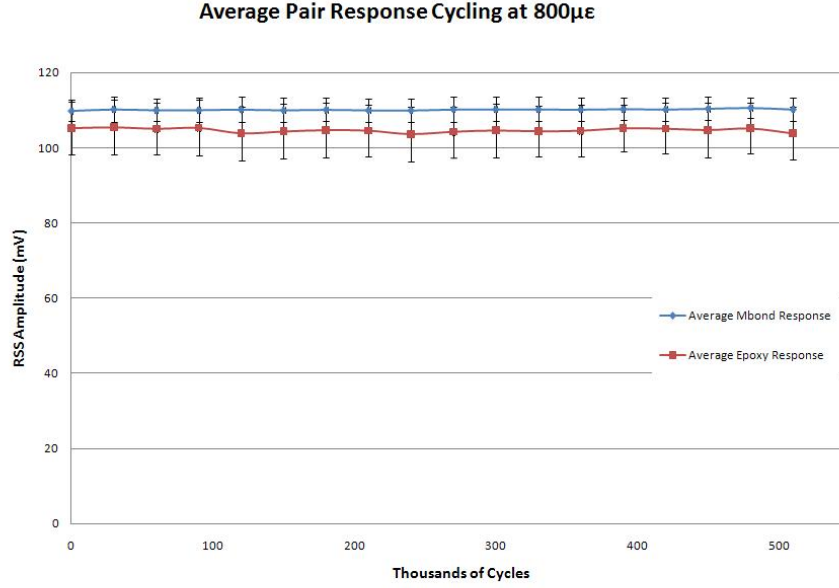


Figure 4.10: Response and standard deviation were steady during the 800  $\mu\epsilon$  cyclic strain testing

standard deviations of both glue types remained constant throughout the test. Table 4.5 provides average responses and standard deviations every 30K cycles.

*4.4.2 t-test Results.* The 800  $\mu\epsilon$  data can be used to address the null hypotheses in Table 3.14:

$H_0$  = Average MBond (or Epoxy) baseline sensor response equals the average MBond (or Epoxy) sensor response after cycling at 800  $\mu\epsilon$  from 0 to 510K cycles.

Since Figure 4.10 shows no large downward trend that may indicate a statistically significant change in response for either MBond or Epoxy pitch-catch pairs between 0 and 510K cycles at 800  $\mu\epsilon$ , a single paired t-test between 0 and 510K cycles responses was made to determine if  $H_0$  should be rejected for each glue type.

For the MBond pitch-catch pairs, the  $p$ -value was 0.5747, indicating  $H_0$  should not be rejected. The non-parametric Wilcoxon test also indicated  $H_0$  should not be rejected, with a  $p$ -value of 0.6250.

Table 4.5: Average response and standard deviation for cycling at 800  $\mu\epsilon$  (5 PZT pairs of each glue type)

Thousands of Cycles @ 800 $\mu\epsilon$	Average MBond Response (mV)	MBond $\sigma$ (mV)	Average Epoxy Response (mV)	Epoxy $\sigma$ (mV)
0	109.9	2.915	105.3	6.941
30	110.3	3.313	105.5	7.303
60	110.1	3.007	105.1	6.911
90	110.1	3.218	105.3	7.357
120	110.2	3.304	103.8	7.143
150	110.1	3.172	104.4	7.260
180	110.2	3.213	104.7	7.221
210	110.0	3.083	104.5	6.894
240	110.0	3.147	103.6	7.386
270	110.3	3.300	104.3	6.756
300	110.3	3.205	104.6	7.103
330	110.3	3.201	104.4	6.849
360	110.2	3.203	104.6	6.955
390	110.3	3.074	105.2	6.126
420	110.3	3.050	105.1	6.740
450	110.5	3.106	104.7	7.212
480	110.7	2.665	105.2	6.757
510	110.3	3.163	103.8	7.001

As with the static strain t-test results, the t-tests using the Epoxy pitch-catch pair responses after 510K cycles at 800  $\mu\epsilon$  produced conflicting results. The paired t-test gave a  $p$ -value of 0.0499, indicating (barely) that  $H_0$  should be rejected but the Wilcoxon test gave a  $p$ -value of 0.1250 indicating that  $H_0$  should not be rejected.

A second paired t-test between the baseline responses and the responses after 480K cycles at 800  $\mu\epsilon$  provides additional information concerning the Epoxy pairs. The paired t-test between baseline and post-480K cycles at 800  $\mu\epsilon$  strain responses is 0.9506, indicating  $H_0$  should not be rejected under either the new or previous value of  $\alpha$ . The Wilcoxon test gave a  $p$ -value of 0.6250, again indicating that  $H_0$  should not be rejected. Adjusting  $p$ -values per section 4.3.2, does not impact the results.

Figure 4.10 does show a slight drop in Epoxy pair response (1.4 mV) between 480K and 510K cycles, but a barely significant  $p$ -value at the 510K level combined

with a non-significant Wilcoxon test and non-significant t-tests at the 480K level does not provide a large amount of evidence to concluded there is a change in response at 510K cycles.

#### 4.5 Cyclic Test Results: 1700 $\mu\epsilon$

4.5.1 *Run 1 Results.* Figures 4.11, 4.12 and 4.13 present the results of the first 1700  $\mu\epsilon$  cyclic strain test. A dogbone specimen with five pitch-catch PZT pairs adhered with each glue type was subjected to 510K cycles at 1700  $\mu\epsilon$ . Data was collected every 30K cycles at a nominal 25  $\mu\epsilon$ . Table 4.7 provides average responses and standard deviations every 30K cycles.

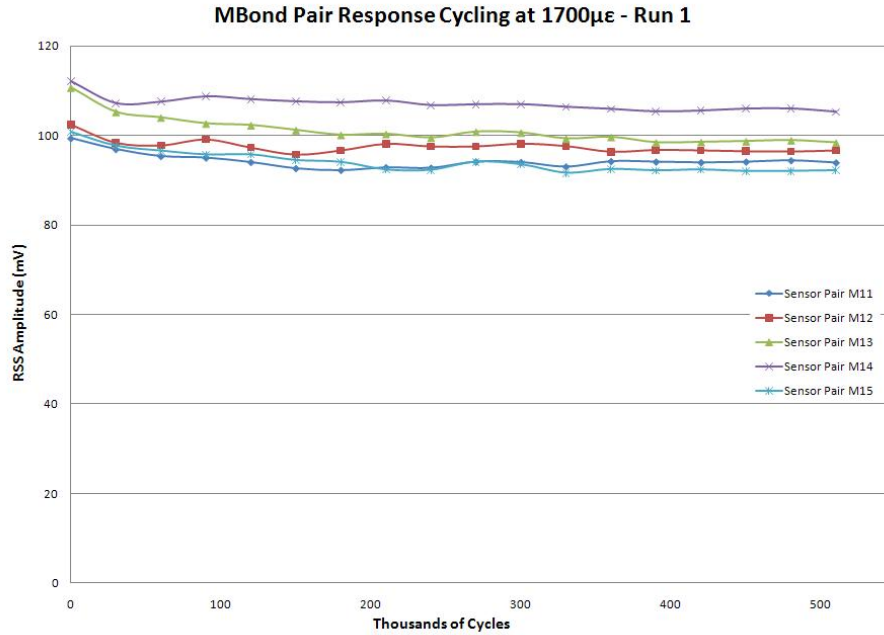


Figure 4.11: MBond sensor pairs showed signal degradation during the 1700  $\mu\epsilon$  cyclic strain testing

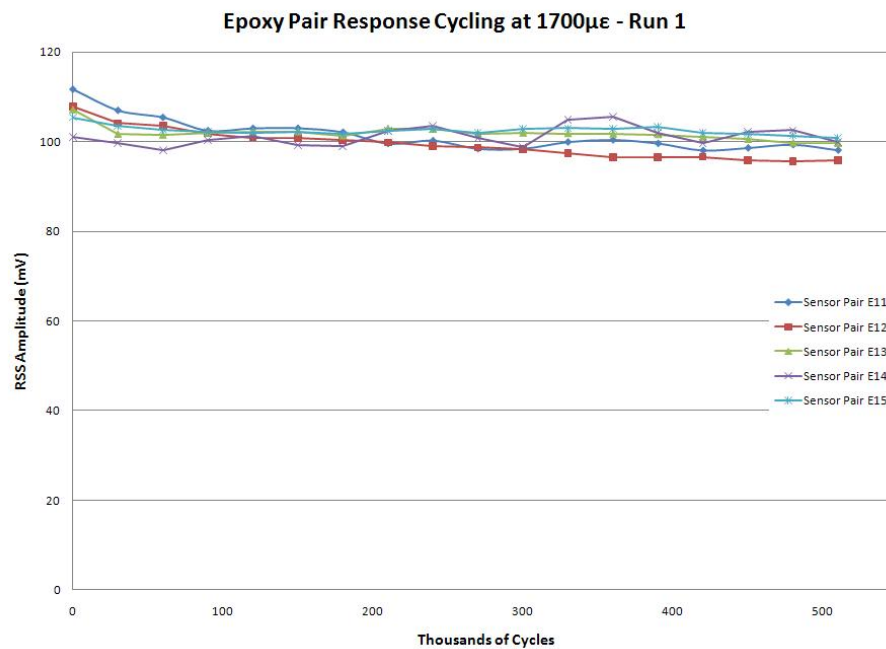


Figure 4.12: Epoxy sensor pairs showed signal degradation during the 1700  $\mu\epsilon$  cyclic strain testing

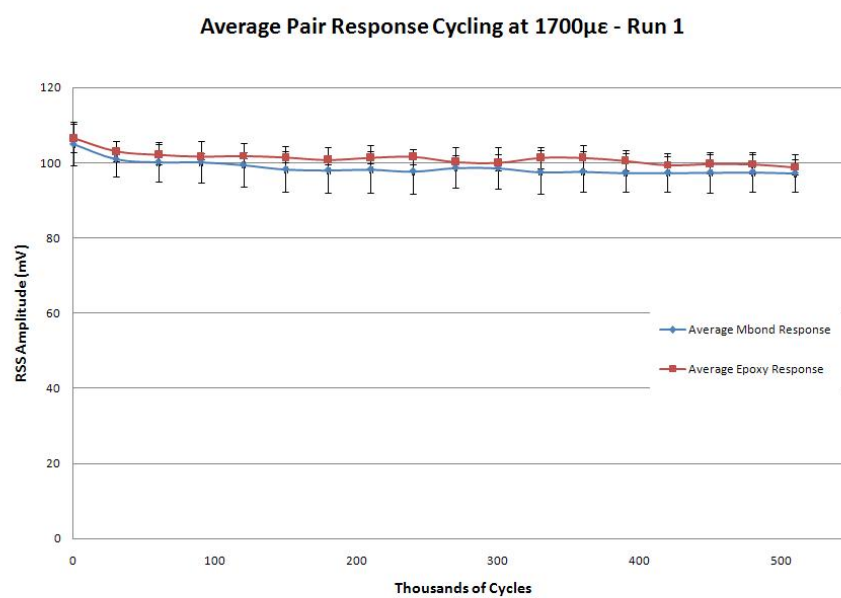


Figure 4.13: Degraded response and steady standard deviation occurred during the 1700  $\mu\epsilon$  cyclic strain testing

Table 4.6: Average response and standard deviation from run 1 cycling at 1700  $\mu\epsilon$   
(5 PZT pairs of each glue type)

Thousands of Cycles @ 1700 $\mu\epsilon$	Average MBond Response (mV)	MBond $\sigma$ (mV)	Average Epoxy Response (mV)	Epoxy $\sigma$ (mV)
0	105.1	5.896	106.6	3.826
30	101.1	4.765	103.2	2.731
60	100.2	5.258	102.2	2.274
90	100.2	5.640	101.2	0.8300
120	99.5	5.728	101.9	0.8193
150	98.3	6.095	101.5	1.497
180	98.1	5.993	100.8	1.278
210	98.3	6.320	101.4	1.571
240	97.7	5.909	101.7	1.978
270	98.7	5.380	100.3	1.632
300	98.6	5.507	100.1	2.144
330	97.6	5.844	101.4	2.860
360	97.7	5.301	101.4	3.339
390	97.3	5.069	100.6	2.623
420	97.4	5.123	99.5	2.170
450	97.4	5.388	99.8	2.614
480	97.5	5.358	99.7	2.645
510	97.3	5.071	99.9	1.927

4.5.2 *Run 2 Results.* Figures 4.14, 4.15 and 4.16 present the results of the second 1700  $\mu\epsilon$  cyclic strain test. A dogbone specimen with five pitch-catch PZT pairs adhered with each glue type was subjected to 510K cycles at 1700  $\mu\epsilon$ . Data was collected every 30K cycles at a nominal 25  $\mu\epsilon$ . Failure of a data collection cable invalidated data from one pitch-catch pair of each glue type (pairs M19 and E19). Table 4.7 provides average responses and standard deviations every 30K cycles.

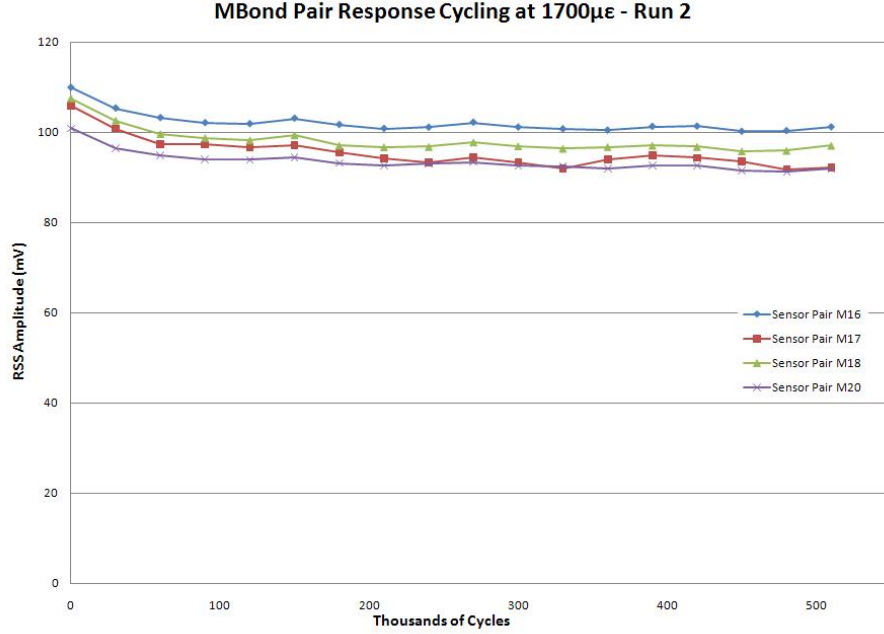


Figure 4.14: MBond sensor pairs showed signal degradation during the 1700  $\mu\epsilon$  cyclic strain testing



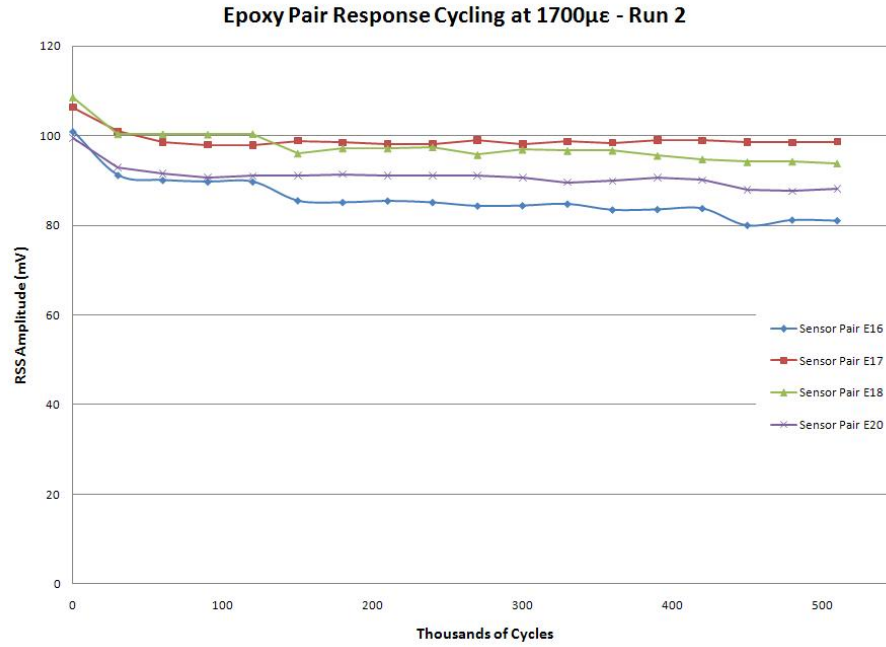


Figure 4.15: Epoxy sensor pairs showed signal degradation during the 1700  $\mu\epsilon$  cyclic strain testing

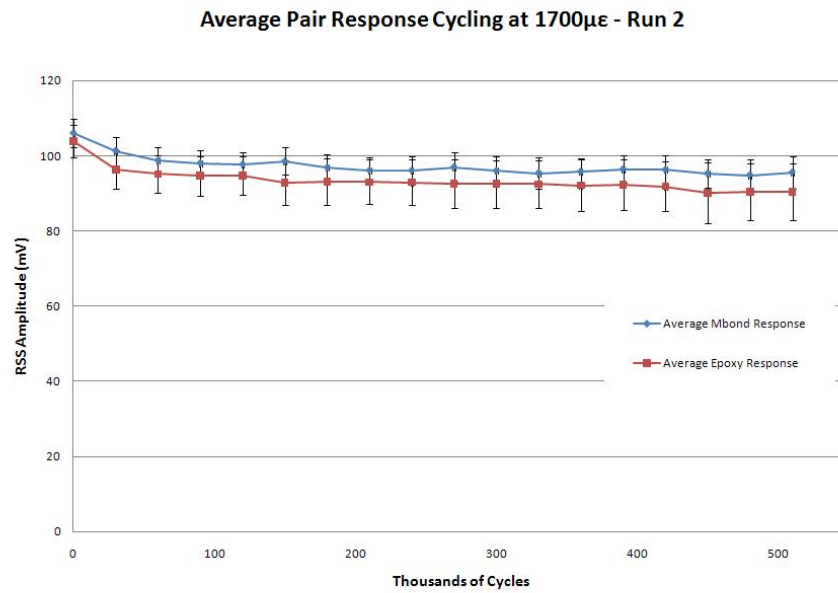


Figure 4.16: Degraded response and Steady standard deviation occurred during the 1700  $\mu\epsilon$  cyclic strain testing

Table 4.7: Average response and standard deviation from run 2 cycling at 1700  $\mu\epsilon$   
(4 PZT pairs of each glue type)

Thousands of Cycles @ 1700 $\mu\epsilon$	Average MBond Response (mV)	MBond $\sigma$ (mV)	Average Epoxy Response (mV)	Epoxy $\sigma$ (mV)
0	106.0	3.822	103.8	4.336
30	101.3	3.741	96.3	5.045
60	98.7	3.565	95.2	5.083
90	98.0	3.394	94.7	5.244
120	97.7	3.312	94.8	5.203
150	98.5	3.629	92.9	5.861
180	96.8	3.590	93.1	6.115
210	96.1	3.594	93.0	5.922
240	96.1	3.742	92.9	6.114
270	96.9	3.953	92.5	6.374
300	96.0	3.935	92.5	6.334
330	95.4	4.092	92.4	6.412
360	95.8	3.669	92.1	6.853
390	96.4	3.685	92.2	6.723
420	96.3	3.775	91.9	6.493
450	95.2	3.723	90.2	8.040
480	94.8	4.176	90.4	7.587
510	95.5	4.419	90.4	7.574

4.5.3 *Run 3 Results.* Figures 4.17, 4.18 and 4.19 present the results of the third 1700  $\mu\epsilon$  cyclic strain test. Failure of a second data collection cable invalidated data from one pitch-catch pair of each glue type (pairs M21 and E21). Table 4.8 provides average responses and standard deviations every 30K cycles.

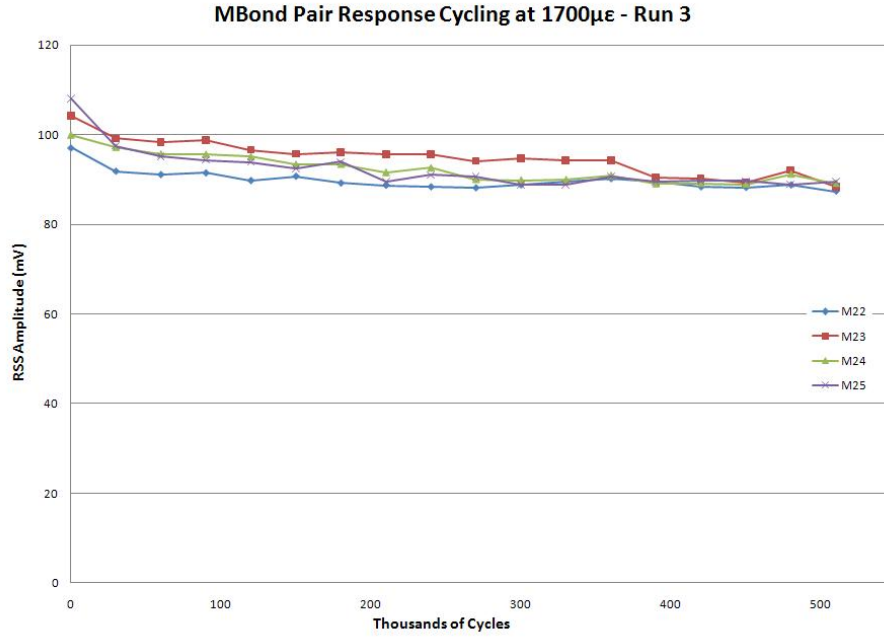


Figure 4.17: MBond sensor pairs showed signal degradation during the 1700  $\mu\epsilon$  cyclic strain testing

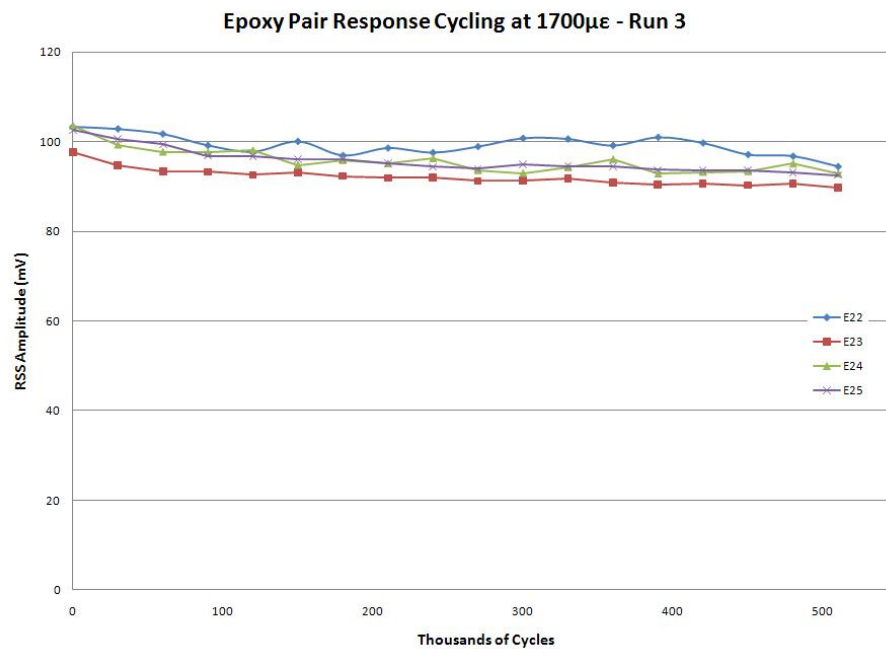


Figure 4.18: Epoxy sensor pairs showed signal degradation during the 1700  $\mu\epsilon$  cyclic strain testing

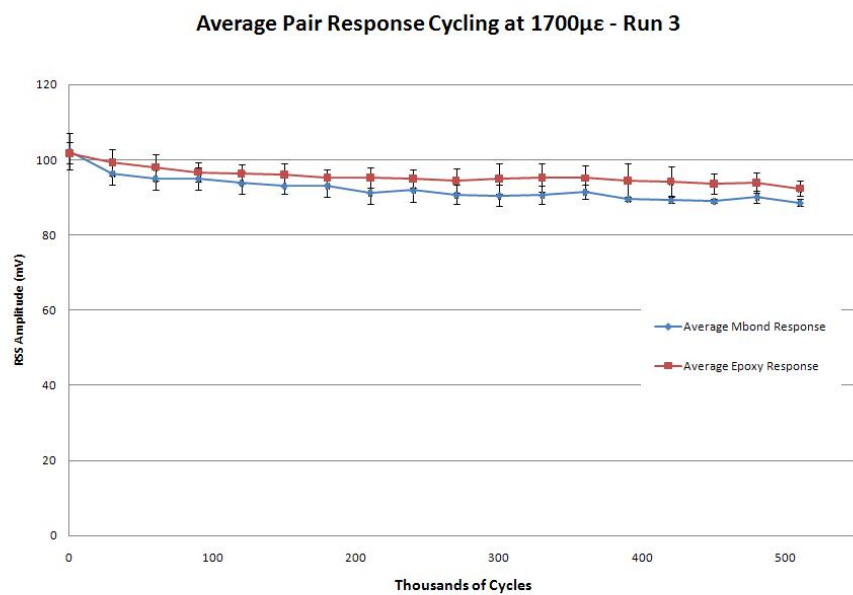


Figure 4.19: Degraded response and steady standard deviation occurred during the 1700  $\mu\epsilon$  cyclic strain testing

Table 4.8: Average response and standard deviation from run 3 cycling at 1700  $\mu\epsilon$   
(4 PZT pairs of each glue type)

Thousands of Cycles @ 1700 $\mu\epsilon$	Average MBond Response (mV)	MBond $\sigma$ (mV)	Average Epoxy Response (mV)	Epoxy $\sigma$ (mV)
0	102.3	4.780	101.7	2.812
30	96.4	3.160	99.3	3.454
60	95.1	3.014	98.1	3.528
90	95.0	3.021	96.7	2.518
120	93.8	2.941	96.3	2.541
150	93.0	2.081	96.0	2.955
180	93.1	2.899	95.3	2.053
210	91.3	3.076	95.2	2.734
240	91.2	3.077	95.1	2.396
270	90.7	2.514	94.4	3.246
300	90.5	2.795	95.0	4.127
330	90.6	2.463	95.3	3.749
360	91.5	1.872	95.2	3.425
390	89.6	0.5814	94.5	4.544
420	89.3	0.7788	94.3	3.850
450	89.0	0.6208	93.6	2.797
480	90.2	1.654	93.9	2.664
510	88.6	0.9707	92.4	1.950

4.5.4 *Combined Results.* Figure 4.20 shows the combined results of all 1700  $\mu\epsilon$  cyclic testing. Thirteen PZT pitch-catch pairs from each glue type are included in the average response and standard deviation calculations.

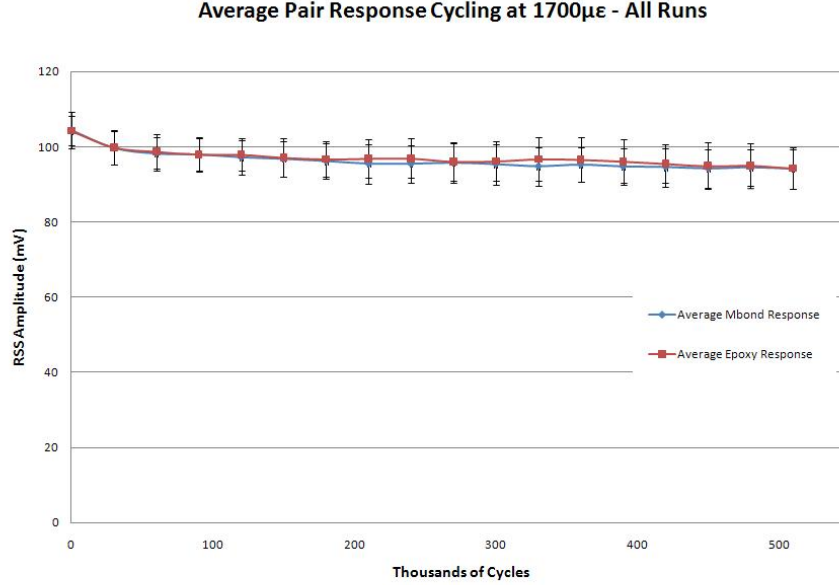


Figure 4.20: Degraded response and steady standard deviation occurred during the 1700  $\mu\epsilon$  cyclic strain testing

4.5.5 *Feature Analysis.* Feature analysis of the individual and combined test runs shows a signal degradation from 0 to 60K for both the MBond and Epoxy pitch-catch pairs, with a generally steady response after approximately 60K cycles. Standard deviation remained stable throughout all of the tests, with no clear indication if MBond or Epoxy pitch-catch pairs have a smaller standard deviation overall. Table 4.9 provides average responses and standard deviations every 30K cycles.

4.5.6 *t-test Results.* The combined data shown above can be used to address the null hypotheses in Table 3.14 at the 1700  $\mu\epsilon$  level. The first two hypotheses state:

$H_0 = \text{Average MBond (or Epoxy) baseline sensor response equals the average MBond (or Epoxy) sensor response after cycling at 1700 } \mu\epsilon \text{ from 0 to 510K cycles.}$

Table 4.9: Average response and standard deviation from all runs cycling at 1700  $\mu\epsilon$  (13 PZT pairs of each glue type)

Thousands of Cycles @ 1700 $\mu\epsilon$	Average MBond Response (mV)	MBond $\sigma$ (mV)	Average Epoxy Response (mV)	Epoxy $\sigma$ (mV)
0	104.5	4.840	104.3	4.003
30	99.7	4.331	99.9	4.535
60	98.2	4.440	98.8	4.635
90	97.9	4.557	98.0	4.325
120	97.2	4.675	98.0	4.404
150	96.7	4.836	97.2	5.088
180	96.2	4.690	96.7	4.818
210	95.4	5.296	96.9	5.103
240	95.4	4.903	96.9	5.290
270	95.7	5.259	96.1	5.120
300	95.3	5.321	96.2	5.202
330	94.8	5.116	96.8	5.695
360	95.2	4.576	96.6	5.948
390	94.7	4.950	96.1	5.759
420	94.5	5.095	95.5	5.220
450	94.2	5.189	94.9	6.190
480	94.5	4.956	95.0	5.934
510	94.1	5.353	94.3	5.609

The paired t-test between the 0 and 510K cycle responses for the MBond pitch-catch pairs gives a  $p$ -value  $\leq 0.0001$  and a Wilcoxon  $p$ -value of 0.0002, both indicating  $H_0$  should be rejected and a statistically significant change in response exists between 0 and 510K cycles at 1700  $\mu\epsilon$ . Following the general process outlined in section 4.3.2, a paired t-test between the 0 and 30K cycle responses also gives a  $p$ -value  $\leq 0.0001$  and a Wilcoxon  $p$ -value of 0.0002, providing evidence the statistically significant change occurs at or before 30K cycles at 1700  $\mu\epsilon$ .

To investigate if the significant changes continue to occur over the span of the test  $\alpha$  is adjusted to 0.0167 ( $\alpha/3$  per section 4.3.2) and a paired t-test between responses at 480K and 510K cycles gives a  $p$ -value of 0.3110 and a Wilcoxon  $p$ -value of 0.5879 indicating  $H_0$  should not be rejected and providing no evidence of a significant change in response between 480K and 510K cycles. Reducing  $\alpha$  to 0.0125 and per-

forming a paired t-test between 450K and 510K cycles gives a  $p$ -value of 0.6461 and a Wilcoxon  $p$ -value of 0.7869 providing no evidence of a significant change in response between 450K and 510K cycles. Reducing  $\alpha$  to 0.01 and performing a paired t-test between 420K and 510K cycles gives a  $p$ -value of 0.0339 and a Wilcoxon  $p$ -value of 0.0061. The Wilcoxon  $p$  is significant at the reduced  $\alpha$  level, but the paired t-test  $p$  is not, providing mixed results concerning statistical significance of signal changes between 420K and 510K cycles at 1700  $\mu\epsilon$ . Based on these results, some evidence exists that responses for MBond pitch-catch pairs changes between 420K and 510K cycles at 1700  $\mu\epsilon$ .

For the Epoxy pitch-catch pairs, the paired t-test between the 0 and 510K cycle responses gives a  $p$ -value  $\leq 0.0001$  and a Wilcoxon  $p$ -value of 0.0002, both indicating  $H_0$  should be rejected and a statistically significant change in response exists between 0 and 510K cycles at 1700  $\mu\epsilon$ . A second paired t-test between the 0 and 30K cycle responses also gives a  $p$ -value  $\leq 0.0001$  and a Wilcoxon  $p$ -value of 0.0002, providing evidence the statistically significant change occurs at or before 30K cycles at 1700  $\mu\epsilon$ , similar to the MBond pitch-catch pairs.

Investigating the extent of the significant changes,  $\alpha$  is reduced to 0.0167 and a paired t-test between responses at 480K and 510K cycles gives a  $p$ -value of 0.0227 and a Wilcoxon  $p$ -value of 0.0327. While much closer to the reduced  $\alpha$  value than the MBond pitch-catch pairs in a similar condition,  $H_0$  is not rejected in this case. Reducing  $\alpha$  to 0.0125 and performing a paired t-test between 450K and 510K cycles gives a  $p$ -value of 0.0449 and a Wilcoxon  $p$ -value of 0.0398, again closer to the reduced  $\alpha$  value, but not providing evidence of a significant change in response between 450K and 510K cycles. Reducing  $\alpha$  to 0.01 and performing a paired t-test between 420K and 510K cycles gives a  $p$ -value of 0.0094 and a Wilcoxon  $p$ -value of 0.0024. Both  $p$ -values are significant at the reduced  $\alpha$  level providing evidence of statistically significant signal changes for Epoxy pitch-catch pairs between 420K and 510K cycles at 1700  $\mu\epsilon$ .



## 4.6 Cyclic Test Results: 2600 $\mu\epsilon$

4.6.1 Run 1 Results. Figures 4.21, 4.22 and 4.23 present the results of the first 2600  $\mu\epsilon$  cyclic strain test. A dogbone specimen with five pitch-catch PZT pairs adhered with each glue type was subjected to 390K cycles at 2600  $\mu\epsilon$ . Data was collected every 30K cycles at a nominal 25  $\mu\epsilon$ . The dogbone specimen failed at 414K cycles, with the final data collection taking place at 390K cycles.

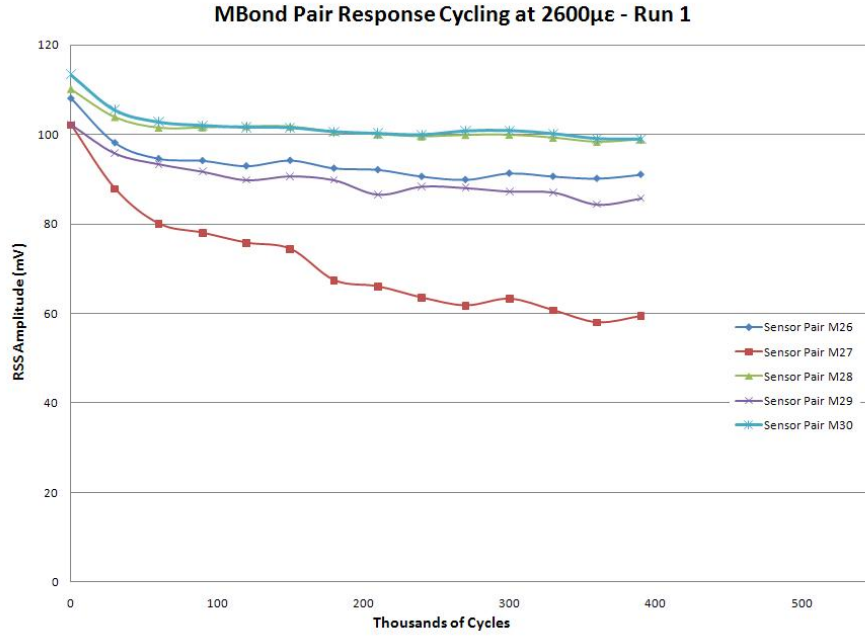


Figure 4.21: MBond sensor pairs showed signal degradation during the 2600  $\mu\epsilon$  cyclic strain testing

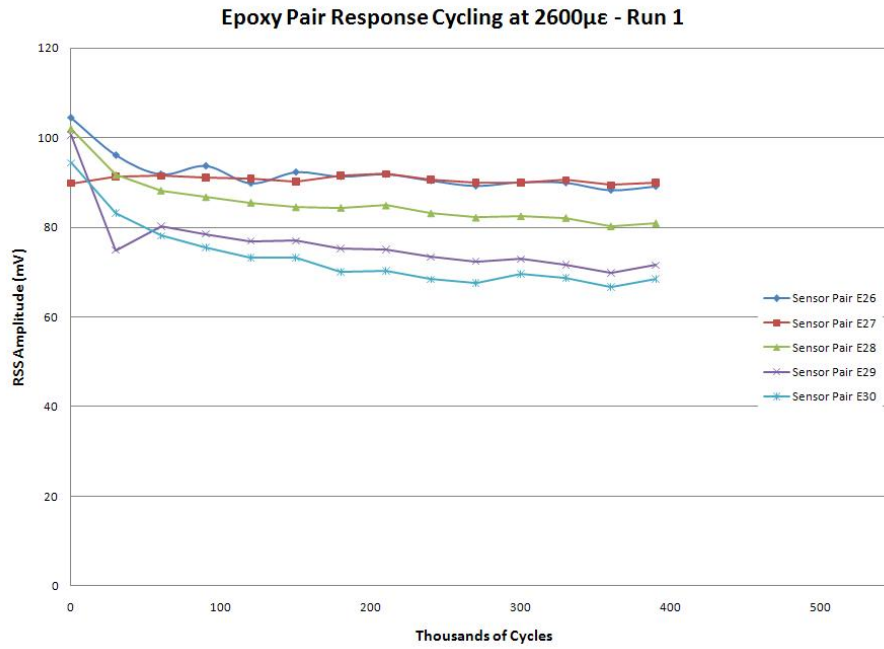


Figure 4.22: Epoxy sensor pairs showed signal degradation during the 2600  $\mu\epsilon$  cyclic strain testing

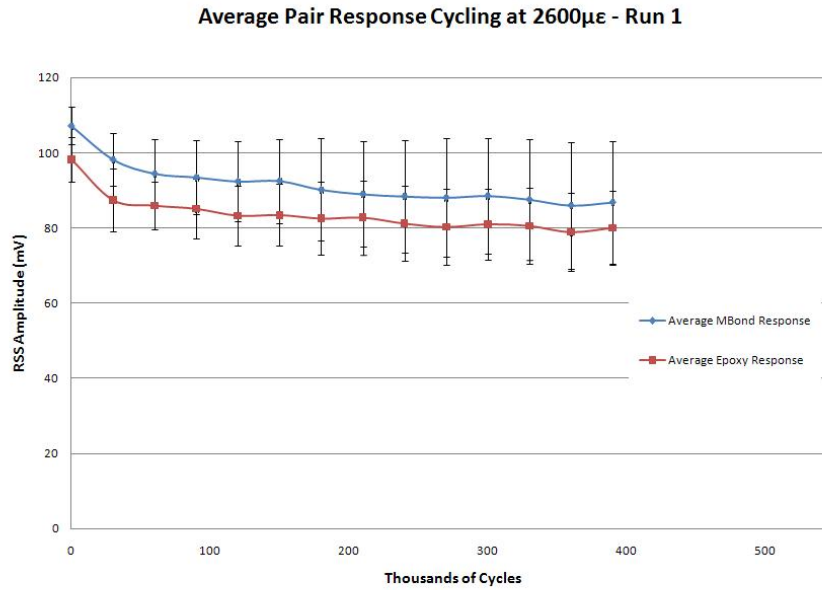


Figure 4.23: Degraded response and increasing standard deviation occurred during the 2600  $\mu\epsilon$  cyclic strain testing

Table 4.10: Average response and standard deviation from run 1 cycling at 2600  $\mu\epsilon$  (5 PZT pairs of each glue type)

Thousands of Cycles @ 2600 $\mu\epsilon$	Average MBond Response (mV)	MBond $\sigma$ (mV)	Average Epoxy Response (mV)	Epoxy $\sigma$ (mV)
0	107.2	5.000	98.2	5.986
30	98.2	7.052	87.4	8.423
60	94.5	9.064	86.0	6.422
90	93.5	9.780	85.1	7.914
120	92.4	10.70	83.3	7.891
150	92.5	11.21	83.5	8.254
180	90.2	13.64	82.5	9.653
210	89.0	14.08	82.8	9.846
240	88.4	14.87	81.2	10.07
270	88.1	15.80	80.2	10.00
300	88.5	15.27	81.0	9.505
330	87.6	16.06	80.6	10.17
360	86.0	16.80	78.9	10.40
390	86.8	16.33	80.0	9.869

*4.6.2 Run 2 Results.* Figures 4.24, 4.25 and 4.26 present the results of the second 2600  $\mu\epsilon$  cyclic strain test. A dogbone specimen with five pitch-catch PZT pairs adhered with each glue type was subjected to 210K cycles at 2600  $\mu\epsilon$ . Data was collected every 30K cycles at a nominal 25  $\mu\epsilon$ . The dogbone specimen failed at 213K cycles, with the final data collection taking place at 210K cycles. Data cable failure also invalidated the data from PZT pitch-catch pairs M31 and E31.

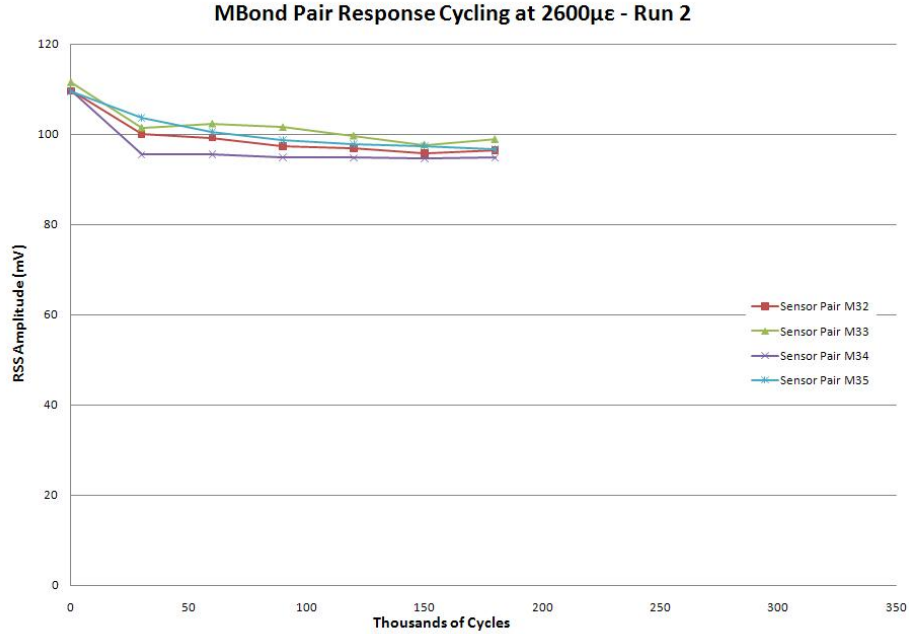


Figure 4.24: MBond sensor pairs showed signal degradation during the second 2600  $\mu\epsilon$  cyclic strain test

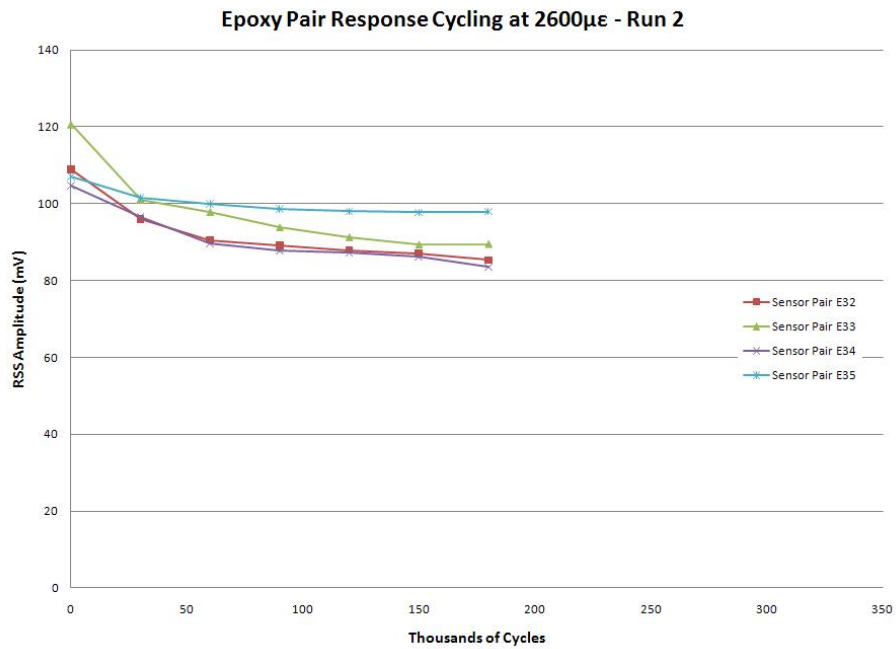


Figure 4.25: Epoxy sensor pairs showed signal degradation during the second 2600  $\mu\epsilon$  cyclic strain test

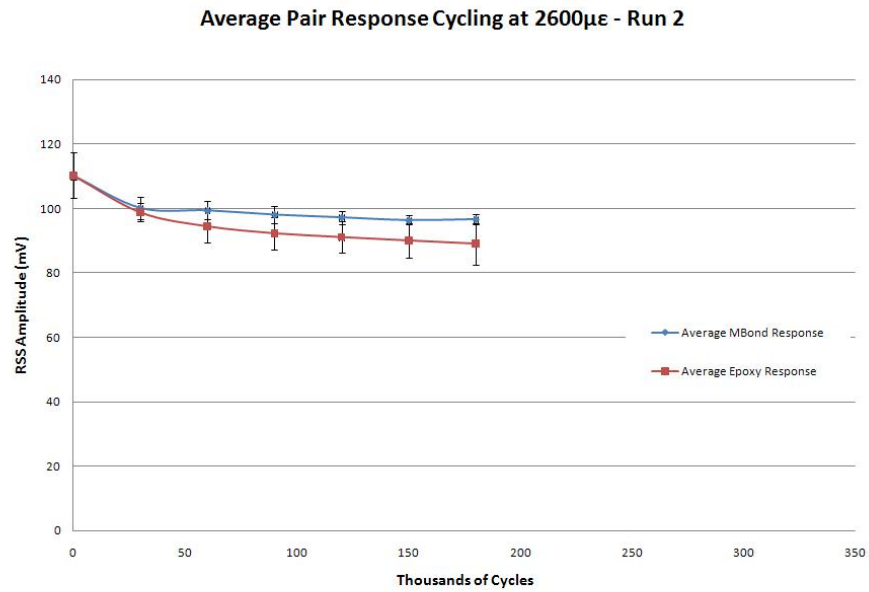


Figure 4.26: Degraded response occurred during the second 2600  $\mu\epsilon$  cyclic strain test

Table 4.11: Average response and standard deviation from run 2 cycling at 2600  $\mu\epsilon$  (4 PZT pairs of each glue type)

Thousands of Cycles @ 2600 $\mu\epsilon$	Average MBond Response (mV)	MBond $\sigma$ (mV)	Average Epoxy Response (mV)	Epoxy $\sigma$ (mV)
0	110.0	1.012	110.3	7.131
30	100.1	3.466	98.8	2.919
60	99.4	2.871	94.5	5.190
90	98.1	2.740	92.3	4.939
120	97.2	2.002	91.1	4.911
150	96.4	1.394	90.1	5.293
180	96.7	1.667	89.1	6.440
210	89.8	13.14	85.0	4.395

*4.6.3 Combined Results.* Figure 4.27 and Table 4.12 show the combined results of all 2600  $\mu\epsilon$  cyclic testing. Nine PZT pitch-catch pairs from each glue type are included in the average response and standard deviation calculations to 210K cycles. The average response and standard deviation calculations from 210K to 390K cycles include five PZT pitch-catch pairs, due to failure of the second 2600  $\mu\epsilon$  test specimen.

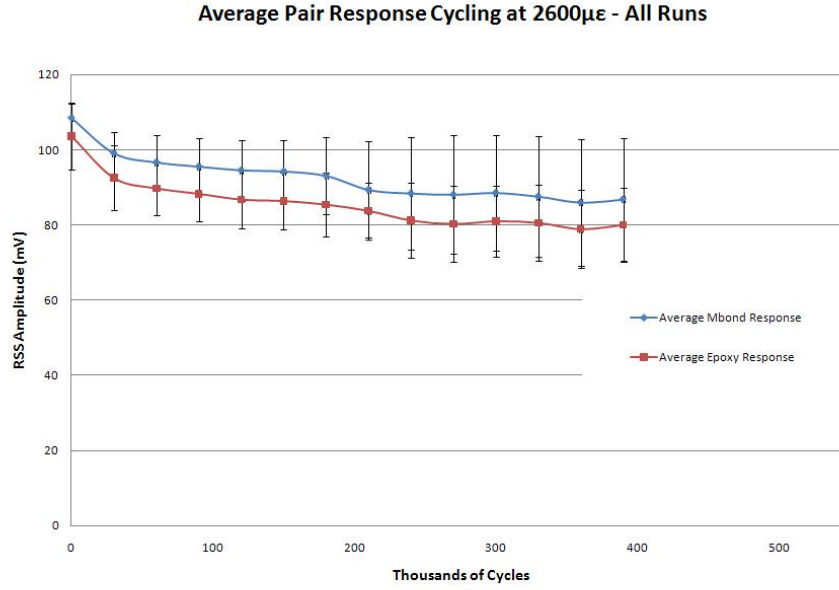


Figure 4.27: Degraded response occurred during the 2600  $\mu\epsilon$  cyclic strain testing

*4.6.4 Feature Analysis.* Feature analysis of the individual and combined test runs shows a signal degradation similar to the degradation observed in the 1700  $\mu\epsilon$  tests, but with a larger signal loss. Standard deviation for both glue types tended to increase for the first test run, but stayed relatively steady for the second test run. A significant signal loss for MBond pitch-catch pair M27 in the first run causes a large increase in the standard deviation for the combined MBond pitch-catch pair population. Table 4.12 provides average responses and standard deviations every 30K cycles.

Table 4.12: Average response and standard deviation from all runs cycling at 2600

Thousands of Cycles @ 2600 $\mu\epsilon$	Average MBond Response (mV)	MBond $\sigma$ (mV)	Average Epoxy Response (mV)	Epoxy $\sigma$ (mV)
0	108.4	3.896	103.6	8.794
30	99.1	5.512	92.5	8.639
60	96.6	7.135	89.6	7.133
90	95.5	7.518	88.3	7.400
120	94.5	8.081	86.8	7.558
150	94.2	8.231	86.4	7.526
180	93.1	10.29	85.4	8.601
210	89.3	12.81	83.8	7.554
240	88.4	14.87	81.2	10.07
270	88.1	15.80	80.3	10.00
300	88.5	15.27	81.0	9.505
330	87.5	16.06	80.6	10.17
360	86.0	16.80	78.9	10.40
390	86.8	16.33	80.1	9.869

*4.6.5 t-test Results.* The combined data shown above can be used to address the null hypotheses in Table 3.14 at the 2600  $\mu\epsilon$  level. The first hypotheses state:

$H_0 = \text{Average MBond (or Epoxy) baseline sensor response equals the average MBond (or Epoxy) sensor response after cycling at 2600 } \mu\epsilon \text{ from 0 to 510K cycles.}$

Due to failure of the second 2600  $\mu\epsilon$  cyclic test specimen before 210K cycles, the paired t-testing will begin between 0 and 1800K cycles to use the entire data set of 9 pitch-catch pairs of each glue type. The paired t-test between the 0 and 1800K cycle responses for the MBond pitch-catch pairs gives a  $p$ -value of 0.0003 and a Wilcoxon  $p$ -value of 0.0039, both indicating  $H_0$  should be rejected and a statistically significant change in response exists between 0 and 180K cycles at 2600  $\mu\epsilon$ . Following the general process outlined in section 4.3.2, a paired t-test between the 0 and 30K cycle responses also gives a  $p$ -value  $\leq 0.0001$  and a Wilcoxon  $p$ -value of 0.0039, providing evidence the statistically significant change occurs at or before 30K cycles at 2600  $\mu\epsilon$ .

To investigate if the significant changes continue to occur over the span of the test  $\alpha$  is adjusted to 0.0167 ( $\alpha/3$  per section 4.3.2) and a paired t-test between re-



sponses at 150K and 1800K cycles gives a  $p$ -value of 0.1775 and a Wilcoxon  $p$ -value of 0.1641 indicating  $H_0$  should not be rejected and providing no evidence of a significant change in response between 150K and 180K cycles. Reducing  $\alpha$  to 0.0125 and performing a paired t-test between 120K and 180K cycles gives mixed results with a  $p$ -value of 0.1277 and a Wilcoxon  $p$ -value of 0.0039, providing some evidence of a significant change in response between 120K and 180K cycles. Reducing  $\alpha$  to 0.01 and performing a paired t-test between 90K and 180K cycles gives a  $p$ -value of 0.0462 and a Wilcoxon  $p$ -value of 0.0039, again providing some evidence of a significant change in response between 90K and 180K cycles at 2600  $\mu\epsilon$ . Based on these results, evidence exists that the effect of cyclic strain at 2600  $\mu\epsilon$  may not continue to degrade the signal after 150K cycles, but the increase in standard deviation of the sample prevents definitive assessment.

For the Epoxy pitch-catch pairs, the paired t-test between the 0 and 180K cycle responses gives a  $p$ -value of 0.0006 and a Wilcoxon  $p$ -value of 0.0078, both indicating  $H_0$  should be rejected and a statistically significant change in response exists between 0 and 180K cycles at 2600  $\mu\epsilon$ . A second paired t-test between the 0 and 30K cycle responses gives a  $p$ -value of 0.0028 and a Wilcoxon  $p$ -value of 0.0078, providing evidence the statistically significant change occurs at or before 30K cycles at 2600  $\mu\epsilon$ , similar to the MBond pitch-catch pairs.

Investigating the extent of the significant changes,  $\alpha$  is reduced to 0.0167 and a paired t-test between responses at 150K and 180K cycles gives a  $p$ -value of 0.0887 and a Wilcoxon  $p$ -value of 0.1641, failing to reject  $H_0$  in this case. Reducing  $\alpha$  to 0.0125 and performing a paired t-test between 120K and 1800K cycles gives a  $p$ -value of 0.0533 and a Wilcoxon  $p$ -value of 0.0547, again failing to reject  $H_0$  and providing no evidence of a significant change in response between 120K and 180K cycles. Reducing  $\alpha$  to 0.01 and performing a paired t-test between 90K and 180K cycles gives a  $p$ -value of 0.0017 and a Wilcoxon  $p$ -value of 0.0078, both providing evidence  $H_0$  should be rejected and that there is a significant change in response between 90 and 180K cycles at 2600  $\mu\epsilon$ . Based on these results, evidence exists that the effect of cyclic

strain at 2600  $\mu\epsilon$  may not continue to degrade the signal after 90K cycles, but the increase in standard deviation of the sample prevents definitive assessment.

#### 4.7 Summary of t-test Results and General Observations

Tables 4.13 through 4.16 provide summaries of the t-test results calculated in sections 4.2 through 4.6. Generally, the MBond and Epoxy pitch-catch pairs reacted in similar ways to the static and cyclic strain testing. Neither glue type showed strong evidence of being affected by static strains up to 3000  $\mu\epsilon$ , with neither MBond paired t-test showing significance and one of two Epoxy paired t-tests showing significance.

The t-testing also showed no strong evidence of a change in response for cyclic testing at 800  $\mu\epsilon$  up to 510K cycles, but strong evidence exists that cycling at 1700  $\mu\epsilon$  or 2600  $\mu\epsilon$  has a significant effect on both MBond and Epoxy pitch-catch pair response prior to 30K cycles. Evidence exists that the cycling effect does not continue, and that the response signal does not change significantly due to strain cycles after a certain number of cycles have been applied. Mixed t-test results do not allow identification of the number of cycles after which the response ceases to change, but evidence exists that it may be as late as 420K cycles for testing at 1700  $\mu\epsilon$  and as early as 120K cycles for testing at 2600  $\mu\epsilon$ .

Table 4.13: Summary of static strain t-test results (\* indicates significance at the given  $\alpha$  level)

Null Hypothesis	p-value	Wilcoxon p-value	$\alpha$ Level	Reject Null	Reference Section
Average MBond and Epoxy baseline responses are equal	0.0292*	0.0356*	0.05	Yes	4.2.4
Average MBond baseline response is equal to the response after static strain application up to 3000 $\mu\epsilon$	0.1639	0.3125	0.05	No	4.3.2
Average Epoxy baseline response is equal to the response after static strain application up to 3000 $\mu\epsilon$	0.0356*	0.1250	0.05	Unclear	See 4.3.2

Table 4.14: Summary of 800  $\mu\epsilon$  cyclic strain t-test results (\* indicates significance at the given  $\alpha$  level)

Null Hypothesis	p-value	Wilcoxon p-value	$\alpha$ Level	Reject Null	Reference Section
Average MBond baseline response is equal to the response after 510K cycles at 800 $\mu\epsilon$	0.5747	0.6250	0.05	No	4.4.2
Average Epoxy baseline response is equal to the response after 510K cycles at 800 $\mu\epsilon$	0.0499*	0.1250	0.05	No / Unclear	See 4.4.2

Table 4.15: Summary of MBond pair 1700  $\mu\epsilon$  cyclic strain t-test results (\* indicates significance at the given  $\alpha$  level)

Null Hypothesis	p-value	Wilcoxon p-value	$\alpha$ Level	Reject Null	Reference Section
Average MBond baseline response is equal to the response after 510K cycles at 1700 $\mu\epsilon$	$\leq 0.0001^*$	0.0002*	0.05	Yes	4.5.6
Average MBond baseline response is equal to the response after 30K cycles at 1700 $\mu\epsilon$	$\leq 0.0001^*$	0.0002*	0.025	Yes	4.5.6
Average MBond response after 480K cycles at 1700 $\mu\epsilon$ is equal to the response after 510K cycles	0.3110	0.5879	0.0167	No	4.5.6
Average MBond response after 450K cycles at 1700 $\mu\epsilon$ is equal to the response after 510K cycles	0.6461	0.7869	0.0125	No	4.5.6
Average MBond response after 420K cycles at 1700 $\mu\epsilon$ is equal to the response after 510K cycles	0.0339	0.0061*	0.01	Unclear	See 4.5.6

Table 4.16: Summary of Epoxy pair 1700  $\mu\epsilon$  cyclic strain t-test results (\* indicates significance at the given  $\alpha$  level)

Null Hypothesis	p-value	Wilcoxon p-value	$\alpha$ Level	Reject Null	Reference Section
Average Epoxy baseline response is equal to the response after 510K cycles at 1700 $\mu\epsilon$	$\leq 0.0001^*$	0.0002*	0.05	Yes	4.5.6
Average Epoxy baseline response is equal to the response after 30K cycles at 1700 $\mu\epsilon$	$\leq 0.0001^*$	0.0002*	0.025	Yes	4.5.6
Average Epoxy response after 480K cycles at 1700 $\mu\epsilon$ is equal to the response after 510K cycles	0.0227	0.0327	0.0167	No	4.5.6
Average Epoxy response after 450K cycles at 1700 $\mu\epsilon$ is equal to the response after 510K cycles	0.0449	0.0398	0.0125	No	4.5.6
Average Epoxy response after 420K cycles at 1700 $\mu\epsilon$ is equal to the response after 510K cycles	0.0094*	0.0024*	0.01	Yes	4.5.6

Table 4.17: Summary of MBond pair 2600  $\mu\epsilon$  cyclic strain t-test results (\* indicates significance at the given  $\alpha$  level)

Null Hypothesis	p-value	Wilcoxon p-value	$\alpha$ Level	Reject Null	Reference Section
Average MBond baseline response is equal to the response after 180K cycles at 2600 $\mu\epsilon$	0.0003*	0.0039*	0.05	Yes	4.6.5
Average MBond baseline response is equal to the response after 30K cycles at 2600 $\mu\epsilon$	$\leq 0.0001^*$	0.0039*	0.025	Yes	4.6.5
Average MBond response after 150K cycles at 2600 $\mu\epsilon$ is equal to the response after 180K cycles	0.1775	0.1641	0.0167	No	4.6.5
Average MBond response after 120K cycles at 2600 $\mu\epsilon$ is equal to the response after 180K cycles	0.1277	0.0039*	0.0125	Unclear	See 4.6.5
Average MBond response after 90K cycles at 2600 $\mu\epsilon$ is equal to the response after 180K cycles	0.0467	0.0039*	0.01	Unclear	See 4.6.5

Table 4.18: Summary of Epoxy pair 2600  $\mu\epsilon$  cyclic strain t-test results (\* indicates significance at the given  $\alpha$  level)

Null Hypothesis	p-value	Wilcoxon p-value	$\alpha$ Level	Reject Null	Reference Section
Average Epoxy baseline response is equal to the response after 180K cycles at 2600 $\mu\epsilon$	0.0006*	0.0078*	0.05	Yes	4.6.5
Average Epoxy baseline response is equal to the response after 30K cycles at 2600 $\mu\epsilon$	0.0028*	0.0078*	0.025	Yes	4.6.5
Average Epoxy response after 150K cycles at 2600 $\mu\epsilon$ is equal to the response after 180K cycles	0.0887	0.1641	0.0167	No	4.6.5
Average Epoxy response after 120K cycles at 2600 $\mu\epsilon$ is equal to the response after 180K cycles	0.0533	0.0547	0.0125	No	4.6.5
Average Epoxy response after 90K cycles at 2600 $\mu\epsilon$ is equal to the response after 180K cycles	0.0017*	0.0078*	0.01	Yes	4.6.5

## 4.8 Modeling the Results

As described in section 3.12.5, a lack of independence of pitch-catch pair responses between numbers of cycles for a given strain level prevents the use of regression analysis to model the experimental data. For this reason, equation fits (linear, polynomial,  $\log(\text{cycles})$ ,  $\log(\text{cycles})\text{-}\log(\text{strain level})$  and power) will be used to determine if (or how) responses can be predicted based on a given number of cycles and strain level. Figures 4.28 and 4.29 show the combined experimental results for the MBond and Epoxy pitch-catch pairs based on cyclic strain level and number of cycles.

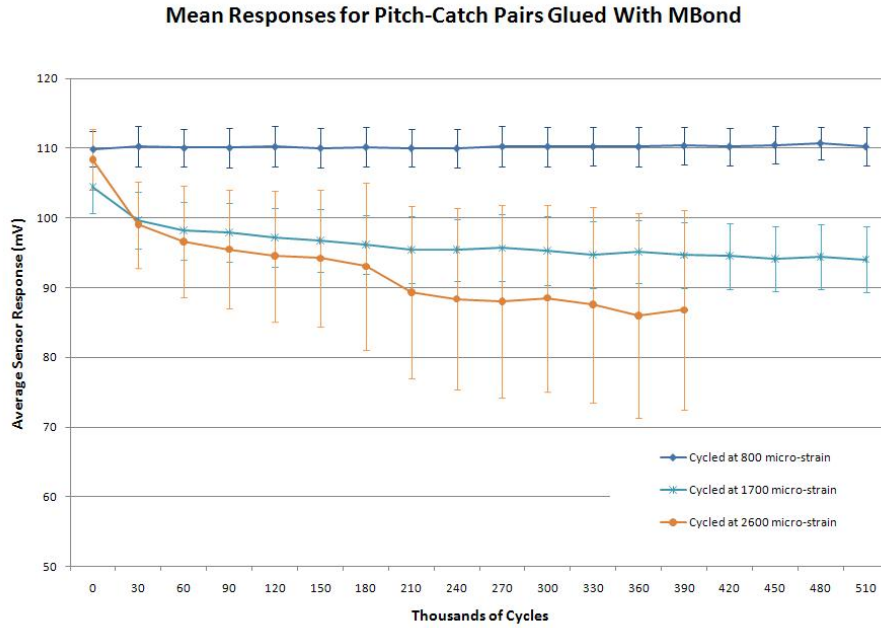


Figure 4.28: Combined MBond test results for modeling

*4.8.1 Power Equation Models.* Reviewing Spanier and Oldham [105], the response changes due to cycles and strain levels resemble a vertical translation of the power function with a negative exponent,  $x^{-n}$ , shown in Figure 4.30.

Using a power equation model of the basic form shown in equation 4.2, Tables 4.19 and 4.20 give the best fit coefficient values determined using MATLAB.

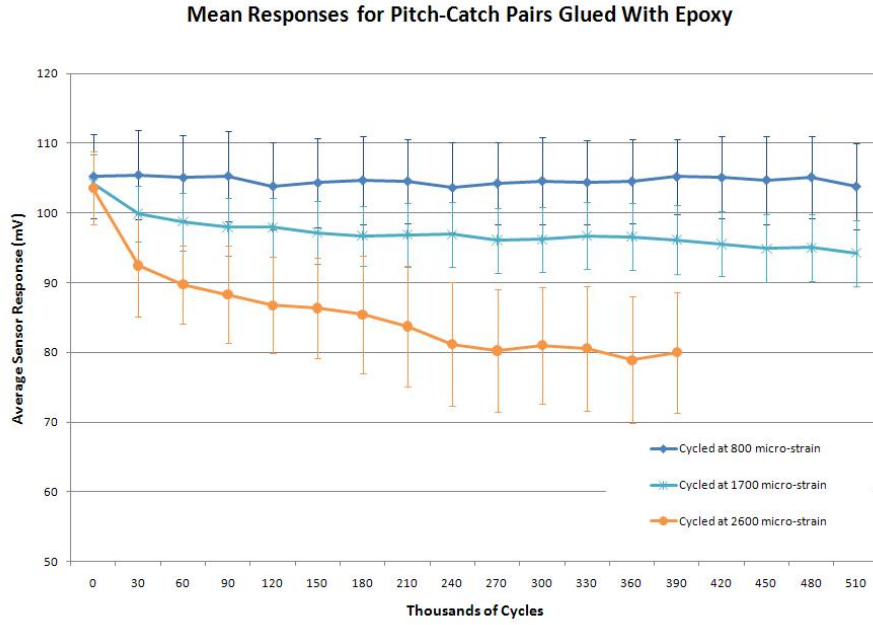


Figure 4.29: Combined Epoxy test results for modeling

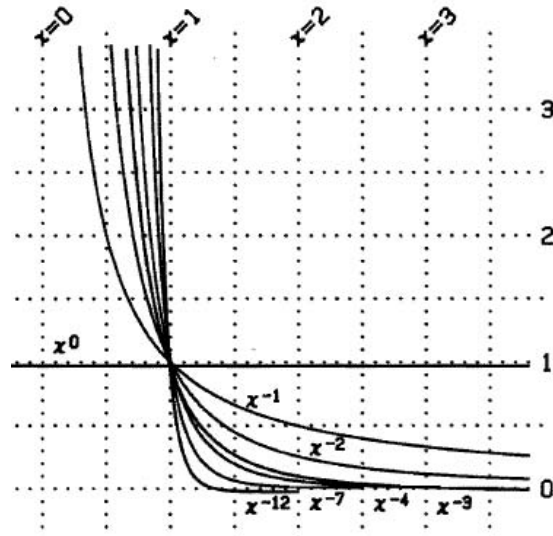


Figure 4.30: Experimental results resemble the power function with  $y = x^{-n}$  (from [105])

$$\text{Response}_{\text{Glue Type, Strain Level}} = \xi_0 * \left( \frac{\text{Number of Cycles}}{1000} \right)^n \quad (4.2)$$



Table 4.19: Power fit coefficients for MBond pitch-catch pair responses

	$\xi_0$	$n$
800 $\mu\epsilon$ Cycling	109.85	6.662e-4
1700 $\mu\epsilon$ Cycling	105.15	0.01730
2600 $\mu\epsilon$ Cycling	111.32	0.03904

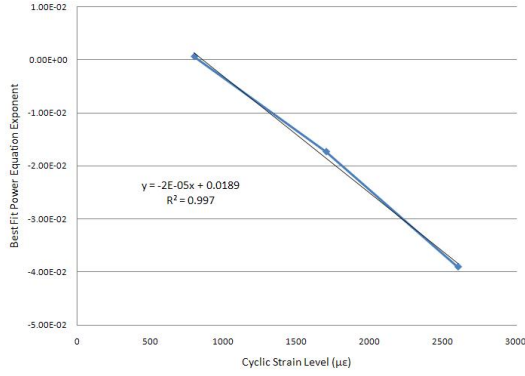
Table 4.20: Power fit coefficients for Epoxy pitch-catch pair responses

	$\xi_0$	$n$
800 $\mu\epsilon$ Cycling	105.39	0.0013
1700 $\mu\epsilon$ Cycling	104.74	0.0149
2600 $\mu\epsilon$ Cycling	106.21	0.0457

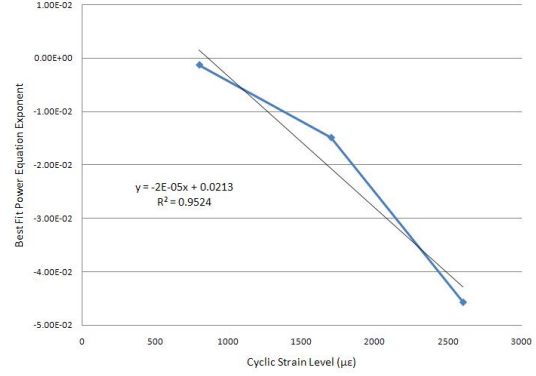
The three sets of coefficients for each glue type must be combined to build a suitable power model that can be applied across a range of cyclic strain levels. The JMP statistical program can build a non-linear model using the experimental data, but it requires a proposed model and coefficient initial conditions. Starting with the basic model given by Equation 4.2, the  $\beta_0$  initial condition can be determined by averaging the three  $\beta_0$  coefficients for each glue type. As shown in Figures 4.28 and 4.28, increasing the cyclic strain level tends to increase the “bend” in the curve in a manner similar to the curves in Figure 4.30. The final form of the power model and remaining coefficient initial conditions can be determined by plotting the best fit exponential values from Tables 4.19 and 4.20 against their respective cyclic strain levels. Figure 4.31 shows the best fit power equation exponents are nearly linear with respect to cyclic strain level for both MBond and Epoxy pitch-catch pairs. This near-linear relationship sets the final form of the power equation model, and the linear fit equations establish the initial conditions for the JMP analysis.

Equation 4.3 gives the final form of the power model equation and Table 4.21 gives the initial conditions used for the JMP analysis.

$$\text{Response}_{\text{Glue Type}} = \xi_0 * \left( \frac{\text{Number of Cycles}}{1000} \right)^{\xi_1 * (\text{Cyclic Strain Level in } \mu\epsilon) + \xi_2} \quad (4.3)$$



(a) MBond Relation



(b) Epoxy Relation

Figure 4.31: Near-linear relationships between the best fit power equation exponent and strain level determine the final form of the power equation model and initial conditions

Table 4.21: Initial conditions for JMP power model analysis

	$\xi_0$	$\xi_1$	$\xi_2$
MBond	108.77	-2e-5	0.0189
Epoxy	105.442	-2e-5	0.0213

Equations 4.4 and 4.5 contain the power model coefficients from the JMP analysis and Figures 4.32 and 4.33 plot the model results against the average experimental responses for each glue type.

$$\text{Response}_{MBond} = 112.63 * \left( \frac{\text{Number of Cycles}}{1000} \right)^{-2.125e-5 * (\text{Cyclic Strain Level in } \mu\epsilon) + 0.009752} \quad (4.4)$$

$$\text{Response}_{Epoxy} = 106.31 * \left( \frac{\text{Number of Cycles}}{1000} \right)^{-2.228e-5 * (\text{Cyclic Strain Level in } \mu\epsilon) + 0.01764} \quad (4.5)$$

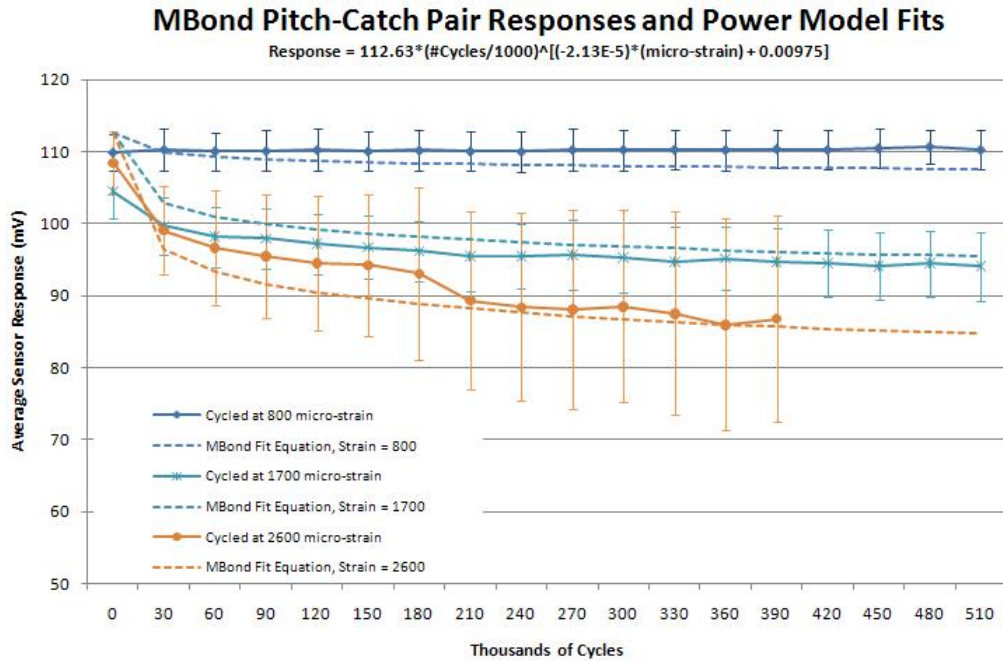


Figure 4.32: Power model predicts responses based on number of cycles and strain level

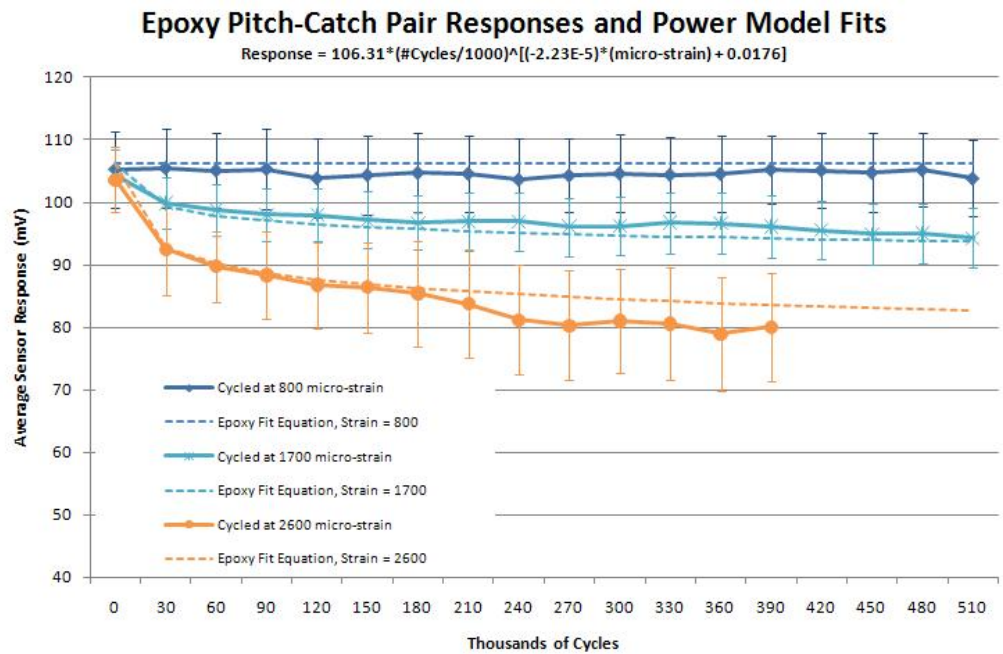


Figure 4.33: Power model predicts responses based on number of cycles and strain level

#### 4.8.2 Other Modeling Attempts.

4.8.2.1 *Linear Models.* It is apparent from Figures 4.28 and 4.29 that the pitch-catch pair response is non-linear with respect to numbers of cycles at 1700 and 2600  $\mu\epsilon$ . For this reason, linear modeling of the results was not pursued, and response modeling focused on the non-linear equation forms.

4.8.2.2 *Polynomial Models.* Second order polynomial models were also built using the technique described in section 3.12.5 and demonstrated in section 4.8.1; however, the MBond and Epoxy models evolved into different forms, requiring a change in the number of model coefficients required to estimate the responses based on glue type. Due to the differences in forms between glue types, polynomial models were not pursued beyond this point in favor of the power models described in section 4.8.1.

4.8.2.3 *Log(Cycles) Models.* Log(cycles) models were included because log(cycles) is a common transformation used to model material failures due to cyclic strain [29]. To determine the final form of the model and the coefficients, log(cycle) equations were fit to each response plot shown in Figure 4.28 and 4.29. Log(cycle) equations did not adequately model the responses for the individual cyclic strain levels, and a combined log(cycle) models were not pursued beyond this point in favor of the power models described in section 4.8.1.

## V. Linking Experimental Results to Changes in Probability of Detection

### 5.1 Introduction

A primary focus of a SHM system, as with any NDE system, is to reliably detect structural flaws. Chapter IV demonstrates how the aircraft environment can affect the performance of SHM sensors. This chapter presents a method to relate changes in SHM *sensor* performance to SHM *systems* performance using  $\text{POD}(a)$  curves.

This chapter begins by describing how  $\text{POD}(a)$  curves are formed using the procedure outlined in MIL-HDBK-1823: Nondestructive Evaluation System Reliability Assessment, and then demonstrates how changes in SHM sensor performance can be incorporated into the  $\text{POD}(a)$  calculations using a  $\text{POD}(a)$  degradation model. Finally, an example combines results from the PZT cyclic strain experiment described in Chapter IV with experimental  $\text{POD}(a)$  data from an ultrasonic SHM crack detection technology. This example demonstrates how the  $\text{POD}(a)$  degradation model can be applied to an existing SHM  $\text{POD}(a)$  curve, and shows how sensor degradation can affect the  $\text{POD}(a)$  of a given SHM system.

### 5.2 Building a $\text{POD}(a)$ curve using MIL-HDBK-1823

MIL-HDBK-1823 [35] “addresses the general requirements for assessing the capability of an NDE system in terms of the probability of detection (POD) as a function of flaw size,  $a$ ” . The procedure described in the handbook defines experimental and analysis requirements to build the  $\text{POD}(a)$  models for a given NDE technique. One type of experimental data used to build  $\text{POD}(a)$  curves is described as “ $a$  vs.  $\hat{a}$ ” data where  $\hat{a}$  represents the measured response of the NDE system for the given crack size.  $\text{POD}(a)$  is modeled by performing linear regression on an “ $a$  vs.  $\hat{a}$ ” functional relation that has normally distributed residuals with constant variance [7, 27, 35, 106]. The  $\text{POD}(a)$  curve is then defined as the probability of  $a$  being greater than the signal threshold ( $\hat{a}_{th}$ ) at a given flaw size, with  $\hat{a}_{th}$  being the value of  $\hat{a}$  below which the signal is indistinguishable from noise.

As described by Berens [7], the output of an NDE system for a given crack size can be described as a probability distribution  $g(\hat{a}|a)$ . Given the above definition of  $\hat{a}_{th}$ , the probability of detecting crack size  $a$  can be expressed as [7, 35, 106]:

$$POD(a) = P(\hat{a} > \hat{a}_{th}) \quad (5.1)$$

Figure 5.1 illustrates how  $POD(a)$  curves are formed from experimental data. Controlled experiments provide the data points plotted in the figure. The crack size information and corresponding system responses are then transformed to obtain a linear regression fit with residuals ( $\varepsilon$ ) distributed approximately normally with mean 0 and standard deviation  $\delta$  (Note: MIL-HDBK-1823 uses the notation  $\delta$  rather than the usual  $\sigma$  to denote the standard deviation of the residuals).

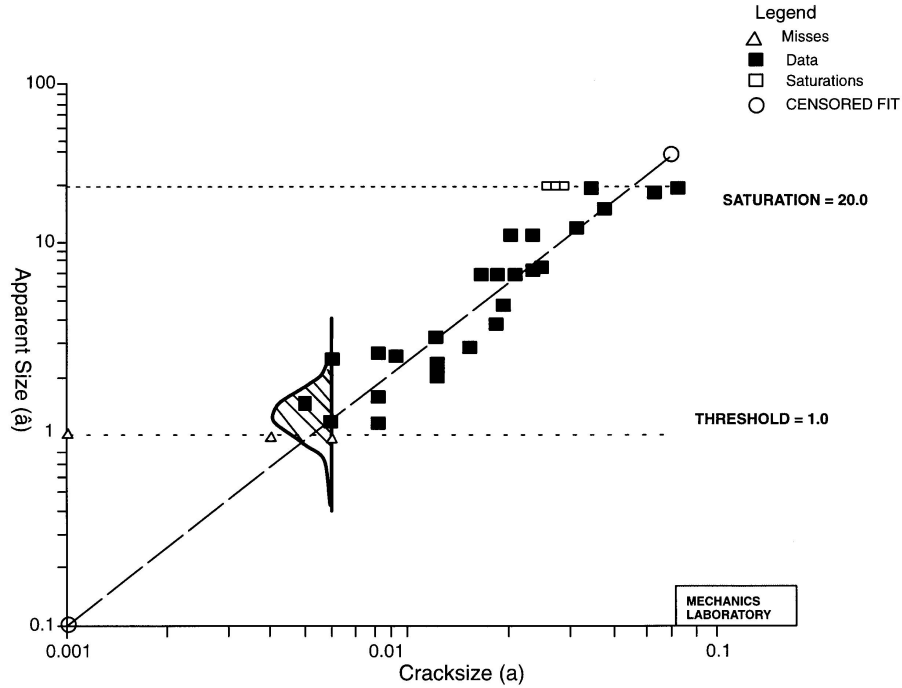


Figure 5.1: Linear regression of the  $\ln(a)$  vs.  $\ln(\hat{a})$  relationship combines with the NDE signal output probability density for a given crack size,  $g(\hat{a}|a)$ , to determine  $POD(a)$  (figure from [35])

The transformations used to obtain normally distributed residuals can take several forms. It has been shown that the relationship between the natural logs of  $a$

and  $\hat{a}$  is often linear, with the required residual distribution [7, 35]. This relation is shown in Figure 5.1. But Cobb, in building a  $POD(a)$  curve for an ultrasonic SHM system, needed to transform the response variable before taking the  $\log_{10}$  of the variable and crack sizes. These additional steps then produced the properly distributed residuals [27] (there is more discussion on this topic in paragraph 5.7).

Assuming the natural log relationship holds, the regression equation shown in Figure 5.1 has the form:

$$\ln(\hat{a}) = \beta_0 + \beta_1 * \ln(a) + \varepsilon \quad (5.2)$$

with  $\beta_0$  and  $\beta_1$  being the intercept and slope parameters that fit the experimental data, and  $\varepsilon$  being the normally distributed residuals described earlier. Solving equation 5.2 for  $\varepsilon$  gives an expression that is also normally distributed, in terms of the regression coefficients, crack size and system response:

$$\varepsilon = \ln(\hat{a}) - \beta_0 - \beta_1 * \ln(a) \quad (5.3)$$

Dividing the right side of equation 5.3 by the standard deviation of the regression residuals,  $\delta$ , results in a standard normal distribution representing the NDE system response distribution for a given crack size,  $g(\hat{a}|a)$ .

$$g(\hat{a}|a) = z = \frac{\ln(\hat{a}) - \beta_0 - \beta_1 * \ln(a)}{\delta} \quad (5.4)$$

The distribution function shown in Figure 5.1 gives the location of the  $g(\hat{a}|a)$  distribution in relation to the experimental regression line and the threshold detection value,  $\hat{a}_{th}$ . At a given crack size, the system response distribution is centered on the regression line, with values greater than the threshold detection value being declared a “hit” for structural damage of size  $a$ . In terms of equation 5.1, the probability of detecting crack size  $a$  is the shaded area in Figures 5.2 and 5.3. This area can be

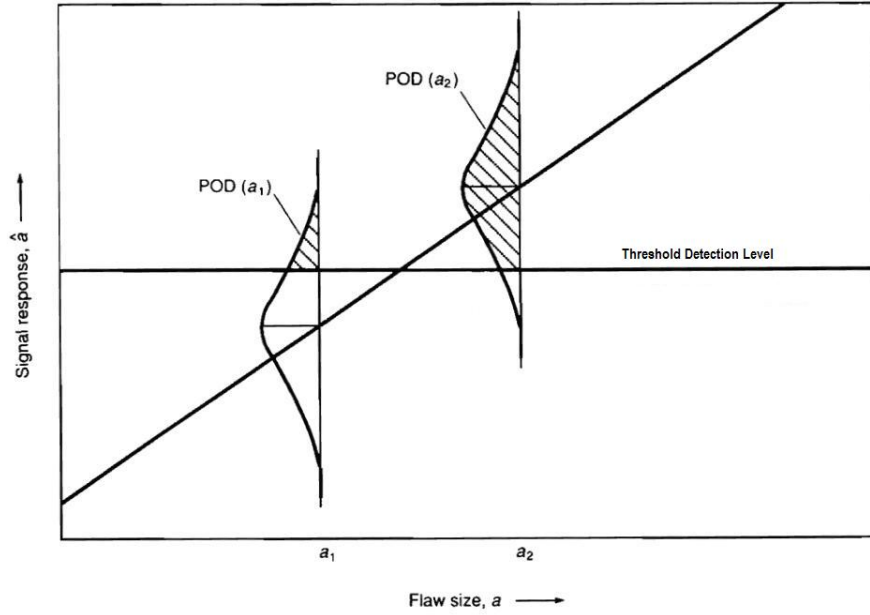


Figure 5.2: The shaded area ( $POD(a)$ ) changes for each crack size based on the system response distribution and the threshold detection level [35]

calculated using the standard normal distribution,  $\Phi(z)$  with:

$$POD(a) = P(\hat{a} > \hat{a}_{th}) = \Phi \left( \frac{\beta_0 + \beta_1 * \ln(a) - \ln(\hat{a}_{th})}{\delta} \right) \quad (5.5)$$

Several items must be noted at this point. First, the signs of the coefficients in the numerator of equation 5.5 have changed from their values in equation 5.3 because the standard normal distribution tables provide area under the curve from minus infinity to a given value, while the  $POD(a)$  calculation requires the area under the curve from the given value ( $\hat{a}_{th}$ ) to infinity. Changing the sign from  $\Phi(z)$  to  $\Phi(-z)$  identifies the proper area. Second, although the  $POD(a)$  function can be expressed as a cumulative distribution function, it does not represent the cumulative probability of *occurrence* of crack size  $a$ . It represents the *probability of detection* of cracks of size  $a$  or smaller. Third, the value of  $POD(a)$  changes for each value of  $a$ . Sweeping equation 5.5 across possible values of  $a$  produces a  $POD(a)$  curve. MIL-HDBK-1823 provided the example “ $\ln(a)$  vs.  $\ln(\hat{a})$ ” data used to generate Figure 5.1, and this data was used



to recreate the regression line shown in Figure 5.1 and to generate the corresponding  $POD(a)$  curve (see Figures 5.3 and 5.4). When comparing the capability of various NDE techniques, previous NDE studies have used the crack sizes detected 50% or 90% of the time ( $a_{50}$  and  $a_{90}$ ) [7, 104]. The smaller the respective crack sizes ( $a_{50}$  and/or  $a_{90}$ ), the “better” the NDE technique. Figure 5.4 shows  $a_{50} = 0.005$  inches and  $a_{90} = 0.007$  inches for the example data contained in MIL-HDBK-1823.

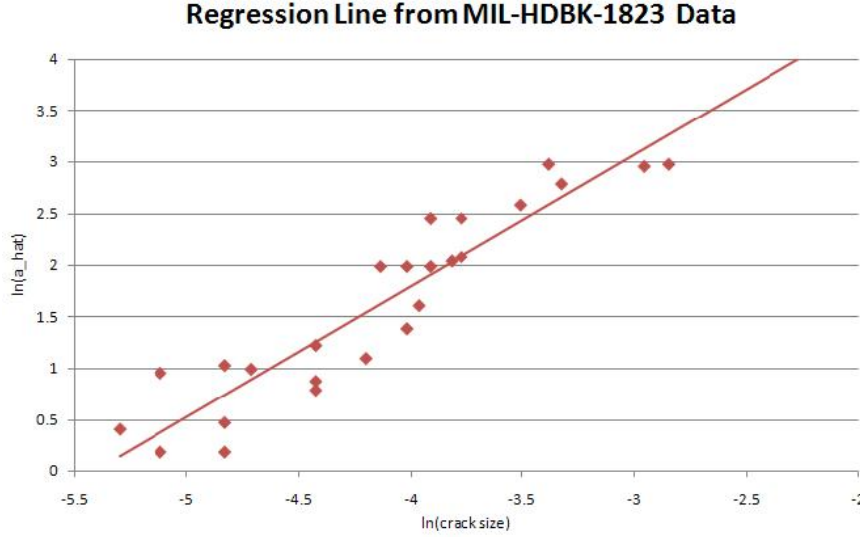


Figure 5.3: MIL-HDBK-1823 provided data to recreate the regression line in Figure 5.1

### 5.3 Building a Notional ROC Curve

Receiver operating characteristic (ROC) curves provide a conceptually simple technique for showing the trade-off between false alarm rates and probability of detection for a sensor system [46, 107].

In a scenario where a NDE system is attempting to detect the existence of a crack, four possible outcomes exist in relation to crack existence and crack detection. If a crack of a given size exists, and the crack detection system provides a crack indication, then the system provides a True Positive; if the system does not provide a crack indication, then the system provides a False Negative or a “miss”. If a crack

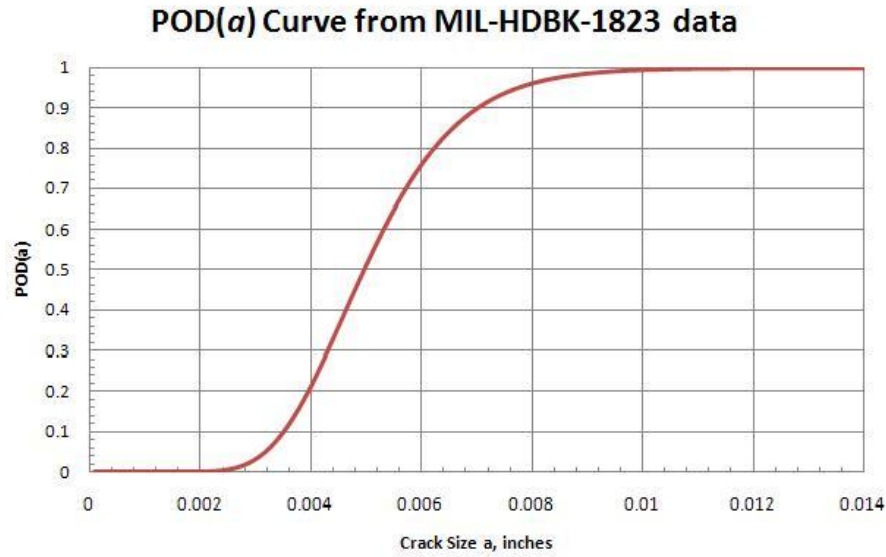


Figure 5.4: MIL-HDBK-1823 provided data to generate a sample  $POD(a)$  curve

of a given size does not exist and the system does not provide a crack indication, the system provides a True Negative; if the system does provide a crack indication it is a False Positive. Matzkanin [74] places these four possibilities in a “confusion matrix” partially recreated in Figure 5.5. These four outcomes lay the foundation for the ROC curve.

Figure 5.6 shows a simplified graphical representation of the values relating to the four possible outcomes. Three main components to build ROC curves are:

1. The system response distribution when no damage exists
2. The system response distribution when damage of a given size exists
3. The system threshold detection level

ROC curves for several current NDE techniques are presented by Matzkanin [74]. Lu [68] gives ROC curves for one SHM technique currently under development.

The crack indication provided by the system is based on the threshold detection level as described in paragraph 5.2. Varying this detection threshold changes the probability of detection and probability of false alarm for a given crack size. If the

		Stimuli (Flaw Presence)	
		Positive	Negative
NDE Signal (Flaw Response)	Positive	True Positive (TP) No Error	False Positive (FP) Type II Error (False Call)
	Negative	False Negative (FN) Type I Error (Miss)	True Negative (TN) No Error

Figure 5.5: The confusion matrix provides the basis for ROC curves

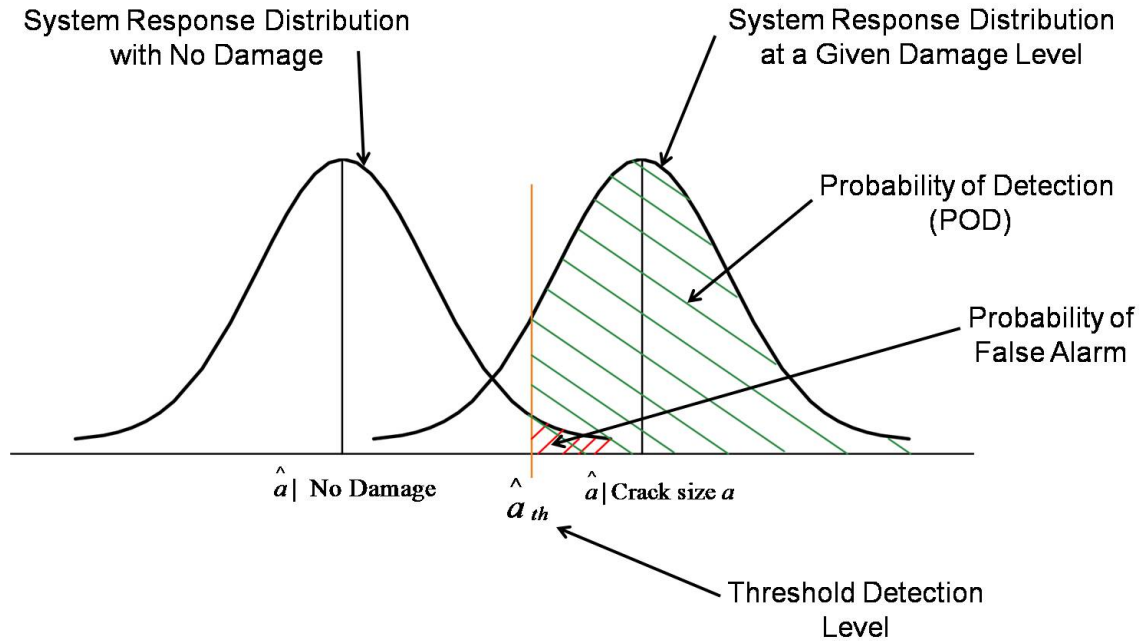


Figure 5.6: Graphical representation of values used to build ROC curves

threshold detection level is low, high probability of detection is possible, but false alarm rate (FAR) also increases. If the threshold value is high, the false alarm rate will be reduced, but the probability of detection will also be reduced. Varying the

threshold detection value from low to high extremes and plotting the corresponding false alarm rate vs. probability of detection produces a ROC curve [74,79].

The MIL-HDBK-1823 example data used to build the  $POD(a)$  curve in Figure 5.4 does not provide the “undamaged” system response distribution needed to generate a true ROC curve, but a notional ROC curve can be constructed after assuming an undamaged response distribution using the following assumptions:

1. Assumption: The undamaged response is normally distributed. Justification: Since the responses for a given damage size,  $g(\hat{a}|a)$ , are normally distributed, it follows undamaged responses are also normally distributed.
2. Assumption: The undamaged response is centered around 0. Justification: No damage provides no signal, or SHM system is calibrated to remove initial biases
3. Assumption: Undamaged response standard deviation is equal to the standard deviation of the regression residuals,  $\delta$ . Justification: The residuals for the damaged condition represent deviation from the “true” response given by the regression line. This deviation is constant for all damage sizes, so it follows this deviation will also hold for the undamaged condition.

Figure 5.7 shows the ROC curve generated from the assumptions listed above. Flaw size is fixed at  $a_{90} = 0.007$  (the crack size detected 90% of the time in the original  $POD(a)$  curve). The threshold crack size  $\hat{a}_{th}$  ranges from 0.01 to 1.5 inches. The diagonal line from (0, 0) to (1, 1) is described by Fawcett [46] as “randomly guessing”. If a system randomly guesses a “hit” half of the time, according to Fawcett, it can be expected to get half of the indications correct and half of them incorrect, giving point (0.5, 0.5) on the ROC chart. If a system guesses a “hit” 90% of the time, the corresponding point on the ROC chart is (0.9, 0.9). For a detection system to be better than random guessing, a ROC curve must lie in the upper triangular region of the ROC chart, with perfect detection being a curve extending from (0, 0) to (0, 1) and then from (0, 1) to (1, 1).

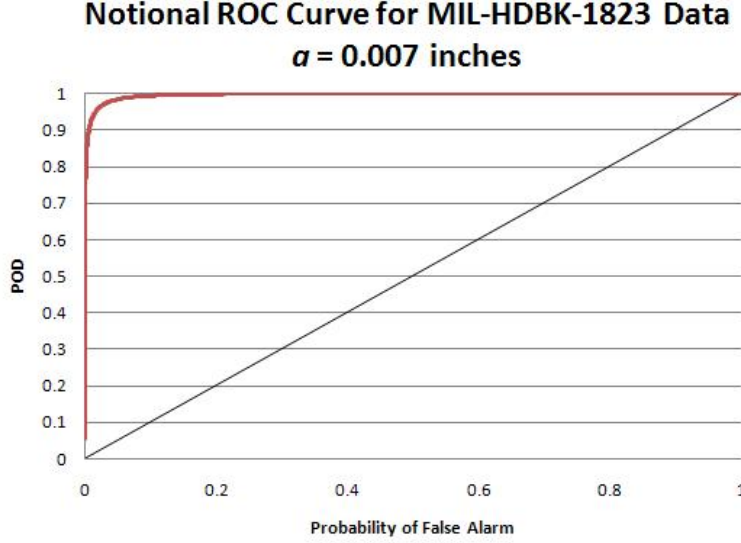


Figure 5.7: ROC curve derived from MIL-HDBK-1823 example data

Comparisons among ROC curves can be made by specifying a maximum probability of false alarm and determining the POD of the given crack size. The higher the POD, the better the crack detection technique. MIL-HDBK-1823 suggests 5% as a maximum allowable probability of false alarm for a given NDE procedure [35]. Referring to Figure 5.7, adjusting  $\hat{a}_{th}$  to detect a 0.007 inch crack 90% of the time will lead to a probability of false alarm of 0.006.

#### 5.4 Incorporating Sensor Degradation Information into $POD(a)$

NDE techniques for determining probability of detection as defined by MIL-HDBK-1823 [35] and by Berens [7] provide a starting point for SHM system probability of detection, but serious issues surround the direct application of NDE  $POD(a)$  techniques to SHM systems. One significant issue concerns changes to the SHM system after installation on the aircraft. Proper system set-up, calibration, and testing against a known standard underpin the probability of detection curves for traditional NDE methods, but these preinspection steps may not directly apply to an installed SHM system. Probability of detection of an installed SHM system can and will change

depending on how the SHM system withstands its operating environment. For SHM systems to be viable, these changes in POD must be anticipated and incorporated into any SHM-based inspection system. Likely changes to the performance of SHM sensors after installation can be explored in terms of sensor response distributions, given that damage exists. But changes in these sensor response distributions depend on how the  $\text{POD}(a)$  calculations are initially developed. A key distinction must be made between SHM sensors and systems that produce *increasing* signal response with increasing crack size and those SHM systems that produce *decreasing* signal response with increasing crack size. Increasing signal response with increasing crack size allows direct application of the MIL-HDBK-1823 techniques, as described in section 5.4.1, where decreasing signal strength with increasing crack sizes requires modification to the MIL-HDBK-1823 techniques, as described in section 5.4.2.

*5.4.1 SHM Systems where  $\hat{a}$  Increases with Increasing Crack Size.* As previously discussed in section 5.2, MIL-HDBK-1823 derives NDE system  $\text{POD}(a)$  based upon a system response distribution for a given crack size,  $g(\hat{a}|a)$ , and a threshold detection value,  $\hat{a}_{th}$ , with mean system response values increasing with increasing crack size. Figure 5.8 shows the relative positions of the SHM system response distributions given no damage exists and given a crack of size  $a$  exists. The figure also shows the areas used to calculate POD and probability of false alarm for a given crack size. Note that the response distribution given crack size  $a$  exists lies to the right of the no damage distribution, reflecting the higher mean response when structural damage exists.

In the direct application of MIL-HDBK-1823 techniques, the initial SHM sensor response to a given crack size at the time of sensor installation will have a known probability distribution as determined by the  $\ln(a)$  vs.  $\ln(\hat{a})$  relationship. At some point after installation, sensor degradation will change the  $\ln(a)$  vs.  $\ln(\hat{a})$  relationship, resulting in changes to the sensor response distribution and the system's probability of detection. If these changes in the  $\ln(a)$  vs.  $\ln(\hat{a})$  relationship can be identified and

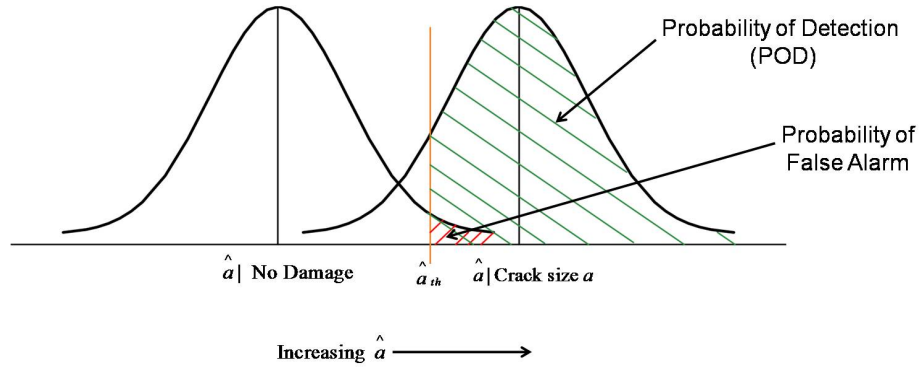


Figure 5.8: For systems where  $\hat{a}$  increases with increasing  $a$ , the “damage” response distribution is to the right of the “no damage” response distribution

predicted, a direct link to changes in  $\text{POD}(a)$  can be made. For example, assume a SHM sensor has a uniform 20% reduction in signal received for each crack size (due to transmit and/or receive signal loss). If a notional second  $\ln(a)$  vs.  $\ln(\hat{a})$  test were performed, the reduced signal would result in data points “translating” down against the given crack sizes, as shown in Figure 5.9 (using the example data from Figure 5.3). This will, in effect, move the sensor response distribution to the left on the  $\hat{a}$  axis, as shown in Figure 5.10, reducing the probability of detection at a given threshold detection level.

Figures 5.11 and 5.12 show the corresponding changes in the  $\text{POD}(a)$  and ROC curves for a 20% sensor signal degradation. Table 5.1 shows  $a_{90}$  increases over 17%, while the probability of false alarm increases from 0.6% to 2.7% when the system is configured to detect a crack of 0.007 inches 90% of the time. Table 5.2 lists original and degraded data used to generate Figures 5.9 and 5.11.

Table 5.1: 20% degradation causes increases in the crack size detectable 90% of the time and false alarm rate

	$a_{90}$	FAR at 90% POD
Original signal	0.007	0.006
20% Degraded signal	0.0082 (+17.1%)	0.027 (+350%)

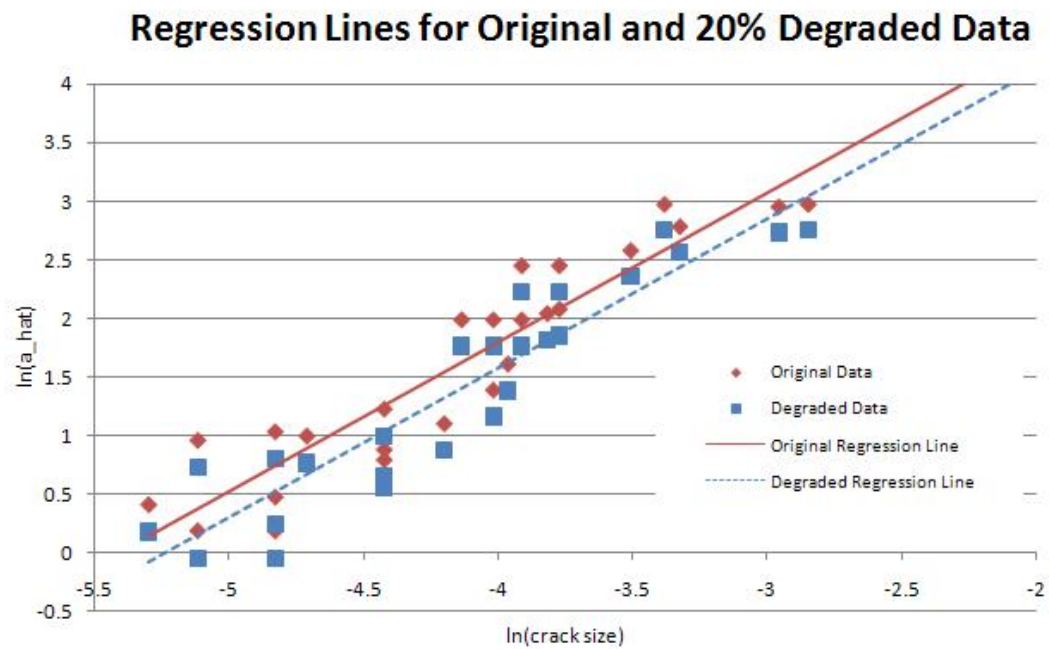


Figure 5.9: Reducing the received signal,  $\hat{a}$  by 20% “translates” the data points at each crack size

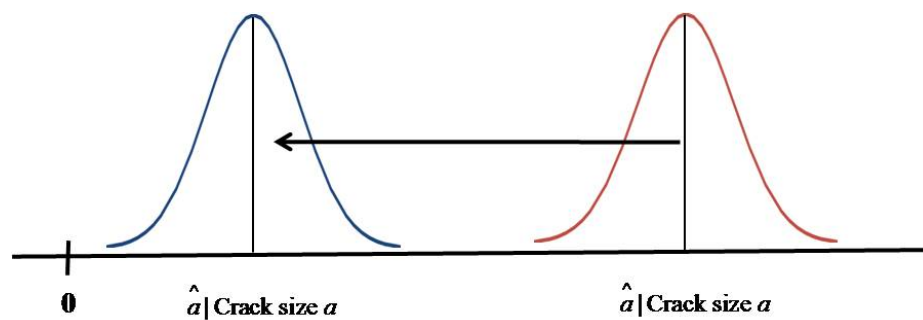


Figure 5.10: Sensor degradation can cause the response distribution to center around a lower value of  $\hat{a}$



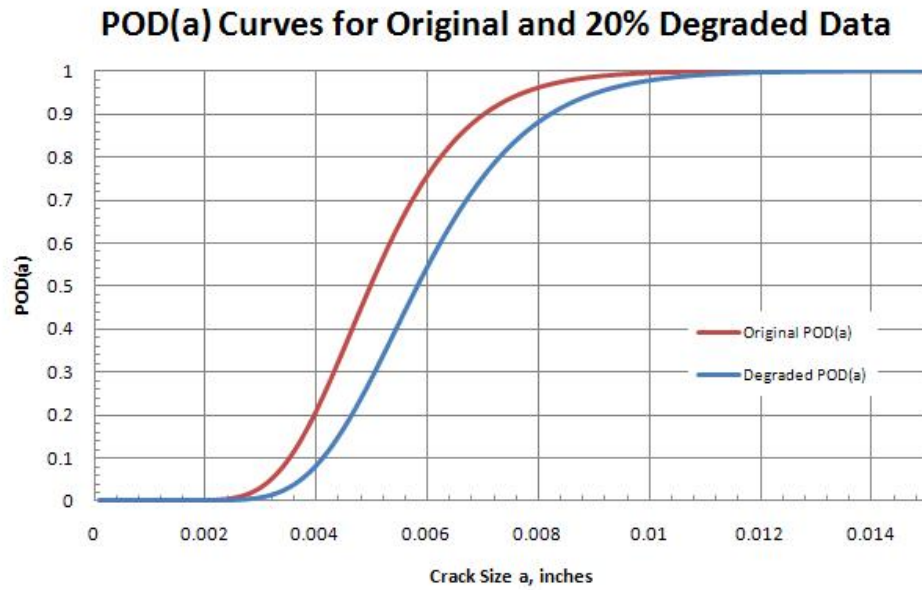


Figure 5.11: Reducing the received signal,  $\hat{a}$  by 20% “translates” the  $POD(a)$  curve to the right, reducing POD at each crack size

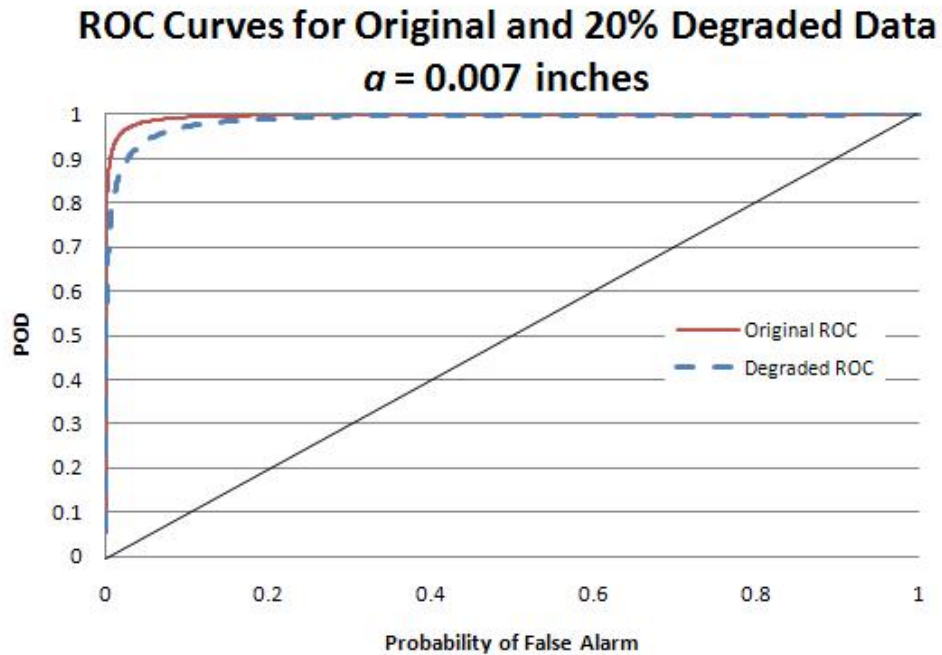


Figure 5.12: Reducing the received signal,  $\hat{a}$  by 20% “shifts” the ROC curve, increasing false alarm rate for higher levels of POD

Table 5.2: Original and 20% degraded  $\ln(a)$  vs.  $\ln(\hat{a})$  data for Figures 5.9 and 5.11

Crack Size $a$	$\ln(a)$	Original Sensor Signal $\hat{a}$	$\ln(\hat{a})$	20% Degraded Sensor Signal $\hat{a}_{Degraded}$	$\ln(\hat{a}_{Degraded})$
0.005	-5.298	1.5	0.4055	1.2	0.1823
0.006	-5.116	1.2	0.1823	0.96	-0.0408
0.006	-5.116	2.6	0.9555	2.08	0.7324
0.008	-4.828	1.2	0.1823	0.96	-0.0408
0.008	-4.828	2.8	1.029	2.24	0.8065
0.008	-4.828	1.6	0.4700	1.28	0.2469
0.009	-4.711	2.7	0.9933	2.16	0.7701
0.012	-4.423	2.2	0.7885	1.76	0.5653
0.012	-4.423	3.4	1.224	2.72	1.001
0.012	-4.423	2.4	0.8755	1.92	0.6523
0.015	-4.200	3	1.099	2.4	0.8755
0.016	-4.135	7.3	1.988	5.84	1.765
0.018	-4.071	7.3	1.988	5.84	1.765
0.018	-4.017	4	1.386	3.2	1.163
0.019	-3.963	5	1.609	4	1.386
0.02	-3.912	7.3	1.988	5.84	1.765
0.02	-3.912	11.6	2.451	9.28	2.228
0.022	-3.817	7.7	2.041	6.16	1.818
0.023	-3.772	11.6	2.451	9.28	2.227
0.023	-3.772	8	2.079	6.4	1.856
0.03	-3.507	13.2	2.580	10.56	2.357
0.034	-3.381	19.6	2.976	15.68	2.752
0.036	-3.324	16.2	2.785	12.96	2.561
0.052	-2.957	19.2	2.955	15.36	2.731
0.058	-2.847	19.6	2.976	15.68	2.752

The translation of the data points observed in Figure 5.9 effectively changes the intercept of the regression equation ( $\beta_0$  in equation 5.2). This change can be modeled using a multiplier (call it  $\alpha_d$ ) in conjunction with the original regression intercept  $\beta_0$ . Changes to  $\alpha_d$  have the same effect on the  $\text{POD}(a)$  curve as translation of the entire data set due to sensor degradation. But changes in sensor performance may affect the  $\ln(a)$  vs.  $\ln(\hat{a})$  relationship ways other than simple translation. For example, sensor degradation could cause an increase in the variance of the response signal, causing the response distribution to “flatten” as shown in Figure 5.13.

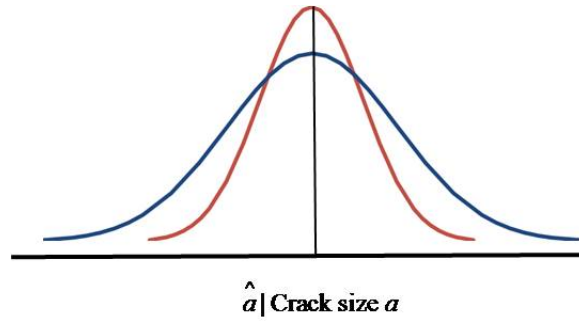


Figure 5.13: Sensor degradation can cause the response distribution variance to increase

Similarly, regression slope and system threshold detection level could also be affected. Changes to these parameters provide the basis for modeling changes in  $\text{POD}(a)$  due to sensor degradation.

*5.4.2 Changes to the MIL-HDBK-1823 Technique when  $\hat{a}$  Decreases with Increasing Crack Size.* Direct application of MIL-HDBK-1823 requires the detection system signal,  $\hat{a}$ , to increase with crack size,  $a$ . With some SHM systems,  $\hat{a}$  may *decrease* with increasing with crack size (for example, due to progressive disruption of an initial “baseline” signal). In this case, the response variable may be transformed to meet the MIL-HDBK-1823 requirements (as done by Cobb [27] and discussed in section 5.7) or modifications to the MIL-HDBK-1823 techniques are necessary.

Figure 5.14 shows the relative positions of the SHM system response distributions given no damage exists and given a crack of size  $a$  exists, for SHM systems

where  $\hat{a}$  decreases with increasing crack size. Note that the response distributions have changed positions with respect to Figure 5.8, reflecting the lower mean response when structural damage exists. Also, the areas under the distributions used to calculate POD and probability of false alarm now fall below the threshold detection value.

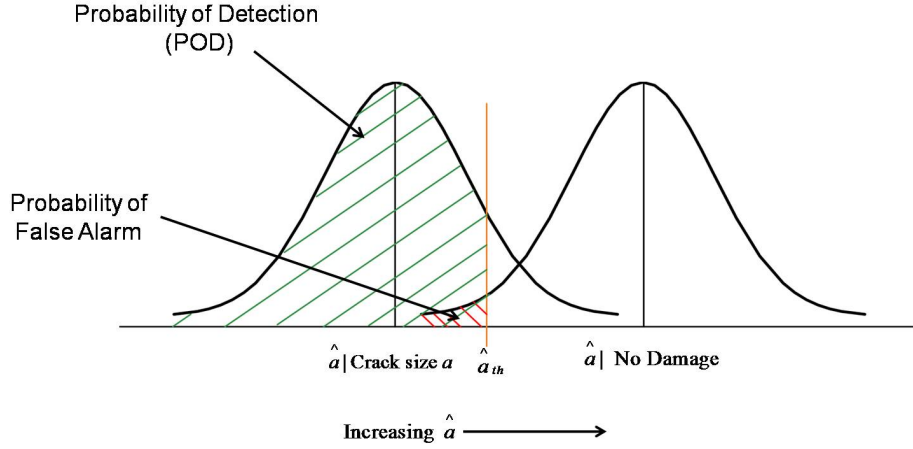


Figure 5.14: For systems where  $\hat{a}$  decreases with increasing  $a$ , the “damage” response distribution is to the left of the “no damage” response distribution

The change in location of the area used to calculate POD would also be evident in a  $\ln(a)$  vs.  $\ln(\hat{a})$  plot obtained from experimental data. Figure 5.15 shows a notional  $\ln(a)$  vs.  $\ln(\hat{a})$  regression line with the area of the  $g(\hat{a}|a)$  distribution used to calculate POD extending below the threshold detection value.

With respect to sensor degradation, having the undamaged response distribution centered around a value of  $\hat{a}$  higher than the damaged response distribution will cause both distributions to shift as the sensor degrades. Assuming the  $\hat{a}$  value nears but will not go below zero (the SHM system will not register a negative  $\hat{a}$ ), proportional degradation of  $\hat{a}$ , as described in section 5.4.1, will cause the distance between the means of the  $\hat{a}|a=0$  and the  $\hat{a}|a$  distributions to be reduced in terms of absolute signal strength. For example, if the undamaged mean  $\hat{a}$  equals 100 mV, and the damaged mean  $\hat{a}$  is 80 mV, a 20% degradation in signal strength will reduce the undamaged mean  $\hat{a}$  to 80 mV and the damaged mean  $\hat{a}$  to 64 mV. The original difference between

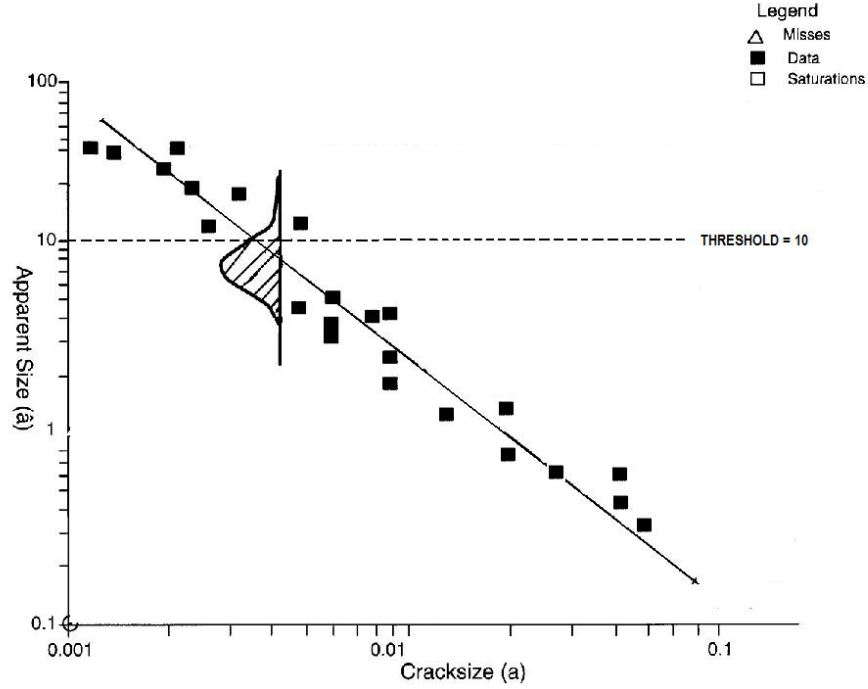


Figure 5.15: Notional linear regression when  $\hat{a}$  decreases with increasing crack size

the undamaged and damaged means was 20 mV before sensor degradation and 16 mV after degradation. Figure 5.16 shows the potential shifts of the  $\hat{a}|a=0$  and the  $\hat{a}|a$  distributions when sensor degradation occurs.

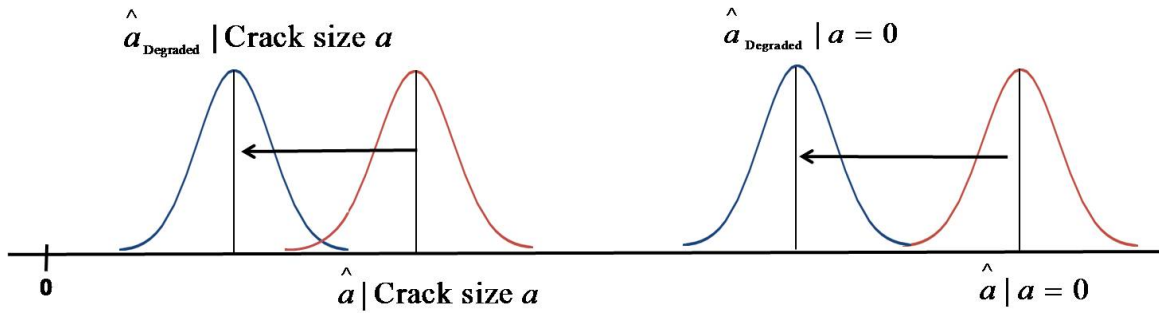


Figure 5.16: Distance between undamaged and damaged mean  $\hat{a}$  will be reduced for proportional signal loss due to sensor degradation

### 5.5 A $POD(a)$ “Degradation” Model

It is proposed to incorporate the sensor signal changes into the  $POD(a)$  model represented by equation 5.5 on page 132 using three methods:

1. By adjusting the regression parameters  $\beta_0$  and  $\beta_1$
2. By adjusting the signal threshold
3. By adjusting the standard deviation of the regression residuals

The proposed  $POD(a)$  degradation model uses multipliers called “Degradation Coefficients” to modify the original  $POD(a)$  model described in equation 5.5, based on the effects of sensor degradation. The model has the following form:

$$POD(a)_{Degraded} = \Phi \left( \frac{(\beta_0 * \alpha_d) + (\beta_1 * \gamma_d) * \ln(a) - \ln(\hat{a}_{th} * \rho_d)}{\delta * \psi_d} \right) \quad (5.6)$$

with degradation coefficients  $\alpha_d$ ,  $\gamma_d$ ,  $\rho_d$ , and  $\psi_d$  modifying the regression coefficients, the threshold detection level and the standard deviation of the regression residuals, respectively. The following analysis describes changes to a generic SHM system, building on the following assumptions:

1. An  $a$  vs.  $\hat{a}$  relationship with normally distributed regression residuals exists for the generic SHM system. The following discussion uses a  $\ln(a)$  vs.  $\ln(\hat{a})$  relationship for consistency with the MIL-HDBK-1823 derivation.
2. Increasing crack size,  $a$ , results in increasing values of system response,  $\hat{a}$ .
3. Proportional sensor degradation occurs at all crack sizes.

The following sections show how adjusting each of the degradation coefficients affects the  $POD(a)$  curve. Each section uses the following basic method:

1. All  $POD(a)$  coefficients are fixed to the values used to generate the  $POD(a)$  curve in Figure 5.4. (See Table 5.3)
2. One degradation coefficient is adjusted to produce a 1%, 5%, 20% and 50% change in its respective  $POD(a)$  parameter

3.  $\text{POD}(a)$  is plotted for each value of degradation coefficient, and the crack size detected 90% of the time ( $a_{90}$ ) is determined
4. Crack size  $a$  is fixed at the original  $a_{90} = 0.007$ , and  $\hat{a}_{th}$  is adjusted to generate a ROC curve for each value of degradation coefficient
5. The probability of false alarm for a 90% POD of crack size 0.007 inches is determined

Where appropriate, sections also include plots of the changes in the original regression line (Figure 5.3) due to the different values of the degradation coefficients.

Table 5.3: Baseline  $\text{POD}(a)$  coefficients associated with Figure 5.4

$\beta_0$	$\beta_1$	$\hat{a}_{th}$	$\delta$	$a_{50}$ (in)	$a_{90}$ (in)
7.5271	1.4195	1	0.3822	0.005	0.007

*5.5.1 Modifying the Regression Intercept,  $\beta_0$ , Using Degradation Coefficient  $\alpha_d$ .* Reduced signal at the catch sensor is a reasonable consequence of sensor degradation. This effect can be modeled through adjustments to  $\alpha_d$  in equation 5.6, effectively changing the regression equation intercept,  $\beta_0$ . In terms of the original  $\text{POD}(a)$  experiment, the natural log of the signal strength,  $\ln(\hat{a})$ , is reduced for each value of natural log crack size,  $\ln(a)$ . Figure 5.17 gives the  $\text{POD}(a)$  curves for the changes in  $\alpha_d$ . Changing  $\text{POD}(a)$  also affects the ROC curve as shown in Figure 5.18. It should be noted that for  $\alpha_d$  less than approximately 0.8, the ROC curve falls below the upper triangle of the ROC chart, indicating performance worse than the system arbitrarily guessing whether a crack exists. Table 5.4 shows the corresponding increases in  $a_{90}$ , and the increase in the probability of false alarm when attempting to detect the original  $a_{90} = 0.007$  inches.

Figure 5.19 shows the corresponding changes in the regression line due to increases in  $\alpha$ . As the regression line “drops”, the area under the  $g(\hat{a} | a)$  distribution shown in Figure 5.1 reduces for a given threshold detection level, thus reducing  $\text{POD}(a)$  for all crack sizes.



Figure 5.17: Decreasing  $\alpha_d$  “lowers” the regression line in Figure 5.1, reducing  $POD(a)$  for all crack sizes

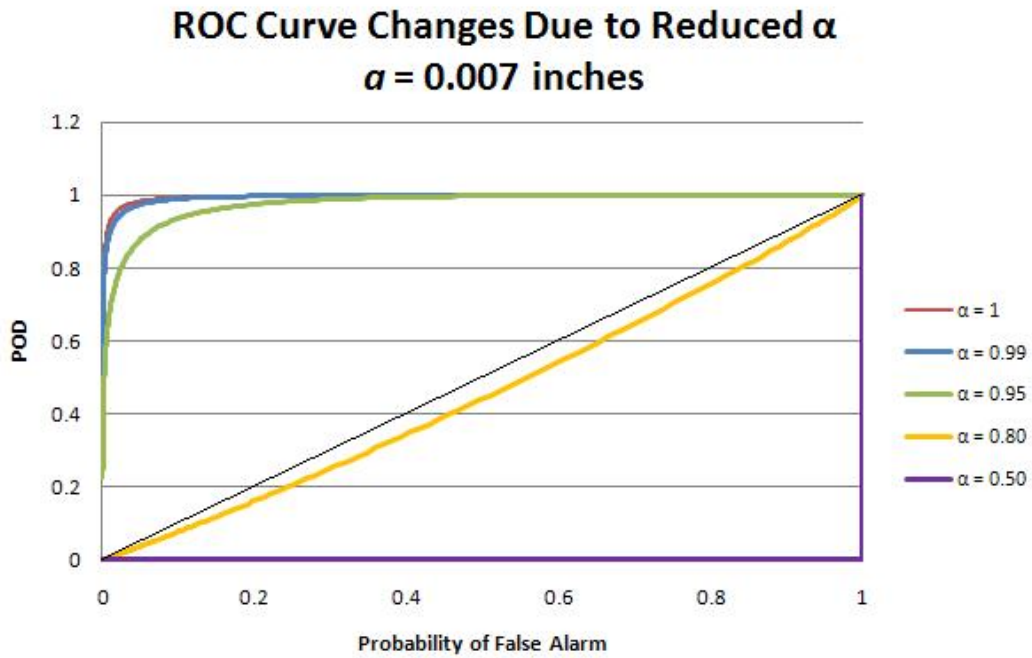


Figure 5.18: Decreasing  $\alpha_d$  shifts the ROC curve to the right, reflecting increased false alarm rates



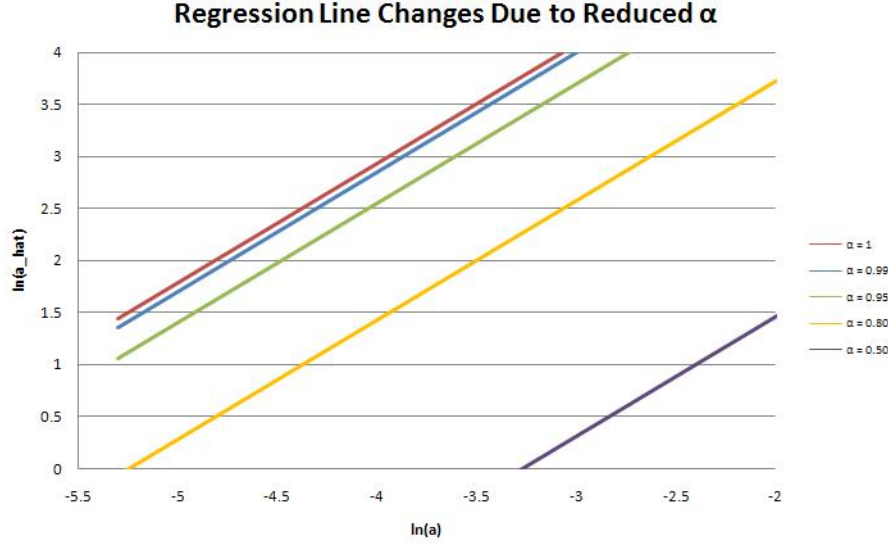


Figure 5.19: Increasing  $\alpha_d$  “lowers” the regression line in Figure 5.1, reducing POD for all crack sizes

Table 5.4:  $a_{90}$  crack length and false alarm rate increase with decreasing  $\alpha_d$

$\alpha_d$	$a_{90}$	FAR for $\text{POD}(0.007) = 0.9$
1	0.007	0.006
0.99	0.0074	0.0102
0.95	0.0091	0.0644
0.80	0.0203	0.9269
0.50	0.0997	1

### 5.5.2 Modifying the Regression Slope, $\beta_1$ , Using Degradation Coefficient $\gamma_d$ .

Sensor degradation may not have the same effect on the  $a$  vs.  $\hat{a}$  relation at all crack sizes, as is implied by the regression line shifts described in section 5.5.1. These unequal shifts may be modeled by increasing  $\gamma_d$  in equation 5.6, effectively changing the regression equation slope. Figure 5.20 gives the  $\text{POD}(a)$  curves for changing  $\gamma_d$ . Table 5.5 shows the corresponding increases in  $a_{90}$  and false alarm rate.

The increase in  $\gamma_d$  increases the slope of the regression line as shown in Figure 5.22. Note that since the natural log of the crack size is negative, the increase in slope results in a “downward” movement of the regression line, rotating around  $\ln(a) = 0$ . As with decreasing  $\alpha_d$ , the area under the  $g(\hat{a}|a)$  distribution shown in Figure

5.1 reduces for a given threshold detection level, thus reducing  $POD(a)$  for all crack sizes.

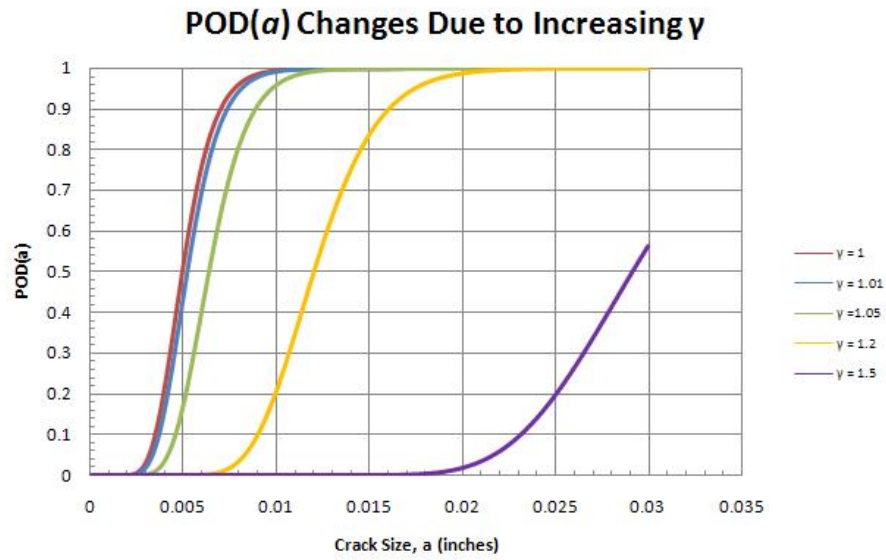


Figure 5.20: Increasing  $\gamma_d$  “shifts” the  $POD(a)$  curve, decreasing POD for all crack sizes

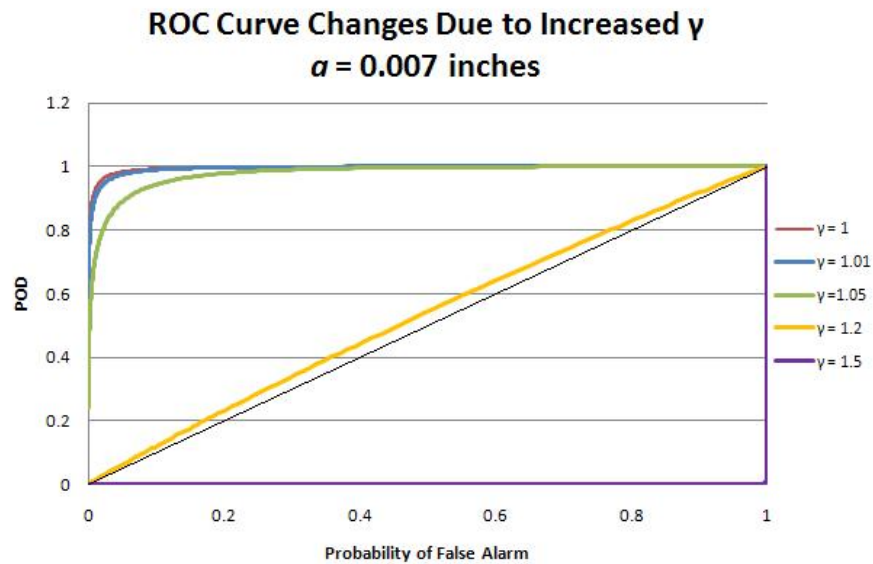


Figure 5.21: Increasing  $\gamma_d$  shifts the ROC curve to the right, reflecting increased false alarm rates

Table 5.5:  $a_{90}$  crack length and false alarm rate increase with increasing  $\gamma_d$

$\gamma_d$	$a_{90}$	FAR for $\text{POD}(0.007) = 0.9$
1	0.007	0.006
1.01	0.0074	0.0102
1.05	0.0089	0.0555
1.20	0.0161	0.8793
1.50	0.0367	1

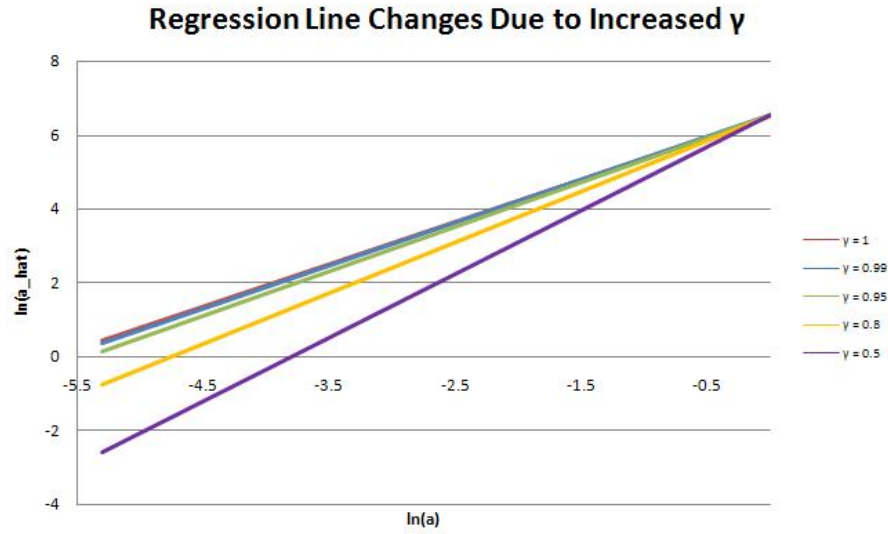


Figure 5.22: Increasing  $\gamma_d$  “rotates” the regression line in Figure 5.1, reducing POD for all crack sizes

5.5.3 *Modifying the Threshold Detection Value,  $\hat{a}_{th}$ , Using Degradation Coefficient  $\rho_d$ .* Changes in the SHM system detection threshold level could also result from degradation of the SHM system sensors. Increases in the threshold level can be modeled by increasing  $\rho_d$  in equation 5.6. The regression line in Figure 5.3 remains unchanged in this case, but the movement of  $\hat{a}_{th}$  changes the area under the SHM response distribution for a given damage size  $g(\hat{a}|a)$  used in the  $POD(a)$  calculation.

ROC curves are not defined for specific changes in  $\hat{a}_{th}$ , since ROC curves are formed by sweeping  $\hat{a}_{th}$  over a range of values for a given crack size and plotting the resulting false alarm rates against the probabilities of detection (see section 5.3).



Figure 5.23: Increasing  $\rho_d$  “reduces” the area under the system response distribution in Figure 5.1, reducing POD for all crack sizes

Table 5.6:  $a_{90}$  crack length increases with increasing  $\rho_d$

$\rho_d$	$a_{90}$
1	0.0070
1.01	0.0071
1.05	0.0072
1.20	0.0080
1.50	0.0094

*5.5.4 Modifying the Regression Residual Standard Deviation,  $\delta$ , Using Degradation Coefficient  $\psi_d$ .* The standard deviation of the regression residuals represents the spread of the experimental data. Degradation of the SHM sensors could result in an increase in this spread. These increases can be modeled by increasing  $\psi_d$  in equation 5.6.

As shown in Figure 5.24, as  $\psi_d$  increases, the  $\text{POD}(a)$  curve becomes more shallow, with a point of rotation around  $a_{50}$ . Although  $a_{50}$  remains constant,  $a_{90}$  is reduced due to the curve shift. Since sensor degradation will not cause improvements in POD at low crack sizes, changes in  $\delta$  will need to be made in conjunction with other degradation parameters to produce a representative degraded  $\text{POD}(a)$  curve for crack sizes less than the original  $a_{50}$ . But since most (if not all) SHM applications will be concerned with POD values well above 50%, further adjustments to  $\delta$  will not be addressed in this analysis. Figure 5.25 and Table 5.7 present the ROC curves and changes to the  $a_{90}$  crack lengths.

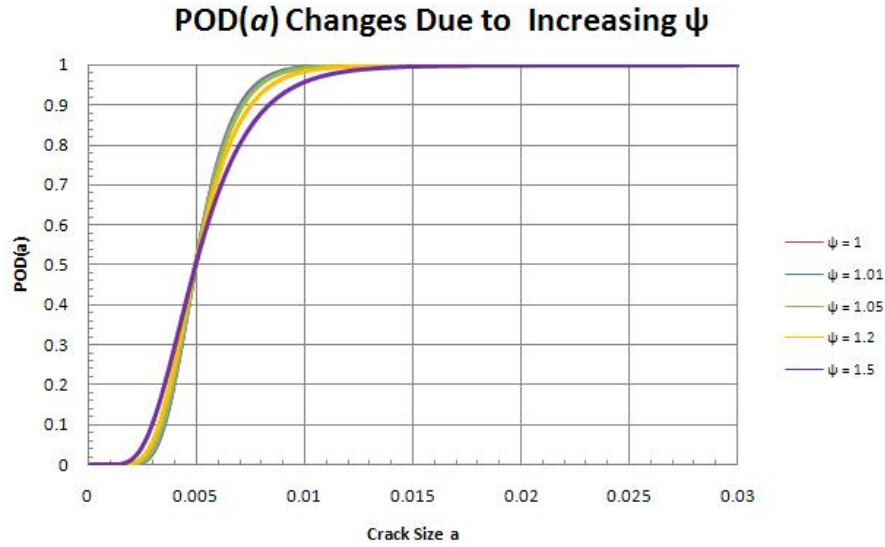


Figure 5.24: Increasing  $\psi_d$  “rotates”  $\text{POD}(a)$  around  $a_{50}$ , requiring additional parameter changes to model changes for crack sizes less than the original  $a_{50}$

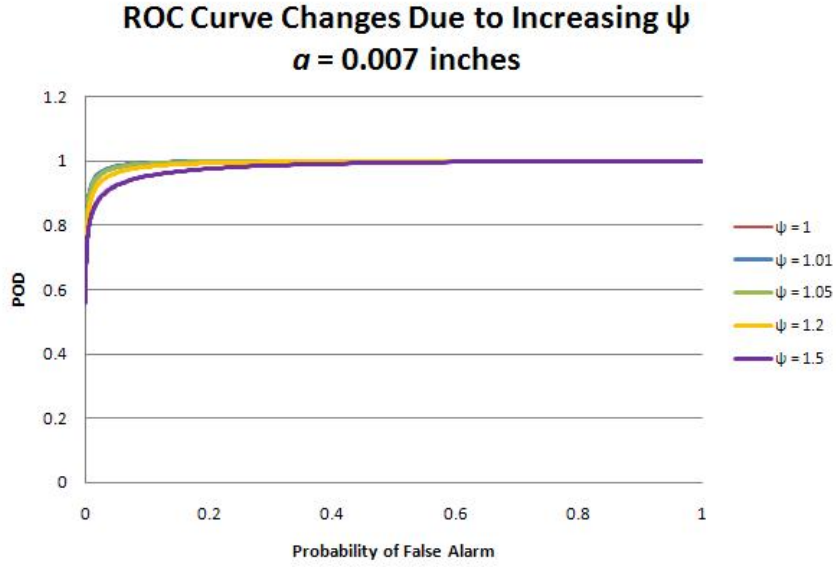


Figure 5.25: Increasing  $\psi_d$  shifts the ROC curve, increasing false alarm rates for some POD values

Table 5.7:  $a_{90}$  crack length and false alarm rate increase slightly with increasing  $\psi_d$

$\psi_d$	$a_{90}$	FAR for $\text{POD}(0.007) = 0.9$
1	0.0070	0.0060
1.01	0.0071	0.0062
1.05	0.0072	0.0070
1.20	0.0075	0.0123
1.50	0.0084	0.0304

## 5.6 Applying the $POD(a)$ Degradation Model Using Experimental Data

Section 5.5 shows how degradation coefficients can be used to change  $POD(a)$  calculations by adjusting the parameters of the original  $POD(a)$  curves. The models of experimental results presented in section 4.8 give changes in sensor response as a function of strain level and number of cycles. It follows that the models generated from the cyclic strain experiment can be used to define the degradation coefficients in the  $POD(a)$  degradation model, thereby tying  $POD(a)$  directly to changes in sensor performance. Degradation coefficients in the  $POD(a)$  degradation model then become functions of the aircraft environmental factors. In this case, the degradation coefficients become functions of strain level and number of cycles.

Although no  $POD(a)$  information exists for the current PZT configuration, the experimental data can be combined with the example data provided in MIL-HDBK-1823 [35] to show how an existing  $POD(a)$  curve can be modified to account for known sensor degradation due to aircraft environmental factors. The following examples use the response models for the MBond PZT pitch-catch pairs.

*5.6.1 Degradation of a Single Parameter.* Section 5.4 discusses an example where sensor degradation causes a decrease in signal loss for all crack lengths, effectively shifting the sensor response distribution to the left (see Figure 5.10 on page 140). Figure 5.26 shows the experimental changes in response after cycling PZT pitch catch pairs at  $1700 \mu\epsilon$ , as described in sections 4.5 and 4.8. These experimental results describe the reduced signal due to degradation, and can be used to specify values for the degradation coefficient  $\alpha_d$ .

Equation 4.4, on page 126, presents the best fit power equation to the experimental data, with  $N$  being the number of cycles in thousands, and  $\epsilon$  being the strain level in microstrain. Selecting  $1700 \mu\epsilon$ , normalizing the results of equation 4.4 provides a proportion of original signal for a given number of cycles at that strain level.

Converting the normalized degraded signal to the proper  $\alpha_d$  depends on the form of the  $a$  vs.  $\hat{a}$  relation in the regression calculation. MIL-HDBK-1823 performs

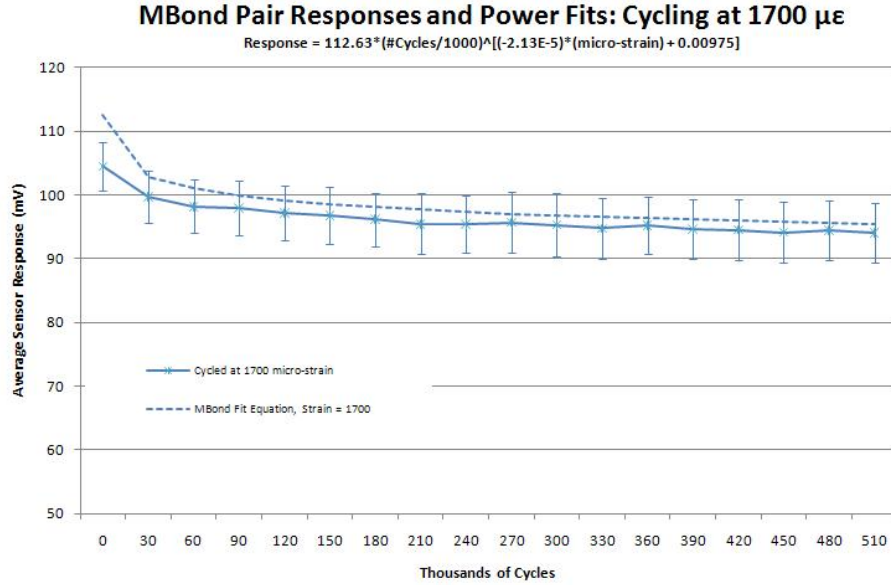


Figure 5.26: Experimental signal degradation due to cycling at 1700  $\mu\epsilon$

the regression on a natural log - natural log scale (see section 5.2), requiring the use of the natural log of the normalized degraded signal to set  $\alpha_d$ . Table 5.8 shows the required calculations.

Table 5.8:  $\alpha_d$  can be calculated based on the original  $\beta_0$  and experimental degradation results

Number of Cycles	Normalized Degraded Signal (NDS)	Revised Intercept $\ln(\text{NDS})+7.5271$	$\alpha_d$ Original/Revised Intercept
0K	1	7.5271	1
50K	0.9020	7.4239	0.9863
100K	0.8856	7.4056	0.9839
200K	0.8700	7.3874	0.9814
500K	0.8488	7.3632	0.9782

Figures 5.27 and 5.28 show the upper portions of the POD( $a$ ) and ROC curves generated when the values of  $\alpha_d$  are used in the POD( $a$ ) degradation model. Table 5.9 shows the increases in  $a_{90}$  and false alarm rate based on the number of cycles at 1700  $\mu\epsilon$ . For 500K cycles,  $a_{90}$  has increased 12.1%, and the false alarm rate for detecting a 0.007 inch crack 90% of the time has increased from 0.006 to 0.0186.



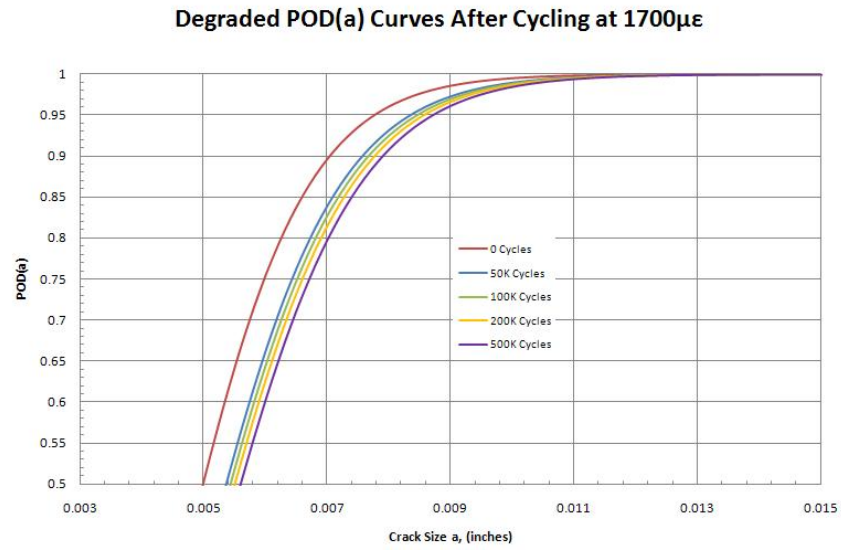


Figure 5.27:  $POD(a)$  changes caused by changing the  $\alpha_d$  degradation coefficient per the PZT signal degradation experimental model

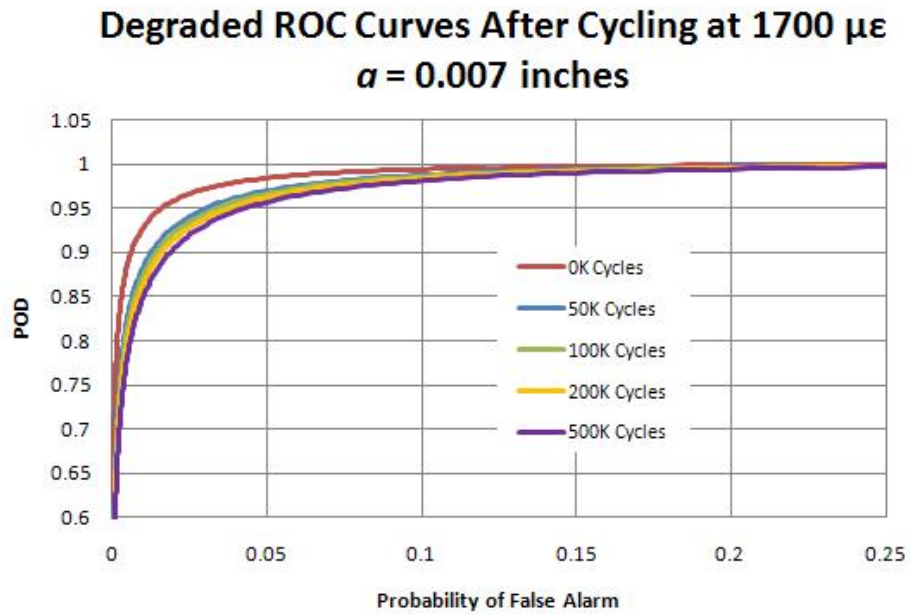


Figure 5.28: ROC curve changes caused by changing the  $\alpha_d$  degradation coefficient per the PZT signal degradation experimental model

Table 5.9: Probability of false alarm and  $a_{90}$  now depend on the number of cycles  
at 1700  $\mu\epsilon$

Number of Cycles	$\alpha_d$	$a_{90}$	FAR for POD(0.007) = 0.9
0K	1	0.007	0.0060
50K	0.9863	0.00755 (+7.1%)	0.0128
100K	0.9839	0.00765 (+9.3%)	0.0143
200K	0.9814	0.00775 (+10.7%)	0.0166
500K	0.9782	0.00785 (+12.1%)	0.0186

5.6.2 *Simultaneous Degradation of Multiple Parameters.* While the results from the cyclic strain experiment showed a signal loss between PZT pitch-catch pairs when cycling at 1700  $\mu\epsilon$ , cycling at 2600  $\mu\epsilon$  caused both signal loss and an increase in the standard deviation between multiple PZT pairs (see sections 4.5 and 4.6). These changes relate to both a shift to the left and a “flattening” of the sensor response distribution, combining the changes shown in Figures 5.10 and 5.13. These changes can be modeled through changes to the  $\alpha_d$  and  $\psi_d$  degradation coefficients.

The  $\alpha_d$  coefficient is calculated in the same manner as in section 5.6.1, but using 2600 in place of 1700 in the MBond power model equation, equation 4.4. Table 4.12 on page 116 shows the increase in sample standard deviation for cycling at 2600  $\mu\epsilon$ . Plotting this increase against numbers of cycles shows an approximately linear fit with standard deviation =  $0.0353 \cdot (\text{Number of Cycles}/1000) + 4.451$ . Normalizing the standard deviations gives the values of  $\psi_d$  used in the POD( $a$ ) degradation model. Table 5.10 gives the values of  $\alpha_d$  and  $\psi_d$ , along with the corresponding increases in  $a_{90}$  and false alarm rate for detecting a 0.007 inch crack 90% of the time. Figures 5.29 and 5.30 show the POD( $a$ ) and ROC curves at several levels of cycling at 2600  $\mu\epsilon$ . Of note is the inflection change in the POD( $a$ ) curve and the ROC curve moving below the upper triangular region of the graph at 500K cycles. In these cases, the sensor response distribution has been changed to such an extent that for some values of the threshold detection level, the probability of false alarm is greater than the probability of detection. Also of note is the increased POD for small crack sizes. As discussed in section 5.5.4, this result requires further adjustments to obtain accurate POD predictions below the original  $a_{50}$ , but since SHM systems will normally operate well above 50% POD, these additional adjustments are not included in this analysis.

Table 5.10: Probability of false alarm and  $a_{90}$  now depend on the number of cycles at 2600  $\mu\epsilon$

Number of Cycles	$\alpha_d$	$\psi_d$	$a_{90}$	FAR for POD(0.007) = 0.9
0K	1	1	0.007	0.0060
50K	0.9764	1.397	0.00915 (+30.7%)	0.0621
100K	0.9721	1.793	0.0107 (+52.9%)	0.1725
200K	0.9680	2.586	0.0144 (+105.7%)	0.5654
500K	0.9624	4.965	0.0337 (+381.4%)	

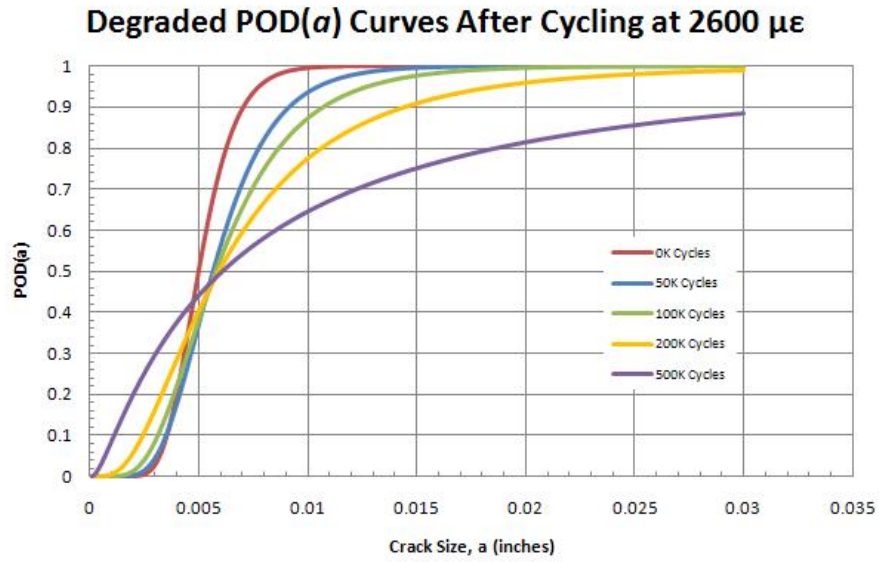


Figure 5.29: POD( $a$ ) changes caused by changing the  $\alpha_d$  degradation coefficient per the PZT 2600  $\mu\epsilon$  signal degradation experimental model

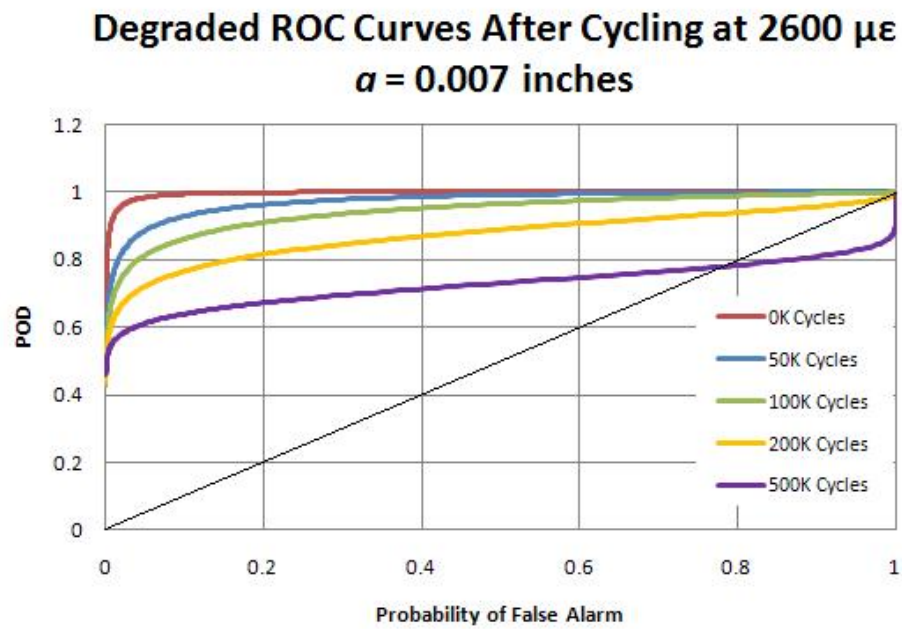


Figure 5.30: ROC curve changes caused by changing the  $\alpha_d$  degradation coefficient per the PZT  $2600 \mu\epsilon$  signal degradation experimental model

5.6.3 A  $POD(a, n)$  Surface. Taken to the next level in this context, the probability of detection curve for the notional PZT-based SHM sensor now depends not only on crack size, but also on the number of cycles ( $n$ ) and cyclic strain level. In effect, the  $POD(a)$  degradation model allows the combination of an original  $POD(a)$  curve, represented by Figure 5.4, with a known sensor degradation model, represented by Figure 4.32 on page 127. Combining the results of the two models gives  $POD$  based on crack size and number of cycles:  $POD(a, n)$ . Figure 5.31 provides a perspective on the resulting  $POD(a, n)$  surface for cycling at  $2600 \mu\epsilon$ .

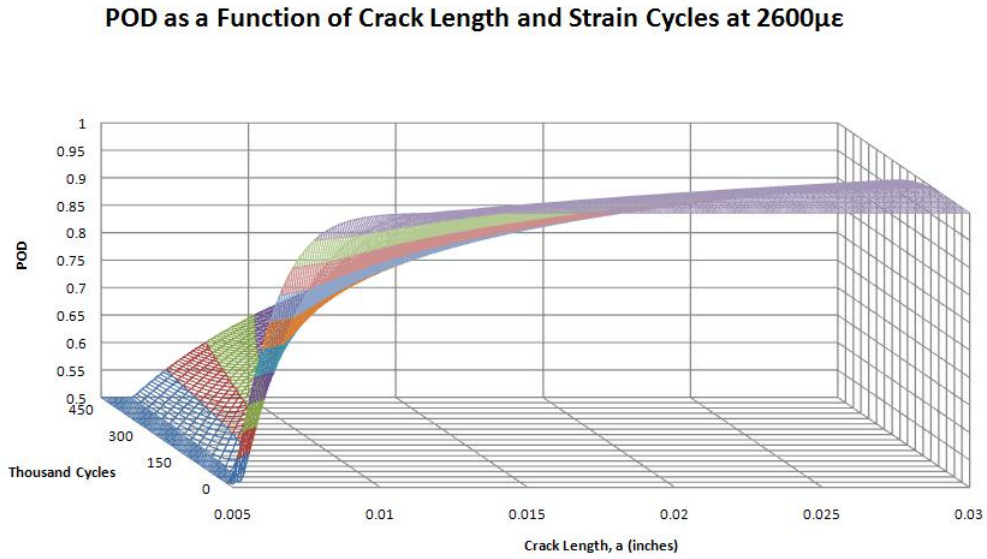


Figure 5.31: The  $POD(a)$  degradation model provides a method to combine  $POD(a)$  and sensor degradation into a  $POD(a, n)$  surface

### 5.7 *An Illustrative Example Using an Ultrasonic SHM Sensor POD( $a$ )*

Cobb, Michaels, Lu, and others (from here, referred to as Cobb) have performed a series of experiments to detect various forms of simulated aircraft structural damage using ultrasonic transducers glued to the surface of simulated aircraft structure [26,27,68,69,79,80]. The following sections use the POD( $a$ ) degradation model described in section 5.5 to combine the sensor degradation data collected in the PZT cyclic strain experiment with published data from Cobb and others to show how the POD( $a$ ) degradation model can be applied to an existing POD( $a$ ) model for a SHM sensor. While the physics of PZT-based crack detection techniques are similar to the physics of Cobb's method, i.e. sending and monitoring structural waves using transducers glued to the surface of aluminum simulated aircraft structure, it must be noted differences in glue type, excitation frequency and data collection system exist between the two techniques. Despite these differences, the similarities between the techniques (and limited POD( $a$ ) analyses from one source [27]) allow a useful example.

*5.7.1 System Introduction.* Figure 5.32 shows the general configuration of Cobb's crack detection method. The method attempts to detect cracks emanating from simulated structural fastener holes in aluminum test specimens. The transmitting ultrasonic transducer sends ultrasonic shear waves into the simulated aircraft structure. The hole simulating the fastener hole prevents the receiving transducer from direct reception of the shear waves, so the energy received at the receiving transducer includes only wave energy diffracted around the hole. (see [26, 80] for additional background on the technique).

Cobb [27] uses changes in received energy to develop POD( $a$ ) curves for cracks emanating from the simulated fastener hole, with  $a$  representing crack depth rather than crack length. The following sections recreate one of Cobb's POD( $a$ ) curves using data published in [27], and repeated in Table 5.11. This POD( $a$ ) curve then forms a basis for the application of the POD( $a$ ) degradation model.

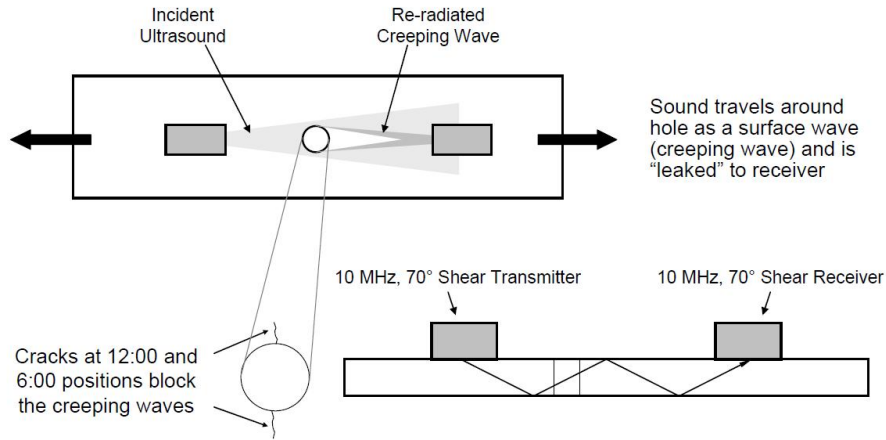


Figure 5.32: Ultrasonic SHM technique used by Cobb [79] to identify cracks at a simulated fastener hole.

Table 5.11: Cobb's ultrasonic SHM system Energy Ratio vs. crack depth data [27]

Energy Ratio	Maximum Crack Depth (mm)	Energy Ratio	Maximum Crack Depth (mm)
0.939	0.1648	0.927	0.2325
0.972	0.1138	0.930	0.3049
0.967	0.2197	0.611	0.4730
0.731	1.110	0.456	0.9752
0.616	0.8255	0.582	1.5926
0.879	1.1532	0.667	0.5032
0.644	0.4343	0.435	0.8299
0.856	0.2395	0.286	0.8097
0.840	0.3780	0.747	0.9539
0.411	1.5440	0.913	0.3547
0.041	2.8270	0.668	0.4654
0.716	0.4773	0.610	0.6435
0.907	0.3559	0.536	0.6657
0.405	1.6575	0.716	0.6464
0.919	0.3878	0.557	1.2645
0.888	0.6532	0.870	0.3251
0.862	0.4548	0.919	0.5137
0.938	0.2937	0.879	0.3644
0.810	0.5881		

5.7.2 Cobb's  $POD(a)$  Curve. Cobb generally follows the methods described in MIL-HDBK-1823 to build  $POD(a)$  curves for the ultrasonic crack detection tech-



nique based on experimental data. But unlike the MIL-HDBK-1823 example, or the PZT cyclic strain experiment, the response variable used by Cobb is not the direct energy reading at the receiving transducer, but a ratio of the energy received at a given time to a baseline energy reading taken at an initial “healthy” condition (see [79]). This energy ratio ( $ER$ ) has the following form:

$$ER = \frac{\text{Energy Received at the “Catch” Transducer}}{\text{Baseline “Healthy” Energy Reading}} \quad (5.7)$$

The  $ER$  ranges from zero to one, and changes in  $ER$  have been shown through testing to relate to fastener hole cracks growing in the directions shown in Figure 5.32 [26, 79, 80]. But Cobb found that plotting the natural log of  $ER$  against the natural log crack size did not meet the requirements to build a  $POD(a)$  curve using the MIL-HDBK-1823  $POD(a)$  technique. Specifically,  $\ln(a)$  vs.  $\ln(ER)$  did not produce a linear  $\ln(a)$  vs.  $\ln(\hat{a})$  relation with normally distributed residuals having constant variance [27]. Cobb instead found  $\log_{10}(a)$  vs.  $\log_{10}(1-ER)$  meets the requirement, and used this formulation as the  $\ln(a)$  vs.  $\ln(\hat{a})$  relation to build the  $POD(a)$  curve. This change will also affect the implementation of the  $POD(a)$  degradation model as will be shown in section 5.7.4.

Cobb’s final regression equation has the form:

$$\log_{10}(1 - ER) = \beta_0 + \beta_1 * \log_{10}(CrackDepth) + \varepsilon \quad (5.8)$$

Incorporating Cobb’s changes into the  $POD(a)$  formula given in MIL-HDBK-1823 gives the form of the  $POD(a)$  equation for the ultrasonic crack detection technique:

$$POD(a) = P(\hat{a} > \hat{a}_{th}) = \Phi \left( \frac{\beta_0 + \beta_1 * \log_{10}(a) - \log_{10}(\hat{a}_{th})}{\delta} \right) \quad (5.9)$$

The coefficients  $\beta_0$  and  $\beta_1$  derive from the regression equation 5.8, and  $\delta$  is the standard deviation of the regression residuals as explained in MIL-HDBK-1823 and section 5.2. Cobb builds  $POD(a)$  curves using several threshold detection values ( $\hat{a}_{th}$ ), with threshold  $ER$  values ranging from 0.03 to 0.12. Cobb found results similar to those in section 5.5.3, where increasing  $\hat{a}_{th}$  shifted the  $POD(a)$  curve to the right, reducing  $POD(a)$  for all crack sizes. The threshold  $ER$  value of 0.03 will be used for all of the following calculations since it represents the highest probability of detection for all crack sizes. Figures 5.33 and 5.34 recreate Cobb's regression calculation and  $POD(a)$  curve using the data listed in Table 5.11.

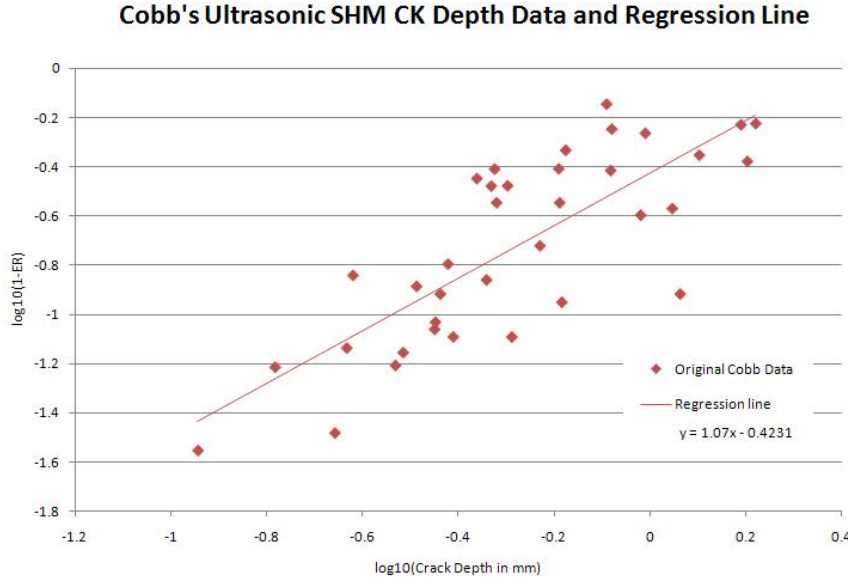


Figure 5.33: Recreation of Cobb's regression line using data from [27]

*5.7.3 Building a ROC Curve With Cobb's Data.* As described in section 5.3, ROC curves provide a conceptually simple technique for showing the trade-off between false alarm rates and the probability of detection for a sensor system by varying the threshold detection level and plotting the resulting FAR vs. POD values.

Of the three pieces of information needed to build a ROC curve for the ultrasonic SHM technique (probability density function of the system response values for a given crack size; system response threshold detection level; and probability density

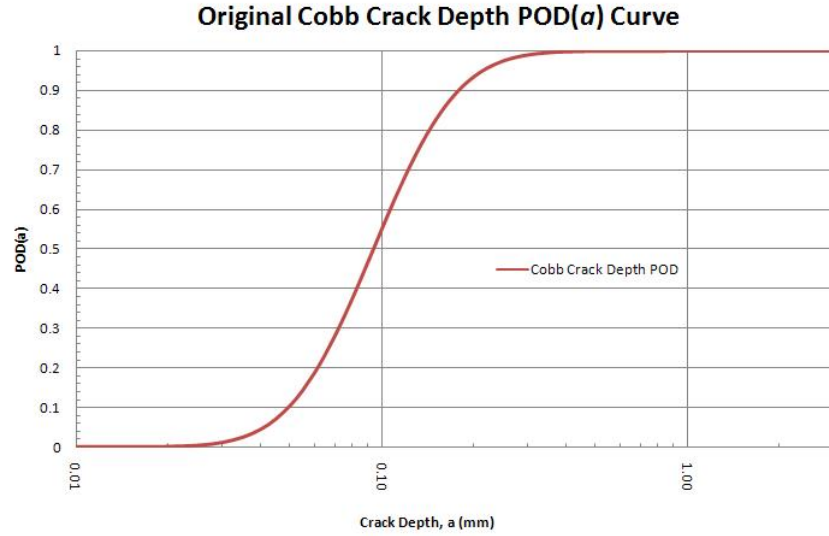


Figure 5.34: Recreation of Cobb's  $POD(a)$  curve using data from [27]

function of the system response values in an undamaged condition), one piece, the undamaged system response probability density function, cannot be directly derived from the data given by Cobb. Cobb gives a value for the standard deviation for system responses in an undamaged condition (0.01 in [27]) but does not give the distribution of the responses. For the purpose of the following calculations, the system response distribution with no damage is assumed to be normally distributed around 1 ( $ER$  for the undamaged condition = 1) with a standard deviation of 0.01. This assumption is justified for two reasons:

1. Damaged responses are assumed to be normally distributed around the regression line, as described by equation 5.4. It follows that undamaged responses are also normally distributed around the nominal value of 1
2. Other potential system response distributions (lognormal, Weibull) require a shape parameter to be specified, which greatly effects the form of the distribution. There is no information in any of Cobb's research to identify a potential shape parameter, and an error in defining a potential shape parameter would cause wide variations in subsequent calculations

Figure 5.35 shows a notional ROC curve based on data from [27] and the assumptions listed above. The original  $a_{50}$  crack depth of 0.095 mm was used while sweeping the threshold detection level from 0.001 to 0.2.

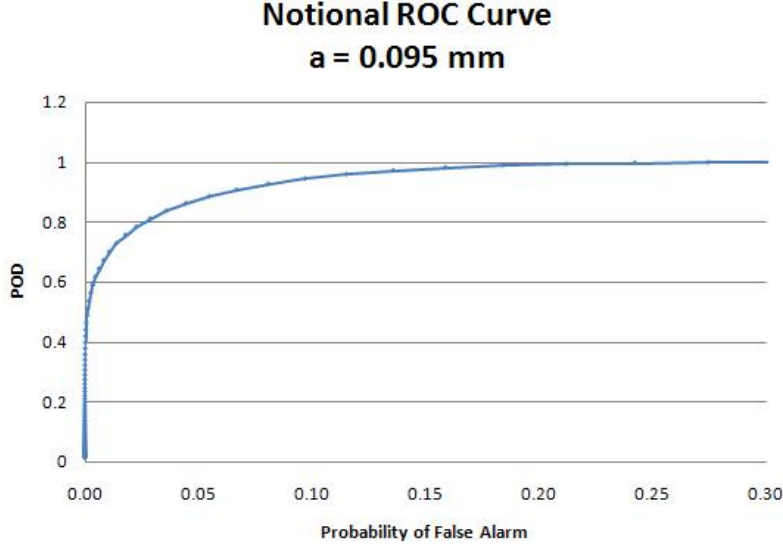


Figure 5.35: ROC Curve Derived from Cobb's Data

*5.7.4 The Effects of Sensor Degradation.* Assuming sensor degradation can occur in Cobb's ultrasonic sensor configuration, the question becomes how will the degradation affect  $POD(a)$  and how can the  $POD(a)$  degradation model account for these changes? Given Cobb's original energy ratio (equation 5.10), degradation of the sensor will cause changes in the numerator of the  $ER$  without a corresponding crack in the structure. This degraded  $ER$  (termed  $ER_D$  for this analysis) is assumed to have the following form:

$$ER_D = \frac{\text{Degradation Factor} * \text{Expected Energy Received at the Catch Transducer}}{\text{Baseline "Healthy" Energy Reading}} \quad (5.10)$$

where *expected* energy at the receiving transducer is the value obtained by Cobb's original ultrasonic testing. But changing the  $ER$  in  $POD(a)$  calculation has a different effect than the simple regression line translation shown in sections 5.5.1 and 5.6. Since the  $ER$  ranges from 0 to 1, and since  $1 - ER$  is the variable used to determine the regression line, changing  $ER$  changes the slope, intercept and residuals of the regression line.

As an example of the changes that can occur to Cobb's  $POD(a)$  curve due to sensor degradation, Figures 5.36 and 5.37 use the sensor degradation equation 4.4 to show the potential changes in Cobb's calculations due to sensor degradation. Degrading Cobb's  $ER$  to a point corresponding to 150,000 cycles at  $1700 \mu\epsilon$ , the crack depth detected 50% of the time increases from 0.095 to 0.215mm, or 126%.

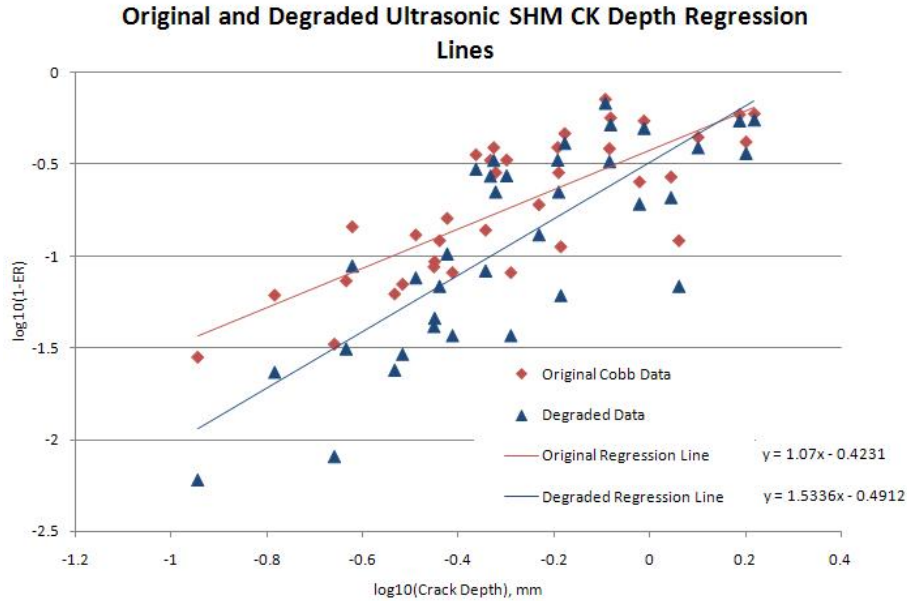


Figure 5.36: Degrading Cobb's regression line by changing  $ER$  per equation 4.4

The changes to the  $POD(a)$  curve also affect the ROC curve. Figure 5.38 shows the original and degraded ROC curves using  $a_{50} = 0.095$  mm as the crack depth.

Using the maximum false alarm rate of 5% as specified in MIL-HDBK-1823, the original ROC curve shows the probability of detecting a 0.095 mm deep crack at 87% with a required threshold detection value of 0.016 mm. A 5% false alarm rate for the

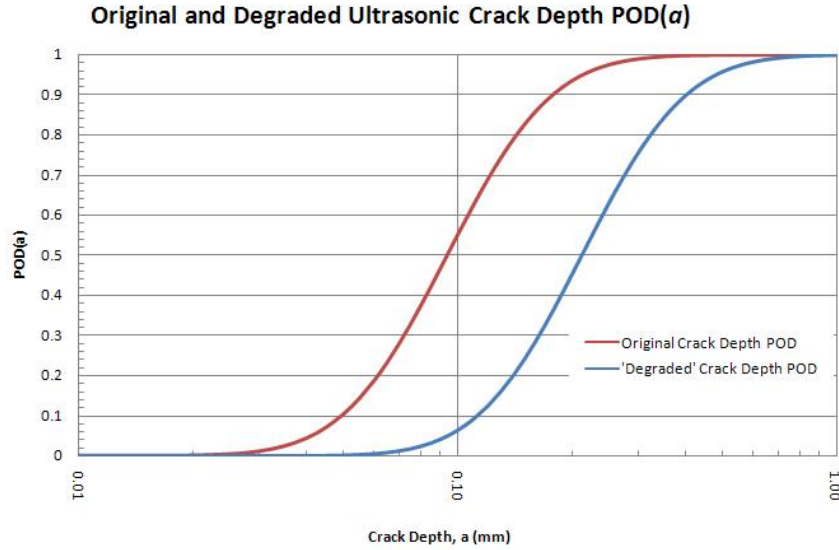


Figure 5.37: Degrading Cobb's  $POD(a)$  curve by changing  $ER$  per equation 4.4

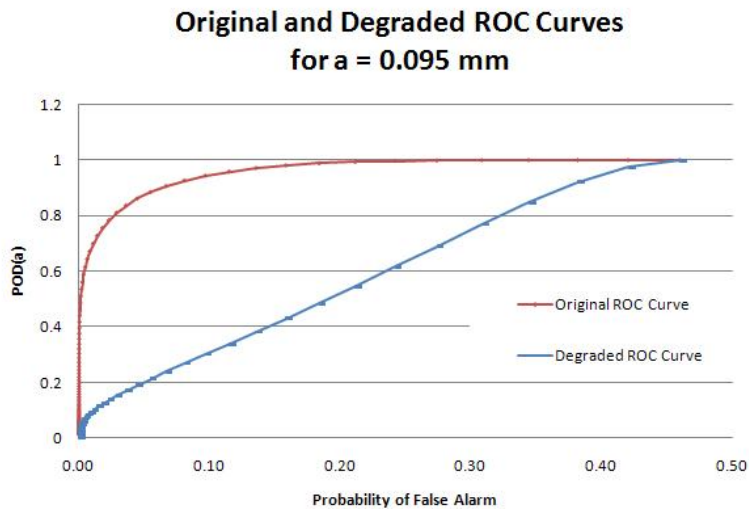


Figure 5.38: Degrading Cobb's ROC curve by changing  $ER$  per equation 4.4

degraded ROC curve lowers the probability of detecting a 0.095 mm deep crack to 20% using the same detection threshold value of 0.016 mm.

*5.7.5 Degradation Coefficients for Cobb's Data.* The  $POD(a)$  degradation model provides a method to define  $POD(a)$  over a range of cycles at a given strain

value. As described in section 5.7.4, the slope, intercept and residual standard deviation all change based on degraded values of  $ER$  in Cobb's sensor configuration. Given the  $POD(a)$  degradation model:

$$POD(a)_{Degraded} = \Phi \left( \frac{(\beta_0 * \alpha_d) + (\beta_1 * \gamma_d) * \ln(a) - \ln(\hat{a}_{th} * \rho_d)}{\delta * \psi_d} \right) \quad (5.11)$$

values for  $\alpha$ ,  $\gamma$  and  $\psi$  will all change based on degradation of Cobb's sensors. Figure 5.39 shows the degrading  $POD(a)$  curve based on numbers of cycles using the sensor degradation model derived from the cyclic strain experiment, equation 4.4.

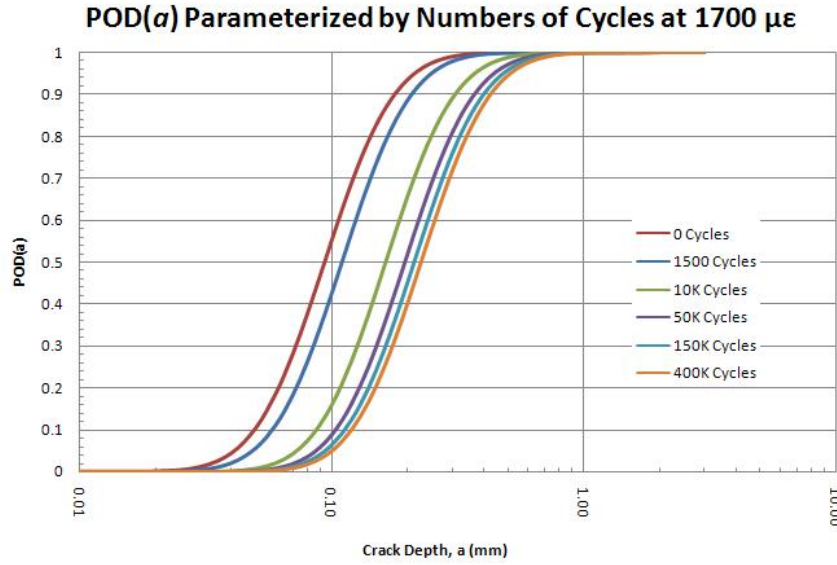


Figure 5.39:  $a_{50}$  increases From 0.095 mm to 0.225 mm after 400K cycles at 1700  $\mu\epsilon$

The corresponding changes in the ROC curve are also significant. Figure 5.40 shows the degrading ROC curve, based on a crack size of 0.095 mm. Probability of detecting this crack size with a 5% false alarm rate has decreased from 87.3% to 16.2% due to sensor degradation.

Table 5.12 shows the corresponding degradation coefficients for the  $POD(a)$  and ROC curves shown in Figures 5.39 and 5.40. These degradation coefficients can also

**ROC Curves at Various Numbers of Cycles at 1700  $\mu\epsilon$**

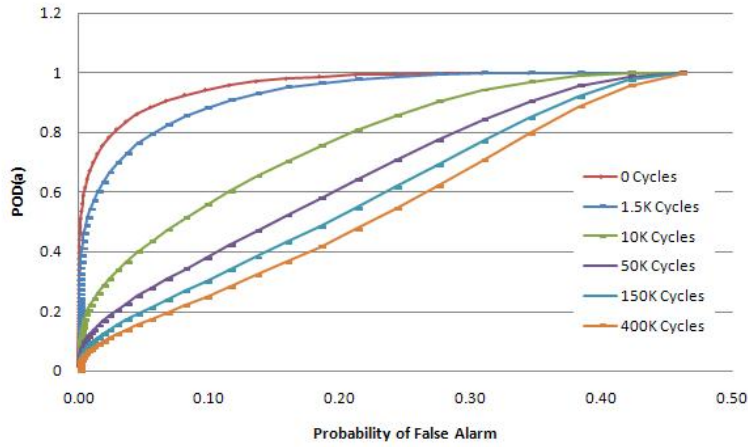


Figure 5.40: Probability of false alarm increases for all crack sizes after 400K cycles at 1700  $\mu\epsilon$

be used to generate a  $POD(a, n)$  surface based on crack size and number of cycles at a given strain level. Figure 5.41 shows a representative surface at 1700  $\mu\epsilon$ .

Table 5.12: Degradation coefficients used to show changes in Cobb's  $POD(a)$

Cycles @ 1700 $\mu\epsilon$	$\alpha_d$	$\gamma_d$	$\psi_d$
0K	1	1	1
1.5K	1.01	1.068	1.061
10K	1.073	1.272	1.256
50K	1.127	1.378	1.365
150K	1.161	1.433	1.421
400K	1.191	1.476	1.464

## 5.8 Summary

This chapter demonstrates a method of relating the changes in SHM sensor signal due to aircraft environmental factors to the capability of an SHM system through the use of a  $POD(a)$  degradation model. This model uses degradation coefficients to manipulate a given probability of detection formula to demonstrate the potential for



**POD as a Function of Crack Depth and Strain Cycles at  $1700\mu\epsilon$**

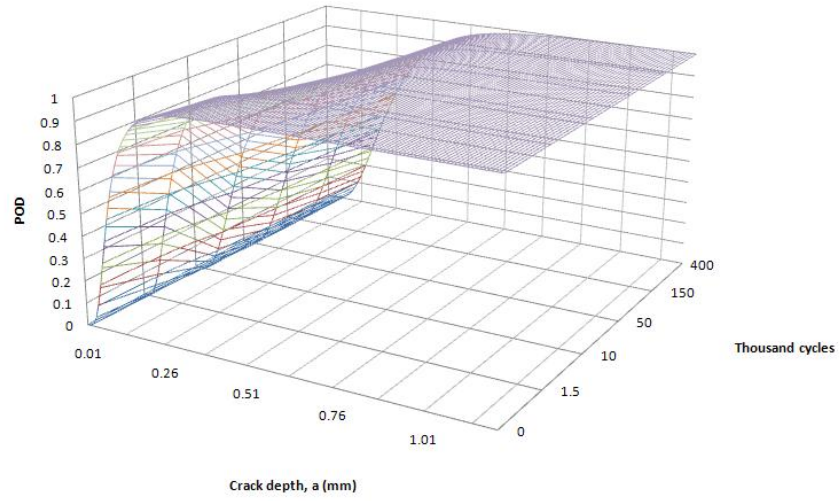


Figure 5.41: The  $POD(a, n)$  surface reflects changes in  $POD(a)$  after cycling at  $1700 \mu\epsilon$

reduced flaw detection capability due to the SHM sensor degradation demonstrated in Chapter IV.

## VI. Conclusions

### 6.1 Addressing the Research Objectives

Section 1.4 listed four research objectives to address two research hypotheses.

Objective 1: *What environmental conditions must a feasible SHM system withstand?* Figure 2.25 shows a cause and effect diagram addressing changes in SHM response due to environmental factors. The causes listed in the diagram were derived from various specifications used to test and qualify airborne equipment. Sections 4.4, 4.5 and 4.6 show that one of the environmental factors (cyclic strain) can affect the performance of PZT-based SHM sensors. Other research, as discussed in section 3.3.3, has shown that temperature fluctuations, humidity and outdoor exposure can also affect PZT performance.

Objective 2: *How can changes in SHM performance due to environmental factors be determined in a statistically significant manner?* Chapter III uses a design of experiments approach to test the effects of static and cyclic strain on the signal strength of pitch-catch PZT pairs. Definition of experimental and nuisance factors in section 3.6, and determination of hypotheses for testing and calculation of required sample sized in sections 3.9 and 3.10 show the elements required to build a statistically significant experiment to address changes in SHM sensor performance due to an aircraft environmental factor.

Objective 3: *How can changes in SHM performance due to aircraft environmental factors be modeled?* Section 4.8.1 shows that changes in PZT pitch-catch pair response due to cyclic strain can be estimated using a power equation model, with coefficients formed from the cyclic strain level and number of cycles. This model estimated the test results more accurately than linear, polynomial or log(cycles) models.

Objective 4: *Demonstrate how models that define changes in SHM performance due to environmental factors can be incorporated into existing SHM system performance calculations.* Sections 5.5 through 5.7 show that the models used to estimate changes in SHM sensor response due to environmental factors can be directly incor-

porated into traditional POD( $a$ ) models. By manipulating POD( $a$ ) coefficients based on the modeled changes in sensor signal, a measure of performance for a SHM system is defined based on both structural crack size and an environmental factor.

These four objectives derived from two baseline research hypotheses: 1) aircraft environmental factors will detrimentally impact the performance of a SHM system; and 2) SHM capability changes due to environmental factors can be identified and modeled, with changes in SHM performance estimated by modifying techniques used to characterize the performance of current non-destructive evaluation systems. Objective one provides evidence to answer hypothesis one in the affirmative, and Objectives two through four provide evidence to answer hypothesis two in the affirmative.

## **6.2 Conclusions Based on Experimental Results and Analysis**

Chapter IV provides data to support several specific conclusions concerning the effects of static and cyclic strain on the responses of PZT pitch-catch pairs.

Experimental Conclusion 1: *Static strain has an insignificant effect on PZT-based SHM sensors up to 3000  $\mu\epsilon$ .* Section 4.3 demonstrates that single cycle strains up to 3000  $\mu\epsilon$  did not have a statistically significant effect on the signal strength between PZTs glued to aluminum test specimens in a pitch-catch configuration.

Experimental Conclusion 2: *Cyclic strain can affect PZT-based SHM sensors depending on strain level and number of cycles.* Sections 4.4, 4.5 and 4.6 show that cyclic strain at 800  $\mu\epsilon$  did not have statistically significant effects on the signal strength between PZTs glued to aluminum test specimens in a pitch-catch configuration. Cyclic strain at 1700 and 2600  $\mu\epsilon$  did have statistically significant effects on the signal strength, demonstrating that cyclic strain effects need to be considered in the design of PZT-based SHM systems.

Experimental Conclusion 3: *Changing glue type from MBond 200 to a more compliant two-part epoxy did not prevent signal loss due to cyclic strain.* Although a difference in signal strength exists between pitch-catch PZT pairs using different glue

types, sections 4.3, 4.4, 4.5 and 4.6 all show a general similarity in how MBond and Epoxy pitch-catch pairs respond to the application of static and cyclic strain.

Experimental Conclusion 4: *Evidence exists that the cyclic strain effects on PZT-based SHM sensors does not continue after a certain number of cycles.* The general leveling of the signal response shown in sections 4.5 and 4.6 indicate changes in response due to cyclic strain may cease after a “break-in” period. Mixed statistical test results prevent the identification of the number of cycles at which the effect ends, but some statistical data exists that it may be as late as 420K cycles at 1700  $\mu\epsilon$  and as early as 120K cycles at 2600  $\mu\epsilon$ .

Experimental Conclusion 5: *Small degradation in SHM sensor signal can result in large changes in flaw detection capability.* Sections 5.5.1 and 5.5.2 show that a 5% change in a POD( $a$ ) model coefficient for a SHM system due to environmental factors can result in an approximate 30% increase in the crack length detected 90% of the time.

### **6.3 General Conclusions**

Several general conclusions can be supported by completed research.

General Conclusion 1: *SHM crack length detection requirements can be scoped based on airframe critical crack lengths and standard repair practices.* Comparing the minimum critical crack lengths in Tables 2.3 and 2.4 to oversize fastener hole diameters in Table 2.5, shows that two distinct levels of crack length detection requirements exist based on the desired SHM system requirements. SHM crack detection requirements based on detecting cracks before reaching a length where relatively minor repairs can no longer be accomplished (oversizing of fastener holes in this case) gives a reliable crack detection length requirement of 0.0155 inches. If the crack length detection requirements are relaxed to reflect reliable crack detection at one-half critical crack size, an analysis of critical crack lengths in the C-130 and F-15 shows the required detection crack sizes can increase by over an order of magnitude.

General Conclusion 2: *Current methods to determine structural inspection intervals and NDE inspection capabilities provide a path for implementation of SHM.* The Aircraft Structural Integrity Program and NDE reliability analysis techniques have addressed and continue to address several issues of interest in the SHM community. Using these established programs as a starting point for SHM implementation allows a common frame of reference,  $POD(a)$ , to compare traditional inspection capabilities to proposed SHM capabilities.

General Conclusion 3: *Time, or some proxy representing time installed on an aircraft, must be a factor when determining SHM capability.* The promise of SHM fundamentally changing the way structural inspections are performed comes at the cost of installing and maintaining a new aircraft system. This research shows that promises of SHM system capability made at the time of installation may not be achievable after an extended time installed in the aircraft environment.

#### **6.4 Recommendations for Application**

Application 1: *Use the  $POD(a)$  degradation model to determine the impacts of environmental effects after  $POD(a)$  has been established for a given SHM technology.* The design of experiments approach and method to determine the impacts of changes in SHM performance can be applied to a wide range of SHM technologies, not just the PZT-based system demonstrated in this research.

Application 2: *Use the  $POD(a)$  degradation model to lay the groundwork for a common method to establish a performance baseline between SHM systems over the remaining life of an aircraft.* By building this baseline, the relative merits of several SHM proposals can be evaluated and better implementation decisions can be made.

Application 3: *Use the  $POD(a)$  degradation model to determine when the performance of an SHM system no longer meets requirements and must be repaired.* This knowledge is critical to the life-cycle cost benefit analyses needed to justify SHM in-

stallation on aircraft, as any time and effort spent repairing SHM system components reduces cost savings assumed from performing fewer manual inspections.

### ***6.5 Recommended Questions for Future Research***

Question 1: *How do combined environmental effects impact SHM performance?*

One key aspect for investigation of the impacts of aircraft environmental factors on SHM performance is the combined impact of multiple simultaneous environmental factors. Experiments, including the testing conducted for this research, normally focus on one aspect of the aircraft environment and seek to control or limit the impact of other environmental factors during testing. But combined effects must now be determined. Are thermal cycling effects and cyclic strain effects additive? How does extended exposure to a corrosive environment impact a sensors ability to resist electromagnetic interference from other aircraft components? Combined effects research is critical to the adaptation and implementation of SHM systems on legacy aircraft.

Question 2: *How does random cyclic strain affect SHM sensor capabilities?* The experiment conducted as part of this research applied cyclic strains at three given strain levels. Further experimentation should be accomplished to determine if the baseline results and models discussed in Chapter IV can be applied or modified for use given random cyclic strain levels.

Question 3: *How can MIL-STD-1530 be revised to include SHM?* The US Air Force has relied on the Aircraft Structural Integrity Program, currently codified in MIL-STD-1530, for nearly 50 years. The current MIL-STD provides an established and well known vehicle to address SHM certification issues from the USAF perspective. Specifically, research should be conducted to add to section 5.4, Certification & Force Management Development. SHM system analysis requirements should be established and guidance given concerning the application of SHM to the different types of structural components defined in the standard.

Question 4: *How can SHM performance be incorporated into Aircraft Structural Risk Assessments?* Aircraft structural risk assessments (as described by Berens, Hovey, et al. [10, 82]) base the risk of structural failure for an aircraft within a fleet on initial crack size probability distributions, crack growth probability distributions, aircraft usage severity distributions, and probabilities of crack detection at inspection. If SHM is implemented on legacy airframes to detect crack initiation and growth, the structural risk assessment must now include a term accounting for the reliability and capability of the SHM system. And as shown by this research, the capability of an SHM system may change over an extended period of time in the aircraft environment.

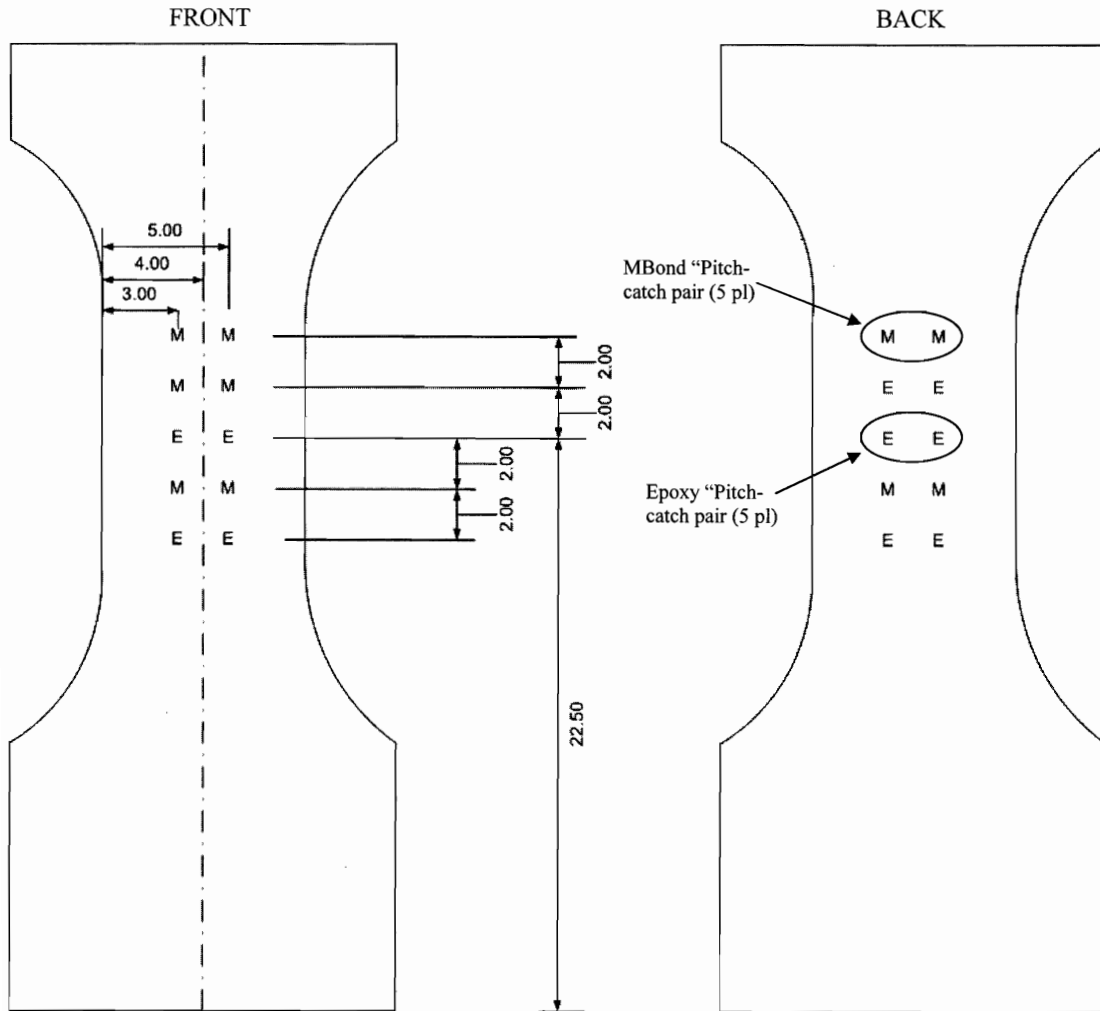
Question 5: *How should manual inspections be combined with SHM?* Envisioning the methods the USAF can use to inspect aircraft structure as a continuum, with all inspections done manually on one extreme and all inspections done using technology on the other, it is evident that a large number of researchers believe the USAF's current reliance on manual structural inspections does not place it at the optimum location on the inspection-type continuum. But given an overall structural inspection cost and a set of inspection requirements, where is the optimum location on the inspection type continuum? What are the primary parameters to determine the mix of manual and technology-based inspections?

## *Appendix A. PZT Installation Instructions*



1. GENERAL INFORMATION: The test specimens fabricated using these instructions will be used to test the ability of aircraft Structural Health Monitoring (SHM) sensors glued to aircraft structure to withstand cyclic straining of the mounting surface. PZT disks are the sensors under test, and two different glue types (MBond 200 and 2 part epoxy) will be compared. Sensors are installed in "pitch-catch pairs" with one PZT sending out an excitation signal and a designated PZT receiving the signal after it passes across the test specimen.

2. SPECIMEN LAYOUT: The specimen is a 1/8" thick, 6061-T6 aluminum dogbone with 10 pitch-catch pairs (5 MBond and 5 Epoxy pairs) glued to the surface. Pitch-catch pairs are placed on the front and the back of the specimen in a specific configuration to allow waveform analysis during data post-processing. The specimen layout:

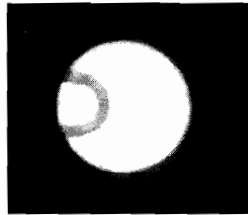


## DRAWING NOTES:

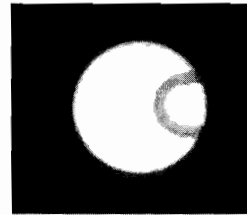
1. All dimensions in centimeters
2. 'M' indicates the installation location of a PZT glued with MBond, 'E' with Epoxy
3. PZT pairs installed on the back are directly opposite those on the front
4. One PZT pair (second from the top) has different glue types for the PZTs installed on the front and on the back (MBond front, Epoxy back). All others have the same glue type on front and back

3. PZT NSTALLATION: PZTs are glued to the specimen in a specific orientation using modified strain gage installation procedures found in Measurements Group Bulletin 309, Student Manual for Strain Gage Technology.

a. PZT INSTALATION ORIENTATION: Since PZT orientation on the specimen can affect signal transmission and reception, the PZTs must be oriented with the small lead facing the near edge of the specimen as shown below



Left Side PZTs



Right Side PZTs

b. INSTALLATION INSTRUCTIONS: The installation setps in the left column below are the original steps contained in Bulletin 309 to install strain gages using MBond 200 adhesive. The right column contains procedure modifications to install PZTs with MBond and with 2 part Epoxy.

#### Original Instuctions

### 3.0 Surface Preparation

Strain gages can be bonded satisfactorily to almost any solid material if the material surface is properly prepared. While there are many surface preparation techniques available, the specific procedures and techniques described here are a carefully developed and thoroughly proven system. They are ideal for both M-Bond 200 and M-Bond AE-10 strain gage adhesives.

The purpose of surface preparation is to develop a chemically clean surface having a roughness appropriate to the gage installation requirements, a surface alkalinity of the correct pH, and visible gage layout lines for locating and orienting the strain gage. The Micro-Measurements system of surface preparation will accomplish these objectives for wrought aluminum and steels in five basic operations:

- Solvent degreasing
- Surface abrading
- Application of gage layout lines
- Surface conditioning
- Neutralizing

To ensure maximum cleanliness and best results, the following should be avoided in all steps:

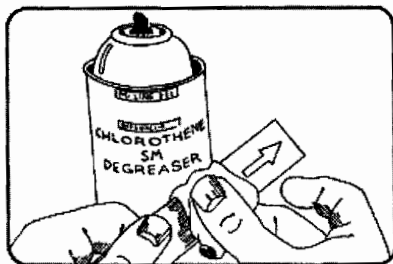
- Touching the surface with the fingers
- Wiping back and forth or reusing swabs or sponges
- Dragging contaminants into the cleaned area from the uncleaned boundary of that area
- Allowing a cleaning solution to evaporate on the surface
- Allowing partially prepared surface to sit between steps in the preparation process or a prepared surface to sit before bonding

Consult Instruction Bulletin B-129 for other test materials and for special precautions and considerations for surface preparation.

#### Instruction Modifications

No Changes

### 3.1 Solvent Degreasing

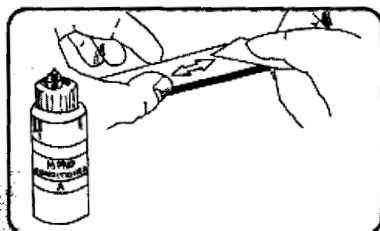


Degreasing is performed to remove oils, greases, organic contaminants, and soluble chemical residues. Degreasing should *always* be the first operation.

Degreasing can be accomplished using a solvent such as Chlorothene SM<sup>®</sup>. Spray applicators are preferred to avoid back-contamination of the parent solvent. Use a clean gauze sponge to clean the entire specimen, if possible, or an area covering 4 to 6 in (100 to 150 mm) on all sides of the gage location.

### 3.2 Surface Abrading

The surface is abraded to remove any loosely bonded adherents (scale, rust, paint, coatings, oxides, etc.), and to develop a surface texture suitable for bonding. For rough or coarse surfaces it may be necessary to start with a grinder, disc sander, or file, but for most specimens a suitable surface may be produced with only silicon-carbide paper of the appropriate grit.



Place a liberal amount of M-Prep Conditioner A in the gaging area and wet-tap with clean 320-grit silicon-carbide paper for aluminum, or 220-grit for steel. Add Conditioner A as necessary to keep the surface wet during the tapping process.

When a bright surface is produced, wipe the surface dry with a clean gauze sponge. A clean surface of the gauze should be used with each wiping stroke. A sufficiently large area should be cleaned to ensure that contaminants will not be dragged back into the gaging area during the steps to follow.

Repeat the above step, using 400-grit silicon-carbide paper for aluminum, or 320-grit for steel.

Degrease using a clean QTip soaked with Isopropyl Alcohol. Discard QTip after a single use

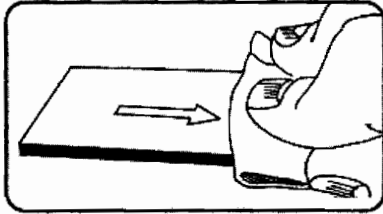
**MBond PZT Installation:** No change

**Epoxy PZT Installation:** Substitute Isopropyl Alcohol for M-Prep Conditioner A

### 3.3 Layout Lines

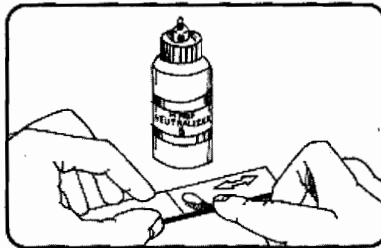
The desired location and orientation of the strain gage on the test surface should be marked with a pair of crossed-perpendicular reference lines. The reference or layout lines should be *burnished*, rather than scored or scribed, on the surface. For aluminum, a medium-hard drafting pencil is satisfactory. For most steels, a ball-point pen or a tampered pin rod may be used. All residue from the burnishing operations should be removed in the following step.

### 3.4 Surface Conditioning



After the layout lines are marked, Conditioner A should be applied repeatedly, and the surface scrubbed with cotton-tipped applicators until a clean tip is no longer discolored by scrubbing. The surface should be kept constantly wet with Conditioner A until the cleaning is completed. When clean, the surface should be dried by wiping through the cleaned area with a *single* slow stroke of a gauze sponge. The stroke should begin inside the cleaned area to avoid dragging contaminants in from the surrounding area. Throw the used gauze away, and with a fresh gauze, make a *single* slow stroke in the opposite direction. Throw the second gauze away.

### 3.5 Neutralizing



To provide optimum alkalinity for Micro-Measurements strain gage adhesives, the cleaned surfaces must be neutralized. This may be done by applying M-Prep Neutralizer 5 liberally to the cleaned surface, and scrubbing the surface with a clean cotton-tipped applicator. The cleaned surface should be kept completely wet with Neutralizer 5 throughout this operation. When neutralized, the surface should be dried by wiping through the cleaned area with a *single* slow stroke of a clean gauze sponge. Throw the gauze away and with another fresh gauze sponge, make a *single* stroke in the opposite direction. Always begin within the cleaned area to avoid recontamination from the uncleaned boundary.

If the foregoing instructions have been followed precisely, the surface is now properly prepared for gage bonding. The gages should be installed within 30 minutes on aluminum or 45 minutes on steel.

No changes, use a medium-hard drafting pencil to mark specimen

MBond PZT Installation: No change

Epoxy PZT Installation: Substitute Isopropyl Alcohol for M-Prep Conditioner A

MBond PZT Installation: No change

Epoxy PZT Installation: Delete step

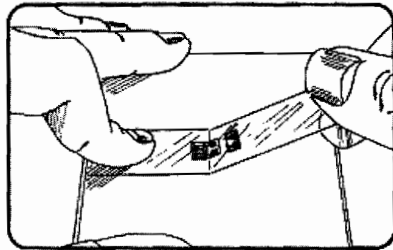
## 4.0 Strain Gage Bonding

The electrical resistance strain gage is capable of making accurate and sensitive indications of strains on the surface of the test part. Its performance is absolutely dependent on the bond between itself and the test part. The procedures outlined below will help ensure satisfactory bonds when using M-Bond 200 or AE-10 Adhesives. While the steps may appear unduly elaborate, these techniques have been used repeatedly in strain gage installations which have yielded consistent and accurate results.

### 4.1 Handling and Preparation

Micro-Measurements strain gages are specially treated for optimum bond formation with all appropriate gage adhesives. No further cleaning is necessary if contamination of the prepared bonding surface is avoided during handling. (Should contamination occur, clean with a cotton swab moistened with a low residue solvent such as M-Line Neutralizer 5 or Isopropyl alcohol. Allow the gage to dry for several minutes before bonding.) Gages should never be touched with the hands.

Remove the strain gage from its acetate envelope by grasping the edge of the gage backing with tweezers, and place on a chemically clean glass plate (or empty gage box) with the bonding side of the gage down. Place the appropriate terminals (if any) next to the strain gage solder tabs, leaving a space of approximately 1/16 in (1.5 mm) between the gage backing and terminal.

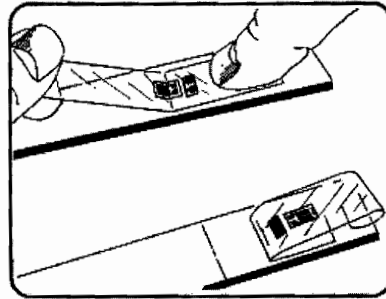
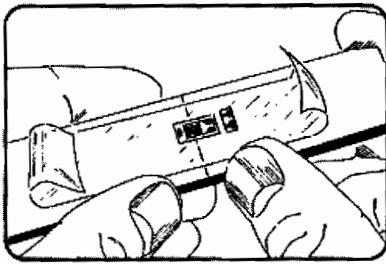


Using a 4 to 6 in (100 to 150 mm) length of M-Line PCT-2 cellophane tape, anchor one end of the tape to the glass plate behind the gage and terminal. Wipe the tape firmly down over the gage and terminals. Pick the gage and terminals up by carefully lifting the tape at a shallow angle (30 to 45 degrees) until the tape comes free with the gage and terminal attached. (The shallow angle is important to avoid over-stressing the gage and causing permanent resistance changes.) Caution: Some tapes may contaminate the bonding surface or react with the bonding adhesive. Use only tapes certified for strain gage installations.

The strain gage is now prepared for positioning on the test specimen. Position the gage/tape assembly so the triangle alignment marks on the gage are over the layout lines on the specimen. Holding the tape at a shallow angle, wipe the assembly onto the specimen surface. If the assembly is misaligned, lift the tape again at a shallow angle until the assembly is free of the specimen. Reposition and wipe the assembly again with a shallow angle.

**MBond PZT Installation:** No changes, substitute 'PZT' for 'gage' in the instructions. NOTE: Orient PZT so the small lead faces the near edge of the specimen as shown in paragraph 3a

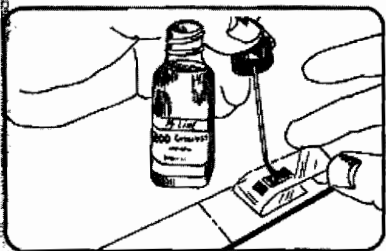
**Epoxy PZT Installation:** Both PZTs in an Epoxy pitch-catch pair must be installed simultaneously to prevent different levels of Epoxy curing at the time of installation. Position both PZTs with the small lead facing the near edge of the specimen prior to proceeding to step 4.2



In preparation for applying the adhesive, lift the end of the tape opposite the solder tabs at a shallow angle until the gage and terminal are free of the specimen. Tack the loose end of the tape under and press to the surface so the gage lies flat with the bonding side exposed.

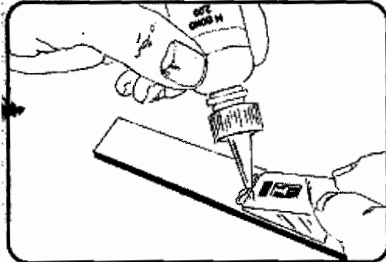
The appropriate adhesive may now be applied. The procedures for M-Bond 200 and M-Bond AE-10 are described in the two sections which follow.

#### **4.2 Bonding with M-Bond 200**



M-Bond 200 catalyst should be applied sparingly in a thin uniform coat. Wipe the brush against the lip of the bottle approximately ten times to remove most of the catalyst. Set the brush down on the gage and swab the gage backing by sliding — not brushing in the painting style — the brush over the entire gage surface. Move the brush to an adjacent tape area prior to lifting from the surface. Allow the catalyst to dry at least one minute under normal ambient laboratory conditions.

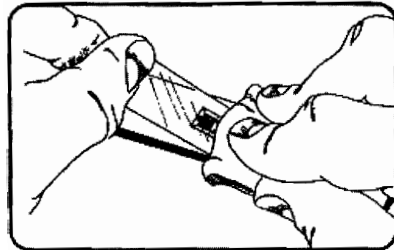
*The next three steps must be completed in sequence within three to five seconds. Read these steps before proceeding.*



Lift the tucked-under tape. Holding the gage/tape assembly in a fixed position, apply one or two drops of M-Bond 200 adhesive at the junction of the tape and specimen surface, about 1/2 in (13 mm) outside the actual gage installation area.

*Immediately rotate the tape to approximately a 30-degree angle so that the gage is bridged over the installation area.*

Holding the tape slightly taut and beginning from the tab end of the gage, slowly and *firmly* make a single wiping stroke over the gage/tape assembly with a clean gauze sponge to bring the gage back down over the alignment marks on the specimen. Release the tape.

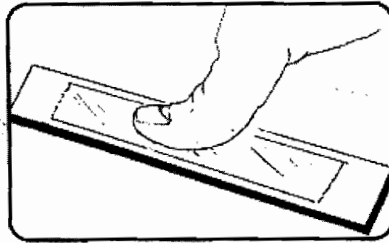


**MBond PZT Installation:** No changes

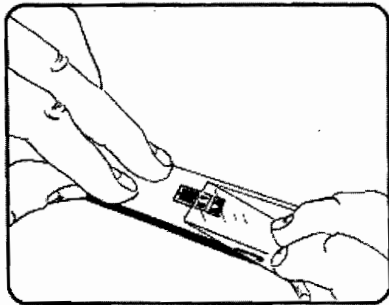
#### **Epoxy PZT Installation:**

1. Substitute Isopropyl Alcohol for M-Bond 200 catalyst
2. Prepare the 2 part epoxy by mixing equal portions of 2 part epoxy in a mixing tray
3. Using a toothpick or the opposite end of a QTip, spread a thin layer of epoxy on both PZTs. NOTE: Avoid air bubbles in the PZT epoxy layer
4. Rotate tape and place both PZTs in contact with the specimen surface. Apply thumb pressure per the strain gage instructions.
5. Do not remove tape until 24 hours after installation to allow full epoxy cure

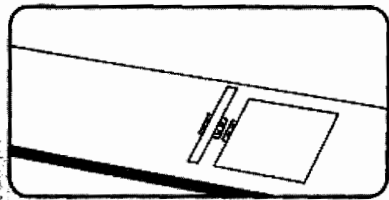
Immediately upon completion of the above step, *discard the gauze* and apply firm thumb pressure to the gage and terminal area. This pressure should be held for at least one minute. Wait two minutes before the next step (tape removal).



The gage and terminals should now be bonded to the specimen. To remove the tape, pull it back directly over itself, *peeling* it slowly and steadily off the surface.



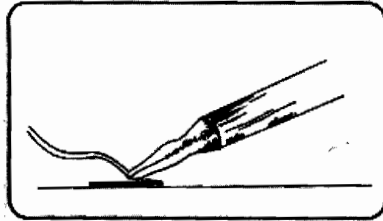
## 5.0 Soldering Techniques





If the strain gage is without encapsulation or pre-attached lead ribbons mask the gage grid area with drafting tape, leaving only the tabs exposed.

After the soldering iron has reached operating temperature, clean the tip with a gauze sponge and tin it with fresh solder. Tin the gage tabs and terminal tabs (if used). Melt a small amount of solder on the tip of the soldering iron, lay the rosin-core solder wire across the gage tab or copper terminal. Firmly apply the iron tip for one second, then *simultaneously* lift both solder and tip. A bright, shiny, even mound of solder should have been deposited on the tab. If not, repeat the process. If spikes are formed rather than smooth beads, it is a sign of inadequate flux, dwelling too long with the iron, and/or an improper iron temperature. Feeding the cored solder into the tab area during heat application will increase the amount of flux available.

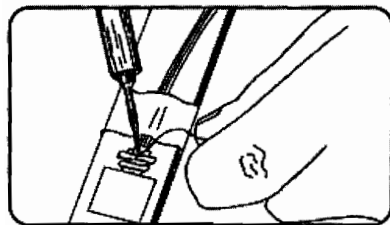


For a three-conductor lead-in wire, separate the individual leads for 3/4 in (20 mm). Strip away 1/2 in (13 mm) of insulation by using the soldering tip to melt the insulation on both sides of each end of the wire 1/2 in (13 mm) from the ends and quickly pulling off the insulation. Warning: Do not use a knife or other blade to cut the insulation. When the main leadwire is stranded and terminal strips are used, it is often convenient to cut all strands but one to fit the size of the copper pad. The long strand can then be used as the jumper wire. Soldering is made considerably easier by this method.

Holding the tip of a finger on the tip of the tinned wire for safety, cut each wire with diagonal wire cutters leaving 1/8 in (3 mm) of exposed, tinned wire.

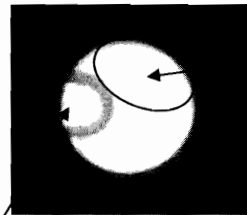
Tack the lead-in wires to the specimen with drafting tape so the tinned end of the wire is spring-loaded in contact with the solder bead. Complete the solder connection as before by applying solder and iron tip for one second and removing simultaneously.

Apply rosin solvent liberally to the solder joints. Drafting tape may be removed by loosening the mastic with rosin solvent. Remove all solvent with a gauze sponge, using a dabbing action. Repeat.



#### Notes:

- 1) Brush a layer of M-Flux soldering flux over the PZT prior to soldering
- 2) Solder approximately 5 ft of strain gage wire to each PZT
- 3) Solder the black strain gage wire to the "small" PZT lead
- 4) Solder the red strain gage wire to the upper half of the "large" PZT lead. See photo below.



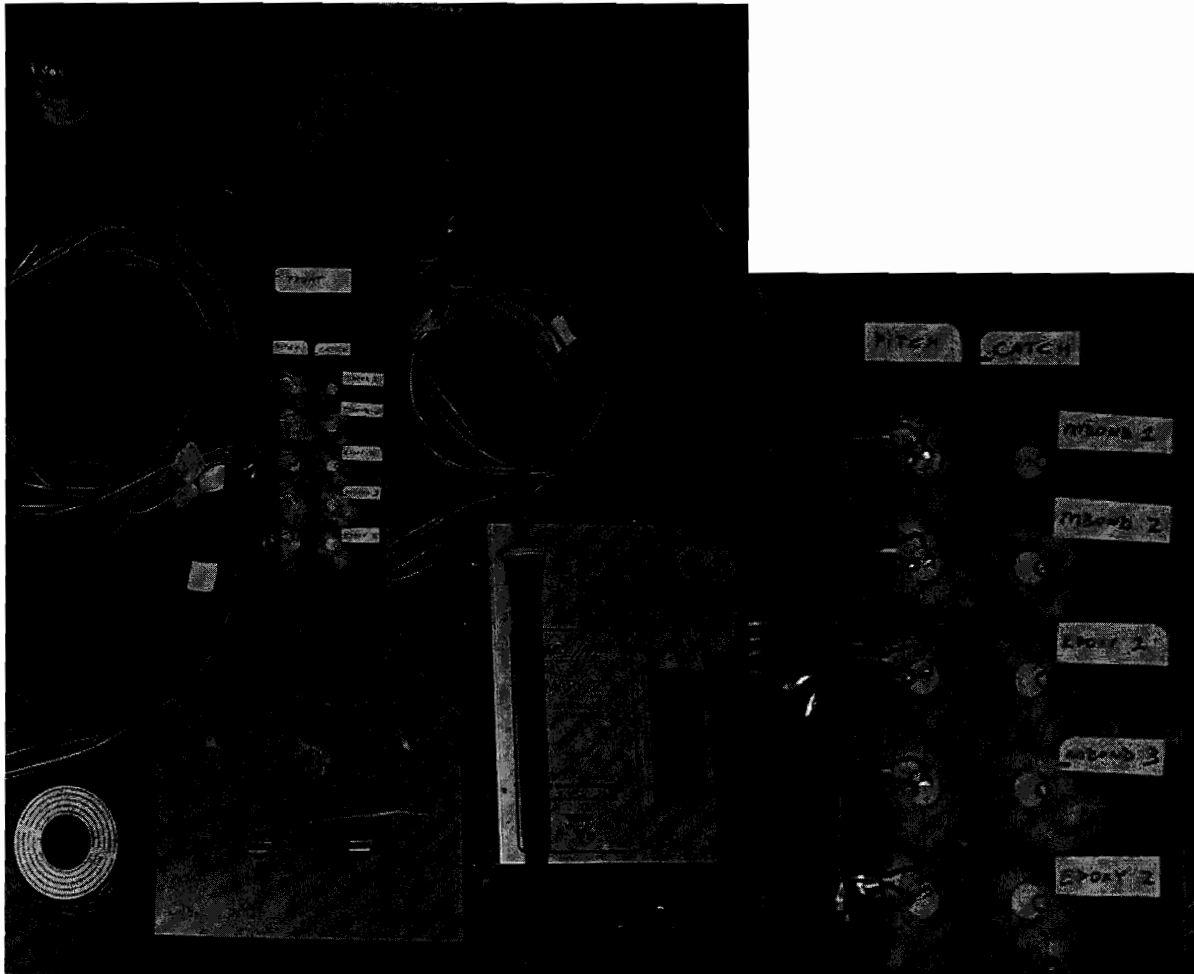
Solder red wire to the upper half of the large PZT lead

Solder black wire to the small PZT lead

Tape or otherwise secure the lead-in wires to the specimen to prevent the wires from being accidentally pulled from the tabs. A stress relief "loop" should be placed between the tape and the solder connections.

Apply a protective coating over the entire gage and terminal area. For most laboratory uses, M-Coat A will provide adequate long-term protection. The coating should be continuous up to and over at least the first 1/8 in (3 mm) of leadwire insulation.

Example of PZT soldering:



## *Appendix B. Representative Test Plan*

50% Cyclic Load Test Plan

Second Run

12-Nov-08

8-Jan-09

<u>Phase</u>	<u>Step</u>	<u>Completed</u>
1.0	Initial Set-up	
1.1	MTS	
1.1.1	Turn on hydraulics	
1.1.1.1	Turn Power supply 'On', push blue 'Reset' button, ensure red 'Emergency Stop' button is Out	<input type="checkbox"/>
1.1.1.2	Move three position switch to 'Start', release to 'Low Press', wait 3 sec	<input type="checkbox"/>
1.1.1.3	Move three position switch to 'High Press'	<input type="checkbox"/>
1.1.2	MTS Computer	
1.1.2.1	At Desktop, select 'Student' profile, 'MTS 793 Software' icon, 'Station Manager' icon, select 'Kuhn' config file and 'Kuhn2' paramter sets in the 'Open Station' window, select 'Open'	<input type="checkbox"/>
1.1.2.2	Select 'Meters' icon from MTS toolbar...move to lower right	<input type="checkbox"/>
1.1.2.2.1	Note 100 kip force reading on meter	<input type="checkbox"/>
1.1.2.3	Select 'Procedure Editor' from MPT toolbar...move to upper right	<input type="checkbox"/>
1.1.2.4	Select Interlock 1 'Reset'	<input type="checkbox"/>
1.1.2.5	Select 'Manual Command' icon from Station Controls toolbar	<input type="checkbox"/>
1.1.2.5.1	Select 'Enable Manual command'	<input type="checkbox"/>
1.1.2.6	Turn on Hydraulics with SW...at HSM1 prompt, select double then triple bar	<input type="checkbox"/>
1.1.2.6.1	In Manual Command window, put '0.0967' kip in the cmd window	<input type="checkbox"/>
1.1.2.6.2	Re-set strain gage and record initial value	<input type="checkbox"/>
1.1.2.6.3	De-select 'Enable Manual command'	<input type="checkbox"/>
1.1.2.7	Select 'New Specimen' from MPT toolbar	<input type="checkbox"/>
1.1.2.7.1	Ensure 'Procedure Name' lists '50Percent_Cyclic.000'	<input type="checkbox"/>
1.1.2.7.2	Change Specimen name to '50Percent_Cyclic'	<input type="checkbox"/>
1.1.2.8	Select 'Reset Procedure' icon from the MPT toolbar	<input type="checkbox"/>
1.1.2	Install specimen	
1.1.2.1	Access 'Station Manager' on control computer	
1.1.2.1.1	Select 'Displacement' control mode	<input type="checkbox"/>
1.1.2.1.2		<input type="checkbox"/>
1.1.2.2	All Grip Controls fully clockwise to the stops	<input type="checkbox"/>
1.1.2.2.1	#1 fully closed	<input type="checkbox"/>
1.1.2.2.2	#2 fully open	<input type="checkbox"/>
1.1.2.3	In 'Station Manager', move displacement to -3.0	<input type="checkbox"/>
1.1.2.4	Hold specimen in grips vertical and even on the top and	<input type="checkbox"/>
1.1.2.5	Turn #2 upper grip control CCW (closed) to tighten top grip	<input type="checkbox"/>
	- If the sample is not properly aligned:	
	- Turn #2 upper grip control CW (open)	
	- Turn #1 upper grip control CCW (open) to release pressure and open the grip	
	- Turn both fully CW and repeat (5)	
1.1.2.6	Place in 'Force' control mode in Station Manager , Manual Controls window, 'Manual Control' = 0.030 KIP	<input type="checkbox"/>
1.1.2.7	Turn #2 lower grip control dial CCW (closed)	<input type="checkbox"/>
1.2	Signal Generator	
1.2.1	Unhook excitation signal connector	<input type="checkbox"/>
1.2.2	Amplitude to 10 VPP	<input type="checkbox"/>
1.2.3	Shift, 'Arblist', dial to 'WAVE', 'Enter'	<input type="checkbox"/>
	NOTE: changes VPP to 9.648	
1.2.4	Shift, 'Burst' for inline waveform	<input type="checkbox"/>

1.2.5 Shift, 'Enter' for menu, Dial to 'A', down arrow to 'Commands', dial to '5-Burst Rate', down arrow, dial '10 Hz', 'Enter'

### 1.3 Labview

#### 1.3.1 Build 'Pitch-Catch' VI

##### 1.3.1.1 Increment to 10,000

##### 1.3.1.2 Set DAQ assistant for 'Pitch-Catch'

ai6 = Excitation 10 / -10 volts  
ai1 = Sensor1 100m / -100m volts  
ai2 = Sensor2 100m / -100m volts  
ai3 = Sensor5 100m / -100m volts  
ai4 = Sensor4 100m / -100m volts  
ai5 = Sensor5 100m / -100m volts

##### 1.3.1.3 Set initial file name

\\KuhnPhase2\XXov08\PC\CycleSet1\Sensor1\Set1\test.lvm

##### 1.3.1.4 Start and stop program to begin Function Gen control

##### 1.3.1.5 Save VI as '50PercentPC\_VI\_XXNov'

#### 1.3.2 Build 'Pulse-Echo' VI

##### 1.3.2.1 Increment to 10,000

##### 1.3.2.2 Set DAQ assistant for 'Pulse-Echo'

ai6 = Excitation 10 / -10 volts  
ai7 = Echo 100m / -100m volts  
ai1 = Opposite 100m / -100m volts

##### 1.3.2.3 Set initial file name

\\KuhnPhase2\XXNov08\PE\CycleSet1\PZT1\Set1\test.lvm

##### 1.3.2.4 Save VI as '50PercentPE\_VI\_2Oct'

### 2.0 Select 'Program Run' icon in MTS Station Manager

### 3.0 Take CycleSet1 (Baseline) Data

#### 3.1 Mbond 'Pitch Catch'

##### 3.1.1 Excite signal cable to Sensor1 Pitch

##### 3.1.2 Configure Cables for Mbond catch

ai1 cable to Sensor1 Catch  
ai2 cable to Sensor2 Catch  
ai3 cable to Sensor3 Catch  
ai4 cable to Sensor4 Catch  
ai5 cable to Sensor5 Catch

##### 3.1.3 Open VI '50PercentPC\_VI\_XXNov'

###### 3.1.3.1 Check Save 'Enabled'

##### 3.1.4 Check filename and DAQ Assistant configuration

per steps 1.3.1.2 and 1.3.1.3

##### 3.1.5 Take Mbond pitch-catch data

Filename change: \\KuhnPhase2\XXNov\PC\CycleSet1\Sensor1\Set1\test.lvm  
\\KuhnPhase2\XXNov\PC\CycleSet1\Sensor2\Set1\test.lvm

	Check prev data file	Change filename	Change Connector	Start data
Sensor1		Sensor1		PC
Sensor2		Sensor2		PC
Sensor3		Sensor3		PC
Sensor4		Sensor4		PC
Sensor5		Sensor5		PC

### 3.2 Epoxy 'Pitch Catch'

3.2.1 Excite signal cable to Sensor6 Pitch

3.2.2 Configure Cables for Epoxy catch

ai1 cable to Sensor6 Catch

ai2 cable to Sensor7 Catch

ai3 cable to Sensor8 Catch

ai4 cable to Sensor9 Catch

ai5 cable to Sensor10 Catch

3.2.3 Take Epoxy pitch-catch data

Filename change: \KuhnPhase2\XXNov\PC\CycleSet1\Sensor6\Set1\test.lvm

\KuhnPhase2\XXNov\PC\CycleSet1\Sensor7\Set1\test.lvm

	Check prev data file	Change filename	Change Connector	Start data
Sensor6		Sensor6		PC
Sensor7		Sensor7		PC
Sensor8		Sensor8		PC
Sensor9		Sensor9		PC
Sensor10		Sensor10		PC

3.2.4 Change filename to \KuhnPhase2\XXNov08\PC\CycleSet2\Sensor1\Set1\test.lvm

3.2.4.1 'CycleSet1' to 'CycleSet2'

3.2.4.2 'Sensor10' to 'Sensor1'

### 3.3 'Pulse-Echo'

3.3.1 Open VI '50PercentPE\_V\_XXNov'

3.3.1.1 Check Save 'Enabled'

3.3.2 Configure cables for Pulse-echo

- Excitation signal cable to splitter box 'Pulser'

- Splitter box 'Crystal' cable to PZT1

- ai1 cable to PZT4

3.3.3 Check filename and DAQ Assistant configuration

per steps 1.3.1.2 and 1.3.1.3

3.3.4 Take Pulse-Echo data

Filename change: \KuhnPhase2\XXNov\PE\CycleSet1\PZT1\Set1\test.lvm

\KuhnPhase2\XXNov\PE\CycleSet1\PZT2\Set1\test.lvm

	Check prev data file	Change filename	Change Connector		Start data
			ai7 (Echo)	ai1 (Opp)	
PZT1			PZT1	PZT4	PE
PZT2			PZT2	PZT13	PE
PZT3			PZT3	PZT5	PE
PZT4			PZT4	PZT1	PE
PZT5			PZT5	PZT3	PE
PZT6			PZT6	PZT9	PE
PZT7			PZT7	PZT18	PE
PZT8			PZT8	PZT10	PE
PZT9			PZT9	PZT6	PE
PZT10			PZT10	PZT8	PE
PZT11			PZT11	PZT14	PE
PZT12			PZT12	PZT15	PE
PZT13			PZT13	PZT2	PE
PZT14			PZT14	PZT11	PE

PZT15			PZT15	PZT12	PE
PZT16			PZT16	PZT19	PE
PZT17			PZT17	PZT20	PE
PZT18			PZT18	PZT7	PE
PZT19			PZT19	PZT16	PE
PZT20			PZT20	PZT17	PE

3.3.5 Change filename to \KuhnPhase2\XXNov08\PE\CycleSet2\PZT1\Set1\test.lvm

3.2.4.1 'CycleSet1' to 'CycleSet2'

3.2.4.2 'PZT20' to 'PZT1'


4.0 Select 'TakeData1' icon in station manager to cycle sample to CycleSet2 (30K cycles)

5.0 Take CycleSet2 Data

5.1 Mbond 'Pitch Catch'

5.1.1 Excite signal cable to Sensor1 Pitch

5.1.2 Configure Cables for Mbond catch

ai1 cable to Sensor1 Catch

ai2 cable to Sensor2 Catch

ai3 cable to Sensor3 Catch

ai4 cable to Sensor4 Catch

ai5 cable to Sensor5 Catch

5.1.3 Open VI '50PercentPC\_VI\_XXNov'

5.1.3.1 Check Save 'Enabled'

5.1.4 Check filename and DAQ Assistant configuration

per steps 1.3.1.2 and 1.3.1.3

5.1.5 Take Mbond pitch-catch data

Filename change: \KuhnPhase2\XXNov\PC\CycleSet2\Sensor1\Set1\test.lvm

\KuhnPhase2\XXNov\PC\CycleSet2\Sensor2\Set1\test.lvm


	Check prev data file	Change filename	Change Connector	Start data
Sensor1		Sensor1		PC
Sensor2		Sensor2		PC
Sensor3		Sensor3		PC
Sensor4		Sensor4		PC
Sensor5		Sensor5		PC

5.2 Epoxy 'Pitch Catch'

5.2.1 Excite signal cable to Sensor6 Pitch

5.2.2 Configure Cables for Epoxy catch

ai1 cable to Sensor6 Catch

ai2 cable to Sensor7 Catch

ai3 cable to Sensor8 Catch

ai4 cable to Sensor9 Catch

ai5 cable to Sensor10 Catch

5.2.3 Take Epoxy pitch-catch data

5.2.4 Filename change: \KuhnPhase2\XXNov\PC\CycleSet2\Sensor6\Set1\test.lvm

\KuhnPhase2\XXNov\PC\CycleSet2\Sensor7\Set1\test.lvm


	Check prev data file	Change filename	Change Connector	Start data
Sensor6		Sensor6		PC
Sensor7		Sensor7		PC

Sensor8	Sensor8	PC
Sensor9	Sensor9	PC
Sensor10	Sensor10	PC

5.2.4 Change filename to \KuhnPhase2\XXNov08\PC\CycleSet3\Sensor1\Set1\test.lvm

5.2.4.1 'CycleSet2' to 'CycleSet3'

5.2.4.2 'Sensor10' to 'Sensor1'

5.3 'Pulse-Echo'

5.3.1 Open VI '50PercentPE\_V\_XXNov'

5.3.1.1 Check Save 'Enabled'

5.3.2 Configure cables for Pulse-echo

- Excitation signal cable to splitter box 'Pulser'

- Splitter box 'Crystal' cable to PZT1

- ai1 cable to PZT4

5.3.3 Check filename and DAQ Assistant configuration

per steps 1.3.1.2 and 1.3.1.3

5.3.4 Take Pulse-Echo data

5.3.5 Filename change: \KuhnPhase2\XXNov\PE\CycleSet2\PZT1\Set1\test.lvm  
\KuhnPhase2\XXNov\PE\CycleSet2\PZT2\Set1\test.lvm

	Check prev data file	Change filename	Change Connector		Start data
			ai7 (Echo)	ai1 (Opp)	
PZT1			PZT1	PZT4	PE
PZT2			PZT2	PZT13	PE
PZT3			PZT3	PZT5	PE
PZT4			PZT4	PZT1	PE
PZT5			PZT5	PZT3	PE
PZT6			PZT6	PZT9	PE
PZT7			PZT7	PZT18	PE
PZT8			PZT8	PZT10	PE
PZT9			PZT9	PZT6	PE
PZT10			PZT10	PZT8	PE
PZT11			PZT11	PZT14	PE
PZT12			PZT12	PZT15	PE
PZT13			PZT13	PZT2	PE
PZT14			PZT14	PZT11	PE
PZT15			PZT15	PZT12	PE
PZT16			PZT16	PZT19	PE
PZT17			PZT17	PZT20	PE
PZT18			PZT18	PZT7	PE
PZT19			PZT19	PZT16	PE
PZT20			PZT20	PZT17	PE

5.3.5 Change filename to \KuhnPhase2\XXNov08\PE\CycleSet3\PZT1\Set1\test.lvm

5.3.5.1 'CycleSet2' to 'CycleSet3'

5.3.5.2 'PZT20' to 'PZT1'

6.0 Select 'TakeData1' icon in station manager to cycle sample to Cycle3 (60K cycles)

7.0 Take CycleSet3 Data

7.1 Mbond 'Pitch Catch'

7.1.1 Excite signal cable to Sensor1 Pitch

7.1.2 Configure Cables for Mbond catch



ai1 cable to Sensor1 Catch  
ai2 cable to Sensor2 Catch  
ai3 cable to Sensor3 Catch  
ai4 cable to Sensor4 Catch  
ai5 cable to Sensor5 Catch

7.1.3 Open VI '50PercentPC\_VI\_XXNov'

7.1.3.1 Check Save 'Enabled'

7.1.4 Check filename and DAQ Assistant configuration  
per steps 1.3.1.2 and 1.3.1.3

7.1.5 Take Mbond pitch-catch data

Filename change: \KuhnPhase2\XXNov\PC\CycleSet3\Sensor1\Set1\test.lvm  
\KuhnPhase2\XXNov\PC\CycleSet3\Sensor2\Set1\test.lvm

	Check prev data file	Change filename	Change Connector	Start data
Sensor1		Sensor1		PC
Sensor2		Sensor2		PC
Sensor3		Sensor3		PC
Sensor4		Sensor4		PC
Sensor5		Sensor5		PC

7.2 Epoxy 'Pitch Catch'

7.2.1 Excite signal cable to Sensor6 Pitch

7.2.2 Configure Cables for Epoxy catch

ai1 cable to Sensor6 Catch  
ai2 cable to Sensor7 Catch  
ai3 cable to Sensor8 Catch  
ai4 cable to Sensor9 Catch  
ai5 cable to Sensor10 Catch

7.2.3 Take Epoxy pitch-catch data

Filename change: \KuhnPhase2\XXNov\PC\CycleSet3\Sensor6\Set1\test.lvm  
\KuhnPhase2\XXNov\PC\CycleSet3\Sensor7\Set1\test.lvm

	Check prev data file	Change filename	Change Connector	Start data
Sensor6		Sensor6		PC
Sensor7		Sensor7		PC
Sensor8		Sensor8		PC
Sensor9		Sensor9		PC
Sensor10		Sensor10		PC

7.2.4 Change filename to \KuhnPhase2\XXNov08\PC\CycleSet4\Sensor1\Set1\test.lvm

7.2.4.1 'CycleSet3' to 'CycleSet4'

7.2.4.2 'Sensor10' to 'Sensor1'

7.3 'Pulse-Echo'

7.3.1 Open VI '50PercentPE\_V\_XXNov'

7.3.1.1 Check Save 'Enabled'

7.3.2 Configure cables for Pulse-echo

- Excitaion signal cable to splitter box 'Pulser'  
- Splitter box 'Crystal' cable to PZT1  
- ai1 cable to PZT4

7.3.3 Check filename and DAQ Assistant configuration  
per steps 1.3.1.2 and 1.3.1.3

#### 7.3.4 Take Pulse-Echo data

Filename change: \KuhnPhase2\XXNov\PE\CycleSet3\PZT1\Set1\test.lvm  
 \KuhnPhase2\XXNov\PE\CycleSet3\PZT2\Set1\test.lvm

	Check prev data file	Change filename	Change Connector		Start data
			ai7 (Echo)	ai1 (Opp)	
PZT1			PZT1	PZT4	PE
PZT2			PZT2	PZT13	PE
PZT3			PZT3	PZT5	PE
PZT4			PZT4	PZT1	PE
PZT5			PZT5	PZT3	PE
PZT6			PZT6	PZT9	PE
PZT7			PZT7	PZT18	PE
PZT8			PZT8	PZT10	PE
PZT9			PZT9	PZT6	PE
PZT10			PZT10	PZT8	PE
PZT11			PZT11	PZT14	PE
PZT12			PZT12	PZT15	PE
PZT13			PZT13	PZT2	PE
PZT14			PZT14	PZT11	PE
PZT15			PZT15	PZT12	PE
PZT16			PZT16	PZT19	PE
PZT17			PZT17	PZT20	PE
PZT18			PZT18	PZT7	PE
PZT19			PZT19	PZT16	PE
PZT20			PZT20	PZT17	PE

#### 7.3.5 Change filename to \KuhnPhase2\XXNov08\PE\CycleSet4\PZT1\Set1\test.lvm

7.2.4.1 'CycleSet3' to 'CycleSet4'

7.2.4.2 'PZT20' to 'PZT1'


8.0 Select 'TakeData1' icon in station manager to cycle sample to Cycle4 (90K cycles)

#### 9.0 Take CycleSet4 Data

##### 9.1 Mbond 'Pitch Catch'

9.1.1 Excite signal cable to Sensor1 Pitch

9.1.2 Configure Cables for Mbond catch

ai1 cable to Sensor1 Catch

ai2 cable to Sensor2 Catch

ai3 cable to Sensor3 Catch

ai4 cable to Sensor4 Catch

ai5 cable to Sensor5 Catch

9.1.3 Open VI '50PercentPC\_VI\_XXNov'

9.1.3.1 Check Save 'Enabled'

9.1.4 Check filename and DAQ Assistant configuration

per steps 1.3.1.2 and 1.3.1.3

9.1.5 Take Mbond pitch-catch data

Filename change: \KuhnPhase2\XXNov\PC\CycleSet4\Sensor1\Set1\test.lvm

\KuhnPhase2\XXNov\PC\CycleSet4\Sensor2\Set1\test.lvm


	Check prev data file	Change filename	Change Connector	Start data
Sensor1		Sensor1		PC
Sensor2		Sensor2		PC

Sensor3	Sensor3	PC
Sensor4	Sensor4	PC
Sensor5	Sensor5	PC

## 9.2 Epoxy 'Pitch Catch'

9.2.1 Excite signal cable to Sensor6 Pitch

9.2.2 Configure Cables for Epoxy catch

ai1 cable to Sensor6 Catch

ai2 cable to Sensor7 Catch

ai3 cable to Sensor8 Catch

ai4 cable to Sensor9 Catch

ai5 cable to Sensor10 Catch

9.2.3 Take Epoxy pitch-catch data

Filename change: \KuhnPhase2\XXNov\PC\CycleSet4\Sensor6\Set1\test.lvm  
 \KuhnPhase2\XXNov\PC\CycleSet4\Sensor7\Set1\test.lvm

	Check prev data file	Change filename	Change Connector	Start data
Sensor6		Sensor6		PC
Sensor7		Sensor7		PC
Sensor8		Sensor8		PC
Sensor9		Sensor9		PC
Sensor10		Sensor10		PC

9.2.4 Change filename to \KuhnPhase2\XXNov08\PC\CycleSet5\Sensor1\Set1\test.lvm

9.2.4.1 'CycleSet4' to 'CycleSet5'

9.2.4.2 'Sensor10' to 'Sensor1'

## 9.3 'Pulse-Echo'

9.3.1 Open VI '50PercentPE\_V\_XXNov'

9.3.1.1 Check Save 'Enabled'

9.3.2 Configure cables for Pulse-echo

- Excitation signal cable to splitter box 'Pulser'

- Splitter box 'Crystal' cable to PZT1

- ai1 cable to PZT4

9.3.3 Check filename and DAQ Assistant configuration

per steps 1.3.1.2 and 1.3.1.3

9.3.4 Take Pulse-Echo data

Filename change: \KuhnPhase2\XXNov\PE\CycleSet4\PZT1\Set1\test.lvm  
 \KuhnPhase2\XXNov\PE\CycleSet4\PZT2\Set1\test.lvm

	Check prev data file	Change filename	Change Connector		Start data
			ai7 (Echo)	ai1 (Opp)	
PZT1			PZT1	PZT4	PE
PZT2			PZT2	PZT13	PE
PZT3			PZT3	PZT5	PE
PZT4			PZT4	PZT1	PE
PZT5			PZT5	PZT3	PE
PZT6			PZT6	PZT9	PE
PZT7			PZT7	PZT18	PE
PZT8			PZT8	PZT10	PE
PZT9			PZT9	PZT6	PE
PZT10			PZT10	PZT8	PE
PZT11			PZT11	PZT14	PE

PZT12			PZT12	PZT15	PE
PZT13			PZT13	PZT2	PE
PZT14			PZT14	PZT11	PE
PZT15			PZT15	PZT12	PE
PZT16			PZT16	PZT19	PE
PZT17			PZT17	PZT20	PE
PZT18			PZT18	PZT7	PE
PZT19			PZT19	PZT16	PE
PZT20			PZT20	PZT17	PE

9.3.5 Change filename to \KuhnPhase2\XXNov08\PE\CycleSet5\PZT1\Set1\test.lvm

9.2.4.1 'CycleSet4' to 'CycleSet5'

9.2.4.2 'PZT20' to 'PZT1'

10.0 Select 'TakeData1' icon in station manager to cycle sample to Cycle5 (120K cycles)

11.0 Take CycleSet5 Data

11.1 Mbond 'Pitch Catch'

11.1.1 Excite signal cable to Sensor1 Pitch

11.1.2 Configure Cables for Mbond catch

ai1 cable to Sensor1 Catch

ai2 cable to Sensor2 Catch

ai3 cable to Sensor3 Catch

ai4 cable to Sensor4 Catch

ai5 cable to Sensor5 Catch

11.1.3 Open VI '50PercentPC\_VI\_XXNov'

11.1.3.1 Check Save 'Enabled'

11.1.4 Check filename and DAQ Assistant configuration

per steps 1.3.1.2 and 1.3.1.3

11.1.5 Take Mbond pitch-catch data

Filename change: \KuhnPhase2\XXNov\PC\CycleSet5\Sensor1\Set1\test.lvm

\KuhnPhase2\XXNov\PC\CycleSet5\Sensor2\Set1\test.lvm

	Check prev data file	Change filename	Change Connector	Start data
Sensor1		Sensor1		PC
Sensor2		Sensor2		PC
Sensor3		Sensor3		PC
Sensor4		Sensor4		PC
Sensor5		Sensor5		PC

11.2 Epoxy 'Pitch Catch'

11.2.1 Excite signal cable to Sensor6 Pitch

11.2.2 Configure Cables for Epoxy catch

ai1 cable to Sensor6 Catch

ai2 cable to Sensor7 Catch

ai3 cable to Sensor8 Catch

ai4 cable to Sensor9 Catch

ai5 cable to Sensor10 Catch

11.2.3 Take Epoxy pitch-catch data

Filename change: \KuhnPhase2\XXNov\PC\CycleSet5\Sensor6\Set1\test.lvm

\KuhnPhase2\XXNov\PC\CycleSet5\Sensor7\Set1\test.lvm

Check prev	Change	Change	Start
------------	--------	--------	-------

	data file	filename	Connector	data
Sensor6		Sensor6		PC
Sensor7		Sensor7		PC
Sensor8		Sensor8		PC
Sensor9		Sensor9		PC
Sensor10		Sensor10		PC

11.2.4 Change filename to \KuhnPhase2\XXNov08\PC\CycleSet6\Sensor1\Set1\test.lvm

11.2.4.1 'CycleSet5' to 'CycleSet6'

11.2.4.2 'Sensor10' to 'Sensor1'

11.3 'Pulse-Echo'

11.3.1 Open VI '50PercentPE\_V\_XXNov'

11.3.1.1 Check Save 'Enabled'

11.3.2 Configure cables for Pulse-echo

- Excitation signal cable to splitter box 'Pulser'

- Splitter box 'Crystal' cable to PZT1

- ai1 cable to PZT4

11.3.3 Check filename and DAQ Assistant configuration

per steps 1.3.1.2 and 1.3.1.3

11.3.4 Take Pulse-Echo data

Filename change: \KuhnPhase2\XXNov\PE\CycleSet5\PZT1\Set1\test.lvm

\KuhnPhase2\XXNov\PE\CycleSet5\PZT2\Set1\test.lvm

	Check prev data file	Change filename	Change Connector		Start data
			ai7 (Echo)	ai1 (Opp)	
PZT1			PZT1	PZT4	PE
PZT2			PZT2	PZT13	PE
PZT3			PZT3	PZT5	PE
PZT4			PZT4	PZT1	PE
PZT5			PZT5	PZT3	PE
PZT6			PZT6	PZT9	PE
PZT7			PZT7	PZT18	PE
PZT8			PZT8	PZT10	PE
PZT9			PZT9	PZT6	PE
PZT10			PZT10	PZT8	PE
PZT11			PZT11	PZT14	PE
PZT12			PZT12	PZT15	PE
PZT13			PZT13	PZT2	PE
PZT14			PZT14	PZT11	PE
PZT15			PZT15	PZT12	PE
PZT16			PZT16	PZT19	PE
PZT17			PZT17	PZT20	PE
PZT18			PZT18	PZT7	PE
PZT19			PZT19	PZT16	PE
PZT20			PZT20	PZT17	PE

11.3.5 Change filename to \KuhnPhase2\XXNov08\PE\CycleSet6\PZT1\Set1\test.lvm

11.2.4.1 'CycleSet5' to 'CycleSet6'

11.2.4.2 'PZT20' to 'PZT1'

12.0 Select 'TakeData1' icon in station manager to cycle sample to CycleSet6 (150K cycles)

13.0 Take CycleSet6 Data

### 13.1 Mbond 'Pitch Catch'

13.1.1 Excite signal cable to Sensor1 Catch

13.1.2 Configure Cables for Mbond catch

ai1 cable to Sensor1 Catch

ai2 cable to Sensor2 Catch

ai3 cable to Sensor3 Catch

ai4 cable to Sensor4 Catch

ai5 cable to Sensor5 Catch

13.1.3 Open VI '50PercentPC\_VI\_XXNov'

13.1.3.1 Check Save 'Enabled'

13.1.4 Check filename and DAQ Assistant configuration

per steps 1.3.1.2 and 1.3.1.3

13.1.5 Take Mbond pitch-catch data

Filename change: \KuhnPhase2\XXNov\PC\CycleSet6\Sensor1\Set1\test.lvm

\KuhnPhase2\XXNov\PC\CycleSet6\Sensor2\Set1\test.lvm

	Check prev data file	Change filename	Change Connector	Start data
Sensor1		Sensor1		PC
Sensor2		Sensor2		PC
Sensor3		Sensor3		PC
Sensor4		Sensor4		PC
Sensor5		Sensor5		PC

### 13.2 Epoxy 'Pitch Catch'

13.2.1 Excite signal cable to Sensor6 Catch

13.2.2 Configure Cables for Epoxy catch

ai1 cable to Sensor6 Catch

ai2 cable to Sensor7 Catch

ai3 cable to Sensor8 Catch

ai4 cable to Sensor9 Catch

ai5 cable to Sensor10 Catch

13.2.3 Take Epoxy pitch-catch data

Filename change: \KuhnPhase2\XXNov\PC\CycleSet6\Sensor6\Set1\test.lvm

\KuhnPhase2\XXNov\PC\CycleSet6\Sensor7\Set1\test.lvm

	Check prev data file	Change filename	Change Connector	Start data
Sensor6		Sensor6		PC
Sensor7		Sensor7		PC
Sensor8		Sensor8		PC
Sensor9		Sensor9		PC
Sensor10		Sensor10		PC

13.2.4 Change filename to \KuhnPhase2\XXNov08\PC\CycleSet7\Sensor1\Set1\test.lvm

13.2.4.1 'CycleSet6' to 'CycleSet7'

13.2.4.2 'Sensor10' to 'Sensor1'

### 13.3 'Pulse-Echo'

13.3.1 Open VI '50PercentPE\_V\_2Oct'

13.3.1.1 Check Save 'Enabled'

13.3.2 Configure cables for Pulse-echo

- Excitaion signal cable to splitter box 'Pulser'

- Splitter box 'Crystal' cable to PZT1

- ai1 cable to PZT4

- 13.3.3 Check filename and DAQ Assistant configuration  
per steps 1.3.1.2 and 1.3.1.3

- 13.3.4 Take Pulse-Echo data

Filename change:    \KuhnPhase2\XXNov\PE\CycleSet6\PZT1\Set1\test.lvm  
                          \KuhnPhase2\XXNov\PE\CycleSet6\PZT2\Set1\test.lvm

	Check prev data file	Change filename	Change Connector		Start data
			ai7 (Echo)	ai1 (Opp)	
PZT1			PZT1	PZT4	PE
PZT2			PZT2	PZT13	PE
PZT3			PZT3	PZT5	PE
PZT4			PZT4	PZT1	PE
PZT5			PZT5	PZT3	PE
PZT6			PZT6	PZT9	PE
PZT7			PZT7	PZT18	PE
PZT8			PZT8	PZT10	PE
PZT9			PZT9	PZT6	PE
PZT10			PZT10	PZT8	PE
PZT11			PZT11	PZT14	PE
PZT12			PZT12	PZT15	PE
PZT13			PZT13	PZT2	PE
PZT14			PZT14	PZT11	PE
PZT15			PZT15	PZT12	PE
PZT16			PZT16	PZT19	PE
PZT17			PZT17	PZT20	PE
PZT18			PZT18	PZT7	PE
PZT19			PZT19	PZT16	PE
PZT20			PZT20	PZT17	PE

- 13.3.5 Change filename to \KuhnPhase2\XXNov08\PE\CycleSet7\PZT1\Set1\test.lvm

13.2.4.1 'CycleSet6' to 'CycleSet7'

13.2.4.2 'PZT20' to 'PZT1'

- 14.0 Select 'TakeData1' icon in station mangaer to cycle sample to CycleSet7 (180K cycles)

- 15.0 Take CycleSet7 Data

- 15.1 Mbond 'Pitch Catch'

- 15.1.1 Excite signal cable to Sensor1 Pitch

- 15.1.2 Configure Cables for Mbond catch

ai1 cable to Sensor1 Catch

ai2 cable to Sensor2 Catch

ai3 cable to Sensor3 Catch

ai4 cable to Sensor4 Catch

ai5 cable to Sensor5 Catch

- 15.1.3 Open VI '50PercentPC\_VI\_XXNov'

15.1.3.1 Check Save 'Enabled'

- 15.1.4 Check filename and DAQ Assistant configuration

per steps 1.3.1.2 and 1.3.1.3

- 15.1.5 Take Mbond pitch-catch data

Filename change:    \KuhnPhase2\XXNov\PC\CycleSet7\Sensor1\Set1\test.lvm  
                          \KuhnPhase2\XXNov\PC\CycleSet7\Sensor2\Set1\test.lvm

Check prev	Change	Change	Start
------------	--------	--------	-------

	data file	filename	Connector	data
Sensor1		Sensor1		PC
Sensor2		Sensor2		PC
Sensor3		Sensor3		PC
Sensor4		Sensor4		PC
Sensor5		Sensor5		PC

## 15.2 Epoxy 'Pitch Catch'

### 15.2.1 Excite signal cable to Sensor6 Pitch

### 15.2.2 Configure Cables for Epoxy catch

ai1 cable to Sensor6 Catch

ai2 cable to Sensor7 Catch

ai3 cable to Sensor8 Catch

ai4 cable to Sensor9 Catch

ai5 cable to Sensor10 Catch

### 15.2.3 Take Epoxy pitch-catch data

Filename change: \KuhnPhase2\XXNov\PC\CycleSet7\Sensor6\Set1\test.lvm  
 \KuhnPhase2\XXNov\PC\CycleSet7\Sensor7\Set1\test.lvm

	Check prev data file	Change filename	Change Connector	Start data
Sensor6		Sensor6		PC
Sensor7		Sensor7		PC
Sensor8		Sensor8		PC
Sensor9		Sensor9		PC
Sensor10		Sensor10		PC

### 15.2.4 Change filename to \KuhnPhase2\XXNov08\PC\CycleSet8\Sensor1\Set1\test.lvm

#### 15.2.4.1 'CycleSet7' to 'CycleSet8'

#### 15.2.4.2 'Sensor10' to 'Sensor1'

## 15.3 'Pulse-Echo'

### 15.3.1 Open VI '50PercentPE\_V\_XXNov'

#### 15.3.1.1 Check Save 'Enabled'

### 15.3.2 Configure cables for Pulse-echo

- Excitaion signal cable to splitter box 'Pulser'

- Splitter box 'Crystal' cable to PZT1

- ai1 cable to PZT4

### 15.3.3 Check filename and DAQ Assistant configuration

per steps 1.3.1.2 and 1.3.1.3

### 15.3.4 Take Pulse-Echo data

Filename change: \KuhnPhase2\XXNov\PE\CycleSet7\PZT1\Set1\test.lvm  
 \KuhnPhase2\XXNov\PE\CycleSet7\PZT2\Set1\test.lvm

	Check prev data file	Change filename	Change Connector		Start data
			ai7 (Echo)	ai1 (Opp)	
PZT1			PZT1	PZT4	PE
PZT2			PZT2	PZT13	PE
PZT3			PZT3	PZT5	PE
PZT4			PZT4	PZT1	PE
PZT5			PZT5	PZT3	PE
PZT6			PZT6	PZT9	PE
PZT7			PZT7	PZT18	PE
PZT8			PZT8	PZT10	PE



PZT9			PZT9	PZT6	PE
PZT10			PZT10	PZT8	PE
PZT11			PZT11	PZT14	PE
PZT12			PZT12	PZT15	PE
PZT13			PZT13	PZT2	PE
PZT14			PZT14	PZT11	PE
PZT15			PZT15	PZT12	PE
PZT16			PZT16	PZT19	PE
PZT17			PZT17	PZT20	PE
PZT18			PZT18	PZT7	PE
PZT19			PZT19	PZT16	PE
PZT20			PZT20	PZT17	PE

15.3.5 Change filename to \KuhnPhase2\XXNov08\PE\CycleSet8\PZT1\Set1\test.lvm

15.2.4.1 'CycleSet7' to 'CycleSet8'

15.2.4.2 'PZT20' to 'PZT1'


16.0 Select 'TakeData1' icon in station manager to cycle sample to Cycle8 (210K cycles)

17.0 Take CycleSet8 Data

17.1 Mbond 'Pitch Catch'

17.1.1 Excite signal cable to Sensor1 Pitch

17.1.2 Configure Cables for Mbond catch

ai1 cable to Sensor1 Catch

ai2 cable to Sensor2 Catch

ai3 cable to Sensor3 Catch

ai4 cable to Sensor4 Catch

ai5 cable to Sensor5 Catch

17.1.3 Open VI '50PercentPC\_VI\_2Oct'

17.1.3.1 Check Save 'Enabled'

17.1.4 Check filename and DAQ Assistant configuration

per steps 1.3.1.2 and 1.3.1.3

17.1.5 Take Mbond pitch-catch data

Filename change: \KuhnPhase2\XXNov\PC\CycleSet8\Sensor1\Set1\test.lvm

\KuhnPhase2\XXNov\PC\CycleSet8\Sensor2\Set1\test.lvm


	Check prev data file	Change filename	Change Connector	Start data
Sensor1		Sensor1		PC
Sensor2		Sensor2		PC
Sensor3		Sensor3		PC
Sensor4		Sensor4		PC
Sensor5		Sensor5		PC

17.2 Epoxy 'Pitch Catch'

17.2.1 Excite signal cable to Sensor6 Pitch

17.2.2 Configure Cables for Epoxy catch

ai1 cable to Sensor6 Catch

ai2 cable to Sensor7 Catch

ai3 cable to Sensor8 Catch

ai4 cable to Sensor9 Catch

ai5 cable to Sensor10 Catch

17.2.3 Take Epoxy pitch-catch data

Filename change: \KuhnPhase2\XXNov\PC\CycleSet8\Sensor6\Set1\test.lvm

\\KuhnPhase2\XXNov\PC\CycleSet8\Sensor7\Set1\test.lvm

	Check prev data file	Change filename	Change Connector	Start data
Sensor6		Sensor6		PC
Sensor7		Sensor7		PC
Sensor8		Sensor8		PC
Sensor9		Sensor9		PC
Sensor10		Sensor10		PC

17.2.4 Change filename to \\KuhnPhase2\XXNov08\PC\CycleSet9\Sensor1\Set1\test.lvm

17.2.4.1 'CycleSet8' to 'CycleSet9'

17.2.4.2 'Sensor10' to 'Sensor1'

17.3 'Pulse-Echo'

17.3.1 Open VI '50PercentPE\_V\_2Oct'

17.3.1.1 Check Save 'Enabled'

17.3.2 Configure cables for Pulse-echo

- Excitation signal cable to splitter box 'Pulser'
- Splitter box 'Crystal' cable to PZT1
- a11 cable to PZT4

17.3.3 Check filename and DAQ Assistant configuration  
per steps 1.3.1.2 and 1.3.1.3

17.3.4 Take Pulse-Echo data

Filename change: \\KuhnPhase2\XXNov\PE\CycleSet8\PZT1\Set1\test.lvm  
\\KuhnPhase2\XXNov\PE\CycleSet8\PZT2\Set1\test.lvm



	Check prev data file	Change filename	Change Connector		Start data
			ai7 (Echo)	ai1 (Opp)	
PZT1			PZT1	PZT4	PE
PZT2			PZT2	PZT13	PE
PZT3			PZT3	PZT5	PE
PZT4			PZT4	PZT1	PE
PZT5			PZT5	PZT3	PE
PZT6			PZT6	PZT9	PE
PZT7			PZT7	PZT18	PE
PZT8			PZT8	PZT10	PE
PZT9			PZT9	PZT6	PE
PZT10			PZT10	PZT8	PE
PZT11			PZT11	PZT14	PE
PZT12			PZT12	PZT15	PE
PZT13			PZT13	PZT2	PE
PZT14			PZT14	PZT11	PE
PZT15			PZT15	PZT12	PE
PZT16			PZT16	PZT19	PE
PZT17			PZT17	PZT20	PE
PZT18			PZT18	PZT7	PE
PZT19			PZT19	PZT16	PE
PZT20			PZT20	PZT17	PE

17.3.5 Change filename to \\KuhnPhase2\XXNov08\PE\CycleSet9\PZT1\Set1\test.lvm

17.2.4.1 'CycleSet8' to 'CycleSet9'

17.2.4.2 'PZT20' to 'PZT1'

18.0 Select 'TakeData1' icon in station manager to cycle sample to CycleSet9 (240K cycles)

#### 19.0 Take CycleSet9 Data

##### 19.1 Mbond 'Pitch Catch'

19.1.1 Excite signal cable to Sensor1 Pitch

19.1.2 Configure Cables for Mbond catch

ai1 cable to Sensor1 Catch

ai2 cable to Sensor2 Catch

ai3 cable to Sensor3 Catch

ai4 cable to Sensor4 Catch

ai5 cable to Sensor5 Catch

19.1.3 Open VI '50PercentPC\_VI\_XXNov'

17.1.3.1 Check Save 'Enabled'

19.1.4 Check filename and DAQ Assistant configuration

per steps 1.3.1.2 and 1.3.1.3

19.1.5 Take Mbond pitch-catch data

Filename change: \KuhnPhase2\XXNov\PC\CycleSet9\Sensor1\Set1\test.lvm

\KuhnPhase2\XXNov\PC\CycleSet9\Sensor2\Set1\test.lvm

	Check prev data file	Change filename	Change Connector	Start data
Sensor1		Sensor1		PC
Sensor2		Sensor2		PC
Sensor3		Sensor3		PC
Sensor4		Sensor4		PC
Sensor5		Sensor5		PC

##### 19.2 Epoxy 'Pitch Catch'

19.2.1 Excite signal cable to Sensor6 Pitch

19.2.2 Configure Cables for Epoxy catch

ai1 cable to Sensor6 Catch

ai2 cable to Sensor7 Catch

ai3 cable to Sensor8 Catch

ai4 cable to Sensor9 Catch

ai5 cable to Sensor10 Catch

19.2.3 Take Epoxy pitch-catch data

Filename change: \KuhnPhase2\XXNov\PC\CycleSet9\Sensor6\Set1\test.lvm

\KuhnPhase2\XXNov\PC\CycleSet9\Sensor7\Set1\test.lvm

	Check prev data file	Change filename	Change Connector	Start data
Sensor6		Sensor6		PC
Sensor7		Sensor7		PC
Sensor8		Sensor8		PC
Sensor9		Sensor9		PC
Sensor10		Sensor10		PC

19.2.4 Change filename to \KuhnPhase2\XXNov08\PC\CycleSet10\Sensor1\Set1\test.lvm

17.2.4.1 'CycleSet9' to 'CycleSet10'

17.2.4.2 'Sensor10' to 'Sensor1'

##### 19.3 'Pulse-Echo'

19.3.1 Open VI '50PercentPE\_V\_2Oct'

19.3.1.1 Check Save 'Enabled'

### 19.3.2 Configure cables for Pulse-echo

- Excitation signal cable to splitter box 'Pulser'
- Splitter box 'Crystal' cable to PZT1
- ai1 cable to PZT4

### 19.3.3 Check filename and DAQ Assistant configuration

per steps 1.3.1.2 and 1.3.1.3

### 19.3.4 Take Pulse-Echo data

Filename change: \KuhnPhase2\XXNov\PE\CycleSet9\PZT1\Set1\test.lvm  
 \KuhnPhase2\XXNov\PE\CycleSet9\PZT2\Set1\test.lvm

	Check prev data file	Change filename	Change Connector		Start data
			ai7 (Echo)	ai1 (Opp)	
PZT1			PZT1	PZT4	PE
PZT2			PZT2	PZT13	PE
PZT3			PZT3	PZT5	PE
PZT4			PZT4	PZT1	PE
PZT5			PZT5	PZT3	PE
PZT6			PZT6	PZT9	PE
PZT7			PZT7	PZT18	PE
PZT8			PZT8	PZT10	PE
PZT9			PZT9	PZT6	PE
PZT10			PZT10	PZT8	PE
PZT11			PZT11	PZT14	PE
PZT12			PZT12	PZT15	PE
PZT13			PZT13	PZT2	PE
PZT14			PZT14	PZT11	PE
PZT15			PZT15	PZT12	PE
PZT16			PZT16	PZT19	PE
PZT17			PZT17	PZT20	PE
PZT18			PZT18	PZT7	PE
PZT19			PZT19	PZT16	PE
PZT20			PZT20	PZT17	PE

### 19.3.5 Change filename to \KuhnPhase2\XXNov08\PE\CycleSet10\PZT1\Set1\test.lvm

19.2.4.1 'CycleSet9' to 'CycleSet10'

19.2.4.2 'PZT20' to 'PZT1'

### 20.0 Select 'TakeData9' icon in station manager to end load program

### 21.0 Turn off hydraulics

21.1 Software HSM icon to two bars then to one bar

21.2 Power down power supply....reverse para 1.1.1

### 22.0 Transfer data files

22.1 MTS data log location: C:\MTS 793\Projects\Project1\MPT\Specimens\Specimen Name from para 1.1.2.7.2\specimen DAT file

## Bibliography

1. Achenbach, J. D. "On the Road from Schedule-Based Nondestructive Inspection to Structural Health Monitoring". *Structural Health Monitoring 2007: Quantification, Validation, and Implementation: Proceedings of the 6th International Workshop on Structural Health Monitoring*, volume 1, 16–28. DEStech Publications, Inc., Lancaster, PA, 2007. ISBN 978-1-932078-71-8.
2. Aerospace Industries Association of America, Inc. *Rivets, Buck Type, Preparation for and Installation of*. National Aerospace Standard NASM 47196. Defense Industrial Supply Center, PA: DISC-AESD, 1999.
3. Albert, Alan P., Efstathios Antoniou, Stephen D. Leggiero, Kimberly A. Tooman, and Ramon L. Veglio. *A Systems Engineering Approach to Integrated Structural Health Monitoring for Aging Aircraft*. Master's thesis, AFIT/GSE/ENY/06-M02. School of Engineering and Management, Air Force Institute of Technology (AU), Wright-Patterson AFB OH, March 2006.
4. Alleyne, D. N. and P. Cawley. "The interaction of Lamb waves with defects". *IEEE Transactions on Ultrasonics, Ferroelectrics and Frequency Control*, 39(3):381–397, 1992.
5. Beard, Shawn J., Amrita Kumar, Peter Qing, Robert Hannum, and R. Ikegami. "Hot-Spot Fatigue Crack Monitoring of Inaccessible Structural Regions in Aircraft Subsystems Using Structural Health Monitoring". *Proceedings of the 9th Joint FAA/DoD/NASA Conference on Aging Aircraft, 6-9 March 2006*. Atlanta, GA, 2006.
6. Beard, Shawn J., Amrita Kumar, Xinlin Qing, H. L. Chan, Chang Zhang, and Teng K. Ooi. "Practical issues in real-world implementation of structural health monitoring systems". *Industrial and Commercial Applications of Smart Structures Technologies*, volume 5762 of *Smart Structures and Materials 2005*, 196–203. San Diego, CA: SPIE, 2005.
7. Berens, Alan P. "NDE Reliability Data Analysis". *ASTM Handbook*, Vol 17, Nondestructive Evaluation and Quality Control:689–701, 1989.
8. Berens, Alan P. "Determining Reinspection Intervals". *Proceedings of the 2007 USAF Aircraft Structural Integrity Program (ASIP) Conference, 4-6 Dec 2007*. Palm Springs CA: Universal Technology Corporation, 2007.
9. Berens, Alan P. and Peter W. Hovey. *Evaluation of NDE Reliability Characterization, Volume I*. Technical Report AFWAL-TR-81-4160, Dayton, OH: University of Dayton Research Institute, December 1981.
10. Berens, Alan P., Peter W. Hovey, and Donald A. Skinn. *Risk Analysis for Aging Aircraft Fleets. Volume 1: Analysis*. Technical Report WL-TR-91-3066, Dayton, OH: University of Dayton Research Institute, October 1991.

11. Blackshire, James L. and Adam Cooney. "Evaluation and improvement in sensor performance and durability for structural health monitoring systems". *Advanced Sensor Technologies for Nondestructive Evaluation and Structural Health Monitoring II*, volume 6179 of *Proceedings of the SPIE*, 1–10. Bellingham, WA: International Society for Optical Engineering, 2006.
12. Blackshire, James L. and Adam T. Cooney. "Characterization of Bonded Piezoelectric Sensor Performance and Durability in Simulated Aircraft Environments". *Review of Progress in Quantitative Nondestructive Evaluation*, 25B:1694–1701, 2006.
13. Blackshire, James L., Victor Giurgiutiu, Adam Cooney, and James Doane. "Characterization of Sensor Performance and Durability for Structural Health Monitoring Systems". *Advanced Sensor Technologies for Nondestructive Evaluation and Structural Health Monitoring*, volume 5770 of *Proceedings of the SPIE*, 66–75. Bellingham, WA: SPIE, 2005.
14. Blackshire, James L., Steven A. Martin, and J. Na. "The Influence of Bond Material Type and Quality on Damage Detection for Surface Bonded Piezoelectric Sensors". *Proceedings of the 6th International Workshop on Structural Health Monitoring: Quantification, Validation and Implementation, Stanford University, 11-13 Sept 2007*, volume 1, 203–210. Lancaster, PA: DEStech Publications Inc, 2007.
15. Blackshire, James L., Steven A. Martin, and Jeong K. Na. "Disbonding effects on elastic wave generation and reception by bonded piezoelectric sensor systems". *Sensor Systems and Networks: Phenomena, Technology, and Applications for NDE and Health Monitoring 2007*, volume 6530 of *Proceedings of the SPIE*, 1–8. Bellingham WA: SPIE, 2007.
16. Boller, C. "Next Generation Structural Health Monitoring and its Integration into Aircraft Design". *International Journal of Systems Science*, 31(no. 11):1333–1349, November 2000.
17. Boller, C. "Ways and Options for Aircraft Structural Health Management". *Smart Materials and Structures*, 10(3):432–440, 2001.
18. Brausch, John, Jeffrey Catron, David Campbell, David Piotrowski, and David Forsyth. "Panel Discussion: USAF NDI Reliability Improvements". *Proceedings of the 2006 Aircraft Structural Integrity Program (ASIP) Conference, 28-30 Nov 2006*. San Antonio, TX: Universal Technology Corporation, 2006.
19. Brown, Jason and Travis Hanson. *A Systems Engineering Process for an Integrated Structural Health Monitoring System for Aging Aircraft III*. Master's thesis, AFIT/GSE/ENV/08-M03. School of Engineering and Management, Air Force Institute of Technology (AU), Wright-Patterson AFB OH, March 2008.
20. Buderath, Matthias. "Review the Progress (sic) of Integrating SHM Systems into Condition Based Maintenance as Part of the Sturctural Integrity Program". *Pro-*

- ceedings of the 2nd European Workshop on Structural Health Monitoring, Munich, Germany, 7-9 July 2004*, 307–316. Lancaster, PA: DEStech Publications Inc, 2004.
21. Buede, Dennis M. *The Engineering Design of Systems : Models and Methods*. New York: Wiley, 2000.
  22. Chambers, Jeffrey T. *Durability Testing of an Aircraft Structural Health Monitoring System*. Master’s thesis, Massachusetts Institute of Technology, Cambridge MA, 2006.
  23. Chambers, Jeffrey T., Brian L. Wardle, and Seth S. Kessler. “Durability assessment of lamb wave-based structural health monitoring nodes”. *47th AIAA/ASME/ASCE/AHS/ASC Structures, Structural Dynamics and Materials Conference*, volume 11, 7920–7931. Reston, VA: American Inst. Aeronautics and Astronautics Inc., 2006.
  24. Chang, Fu-Kuo. “A Summary Report of The 2nd Workshop on Structural Health Monitoring”. *Proceedings of the 3rd International Workshop of Structural Health Monitoring: The Demands and Challenges, Stanford University, 12-14 Sept 2001*, xxi–xlvi. Boca Raton, FL: CRC Press, 2000.
  25. Christiansen, Peter. “C-130 Center Wing Fatigue Cracking Lessons Learned: Application to ASIP Force Management Execution”. *Proceedings of the 2007 USAF Aircraft Structural Integrity Program (ASIP) Conference, 4-6 Dec 2007*. Palm Springs CA: Universal Technology Corporation, 2007.
  26. Cobb, Adam C. *A state estimation framework for ultrasonic structural health monitoring of fastener hole fatigue cracks*. Ph.D. thesis, Georgia Institute of Technology, 2008.
  27. Cobb, Adam C., Jennifer E. Michaels, and Thomas E. Michaels. “Ultrasonic Structural Health Monitoring: a Probability of Detection Case Study”. *Review of Progress in Quantitative Nondestructive Evaluation*, 28:1800–1807, 2009.
  28. Cohen, Jacob. “A Power Primer”. *Psychological bulletin*, 112(1):155–159, 1992.
  29. Collins, Jack A. *Failure of Materials in Mechanical Design: Analysis, Prediction, Prevention, 2nd Edition*. New York: John Wiley & Sons, 1993.
  30. Crider, Jeffrey S. *Damage Detection Using Lamb Waves for Structural Health Monitoring*. Master’s thesis, AFIT/GA/ENY/07-M05. School of Engineering and Management, Air Force Institute of Technology (AU), Wright-Patterson AFB OH, March 2007.
  31. Department of Defense. *Handbook for Reliability Test Methods, Plans, and Environments for Engineering, Development Qualification and Production*. MIL-HDBK-781A. Arlington, VA: Space and Naval Warfare Systems Command, 1 Apr 1996.

32. Department of Defense. *Test Method Standard for Environmental Engineering Considerations and Laboratory Tests*. MIL-STD-810F. Wright-Patterson AFB OH: ASC/ENFS, 1 Jan 2000.
33. Department of Defense. *Aircraft Structural Integrity Program (ASIP)*. MIL-STD-1530C(USAF). Wright-Patterson AFB, OH: ASC/ENOI, 1 November 2005.
34. Department of Defense. *Inspection Program Requirements Nondestructive for Aircraft and Missile Materials and Parts*. MIL-HDBK-6870A. Wright-Patterson AFB OH: AFRL/MLSA, 28 Aug 2001.
35. Department of Defense. *Nondestructive Evaluation System Reliability Assessment*. MIL-HDBK-1823. Wright-Patterson AFB OH: ASC/ENSI, 30 April 1999.
36. Department of Defense. *Metallic Materials and Elements for Aerospace Structures*. MIL-HDBK-5J. Wright-Patterson AFB, OH: AFRL/MLSC, 31 Jan 03.
37. Department of the Air Force. *Aircraft Battle Damage Repair Instructions, USAF Series C-130E and C-130H Aircraft, Change 4*. Technical Order 1C-130A-39. Robins AFB, GA: WR-ALC/LUTD, 1 June 2000.
38. Department of the Air Force. *Inspection and Maintenance Requirements Manual, USAF Series F-15A/B/C/D Aircraft, Change 17*. Technical Order 1F-15A-6. Robins AFB, GA: 569 ACSS/GFIA, 1 May 2006.
39. Department of the Air Force. *Nondestructive Inspection USAF Series F-15A 73-085 and Up, F-15B 73-108 and Up, F-15C, F-15D and F-15E Aircraft, Change 7*. Technical Order 1F-15A-36. Robins AFB, GA: 569 ACSS/GFIA, 1 November 2006.
40. Department of the Air Force. *Nondestructive Inspection Methods, Basic Theory*. Technical Order 33B-1-1. Tinker AFB, OK: AFRL/MLS-OL, 15 June 2007.
41. Department of the Air Force. *Nondestructive Inspection Procedures, USAF Series C-130 Airplanes, Change 50*. Technical Order 1C-130A-36. Robins AFB, GA: WR-ALC/LUTD, 15 June 2007.
42. Department of the Air Force. *Operational Supplement Technical Manual, Inspection and Maintenance Requirements Manual, USAF Series F-15A Aircraft*. Technical Order 1F-15A-6S-368. Robins AFB, GA: 569 ACSS/GFIA, 16 Jan 2007.
43. Department of the Air Force. *Aircraft and Equipment Maintenance Management*. Air Force Instruction 21-101. Washington: HQ USAF/A4MM, 29 June 2006.
44. Derriso, M., P. Faas, J. Calcaterra, J. Barnes, and W. Sotomayer. "Structural Health Monitoring Applications for Current and Future Aerospace Vehicles". *Proceedings of the 3rd International Workshop of Structural Health Monitoring: The Demands and Challenges, Stanford University, 12-14 Sept 2001*, 3–11. Boca Raton, FL: CRC Press, 2001.



45. Derriso, M., S. E. Olson, M. P. DeSimio, and D. M. Pratt. "Why Are There Few Fielded SHM Systems for Aerospace Structures?" *Proceedings of the 6th International Workshop on Structural Health Monitoring: Quantification, Validation and Implementation, Stanford University, 11-13 Sept 2007*, volume 1, 44–55. Lancaster, PA: DEStech Publications Inc, 2007.
46. Fawcett, Tom. "An introduction to ROC analysis". *Pattern Recognition Letters*, 27(8):861–874, 2006.
47. Giurgiutiu, V., J. Bao, and W. Zhao. "Active Sensor Wave Propagation Health Monitoring of Beam and Plate Structures". *Proceedings of the SPIEs 8th International Symposium on Smart Structures and Materials*. 4-8 March 2001, Newport Beach, CA, 2001.
48. Giurgiutiu, V., J. Bao, and W. Zhao. "Piezoelectric wafer active sensor embedded ultrasonics in beams and plates". *Experimental Mechanics*, 43(4):428–449, 2003.
49. Giurgiutiu, Victor. "Tuned lamb wave excitation and detection with piezoelectric wafer active sensors for structural health monitoring". *Journal of Intelligent Material Systems and Structures*, 16(2):291–305, 2005.
50. Giurgiutiu, Victor and Adrian Cuc. "Embedded non-destructive evaluation for structural health monitoring, damage detection, and failure prevention". *Shock and Vibration Digest*, 37(2):83–105, 2005.
51. Gomez, Javier, Joseba Zubia, Gerardo Aranguren, Jon Arrue, Hans Poisel, and Idurre Saez. "Comparing polymer optical fiber, fiber Bragg grating, and traditional strain gauge for aircraft structural health monitoring". *Applied Optics*, 48(8):1436, -03-10 2009.
52. Grunden, Beverly. Statistical Consultant, Mathematics and Statistics Department, Wright State University, Dayton OH. Personal Interview, 8 April 2009.
53. Ihn, Jeong-Beom and Fu-Kuo Chang. "Multicrack growth monitoring at riveted lap joints using piezoelectric patches". *Proceedings of the SPIE - The International Society for Optical Engineering*, volume 4702 of *Smart Structures and Materials 2002*, 29–40. Newport Beach, CA: SPIE, 2002.
54. Ikegami, R. and E. D. Haugse. "Structural Health Management for Aging Aircraft". *Industrial and Commercial Applications of Smart Structures Technologies*, volume 4332 of *Smart Structures and Materials 2001*, 60–67. Newport Beach, CA: SPIE, 2001.
55. International Council on Systems Engineering. "What is Systems Engineering?" Article Excerpt. <http://www.incose.org/>, 14 Jun 2004.
56. Kearns, J., J. Pena-Macias, A. Southward Criado-Abad T., D. Evans, and M. Malkin. "Development and Flight Demonstration of a Piezoelectric Phased

- Array Damage Detection System”. *Proceedings of the 6th International Workshop on Structural Health Monitoring: Quantification, Validation and Implementation, Stanford University, 11-13 Sept 2007*, volume 1, 93–100. Lancaster, PA: DEStech Publications Inc, 2007.
57. Kessler, Seth S. “Certifying a Structural Health Monitoring System: Characterizing Durability, Reliability and Longevity”. *Proceedings of the 1st International Forum on Integrated Systems Health Engineering and Management in Aerospace, Napa, CA, 7-10 November 2005*. 2005.
  58. Kim, S. B. and Hoon Sohn. “Instantaneous Crack Detection in Thin Metal Plates and Aircraft Panels”. *Structural Health Monitoring 2007: Quantification, Validation, and Implementation: Proceedings of the 6th International Workshop on Structural Health Monitoring*, volume 1, 169. DEStech Publications, Inc., Lancaster, PA, 2007.
  59. Kim, Yool, Stephen Sheehy, and Darryl Lenhardt. *A Survey of Aircraft Structural-Life Management Programs in the U.S. Navy, the Canadian Forces, and the U.S. Air Force*. Technical Report MG-370-AF, Santa Monica, CA: RAND, 2006.
  60. Kudva, J. N., C. Marantidis, J. Gentry, and E. Blazic. “Smart Structures Concepts for Aircraft Structural Health Monitoring”. *Proceedings of the SPIE - Smart Structures and Intelligent Systems*, volume 1917 of *Smart Structures and Materials 1993*, 964–71. Albuquerque, NM: SPIE, 1993.
  61. Kudva, J. N., C. Marantidis, C. Van Way, J. Alper, and C. Paul. “Guidelines for Smart Structural Health Monitoring Systems for Military Aircraft-Lessons Learned from the Smart Structures Concept Requirements Definition (SSCORE) Contract”. *Smart Sensing, Processing, and Instrumentation*, volume 2191 of *Smart Structures and Materials 1994*, 210–15. Orlando, FL: SPIE, 1994.
  62. Kusaka, T. and P. X. Qing. “Characterization of loading effects on the performance of smart layer embedded or surface-mounted on structures”. *Proceedings of the 4th International Workshop on Structural Health Monitoring: From Diagnostics & Prognostics to Structural Health Management, Stanford University, 15-17 Sept, 2003*, 1539–1546. Lancaster, PA: DEStech Publications, Inc, 2003.
  63. Lathi, B. P. *Signal Processing and Linear Systems*. New York, NY: Oxford University Press, 1998.
  64. Lee, B. C. and W. J. Staszewski. “Modelling of Lamb waves for damage detection in metallic structures: Part I. Wave propagation”. *Smart Materials and Structures*, 12:804, 2003.
  65. Lehman, Ann, Norm O’Rourke, Larry Hatcher, and Edward Stepaniski. *JMP for Basic Univariate and Multivariate Statistics*. SAS Institute Inc., Cary, NC, 2005.

66. Lin, Mark, Xinlin Qing, Amrita Kumar, and Shawn J. Beard. "SMART Layer and SMART Suitcase for structural health monitoring applications". *Smart Structures and Materials 2001-Industrial and Commercial Applications of Smart Structures Technologies*, volume 4332 of *Proceedings of the SPIE*, 98–106. Newport Beach, CA: Society of Photo-Optical Instrumentation Engineers, 2001.
67. Lincoln, John W. "The USAF Approach to Attaining Structural Integrity of Aging Aircraft". *1995 ASME International Mechanical Engineering Congress and Exposition*, 9–19. San Francisco, CA: ASME, 1995.
68. Lu, Yinghui. *Analysis and modeling of diffuse ultrasonic signals for structural health monitoring*. Ph.D. thesis, Georgia Institute of Technology, 2007.
69. Lu, Yinghui and Jennifer E. Michaels. "Discriminating Damage from Surface Wetting Via Feature Analysis for Ultrasonic Structural Health Monitoring Systems". *AIP Conference Proceedings*, 975(1):1420–1427, 02/28 2008.
70. Lynn, Paul A. and Wolfgang Fuerst. *Introductory Digital Signal Processing with Computer Applications*. New York, NY: John Wiley and Sons, New York, 1994.
71. Majumder, Mousumi, Tarun Kumar Gangopadhyay, Ashim Kumar Chakraborty, Kamal Dasgupta, and D. K. Bhattacharya. "Fibre Bragg gratings in structural health monitoring, present status and applications". *Sensors and Actuators A: Physical*, 147(1):150–164, 09/15 2008.
72. Malkin, M., M. Leonard, M. Derriso, and E. D. Haugse. "Hot Spot Monitoring: Development of a Framework for SHM System Design". *Proceedings of the 6th International Workshop on Structural Health Monitoring: Quantification, Validation and Implementation, Stanford University, 11-13 Sept 2007*, volume 1, 786–792. Lancaster, PA: DEStech Publications Inc, 2007.
73. Martin, Steven A. and James L. Blackshire. "Effect of adhesive material properties on induced stresses in bonded sensors". *Sensor Systems and Networks: Phenomena, Technology, and Applications for NDE and Health Monitoring 2007*, volume 6530 of *Proceedings of the SPIE*, 65300J–1 through 12. Bellingham WA: SPIE, 2007.
74. Matzkanin, George A. and Thomas H. Yolken. *Probability of Detection for Non-destructive Evaluation (NDE)*. Technical Report NTIAC-TA-00-01, Nondestructive Testing Information Analysis Center, 2001.
75. McDonnell Douglas Aerospace. "F-15 Force Structural Maintenance Plan". Unpublished Report Number MDC A9236, 31 May 2004.
76. McDonnell Douglas Aerospace. "F-15 Damage Tolerance Assessment, Revision G". Unpublished Report Number MDC A7467, 31 May 2004.
77. Measurements Group Inc., Education Division. *Student manual for strain gauge technology, a brief introduction and guide to selection, installation, instrumentation*. Technical Report Bulletin 309, Measurements Group Inc., 1983.

78. Mercer Engineering Research Center. "C-130 Force Structural Maintenance Plan". Unpublished Report Number 14RJ12-07008-D1, 28 Sept 2007.
79. Michaels, Jennifer E. "Ultrasonic structural health monitoring: strategies, issues and progress". *Smart Sensor Phenomena, Technology, Networks, and Systems 2008*, volume 6933. Proceedings of the SPIE, San Diego, CA, 2008.
80. Michaels, Jennifer E., Thomas E. Michaels, and Bao Mi. "An ultrasonic angle beam method for in situ sizing of fastener hole cracks". *Journal of Nondestructive Evaluation*, 25(1):2–15, 2006.
81. Mickey, Ruth M., Olive Dunn, and Virginia A. Clark. *Applied Statistics: Analysis of Variance and Regression*. Wiley Series in Probability and Statistics. John Wiley & Sons, Inc, Hoboken, NJ, 2004.
82. Miedlar, P., Alan P. Berens, Peter W. Hovey, T. Boehnlein, and H. Lorenz. *PRoF v3 Probability of Fracture, Aging Aircraft Risk Analysis Update*. Technical Report UDR-TR-2005-00240, Dayton, OH: University of Dayton Research Institute, December 2005.
83. Montgomery, Douglas C. *Design and Analysis of Experiments, 6th Edition*. Hoboken, NJ: John Wiley & Sons, 2005.
84. Mrad, Nezhir. "Potential of bragg grating sensors for aircraft health monitoring". *Transactions of the Canadian Society for Mechanical Engineering*, 31(1), 2007.
85. Negaard, Gordon. *The History of the Aircraft Structural Integrity Program*. Technical Report 680.1B, Wright-Patterson AFB OH: Aerospace Structures Information and Analysis Center, Jun 1980.
86. Neter, John, Michael Kutner, Christopher Nachtsheim, and William Wasserman. *Applied Linear Regression Models, Third Edition*. Richard D. Erwinm Inc., Chicago, IL, 1996.
87. Neumair, Manfred, Klaus P. Kress, and Matthias Buderath. "State of the Art and Experiences with Structural Health Monitoring". *Proceedings of the 3rd International Workshop of Structural Health Monitoring: The Demands and Challenges, Stanford University, 12-14 Sept 2001*, 206–220. Boca Raton, FL: CRC Press, 2000.
88. Nienwenhui, J. H., Jr. Neumann, J. J., D. W. Greve, and I. J. Oppenheim. "Generation and detection of guided waves using PZT wafer transducers". *IEEE Transactions on Ultrasonics, Ferroelectrics and Frequency Control*, 52(11):2103–2111, 2005.
89. Olson, S. E., M. P. DeSimio, and M. Derriso. "Piezo-Generated Lamb Waves for Structural Health Monitoring", Unpublished Draft, 26 October 2006.
90. Park, Gyuhae, Charles Farrar, Francesco Lanza di Scalea, and Stefano Coccia. "Performance assessment and validation of piezoelectric active-sensors in structural health monitoring". *Smart Materials and Structures*, 15(6):1673, 2006.

91. Park, Gyuhae, H. Wait, Hoon Sohn, and Charles Farrar. "Sensing System Development for Damage Prognosis". *Structural Health Monitoring 2003: From Diagnostics and Prognostics to Structural Health Management. Proceedings of the 4th International Workshop on Structural Health Monitoring*, 591. DEStech Publications, Inc, Lancaster, PA, 2003.
92. Pearson, E. S. and H. O. Hartley. *Biometrika Tables for Statisticians, Volume II*. New York, NY: Cambridge University Press, 1972.
93. PR Web News Release News Wire. "The LAHMP(TM) Health Monitoring System Recently Passed a Flight Test Aboard an F-15". Press Release. <http://www.emediawire.com/releases/system/flight/emw499270.htm>, 22 Jan 07.
94. Pyles, Raymond A. *Aging Aircraft, USAF Workload and Material Consumption Life Cycle Patterns*. Technical Report MR-1641-AF, Santa Monica CA: RAND, 2003.
95. Radio Technical Commission for Aeronautics. *Environmental Conditions and Test Procedures for Airborne Equipment*. RTCA/DO-160E. RTCA, Inc: Washington DC, Dec 2007.
96. Ragab, Abdel-Rahman and Salah Eldin Bayoumi. *Engineering Solid Mechanics, Fundamentals and Applications*. Boca Raton, FL: CRC Press, 1999.
97. Rice, T., R. Duncan, D. Gifford, B. Childers, K. Cooper, and K. Furrow. "Fiber optic distributed strain, acoustic emission, and moisture detection sensors for health maintenance [aircraft testing applications]". *Proceedings of the IEEE Systems Readiness Technology Conference: Future Sustainment for Military and Aerospace*. IEEE Aerospace and Electronic System Society, Piscataway, NJ, 2003.
98. Roach, Dennis, Kirk Rackow, Waylon DeLong, Steve Yopez, Dave Reedy, and Scott White. *Use of Composite Materials, Health Monitoring and Self-Healing Concepts to Refurbish Our Civil and Military Infrastructure*. Technical Report SAND2007-5574, Albuquerque, NM: Sandia National Laboratories, September 2007.
99. Rose, Joseph L. *Ultrasonic Waves in Solid Media*. Cambridge, MA: Cambridge University Press, 1999.
100. Rummel, Ward D. and Georgr A. Matzkanin. *Nondestructive Evaluation (NDE) Capabilities Data Book (3rd Edition)*. Technical Report AD-A286 978, Ft Belvoir, VA: Defense Technical Information Center, November 1997.
101. Sandia National Laboratories. "Application and Certification of Comparative Vacuum Monitoring Sensors for In-situ Crack Detection, Team Update", Unpublished Report, Mar 1 2007.

102. SAS Institute. *JMP Statistics and Graphics Guide, JMP Version 4*. SAS Institute Inc, Cary, NC, 2000.
103. Shapiro, S. W. and M. B. Wilk. "An analysis of variance test for normality (Complete Samples)". *Biometrika*, 52:591–611, 1965.
104. Singh, Ripudaman. *Three Decades of NDI Reliability Assessment*. Technical Report Karta-3510-99-01, San Antonio, TX: Karta Technologies, Inc, May 2000.
105. Spanier, Jerome and Keith B. Oldham. *An Atlas of Functions*. Hemisphere Publishing Corp, New York, 1987.
106. Spencer, Floyd W. "The Calculation and Use of Confidence Bounds in POD Models". *AIP Conference Proceedings*, 894(1):1791–1798, 2007.
107. Swets, J. "Measuring the Accuracy of Diagnostic Systems". *Science*, 1988.
108. Twisk, Jos W. *Applied Longitudinal Data Analysis for Epidemiology, A Practical Guide*. Cambridge University Press, New York, NY, 2003.
109. Underwood, Roman T. *Damage Detection Analysis Using Lamb Waves in Restricted Geometry for Aerospace Applications*. Master's thesis, AFIT/GAE/ENY/08-M29. School of Engineering and Management, Air Force Institute of Technology (AU), Wright-Patterson AFB OH, March 2008.
110. Underwood, Roman T. and Eric D. Swenson. School of Engineering and Management, Air Force Institute of Technology (AU), Wright-Patterson AFB, OH. Personal Interview, 2008.
111. Underwood, Roman T., Eric D. Swenson, and SomR Soni. "Structural health monitoring of aerospace applications with restricted geometry". *Health Monitoring of Structural and Biological Systems 2008*, volume 6935, 69350D. Proceedings of the SPIE, 2008.
112. Van Way, C. B., C. Marantidis, J. N. Kudva, and M. N. West. "Design Requirements and System Payoffs for an On-board Structural Health Monitoring System (SHMS)". *Proceedings of the SPIE - The International Society for Optical Engineering*, volume 2191 of *Smart Structures and Materials 1994*, 168–175. Orlando, FL: SPIE, 1994.
113. Vardeman, Stephan B. *Statistics for Engineering Problem Solving*. PWS Publishing Company, Boston, MA, 1994.
114. Wallace, M., H. Azzam, and S. Newman. "Indirect approaches to individual aircraft structural monitoring". *Proceedings of the Institution of Mechanical Engineers, Part G (Journal of Aerospace Engineering)*, 218:329–46, 2004.

<b>REPORT DOCUMENTATION PAGE</b>					<i>Form Approved</i> <b>OMB No. 0704-0188</b>	
The public reporting burden for this collection of information is estimated to average 1 hour per response, including the time for reviewing instructions, searching existing data sources, gathering and maintaining the data needed, and completing and reviewing the collection of information. Send comments regarding this burden estimate or any other aspect of this collection of information, including suggestions for reducing this burden to Department of Defense, Washington Headquarters Services, Directorate for Information Operations and Reports (0704-0188), 1215 Jefferson Davis Highway, Suite 1204, Arlington, VA 22202-4302. Respondents should be aware that notwithstanding any other provision of law, no person shall be subject to any penalty for failing to comply with a collection of information if it does not display a currently valid OMB control number. <b>PLEASE DO NOT RETURN YOUR FORM TO THE ABOVE ADDRESS.</b>						
<b>1. REPORT DATE (DD-MM-YYYY)</b> 30-09-2009		<b>2. REPORT TYPE</b> Doctoral Dissertation			<b>3. DATES COVERED (From — To)</b> Aug 2006 — Sep 2009	
<b>4. TITLE AND SUBTITLE</b>  Changes in Structural Health Monitoring System Capability Due to Aircraft Environmental Factors				<b>5a. CONTRACT NUMBER</b>		
				<b>5b. GRANT NUMBER</b>		
				<b>5c. PROGRAM ELEMENT NUMBER</b>		
<b>6. AUTHOR(S)</b>  Kuhn, Jeffrey D., Major, USAF				<b>5d. PROJECT NUMBER</b>		
				<b>5e. TASK NUMBER</b>		
				<b>5f. WORK UNIT NUMBER</b>		
<b>7. PERFORMING ORGANIZATION NAME(S) AND ADDRESS(ES)</b> Air Force Institute of Technology Graduate School of Engineering and Management (AFIT/EN) 2950 Hobson Way WPAFB OH 45433-7765					<b>8. PERFORMING ORGANIZATION REPORT NUMBER</b>  AFIT/DS/ENV/09S-01	
<b>9. SPONSORING / MONITORING AGENCY NAME(S) AND ADDRESS(ES)</b>  Intentionally left blank					<b>10. SPONSOR/MONITOR'S ACRONYM(S)</b>	
					<b>11. SPONSOR/MONITOR'S REPORT NUMBER(S)</b>	
<b>12. DISTRIBUTION / AVAILABILITY STATEMENT</b>  Approval for public release; distribution is unlimited.						
<b>13. SUPPLEMENTARY NOTES</b>						
<b>14. ABSTRACT</b> Structural Health Monitoring (SHM) promises to decrease the maintenance cost and increase the availability of aging aircraft fleets by fundamentally changing the way structural inspections are performed. But this promise can only be realized through the consistent and predictable performance of a SHM system throughout the entire remaining life of an aircraft. A design of experiments approach is used to build and execute an experiment to determine the effect of one aircraft environmental factor (cyclic strain) on a common SHM technology (PZT-based sensors). Analysis of results shows the sensors to be significantly affected by cyclic strain, and that the effects can be estimated using a power equation model. A “probability of detection (POD) degradation model” is also developed by extending existing nondestructive evaluation (NDE) POD analysis techniques. This model demonstrates how changes in sensor performance due to an aircraft environmental factor can be used to estimate the change in overall performance of the SHM system and provides a common framework to predict changes in SHM system performance over the remaining life of an aircraft.						
<b>15. SUBJECT TERMS</b>  Structural Health Monitoring, Piezoelectric Transducers, Sensor Durability, Probability of Detection						
<b>16. SECURITY CLASSIFICATION OF:</b>			<b>17. LIMITATION OF ABSTRACT</b>		<b>18. NUMBER OF PAGES</b>	
a. REPORT	b. ABSTRACT	c. THIS PAGE	UU		243	
U	U	U	<b>19a. NAME OF RESPONSIBLE PERSON</b> Dr. Som R. Soni			
						<b>19b. TELEPHONE NUMBER (include area code)</b> (937) 255-3636, ext 3420; som.soni @ afit.edu